Experiments and Modeling of Impinging Jets and Premixed Hydrocarbon Stagnation Flames

Thesis by

Jeffrey Myles Bergthorson

In Partial Fulfillment of the Requirements

for the Degree of

Doctor of Philosophy

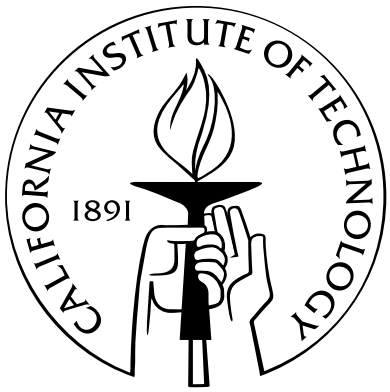

California Institute of Technology

Pasadena, California

2005

(Submitted May 26, 2005)

Acknowledgements

I would like to thank my advisor, Professor Paul Dimotakis, for his mentorship, guidance, and support during my time at Caltech. His enthusiasm for science, and his belief that his students are capable of anything, continue to inspire me. I appreciate the freedom that I was given in guiding the course of the research, it allowed me to explore and learn more than I otherwise might have.

I am also indebted to the other members of my committee, Professors David Goodwin, Aron Kuppermann, Dan Meiron, and Joseph Shepherd, for their constructive criticism of this thesis. Their suggestions improved the work considerably. I would especially like to thank Prof. David Goodwin for his assistance with the CANTERA software package, both for developing this powerful scientific tool and for his assistance with problems that arose in its use. Prof. Joe Shepherd's many valuable comments on this work over the years always inspired me to think along a different line and improved the quality of the work considerably.

This thesis contains the input of many collaborators whose help I am grateful for. Kazuo Sone performed the direct numerical simulations of the impinging jet, and our discussions led to improvements in both my experiments and in his numerical studies. Trent Mattner always inspired me to look deeper into the problem at hand and he performed potential-flow simulations of the impinging jet that are included in this thesis. Laurent Benezech assisted me with many of the experiments and analysis reported here. His quick laugh and friendly nature helped make both the office and the lab an enjoyable place to be.

This work would not have been possible without the genious of Dr. Dan Lang. His assistance with digital imaging, electronics, data acquisition, and all computer matters was invaluable. Garrett Katzenstein was always there for me to bounce mechanical design ideas off of, and his assistance helped make the experiments a success. I would also like to thank the gentlemen of the Aeronautics machine shop for their hard work and care in creating the parts that made up the experimental apparatus. Christina Mojahedi helped to keep things running so that I could focus on my work, and was always there for a coffee break to clear my thoughts. Caltech has been a great place to study because of the great people that make up GALCIT. I would also like to acknowledge the hard work of the Caltech library staff in making my thesis data available on the web.

This work was funded by the Air Force Office of Scientific Research, with additional funding

through the Caltech Northrop Chair. Kazuo Sone received funding through the Caltech center of the Department of Energy's Accelerated Strategic Computing Inititative (ASC).

My years at Caltech would not have been as enjoyable without the many friends I have shared them with. Michael Johnson's constant smile brightened every day, and our many discussions greatly improved the quality of this research. Thanks to Andy Spakowitz, David Barsic, Ali Husain, Will Green, and Carl Hansen for being great friends and for teaching me a little about their respective fields of study. The Caltech Rugby Football Club provided me with an outlet for my frustrations and I am grateful to all of the past and current members of the team for their friendship.

I thank my family for their unconditional love and support. It was my parents who first instilled in me the drive for learning and the desire for perfection that led me to seek out this path of higher education. This thesis is dedicated to my wife, Melanie, for her constant support and encouragement as I completed this phase of my education. She supported me in this endeavor even when it meant that we would be separated for three years, and her ability to listen allowed me to discover many of the answers to my own questions. She was always willing to help in any way, and her careful proofreading of various papers and this thesis have improved the quality of all of my work.

Abstract

The development of a predictive chemical-kinetic model to describe the combustion of hydrocarbon fuels is one of the most important research areas in combustion. The key to understanding and modeling the combustion of hydrocarbon fuels is to obtain an accurate chemical-kinetic model for the oxidation of C_1 and C_2 hydrocarbons. As longer hydrocarbon chains are investigated, all of the reactions associated with smaller hydrocarbons must be included, as well as reactions that account for the breaking up of these chains into C_1 and C_2 fragments. In order to model the combustion of gasoline, kerosene, or other long-chain hydrocarbon fuels, the combustion chemistry of methane, ethane, ethylene, etc., must first be accurately modeled. Unfortunately, due to a lack of kinetically independent experimental data, a generally accepted mechanism for methane is still elusive.

This experimental study is aimed at developing a technique that can quickly and accurately obtain measurements to further constrain and validate these mechanisms, towards the eventual development of a fully constrained kinetics mechanism for small hydrocarbons. The approach presented here relies on detailed measurements of strained flames in a jet-wall stagnation flow. This setup yields a flow with boundary conditions that can be accurately specified, facilitating simulation and comparisons with experiment. The diagnostics are optimized for accuracy, minimal flame disturbance, and rapid simultaneous recording of flow velocity and CH radical profiles. Flame simulations utilize a one-dimensional hydrodynamic model, a multicomponent transport formulation, and various detailed-chemistry models. Direct comparisons between experiment and simulation allow for an assessment of the various models employed, with an emphasis on the chemistry model performance.

Cold impinging jets are an important flow in many contexts and are utilized to stabilize premixed stagnation flames. Particle Streak Velocimetry (PSV) is used to measure axial velocity profiles for laminar impinging jets as a function of the nozzle-to-plate separation distance and Reynolds number. The velocity profiles for impinging jets are modeled using empirical fits, a one-dimensional streamfunction model, an axisymmetric potential-flow model, and direct numerical simulation. The flow field for an impinging laminar jet is found to be independent of the nozzle-to-plate separation distance if velocities are scaled by the Bernoulli velocity. The one-dimensional formulation is found to accurately model the stagnation flow if the velocity boundary conditions are appropriately specified. The boundary-layer-displacement-thickness corrected diameter is found to be an appropriate scale

for axial distances and allows the identification of an empirical, analytical expression for the flow field of the impinging laminar jet.

Strained methane-air flame experiments confirm that the reacting flow is also independent of the nozzle-to-plate separation distance. Methane, ethane, and ethylene flames are studied as functions of the applied strain rate, mixture dilution, and mixture fraction. The model performance is found to be relatively insensitive to both the mixture dilution and the imposed strain rate, while exhibiting a stronger dependence on the flame stoichiometry. The approach and diagnostics presented here permit an assessment of the numerical simulation predictions of strained-hydrocarbon flames. While GRI-Mech 3.0 and the C_3-Davis models accurately predict experiment in some cases, the 2005 revision of the San Diego mechanism is found to give the best agreement with experiment for methane, ethane, and ethylene flames. The data presented in this thesis are made available to kineticists looking for optimization targets, with the goal of developing a fully constrained, predictive, kinetics model for hydrocarbon fuels. The methodology described here can allow new optimization targets to be rapidly measured, reducing the experimental burden required to fully constrain the chemistry models.

Contents

List of Figures

List of Tables

Chapter 1

Introduction

Science is a business of developing and testing models of the physical world. Significant progress has been made in the simulation of complicated fluid mechanics problems. The simulation of realistic combustion problems has, however, faced several difficulties. In fluid mechanics, general conservation equations (mass, momentum, energy) and an equation of state suffice to describe the behavior. The complexity associated with many flows indicates the wide variety of behavior that these equations allow. In combustion, the inclusion of chemistry requires a conservation equation for each *species* present in the flame, including source and sink terms due to chemical reactions. The reaction rates in the source and sink terms are themselves functions of the local composition, temperature, and, in some cases, pressure. Each chemical reaction must be modeled to account for these dependencies. A chemical-kinetics mechanism is a compilation of these individual reactions, each with an associated rate constant expression, that models the combustion chemistry. The inclusion of chemistry results in a very large, complicated, and numerically stiff problem. The large computational cost associated with implementing realistic chemistry models has impeded progress towards simulating practical combustor geometries. To reduce the computational cost, premixed laminar "flamelets" have been used to simulate turbulent combustion problems (*e.g.*, Peters 1986; Williams 2000; Law & Sung 2000). These laminar flamelets rely on modeling, simulations, and experiments to determine the flame response to turbulent straining. The simulations of flamelets are typically performed using simplified one-dimensional hydrodynamic equations. In these simplified flows, detailed chemistry models may be utilized without excessive computational cost. Examples of such simplified flame geometries are the premixed laminar flame and the strained stagnation-point flame. It is interesting to note that even 50 years ago, many chemists "dismiss(ed) flames as being too hopelessly complicated for fruitful study in any fundamental way" (Fristrom & Westenberg 1965; preface). The large number of species and reactions required to describe the flame propagation of simple hydrocarbon fuels such as methane and ethylene supports this pessimistic view.

A chemical-kinetic mechanism can be considered adequate only if it can describe all relevent chemical responses over the diverse range of parametric and system variations that are expected

to occur (Law *et al.* 2003). An ongoing problem in combustion research is the fact that such kinetic models are lists of reaction-rate coefficients that contain uncertainties. The nonlinearity of the chemical source terms results in a high-sensitivity of the numerical results to several of the important chemical reactions and their associated uncertainties. These can then be propagated through the problem and can result in a large uncertainty in the computed results (Turányi *et al.* 2002). Usually these mechanisms are composed of elementary reactions whose rate parameters are collected from literature recommendations. While the individual parameters may have been validated under isolation, the combined model usually does not reproduce experimental results. Thus, assigning best-fit values to individual parameters does not necessarily result in a best-fit mechanism (Frenklach *et al.* 1992).

The chemical-rate uncertainties stem from the fact that direct experimental measurement of many of the reaction rates is difficult. In addition, theoretical estimates of kinetic rates contain uncertainty due to modeling assumptions (Wagner 2002). Progress in the field of chemical kinetics will determine an increasing number of the reaction-rate parameters to higher accuracy. At present, only for a few reactions are the rate constants known better than within a factor of two (Frenklach & Bornside 1984; Williams 2000). In addition to chemical-kinetic rates, other model parameters, such as thermodynamic and transport properties, contain uncertainty (Burcat 1984; Law *et al.* 2003; Frenklach *et al.* 2003; Simmie 2003). For example, transport coefficients (Paul & Warnatz 1998; Yang *et al.* 2001), as well as the enthalpy of formation of OH (Herbon *et al.* 2002), have undergone recent revision. It has been shown, for example, that in the simulation of laminar flame speeds of hydrogen-air mixtures the sensitivity coefficients computed for the binary diffusion coefficients of H-N_2 are larger than those computed for the rate constant of the $H + O_2 \rightarrow O + H$ chain branching reaction (Yang *et al.* 2001; Law *et al.* 2003). For hydrocarbon flames it is also found that the influence of H-atom diffusion is comparable to that of the same branching process.

Turányi *et al.* (2002) have found that the predicted methane-air laminar flame speed has an associated error of $2-5$ cm/s, when the uncertainties of the individual reaction rates and thermodynamic data are propagated. The calculated maximum concentration of CH and CH_2 radicals also had high associated uncertainties. A small number of reactions were found to cause the most uncertainty in the calculated burning velocity and radical concentration profiles of hydrogen-, methane-, and propane-air flames. The authors also point out that the "agreement" between experimental flame velocities and simulation is essentially a result of "fine tuning" of the mechanisms. Moreover, multiple reaction mechanisms have been developed that use very different rate expressions yet produce similar results (Simmie 2003). The disturbing conclusion is that the oxidation chemistry of simple fuels such as CO, CH_4 and C_2H_6 is still not well-characterized at an elementary level (Hughes *et al.* 2001).

Combining the uncertainties of each reaction (or other parameter) creates a hypercube in the

parameter space (Frenklach *et al.* 1992). This author points out that each point in the hypercube is equally probable and physically reasonable. He remarks that the optimum strategy towards achieving a physically reasonable model is to reduce the individual parameter uncertainties in isolation of the rest. However, this remains elusive even with significant advances in both theory and experiment. It is important to note that the uncertainties from both experiment and theoretical predictions are usually miscontrued to be percentage-magnitude random error of individual measurements, rather than being correctly ascribed to systematic error (Warnatz 1984b; Frenklach *et al.* 1992). One of the most promising approaches taken to produce a physically relevent model is to "tune" a kinetics model, within the individual parameter uncertainties, to fit a set of experimental data (*e.g.*, Smith *et al.*; Frenklach 1984; Frenklach *et al.* 1992, 2003), thus resulting in the location of the optimal point within the uncertainty hypercube. Unfortunately, this optimization is often ill-resolved due to an insufficient number of degrees of freedom resulting from a lack of mathematically independent experimental data (Frenklach *et al.* 1992; Qin *et al.* 2000). It is not necessary to search for a single experimental condition in which all of the parameters of interest are active. Instead, a strategy of performing experiments where different subsets of parameters are active and combining the results into a joint optimization can be adopted (Frenklach *et al.* 1992). Thus, the goal of mechanism development should be to accurately predict *all* existing relevant experimental data (Frenklach *et al.* 1992, 2002). The resulting mechanism should be a *living model*: not the ultimately right one, but the best possible *today*, consistent with all available data and research results (Frenklach *et al.* 2002).

A recent validation and optimization study (GRI-Mech 3.0: Smith *et al.*) relied on the use of shock tube initiation data and species profiles (*e.g.*, Eiteneer & Frenklach 2003), laminar flame-speed measurements (*e.g.*, Vagelopoulos *et al.* 1994), maximum radical concentrations (*e.g.*, CH: Luque *et al.* 1996), and flow reactor data (*e.g.*, Glarborg & Miller 1994) as optimization targets. The use of such diverse experimental targets in the optimization is possible through the use of surface mapping or the response-surface method (Frenklach & Bornside 1984; Frenklach *et al.* 2002, 2003). Such surface mapping techniques rely on replacing the computationally prohibitive differential equation models of combustion with polynomial response functions in the optimization variables (Frenklach & Bornside 1984; Frenklach 1984; Frenklach *et al.* 1992, 2003). These response functions model the effect that a change in each included parameter has on the experimentally observed quantity. Recent results by Davis & Wang (2002) indicate that the response surface may be estimated through the use of local, explicit, sensitivity analysis. These authors showed that, in many cases, the resulting response surfaces more accurately modeled the phenomenon than traditional factorial designs (factorial design: Box *et al.* 1978; Frenklach 1984; Frenklach & Bornside 1984), while resulting in an order of magnitude decrease in computational cost. The use of sensitivity analysis to determine the response surface increases the flexibility of the overall methodology. The response-surface method

allows the optimization problem to be decoupled from the simulation of the individual experimental phenomena, resulting in a computationally tractable problem that can support varied experimental data.

To allow a kinetics mechanism to be optimized against all available experimental data, the collaborative data approach is recommended by Frenklach *et al.* (2003). In the collaborative data approach to combustion modeling, reporting an experiment consists of documenting the measured outcome of the experiment, the estimated experimental uncertainty, and a model of the experimental system. This approach is flexible enough to allow an experimenter to choose an experimental configuration and techniques that can be performed and modeled to the highest possible accuracy. Although the technique allows for the use of a large amount of data, due to the lack of independent experimental optimization targets, a unique model for methane combustion is still elusive (Frenklach *et al.* 1992).

A comprehensive study of the performance of a combustion chemistry model must include extensive and independent variations in the system pressure, characteristic temperature, and concentrations of the reacting mixture (Law *et al.* 2003). In addition, laminar flame properties as a function of stoichiometry and pressure, as well as the properties of methane-additive mixtures, should be studied (Frenklach *et al.* 1992). Such a study must produce experimental data of high-fidelity for model comparisons to be valid and to allow subsequent optimization in regions where the model fails (Law *et al.* 2003). In that paper, the authors advocate that "a concerted experimental and modeling effort be implemented to develop detailed, comprehensive mechanisms that are capable of describing diverse combustion and flame phenomena." Thus, it is critical to the advancement of our knowledge of hydrocarbon combustion to increase the available experimental database against which such models can be validated and/or optimized. It should also be noted that not every experimental data point will increase the number of degrees of freedom, or system constraints, required for improved model performance (Frenklach *et al.* 1992). The use of the response-surface method should allow the identification of experiments that will improve the accuracy of the predictive model (Frenklach *et al.* 1992, 2002). A major goal of this work is to develop an experimental approach of high accuracy that can be used to assess current model performance and produce data that could be used as optimization targets for the next generation of combustion models. This experimental approach must be coupled with the ability to accurately simulate the phenomenon to allow its inclusion in future model optimizations.

The study of chemistry in complex reaction systems is facilitated through a choice of simple flow conditions and a simple geometry (Warnatz 1992). A "simple" flow is one that can be described by a reduced hydrodynamic equation, thus allowing the inclusion of detailed chemistry and multicomponent transport in the simulations. One example of such a simplified flow is the premixed laminar flame. The use of laminar flames and flame structure to investigate chemical kinetic and transport models has a long history, with considerable progress in the field due to these experimental investi-

gations (Fristrom & Westenberg 1965). One flow geometry that has received significant attention in the combustion community is the use of stagnation-point flows to study planar, strained, premixed flames. To study the pertinent chemical phenomena, these flames should be amenable to "one-dimensional analysis," even though the experimental flame may be geometrically complex (Miller *et al.* 1990). In addition, the flames must be amenable to experimental diagnostics so that chemical information can be extracted (Miller *et al.* 1990). Stagnation flames can provide an invaluable development, validation, and optimization test bed for transport and kinetics models as they can be simulated using a one-dimensional hydrodynamic model. As numerical and experimental techniques advance, an improved ability to make detailed comparisons between experiment and models leads to the development of increasingly accurate models. The study of strained flames can also provide data for laminar flamelet models, which can then be applied to complicated turbulent combustion flows. Stagnation-point flames are important in many technical applications, such as Chemical Vapor Deposition (CVD), the modification of thin polymer films, and altering metal surfaces to create carbides (Kee *et al.* 2003).

Experimental work in stagnation flames have utilized a jet-wall configuration (*e.g.*, Law *et al.* 1981; Egolfopoulos *et al.* 1997; Vagelopoulos & Egolfopoulos 1998; Dong *et al.* 2002), or an opposed-jet stagnation flow (Ishizuka & Law 1982; Sato 1982; Chao *et al.* 1997). The jet-wall configuration typically results in nonadiabatic flames due to heat loss to the solid wall, while the opposed-jet configuration allows the study of essentially adiabatic flames due to the symmetry of the dual-flame configuration. Cool stagnation walls introduce a heat sink to the flow, and for sufficiently large degrees of cooling, and sufficiently large rates of strain, extinction will be induced (Libby & Williams 1983). Libby and coworkers also note that the density decrease near the wall, resulting from the flame heat release, creates a form of fluid-mechanical insulation that reduces gradients and heat loss (Libby & Williams 1983; Libby *et al.* 1983). Indeed, heat loss can tend to make the planar flame more robust to cellular instabilities. In studies of opposed-jet flames, difficulties arise in determining the location of the stagnation point, exacerbated if slight fluctuations or time variations in jet momentum cause this point to move in space during the course of an experiment. In addition, the coupling of the acoustic properties of the two jets could lead to oscillations and instabilities in the flames. Impinging-jet flames are found to be more stable than those in the opposed-jet configuration (Egolfopoulos *et al.* 1997).

Typical experiments in stagnation flows rely on mapping the velocity field for a range of imposed strain rates and extrapolating the strained flame data to zero strain rate to yield an estimate of the laminar flame speed (Wu & Law 1984; Egolfopoulos *et al.* 1989, 1990; Hirasawa *et al.* 2002). More recently, measurements have also made use of the planar-Bunsen transition to measure the "true laminar flame speed" as the flame transitions from positive (planar) to negative (Bunsen) stretch (Vagelopoulos & Egolfopoulos 1998; Dong *et al.* 2002). These studies comprise a large dataset

on laminar flame speeds for low-carbon number hydrocarbons (*e.g.*, methane, ethane, ethylene). Laminar flame speeds are typically calculated through the use of one-dimensional freely propagating flame-simulation codes (Grcar *et al.* 1986), using detailed chemistry and multicomponent transport models. This allows partial validation of the chemical-kinetics models through comparison with the available experimental dataset. However, the various laminar flame speed measurements inherently contain uncertainty as the flame speed is measured indirectly. Such measurements can rely on extrapolations to zero strain rate, which can introduce significant errors due to non-linearity in the flame-speed, strain-rate relationship (Tien & Matalon 1991; Vagelopoulos *et al.* 1994; Holley *et al.* 2003), or planar-Bunsen transitions, which may be unsteady, occur in a very short timescale, or entail non-one-dimensional flow effects, making it difficult to capture "zero-strain-rate flame" behavior. Andrews & Bradley (1972) note that the

> Burning velocity is a physicochemical constant for a given combustible mixture. It is the velocity, relative to the unburnt gas, with which a plane, one-dimensional flame front travels along the normal to its surface. It is the eigenvalue of the one-dimensional flame equations. Unfortunately, although its theoretical definition is simple, the same cannot be said of its practical measurement.

These authors present a thorough review of flame speed measurements, and show the large amount of scatter in the measured flame speed data for methane-air, and other simple hydrocarbon, flames. While significant scatter exists in the available datasets, it appears that more recent measurements are converging, possibly due to the use of more refined experimental techniques (Bosschaart & de Goey 2004). Such laminar flame speed measurements do not provide information on the strained flame response, and have not been able to provide sufficient data to fully constrain current kinetics models. It should also be noted that the determination of laminar flame speeds from stagnation flame experiments typically requires many experiments at each equivalence ratio. The single number obtained from this multitude of experiments is then compared to model predictions. The research presented in this thesis is aimed at making direct comparisons between model predictions and detailed experimental data in stagnation-point flows. This methodology allows each experiment to be compared directly with simulations, reducing the experimental burden required to acquire data that can further constrain the chemistry model.

The hydrodynamics of axisymmetric stagnation-point flows have been modeled using a one-dimensional streamfunction that is an extension of Hiemenz flow (see Schlichting 1960; Sivashinsky 1976; Seshadri & Williams 1978; Kee *et al.* 2003). This hydrodynamic model has been used in studies of strained-premixed flamelets (Sivashinsky 1976; Seshadri & Williams 1978; Buckmaster 1978). Two reviews of laminar flame, or flamelet, research are given by Williams (2000) and Law & Sung (2000). Due to advances in combustion research over the last 30 years, the basic laminar

flamelet structure is now considered to be well-understood. This progress was due to advances in large activation energy asymptotics (*e.g.*, Durbin 1982), the ability to numerically simulate flamelets with simple chemistry (*e.g.*, Rogg 1988), and the introduction of detailed chemistry and transport into these flow models (*e.g.*, Kee *et al.* 1988).

Durbin (1982) discusses the premixed flame in uniform straining flow using activation-energy asymptotics. This author finds that heat loss tends to promote extinction by straining, a result confirmed by the experiments of Ishizuka *et al.* (1982). A large amount of theoretical work (large activation-energy asymptotics) on the effects of strain rate, nonadiabaticity, and Lewis number on premixed flames is presented in a series of papers by Libby and coworkers (Libby & Williams 1983; Libby *et al.* 1983; Libby & Williams 1987). This high activation-energy asymptotic formulation was also studied numerically (Darahiba *et al.* 1986). Laminar flamelets in stagnation flows were studied numerically by Rogg (1988) using an 18-step chemical model. The effect of stretch on flames has also been studied using an integral approach by Law and coworkers (Chung & Law 1988, 1989; Sun *et al.* 1999; Sun & Law 2000), with several of the studies including non-adiabatic effects (Chung & Law 1988; Sun & Law 2000). Tien & Matalon (1991) found that the flame speed varied nonlinearly with the applied flame stretch, indicating that laminar flame speeds should be estimated by a nonlinear extrapolation to zero strain. Premixed flames in counterflowing jets are discussed analytically, numerically, and experimentally by Chao *et al.* (1997). These authors find that the nonlinear variation of the minimum velocity point with varying strain can be minimized by utilizing nozzles with large separation distances. Another analytical study showed that the use of a hot wall could result in the appearance of new flame bifurcations (Ju & Minaev 2002). Additional analyses on stretched premixed flames are also available (Bechtold & Matalon 1999; Davis *et al.* 2001; Davis & Searby 2002).

The first comparisons between predictions of the one-dimensional streamfunction model (utilizing potential-flow boundary conditions) and flame experiments in jet-wall stagnation flow is given in a pair of papers by Smith *et al.* (1971) and Fang *et al.* (1971). They remarked that "such comparisons would seem to provide a useful means of studying kinetics of combustion reactions in certain instances and of investigating the basic behavior of combustible mixtures when convection, diffusion and finite-rate chemical kinetics are of interest." Global extinction strain rates (nozzle velocities divided by the diameter) and heat flux measurements were compared to predictions.

Experiments in jet-wall stagnation flow are discussed in a series of papers by Mendes-Lopes and coworkers (Daneshyar & Mendes-Lopes 1982; Daneshyar *et al.* 1982; Mendes-Lopes & Daneshyar 1985). Laser-Doppler Velocimetry (LDV) was utilized to measure axial and radial velocity profiles in cold and reacting stagnation flames with separation distances between 0.74 and one nozzle diameter. The radial profile of the axial velocity was shown to exhibit a velocity defect at the nozzle centerline, while the axial and radial velocity profiles exhibited characteristics typical of stagnation-point flow

(Daneshyar *et al.* 1982). They also found that the flow could be approximated by a dual axisymmetric stagnation-point flow, where the first stagnation flow is toward an apparent plane determined by the flame dilatation, and the secondary flow impinging on the stagnation surface (Mendes-Lopes & Daneshyar 1985). It was also found that the strain rate did not depend on the nozzle-plate separation distance, although the flame stability was dependent on this distance (Mendes-Lopes 1983). Experimentally measured velocity profiles, using LDV, and temperature profiles, using thermocouples, were compared to theoretical predictions using several matching parameters, such as the upstream and downstream strain rates, flame thickness and burning velocity. Good agreement was found between the "fit" profiles and their data, indicating that the model can capture the basic features of the flow. These authors find that increasing strain rate tends to decrease the burning velocity, and that the effect of straining is more pronounced when there is heat loss from the reaction zone to the cold stagnation plate (Daneshyar *et al.* 1982; Mendes-Lopes & Daneshyar 1985). The Ph.D. thesis of Mendes-Lopes (1983) contains some of the only available velocity profile data for cold impinging-jet flows. This author discusses that the gradients in the near wall region are not sensitive to the separation distance and depend only on the nozzle-exit velocity. The axial velocity profile was found to contain all of the information required for their analysis and the plate temperature did not exhibit a strong influence on the flame. The experimental data of Mendes-Lopes and Daneshyar is compared to theoretical predictions by Eteng *et al.* (1986) and Kim & Matalon (1988), through fitting of the potential flow model to the strain rate just upstream of the flame. Again, the theoretical model is able to capture the basic flow features, if the input parameters are appropriate. The displacement effects of laminar flames are discussed by Kim *et al.* (1992). They find that the dilatation introduced to the flow by the accompanying heat release can significantly alter the strain rate in the flow external to the flame. This indicates that care must be taken when determining the strain-rate parameter to ensure that valid comparisons are made between theoretical predictions and experimental results.

The computation of flames in opposed and impinging jets is also discussed by Libby & Smooke (1997). The two standard boundary condition formulations (potential- and plug-flow) are discussed, along with the fact that the practice of shifting experimental data to achieve agreement with calculations results in questionable rates of strain to be attributed to the data. Libby (1998) presents results from an asymptotic model for premixed flames in jet-wall stagnation flows, where the flame is separated from the stagnation surface. In that work, the inlet-velocity-gradient boundary condition is considered arbitrary, and the results are compared to experimental velocity profiles measured by Bédat & Cheng (1996). It is noteworthy that the comparison was made to experimental data from a buoyancy-stabilized flame, obtained by issuing a premixed jet from a downward-pointing nozzle, due to a dearth of published data in this flow geometry. The velocity profile in this flame exhibits typical stagnation-flow features, with a stagnation point being created due to the opposition of the

jet momentum and buoyancy forces. The flowfield was measured using a two-component LDV system in that study (Bédat & Cheng 1996). The results indicate that this simple model exhibits the main features of the experimental flow, although there are a large number of adjustable parameters used to fit to the data (Libby 1998). Frouzakis *et al.* (1998) simulated an opposed-jet diffusion flame in an axisymmetric flow geometry using the spectral-element technique. These authors utilized both parabolic and plug-flow boundary conditions at the jet exits and found that the traditional one-dimensional streamfunction can adequately model the flow if the nozzle-exit profile is uniform, up to a nozzle diameter-to-nozzle separation ratio of one.

Including full transport and chemistry models with the one-dimensional hydrodynamic model allows the simulation of experimental strained premixed flames (Kee *et al.* 1988; Dixon-Lewis 1990). However, few comparisons have been performed between these models and experimental data. Temperature and concentration measurements made using thermocouples and a microprobe gas chromatograph are compared to numerical simulations using such a model by Smooke *et al.* (1990). Law and coworkers studied methane-air, opposed-jet flames for lean, stoichiometric, and rich mixtures, using LDV and Coherent Anti-Stokes Raman Spectroscopy (CARS) for velocity, temperature, and major-species measurements, in an effort to quantify the effect of stretch on flame structure (Law *et al.* 1994; Sung *et al.* 1994, 1996a,b; Sun *et al.* 1996). To compare experimental and simulated data, a potential-flow boundary condition with a variable inflow mass flux is used to visually match the profiles (Law *et al.* 1994). The authors report general agreement for temperature and major species profiles when the flame location is adjusted to match the measurements. A consistent comment in these papers is the lack of experimental data on flames in stagnation flows.

The effects of thermophoresis on the measurement of velocity profiles in flames is discussed in a pair of papers by Sung and coworkers (Sung *et al.* 1994, 1996a). They found that considerable lag could result between the measured and computed velocity profiles in the post-flame region, even for the submicron-sized particles used in those studies. These authors utilize the simulated velocity and temperature profiles to estimate the expected particle velocity profile when thermophoretic effects are included. The effects of thermophoresis are more pronounced for flames close to the stagnation surface (highly strained flames), due to the comparable magnitudes of the local flow and thermophoretic velocities (Sung *et al.* 1996a). In the work of Sung *et al.* (1996a; Appendix), an initial simulation utilizing the plug-flow boundary condition was performed. Through a continuation method (see Nishioka *et al.* 1996), the inlet velocity and velocity gradient were adjusted to determine the inlet boundary condition that matched the (cold-flow) experimental data.

Experimental velocity profiles, measured using LDV, in premixed flames are presented in Yang & Puri (1993). Cold and reacting turbulent stagnation flows are studied experimentally by Escudié *et al.* (1999), who note the existence of a virtual stagnation point in the reacting flows. Jackson *et al.* (2003) discuss flame strengthening due to hydrogen addition in lean premixed methane flames

in highly strained flows. They comment that the use of bulk flows for velocity determination is not appropriate, but that experimental velocity-profile measurements should be used. They also indicate that the submicron-sized particles used in their LDV measurments did not capture the sharp velocity gradients in the flame and post-flame zone, and suggest thermophoretic forces to be responsible, as found in earlier studies (Sung *et al.* 1994, 1996a).

Ishizuka *et al.* (1982) studied the effects of heat loss, preferential diffusion and flame stretch on the stability and extinction properties of propane-air mixtures in jet-wall stagnation flows. These authors discuss the possible flame configurations in jet-wall flows (and the hysteresis exhibited by these flames) and found that even a small amount of heat loss to the wall can result in extinction at a finite distance from the wall. Egolfopoulos *et al.* (1997) studied the effects of a variable temperature wall on the propagation and extinction of premixed laminar flames. This study showed that radical recombination at the wall is unimportant for wall temperatures below approximately 1000 K. They also found that extinction is largely controlled by the heat loss to the plate, but that the extinction strain rate is weakly dependent on the wall temperature, similar to the results found by Law *et al.* (1981). The reference flame speed, $S_{u,\mathrm{ref}}$, for flames well-separated from the wall was found to be independent of the wall temperature. These authors also note that impinging-jet flows result in more stable flames compared to the opposed-jet configuration (Egolfopoulos *et al.* 1997).

The one-dimensional stagnation-flow model also allows for the simulation of extinction strain-rates (Giovangigli & Smooke 1992), allowing comparisons to experimental measurements (*e.g.*, Egolfopoulos *et al.* 1997; Zhang & Egolfopoulos 2000; Dong *et al.* 2003). Davis *et al.* (2001) found that the simulated extinction strain rate was sensitive to the choice of upstream boundary conditions (*e.g.*, plug- or potential-flow), with considerable differences in the resulting predicted values, *i.e.*, outside of typical experimental uncertainty. To compare extinction data with simulations, the simulated flowfield must accurately capture the experimental flow.

Laminar flame-speed and extinction strain-rate data study two extreme values of the range of strain rates that flames can be subject to. To probe the models over a wide variety of conditions (*e.g.*, equivalence ratio, ambient pressure, strain-field) studies of strained laminar flames in additional environments are desirable. The high parametric dimensionality of the kinetic and transport models requires many detailed and accurate experiments over a sufficiently large range of conditions. The experimental burden imposed by these requirements is exacerbated when performing laminar flame speed measurements, as multiple experimental datasets are required to produce a single optimization target. The approach in the research presented here is to directly compare measurements of strained premixed flames to simulations, resulting in a possible optimization target for every experiment performed. Such experiments could be used to produce a dataset with sufficient parametric dimensionality to fully constrain the kinetics optimization. Strained-flame experiments are enhanced by simultaneous diagnostics that permit detailed flow and chemical-species data to be

recorded and compared to model predictions. The approach here relies on detailed measurements of strained flames in a jet-wall stagnation flow. This setup yields a flow with boundary conditions that can be accurately specified, facilitating simulation and comparisons with experiment. This flow can also, with care, be stable to high Reynolds numbers. The diagnostics are optimized for accuracy, minimal flame disturbance, and rapid simultaneous recording of flow velocity and CH radical profiles.

Flow velocities in impinging jets and strained premixed flames have been measured by various means, such as Laser-Doppler Velocimetry (LDV) (Rolon *et al.* 1991; Kurosoy & Whitelaw 2001; Wu & Law 1984; Zhu *et al.* 1988; Egolfopoulos *et al.* 1997) or Particle Image Velocimetry (PIV) (Maurel & Solliec 2001; Hishida & Sakakibara 2000; Dong *et al.* 2002; Hirasawa *et al.* 2002). In this study, Particle Streak Velocimetry (PSV, see Appendix B) is used to obtain instantaneous flowfield measurements and, in particular, axial velocities along the flow centerline. Improvements to the methodology are implemented in this work, including the addition of digital imaging, image processing, and new analysis techniques. The implementation yields a Lagrangian measurement of velocity that, in principle, requires only a single particle traversing a flame. These improvements allow quantitative velocity data to be obtained throughout the flowfield with PSV, without excessive post-processing. The resulting PSV implementation can achieve accuracies that compete with LDV or PIV, while providing many advantages such as low particle mass loading, short run time experiments, and high accuracy velocity measurement from single Lagrangian particle trajectories. The one to two order of magnitude reduction in particle loading compared to competing techniques minimizes flame disturbances, and Mie-scattering and stray-light interference in fluorescence images. The static (Bernoulli) pressure drop across the nozzle contraction was measured concurrently, providing a further check, measurement redundancy, and a valuable independent parameter.

A first part of the work reported here focuses on cold impinging jets, an important flow in many contexts. Impinging jets are important in Chemical Vapor Deposition (CVD) processes (Houtman *et al.* 1986; Coltrin *et al.* 1989; Glumac & Goodwin 1996), as well as being the base flow in which strained planar flames are stabilized. A thorough review of the literature reveals that detailed axial velocity profile measurements for laminar impinging jets at separation distances the order of the nozzle diameter are not available. While some data are available in the Ph.D. thesis of Mendes-Lopes (1983), systematic study of this geometry has not been performed. In this work, velocity measurements are performed along the axis of impinging-laminar jets using PSV. The axial velocity profiles are modeled using empirical fits, the one-dimensional streamfunction model, an axisymmetric potential-flow model, and direct numerical simulation. An analytic model is proposed that allows a full-specification of the flowfield through measurement of the Bernoulli velocity alone. The ability of the one-dimensional formulation to model finite-nozzle-diameter experiments is assessed, and a new methodology for specifying velocity boundary conditions is presented in this study.

A second part of this work focuses on premixed stagnation flames, where, in addition to velocity, CH concentration profiles, equivalence ratio, and stagnation-plate temperature are also measured and compared to simulation. Planar Laser Induced Fluorescence (PLIF, see Appendix C) of the CH radical is used in this study as it is a short-lived radical with a narrow spatial profile within the reaction zone. The experimental CH profile can be directly compared to the one-dimensional simulation predictions, and can allow deficiencies in the chemical kinetics to be identified. Simultaneous measurements of air, fuel, and diluent mass fluxes, as well as stagnation-plate temperature, allow an accurate specification of simulation boundary conditions. Experimental velocity and CH profiles are compared to one-dimensional simulation predictions, using the CANTERA software package developed by Goodwin (2003). The simulations utilize a multicomponent transport model (Kee *et al.* 2003). Several published chemistry models, GRI-MECH 3.0 (Smith *et al.*), a C_3 mechanism due to Davis *et al.* (1999), and two versions of the San Diego mechanism (see Bibligraphy: San Diego mechanism), are utilized in the simulations. In this study, velocity data in the cold-flow region upstream of the flame are used to specify boundary conditions for simulations by exploiting the quadratic cold-flow solution to the one-dimensional equations.

The key to understanding and modeling the combustion of hydrocarbon fuels in flames is obtaining an accurate chemical-kinetic model for the oxidation of C_1 and C_2 hydrocarbon fuels (Miller *et al.* 1990). This is due to the fact that in flames of higher alkanes and alkenes, reactions leading to C_1 and C_2 fragments are too fast to limit the overall rate of combustion (Warnatz 1984a; Miller *et al.* 1990). Thus, this study investigates C_1 and C_2 hydrocarbon flames. Strained, methane-air flames are studied as a function of the nozzle-to-plate separation distance, L, to assess the simplified hydrodynamic model. Flame temperature dependence is studied by mixture dilution with excess nitrogen. The diagnostics are applied to methane-air flames, under similar strain-rate conditions, as a function of equivalence ratio, Φ. The effect of strain-rate variations is studied for lean, near-stoichiometric, and rich mixtures. Further studies of hydrocarbon chemistry are made by studying ethane- and ethylene-air flames as functions of the applied strain rate and the mixture fraction. The approach and diagnostics permit an assessment of the numerical simulation predictions of strained-flames for low-carbon-number hydrocarbons. The performance of several recently published chemistry models is assessed through direct comparison with experiment. These data will also be made available to kineticists looking for optimization targets, following the recommendations of the collaborative data approach (Frenklach *et al.* 2003).

Chapter 2

Experimental method

2.1 Introduction

The experiments documented here utilize stagnation flows created by the impingement of a jet onto a solid wall. Stability and control of flames stabilized in these stagnation flows was the primary design driver for each component. The experimental apparatus was upgraded and enhanced over the course of this work; here only the most important parts of the assembly will be highlighted. The apparatus consisted of

- a gas delivery system for metering, measuring, and mixing the individual gas streams,
- a nozzle assembly consisting of a plenum, or turbulence-management section, and a high-contraction-ratio nozzle,
- a stagnation plate (water-cooled for flame experiments),
- lasers, optics, and detectors for the fluorescence and velocimetry diagnostics,
- as well as a system for acquiring pressure, mass-flow, and plate-temperature data.

2.2 Gas delivery

A general schematic of the flow system utilized in this work is given in Figure 2.1. Fuel, air and diluent gas flows are delivered from standard gas cylinders, regulated (Matheson 81H-580 & 3283-580 (inert), 81H-350 (methane), and 8-250 (air)) to pressures sufficient to ensure sonic flow through the metering needle valves (Swagelok Nupro SS-SS4-VH & SS-4MG-MH). The mass flow rates of each gas stream were measured using thermal mass flowmeters (Omega FMA868-V, FMA869-V and FMA872-V; Alicat Scientific M-20SLPM-D). These flowmeters were each calibrated using a high-accuracy piston prover (Bios International DryCal ML-500). The maximum estimated uncertainty in the DryCal standardized flow measurements is 0.4% of reading. On-site calibration was found to

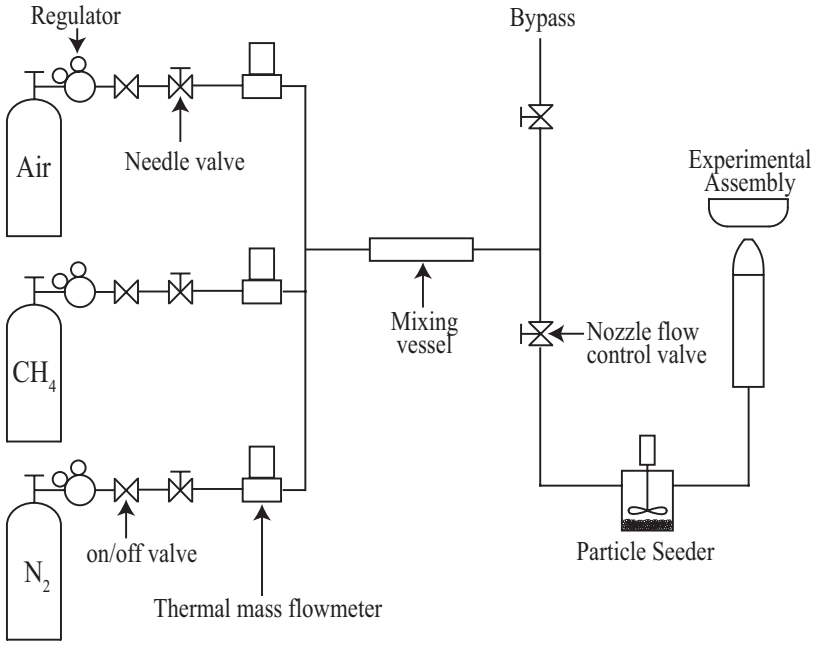

Figure 2.1: Gas delivery flow diagram.

be essential, as systematic errors as large as 6% were found in the Omega flowmeters, even though the flowmeters were calibrated by two outside vendors. The systematic error was found to be in the "gas conversion factor" of the methane flowmeter. This was undetected by the original and independent calibrations, which use nitrogen as a "surrogate gas" according to industry standard practice. Mass flowmeters were calibrated at multiple set points and the resulting data were fit using a cubic (see Appendix F). This fit allowed nonlinearities in the flow-voltage response curve to be accounted for. The remaining uncertainty is due to non-repeatability and was observed to be less than 0.4% of reading, or relative error, when calibrations over multiple months were compared, in accord with the manufacturer specifications. The individual gas streams are combined and mixed in a mixing vessel. The flow rate of the fuel-air-diluent mixture to the experimental apparatus is metered through the use of a bypass flow. This allows the nozzle-exit velocity to be adjusted independently of the fuel-air-diluent mixture fractions.

These experiments typically relied on mixtures of fuel, air, and sometimes excess nitrogen. The volume flow rates of fuel, Q_{fuel}, and air, Q_{air}, determine the equivalence ratio,

$$\Phi = \frac{(Q_{\text{fuel}}/Q_{\text{air}})}{(Q_{\text{fuel}}/Q_{\text{air}})_{\Phi=1.0}} , \tag{2.1}$$

where the stoichiometric fuel to air ratio, $(Q_{\text{fuel}}/Q_{\text{air}})_{\Phi=1.0}$, is determined as the ratio of moles of fuel to moles of air required for complete conversion of the reactants into products. This ratio is $(Q_{\text{fuel}}/Q_{\text{air}})_{\Phi=1.0} = 1/9.52$ for methane, 1/16.66 for ethane, and 1/14.28 for ethylene. The volume

flow rate of the air and excess nitrogen diluent determine the percent of the "air" that is made up of oxygen,

$$\%O_2 : (O_2 + N_2) = 100 \times \frac{\chi_{O_2}}{\chi_{O_2} + \chi_{N_2}}\% \tag{2.2}$$

$$= 100 \times \frac{0.21\, Q_{\text{air}}}{Q_{\text{air}} + Q_{N_2}}\% \,, \tag{2.3}$$

where χ_A is the mole fraction of species A and Q_{N_2} is the volume flow rate of the excess nitrogen. The uncertainty in the measured values of the equivalence ratio, Φ, and the oxygen percentage, $\%O_2$:(O_2+N_2), are estimated to be 0.8% and 0.2%, respectively, when the mass flow meter uncertainty is propagated.

The flow was seeded with particles using an in-house seeder before entering the jet-plenum, where screen (coarse to fine mesh) and honeycomb (1/8 in cell size, 1 in thick) sections were located for flow-uniformity and turbulence management. The flow is then accelerated through a high-contraction-ratio nozzle and impinges onto a stagnation plate. Flames are ignited in the stagnation flow using a custom spark igniter assembled from a commercially available "stun gun" (Panther 100,000 V). The apparatus is contained within an enclosing chamber to reduce drafts and prevent the small particles relied upon for velocimetry from entering the room. This chamber has openings to allow the laser beams to pass through the experimental assembly and allows for optical access for the imaging devices. The gas within this chamber is exhausted to the atmosphere after passing through a HEPA filter to remove particulates.

2.3 Nozzle and plate assembly

2.3.1 Mark I

The experimental assembly utilized in the study of cold impinging jets (see Chapter 4) is depicted in Figure 2.2. Room-temperature jets are generated in atmospheric pressure air from a contoured nozzle with an internal (nozzle-exit) diameter of $d = 9.9$ mm. The nozzle interior was designed by optimizing the inner radius profile, $r(x)$, through the contraction-section, expressed in terms of a 7th-degree polynomial, to minimize the exit boundary-layer displacement thickness and avoid the formation of Taylor-Görtler vortices in the concave section (see Fig. 2.2, Appendix E, and Drazin & Reid 1981; Dowling 1988). The nozzle exterior was designed with attention to the upstream entrainment-induced flow, and to avoid flow separation and unsteadiness (see Fig. 2.2, Appendix E, and Landau & Lifshitz 1987). The nozzle-plenum system produced a uniform velocity profile in a free-jet configuration. The jet-exit velocity profile was measured with a flattened pitot probe ($d_{\text{pitot}} \approx 0.4$ mm in the radial direction) and an electronic-capacitance manometer (BOC Edwards

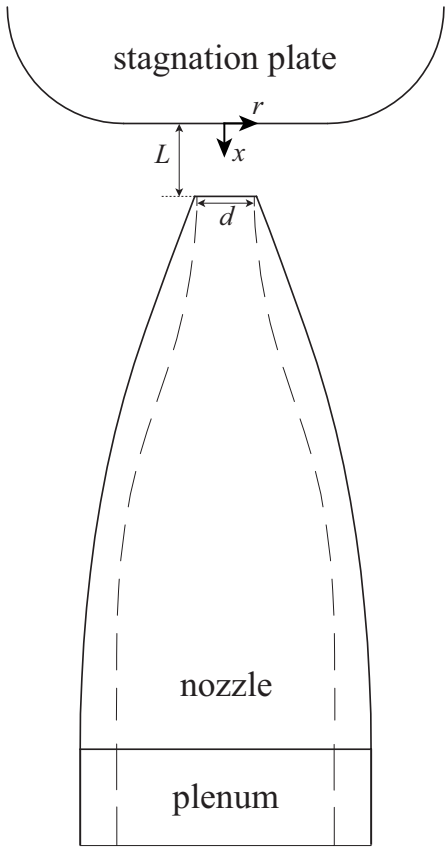

Figure 2.2: Schematic of nozzle and stagnation plate apparatus

W57401100) with a temperature-stabilized 1 torr differential-pressure transducer (BOC Edwards W57011419). Figure 2.3 compares the nozzle-exit velocity profile with the profile obtained from an axisymmetric-viscous simulation (performed by K. Sone), at a Reynolds number

$$Re_{\mathrm{j}} \equiv \frac{\rho\, d\, U_{\mathrm{j}}}{\mu} \cong 1400\ , \tag{2.4}$$

where U_{j} is the centerline velocity at the jet exit, ρ is the density, and μ is the viscosity. The profile is uniform, with less than 1% variation outside the wall boundary layers ($r/R \leq 0.6$, $R = d/2$). The slight disagreement between simulation and experiment in the wall boundary layer region is attributable to the finite pitot-probe extent, d_{pitot}, in the radial direction, for which no corrections were applied.

The jet axis was aligned normal to a solid wall (stagnation-plate assembly). The stagnation plate was a circular copper block, 7.62 cm (3 in) in diameter and 5.08 cm (2 in) thick, with a 2.03 cm (0.8 in) bottom-edge radius. A bottom-edge radius was introduced to mitigate upstream effects of flow-separation and edge-flow unsteadiness in the stagnation-flow region (see Fig. 2.2).

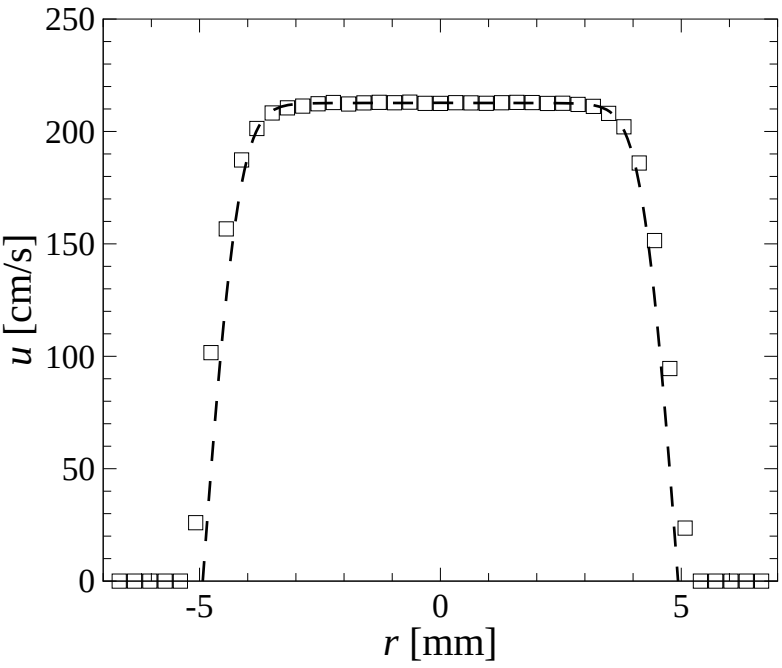

Figure 2.3: Nozzle-exit velocity profile ($d = 9.9\,\mathrm{mm}$, $Re_\mathrm{j} = 1400$). (□) experimental data. (dash line) viscous-simulation results. Pitot-probe internal opening was $d_\mathrm{pitot} \approx 0.4\,\mathrm{mm}$.

2.3.2 Mark II

Preliminary flame experiments were performed using the first apparatus. While steady flames could be stabilized over a wide range of conditions with this apparatus, for some combinations of the equivalence ratio, jet velocity, and separation distance, the flame would become unstable. This instability manifested itself as a "flapping" of the flame edges in the shear-layer region and appeared to be linked to a Helmholtz resonance of the nozzle-plenum-plate system and the flame. It was thought that the vortex roll-up in the annular jet-shear-layer could be responsible for exciting the resonance. In an effort to eliminate this instability, a new coflow nozzle was designed to stabilize the annular shear-layer at the edge of the flame. The coflow apparatus is depicted in Fig. 2.4. The inner profile of the inner nozzle was identical to that utilized in the impinging-jet study discussed above (see Fig. 2.2). The outer profile of the inner nozzle was designed to smoothly join the outer surface of the inner plenum and the tip of the nozzle and provide vertical outflow in the annular jet. The inner profile of the outer nozzle was identical to the outer profile of the inner nozzle, and acceleration was achieved through the reduction in area due to the radial contraction. The outer profile of the outer nozzle was designed to match with the entrained flow streamlines, as was done in the single-nozzle apparatus discussed above (see Fig. 2.2). Experiments were performed using either nitrogen or helium as the co-flow gas. Both inerts improved the stability of the flame. The density of helium is more closely matched to the hot-gas (post-flame) density, resulting in improved

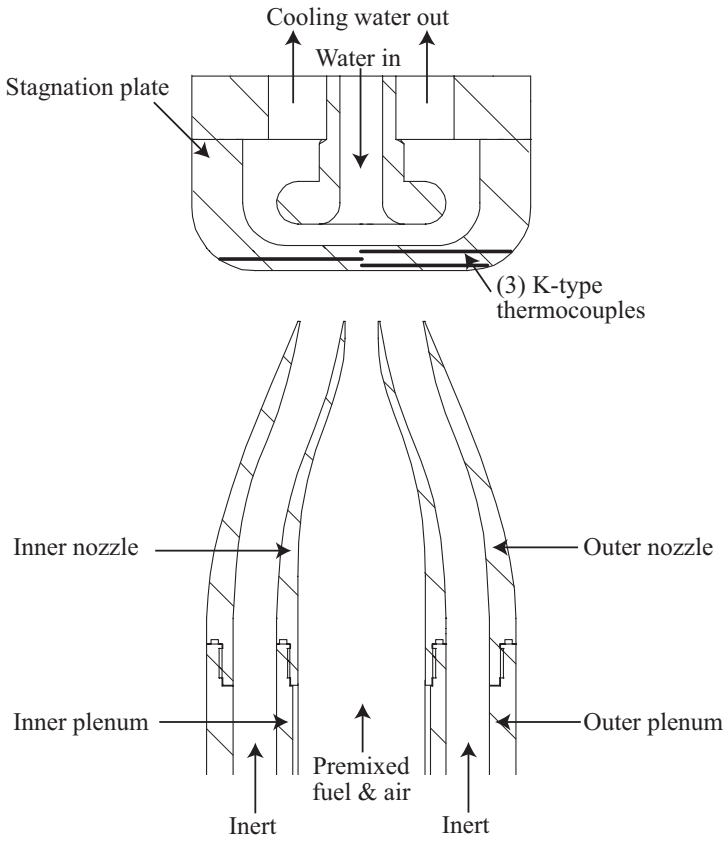

Figure 2.4: Coflow nozzle apparatus with water-cooled stagnation plate.

planarity in the "wing" regions. The flatter flames tended to produce superior velocimetry images and thus helium was utilized for the majority of the data presented here. The use of an inert co-flow also reduced the tendency of the flames to attach to the nozzle rim, as noted previously (Ishizuka *et al.* 1982).

One of the required boundary conditions for the simulation of premixed flames in stagnation flow is the wall temperature. It was desired to control and accurately measure the wall temperature for the archival flame experiments. Thus, a water-cooled stagnation plate was designed and fabricated (see Fig. 2.4). The stagnation wall was a circular copper plate, 10.16 cm (4 in) in diameter and 5.84 cm (2.3 in) thick, with a 1.91 cm (0.75 in) bottom-edge radius. The plate diameter was chosen to be large enough to ensure one-dimensional flow over the central region of the plate, but also small enough to ensure that the collection optics for the fluorescence measurements could be situated close to the experiment. This allows the maximum possible magnification for the fluorescence imaging. The plate is cooled by a flow of water that is introduced along the centerline of the plate, in a stagnation-type flow. The water flows radially outwards along the rear portion of the stagnation surface and out through (4) outlet ports radially distributed around the plate. The water flow is metered using a needle valve (Swagelok Nupro SS-4MG-MH), and allows the wall temperature to be (open-

loop) controlled to a reasonable accuracy. The plate has three embedded K-type thermocouples on the centerline, spaced vertically between the stagnation and cooled surface, to allow accurate measurement of the wall temperature and temperature gradient.

2.4 Laser diagnostics

In this work we utilize two simultaneous laser diagnostic techniques to measure velocity fields and CH radical profiles. Particle Streak Velocimetry (PSV) is used to record axial velocity profiles, while Planar Laser Induced Fluorescence (PLIF) is utilized to measure relative concentration profiles of the CH radical. Previously, Carter *et al.* (1998) performed simultaneous CH PLIF and Particle Image Velocimetry (PIV) measurements in a turbulent, non-premixed flame. Han & Mungal (2003) performed simultaneous PIV and CH PLIF measurements in turbulent jet-flames in co-flow. Simultaneous CH and OH PLIF has also been demonstrated (Stårner *et al.* 1992; Donbar *et al.* 2000; Ratner *et al.* 2000).

2.4.1 Particle Streak Velocimetry (PSV)

Velocity measurements in this study consist of axial velocity profiles measured along the axis of the stagnation flow/flame. Velocity measurements are typically performed in premixed flames using the techniques of Laser Doppler Velocimetry (LDV: Wu & Law 1984; Zhu *et al.* 1988), or, more recently, Particle Image Velocimetry (PIV: Dong *et al.* 2002; Hirasawa *et al.* 2002). In this study, velocity measurements were performed with the technique of Particle Streak Velocimetry (see Appendix B and Bergthorson *et al.* 2005a). PSV offers several advantages over other velocity measurement techniques in the study of premixed laminar flames. Particle loading required for accurate velocity measurements is an order of magnitude, or more, lower than that required for LDV or PIV. In a single PSV image frame, one or two particles traversing the vertical extent of the image are sufficient for profile measurement. In contrast, PIV measurements require a dispersion of particles throughout the domain in any one (short-time) exposure. In PIV, the higher required particle number densities and the high spectral intensity of the Nd:YAG laser pulses can cause interference in laser induced fluorescence measurements (Carter *et al.* 1998). With LDV, high particle number densities are required to obtain converged statistics in a reasonable time. Particle loading can also be an important factor in chemically reacting flows, as the heat capacity (Ancimer *et al.* 1999) and surface-catalytic properties of particles can potentially alter flame/combustion behavior. The technique is fast; a single image frame can capture the entire velocity field, allowing PSV to be implemented in short run-time experiments. In axisymmetric-steady flow the axial velocity component along the centerline of the flow field can be reliably measured. Particle paths do not cross or overlap, and out-of-plane particle displacements are small and easily discernible when they occur (in-focus/out-of-focus

streaks). Further, the high sensitivity of the scattering cross section to particle size, in the size range employed, allows easy identification of agglomerates that may not track the high spatial-gradient regions in the flow. Streaks used for PSV processing were from in-plane, non-agglomerated particles. The PSV technique utilized here has been documented previously (Bergthorson *et al.* 2005a), and a complete description of the PSV experimental setup and analysis technique is given in Appendix B.

2.4.2 Planar Laser Induced Fluorescence (PLIF)

In order to assess the performance of the chemistry and transport models employed in this work, it was desirable to perform detailed measurements of a reactive intermediate and compare the results with numerical simulations. In the study of hydrocarbon flames, several laser diagnostic techniques have been applied. Major species profiles can be measured using Coherent Anti-Raman Scattering (CARS) techniques, while minor species concentrations in flames are typically measured using Laser Induced Fluorescence (LIF) techniques (Eckbreth 1996). Major species profiles have been shown to be insensitive to the imposed strain on the system (Law *et al.* 1994). The technique of Planar Laser Induced Fluorescence (PLIF) allows the two-dimensional concentration field of reactive intermediates to be measured (Hanson *et al.* 1990).

Most PLIF applications to combustion experiments study OH. OH radicals are produced within the reaction zone, but due to the relatively slow destruction reactions, tend to persist in the flow where the temperature is high (Crosley 1989). Sample profiles for several intermediates, including OH, in a $\Phi = 1.0$ methane-air flame are presented in Fig. D.6 (see Appendix D). OH fluorescence is relatively easy to measure, as it produces a high signal due to the high number densities of OH within the reaction and product zones. However, the UV fluorescence requires the use of high $f/\#$ UV optics, resulting in reduced collection efficiency, and S-20 photocathode materials with relatively low quantum efficiency. According to Crosley, intermediate species that rise and fall within the reaction zone are much more revealing. CH exists near the flame front and reveals where the combustion chemistry is taking place (Crosley 1989). Its narrow spatial profile is well-correlated with flame location and provides a sensitive test of strained-flame models. Also, CH has been suggested as being an important participant in prompt-NO production (Crosley 1989; Norton & Smyth 1991). Accurate modeling of CH production is thus essential for the prediction of these important pollutant emissions, especially for low-temperature flames where the prompt mechanism can dominate (Renfro *et al.* 2001). Succesful predictions of CH profiles can also help validate the chemistry and transport models utilized in detailed numerical simulations (Luque *et al.* 1996). Thus, for this work, species profiles of the CH radical are measured using Planar Laser Induced Fluorescence (PLIF).

PLIF measurements of the CH radical can be performed using excitation from the ground state (X) to the first (A), second (B), or third (C) excited electronic states. One of the most successful excitation-detection schemes relies on excitation to the B state near 390 nm, and detecting the

fluorescence from the A–X transition (*e.g.*, Carter *et al.* 1998; Sutton & Driscoll 2003). This scheme results in a large separation between excitation and detection wavelengths, allowing the use of a long-pass filter to block the scattered excitation light, while transmitting a high percentage of the fluorescence. High transmission is essential due to the low fluorescence signal resulting from the small CH concentrations in flames, typically a few parts-per-million. As well, Sutton & Driscoll (2003) have shown that by measuring the fluorescence signal on a CH resonance line, and subtracting the signal obtained off-resonance, relative CH concentrations can be measured as a function of fuel type and mixture fractions. While absolute CH concentration measurements have been performed, these studies have been limited in the range of parameters studied and are typically restricted to sub-atmospheric pressures (*e.g.*, Luque & Crosley 1996; Luque *et al.* 1996). An exception is the study of Luque *et al.* (2002), where absolute measurements of the CH radical were made in a burner flame at atmospheric pressure. Relative concentration profiles will be studied in this work, although studies such as Luque *et al.* (2002) can be utilized to anchor the results at a single point, converting relative concentration profiles to absolute measurements. Appendix C and Bergthorson *et al.* (2005a) provide more detailed information on the CH PLIF diagnostic used in this study.

2.5 Data acquisition

The (Bernoulli) static-pressure difference between the plenum interior, at the straight section upstream of the nozzle-contraction curvature, and a point outside the jet-core flow region is measured with an electronic-capacitance manometer (BOC Edwards W57401100) and a temperature-stabilized, 1 torr full-scale, differential-pressure transducer (BOC Edwards W57011419). The Bernoulli velocity,

$$U_{\mathrm{B}} \;=\; \sqrt{\frac{2\,\Delta p/\rho}{1\;-\;(d/d_{\mathrm{P}})^4}}\;, \tag{2.5}$$

is then calculated, where Δp is the static pressure drop across the nozzle, ρ is the density of the jet fluid, $d \cong 10\,\mathrm{mm}$ is the diameter of the nozzle exit, and $d_{\mathrm{P}} \cong 38\,\mathrm{mm}$ (1.5 in) is the plenum diameter. At the flow velocities in this study, Bernoulli pressure differences are in the range of 0.1–3 Pa. At the lowest speeds investigated, an error of $< 0.01\,U_{\mathrm{B}}$ requires an absolute measurement accuracy for the Bernoulli pressure drop of $\delta(\Delta p) \leq 2\times10^{-3}\,\mathrm{Pa} = 2\times10^{-8}\,\mathrm{bar}$. This accuracy is achievable with the differential-pressure tranducer employed if instrumental drifts and offsets are monitored.

Bernoulli pressure, mass-flow, and stagnation-plate temperature data are acquired using the National Instruments LabView hardware/software environment, synchronized to the digital-image acquisition to allow accurate specification of simulation boundary conditions.

2.6 Uncertainty analysis

To perform detailed comparisons between experimental results and model predictions, the uncertainty in the measured profiles and boundary conditions must be estimated. In this work, velocity profiles measured with PSV are compared to modeled-PSV profiles estimated from model predictions. The PSV technique results in a root-mean-squared (rms) error of $\approx 1.5\% U_{\mathrm{B}}$, when data are compared to fits of the form described in Eq. (B.2). Linear regression analysis of the parabolic fits to the velocity data in the cold flow region (see Section 3.1.2 and B.3) is used to determine the 95% confidence bounds on the fit. The uncertainty in the velocity boundary condition is taken as the 95% bound at the specified location, ℓ. To determine the uncertainty in the specified velocity gradient at the simulation inlet, parabolas were fit to the max (min) bound at the start of the fit domain, the fit value at ℓ, and the min (max) bound at the end of the fit domain. These two parabolas represent the minimum and maximum possible slope at ℓ for the given confidence bounds. The average difference in the slope between these two fits and the optimal fit represent a maximum uncertainty in the measured velocity gradient. It should be noted that CANTERA requires the spreading rate, V_ℓ, be specified, which is equal to one half of the axial velocity gradient in cold regions of the flow. The uncertainty in V_ℓ is the same as that in the velocity gradient.

Uncertainty in the PLIF profiles is estimated to be the standard deviation of the fit parameters found from the 1000 image data record (see Appendix C). The uncertainty in the measured CH profile location is estimated to be $\approx 5\% \delta_{\mathrm{CH}}$, where δ_{CH} is the CH profile thickness used to normalize differences between experimental measurements and simulation predictions. The rms uncertainty for the relative CH concentrations and CH profile thicknesses are reported by error bars in their associated figures. The finite Point-Spread-Function (PSF) width of the intensified CCD system introduces a systematic uncertainty in the PLIF profile, which is accounted for when comparisons are made between measured and simulated CH profile widths. The effect of beam steering due to the index of refraction gradient resulting from the flame temperature rise was estimated to be less than a pixel for both the PSV and PLIF measurements.

The uncertainties in the Bernoulli velocity and wall temperature measurements are estimated to be the standard deviation of the respective data acquisition record. The uncertainty in the inlet equivalence ratio, Φ, and the oxygen percentage, $\%O_2{:}(O_2{+}N_2)$, are estimated by propagating the mass flowmeter uncertainties using standard error propagation. Each mass flowmeter has an associated uncertainty of $\pm 0.6\%$ when calibrated against a high accuracy device (see Appendix F). The inlet temperature uncertainty is estimated to be the accuracy of the thermometer employed to measure the (climate-controlled) room temperature. Uncertainty in the pressure is neglected as simulations exhibit a relatively low sensitivity to these (small) barometric pressure fluctuations. Table 2.1 summarizes the estimated uncertainty in the measurements and boundary conditions.

		uncertainty
Measurements:	U_{B}	$\pm 2.0\%$
	x_{CH} (PLIF)	$\pm 5.0\%\, \delta_{\mathrm{CH}}$
	u (PSV)	$\pm 1.5\%\, U_{\mathrm{B}}$
Boundary conditions:	Φ	$\pm 0.8\%$
	$\%O_2$:(O_2+N_2)	$\pm 0.2\%$
	u_ℓ	$\pm 0.8\%$
	V_ℓ	$\pm 5.0\%$
	T_ℓ	$\pm 0.2\%$
	T_{wall}	$\pm 0.2\%$

Table 2.1: Summary of measurement uncertainties.

The logarithmic sensitivities are calculated for each boundary condition (see Section D.3) and allow the uncertainty in the measured boundary conditions to be propagated through the simulation predicitions. The boundary condition uncertainties are assumed to be independent and the uncertainty in the predicted CH location is estimated as

$$\sigma_{x_{\mathrm{CH}}}^2 = \sum_{\mathrm{B.C.}} \left(\frac{\partial x_{\mathrm{CH}}}{\partial \mathcal{V}_{\mathrm{B.C.}}} \right)^2 \sigma_{\mathrm{B.C.}}^2 \tag{2.6}$$

where the sum is performed over all of the imposed boundary conditions, $\sigma_{x_{\mathrm{CH}}}$ is the uncertainty in the predicted location of the CH profile, x_{CH}, and $\sigma_{\mathrm{B.C.}}$ is the uncertainty in the measured boundary condition, $\mathcal{V}_{\mathrm{B.C.}}$. The derivatives can be replaced by the logarithmic sensitivities so that

$$\sigma_{x_{\mathrm{CH}}}^2 \cong \sum_{\mathrm{B.C.}} \left(\frac{\Delta x_{\mathrm{CH}}}{\Delta \mathcal{V}_{\mathrm{B.C.}}} \right)^2 \sigma_{\mathrm{B.C.}}^2 \tag{2.7}$$

$$\sigma_{x_{\mathrm{CH}}}^2 \cong x_{\mathrm{CH}}^2 \sum_{\mathrm{B.C.}} \left(\frac{\Delta x_{\mathrm{CH}}/x_{\mathrm{CH}}}{\Delta \mathcal{V}_{\mathrm{B.C.}}/\mathcal{V}_{\mathrm{B.C.}}} \right)^2 \left(\frac{\sigma_{\mathrm{B.C.}}}{\mathcal{V}_{\mathrm{B.C.}}} \right)^2 \tag{2.8}$$

$$\frac{\sigma_{x_{\mathrm{CH}}}}{\delta_{\mathrm{CH}}} \cong \frac{x_{\mathrm{CH}}}{\delta_{\mathrm{CH}}} \sqrt{\sum_{\mathrm{B.C.}} \left(L.S.(x_{\mathrm{CH}})_{\mathrm{B.C.}}\right)^2 \left(\frac{\sigma_{\mathrm{B.C.}}}{\mathcal{V}_{\mathrm{B.C.}}} \right)^2}\,, \tag{2.9}$$

where $L.S.(x_{\mathrm{CH}})_{\mathrm{B.C.}}$ is the logarithmic sensitivity of the simulation to each boundary condition, and δ_{CH} is the CH width used to normalize differences between experiments and simulations. Propagating the boundary condition uncertainties through simulations of lean, stoichiometric and rich methane-air flames leads to a total estimated uncertainty in x_{CH} of $50\%\, \delta_{\mathrm{CH}}$, or half of the (stoichiometric) CH layer thickness.

Chapter 3

Numerical method

In the study of cold impinging jets, three different numerical simulations are performed at varying levels of complexity. The first is an axisymmetric viscous Navier-Stokes simulation, the second is a potential-flow calculation, and the third is a one-dimensional streamfunction formulation. The axisymmetric viscous simulation results are part of the Ph.D. research of K. Sone and the potential-flow simulations were performed by T. W. Mattner. The formulations of these two numerical methods are presented in Bergthorson *et al.* (2005b) and the results are compared to experimental measurements of cold impinging jets in Chapter 4. Simulations of both cold and reacting stagnation-point flows are performed using the CANTERA software package, which relies on a one-dimensional streamfunction model. The cold-flow comparisons are used to assess the ability of the one-dimensional hydrodynamic model to capture the experimental flow. These results are presented in Chapter 4. Reacting-flow simulations are compared to experimental data of stagnation-point flames in Chapter 5 to assess the validity of the chemistry and transport models employed.

3.1 One-dimensional streamfunction formulation

Axisymmetric stagnation flow and premixed flame simulations are performed using the CANTERA reacting-flow software package, developed by Goodwin (2003). The one-dimensional model for stagnation flows relies on a streamfunction

$$\psi\left(x,r\right)=r^{2}\mathcal{U}\left(x\right)\ , \tag{3.1}$$

with

$$\mathcal{U}\left(x\right)=\frac{\rho(x)\,u(x)}{2}\ , \tag{3.2}$$

where $\rho(x)$ is the density and $u(x)$ is the axial velocity (Kee *et al.* 1988; Dixon-Lewis 1990; Kee *et al.* 2003). The radial velocity is then

$$v\,(x,r) = -\frac{r}{\rho(x)}\,\frac{\mathrm{d}\mathcal{U}(x)}{\mathrm{d}x}\ . \tag{3.3}$$

The axisymmetric Navier-Stokes equations then become

$$2\mathcal{U}\frac{\mathrm{d}}{\mathrm{d}x}\left(\frac{1}{\rho}\frac{\mathrm{d}\mathcal{U}}{\mathrm{d}x}\right) - \frac{1}{\rho}\left(\frac{\mathrm{d}\mathcal{U}}{\mathrm{d}x}\right)^2 - \frac{\mathrm{d}}{\mathrm{d}x}\left[\mu\frac{\mathrm{d}}{\mathrm{d}x}\left(\frac{1}{\rho}\frac{\mathrm{d}\mathcal{U}}{\mathrm{d}x}\right)\right] = \Lambda\ . \tag{3.4}$$

In this formulation,

$$\Lambda = \frac{1}{r}\,\frac{\mathrm{d}p}{\mathrm{d}r} \tag{3.5}$$

is termed the radial-pressure eigenvalue, and must be a constant (Kee *et al.* 1988; Dixon-Lewis 1990; Kee *et al.* 2003).

The third-order ordinary differential equation requires three boundary conditions at $x = 0$. It is common to specify boundary conditions at $x = 0$ and $x = \ell$ with $0 < \ell \leq L$ some interior point, by adjusting the curvature boundary condition at $x = 0$ to achieve the desired boundary condition at $x = \ell$. A fourth boundary condition can be satisfied by adjusting Λ. Treating Λ as unspecified, four boundary conditions are imposed on this third-order ordinary differential equation at $x = 0$ and $x = \ell$, with $0 < \ell \leq L$ a suitably chosen interior point, permitting

$$\begin{aligned} \mathcal{U}(0) &= 0 \\ \mathcal{U}'(0) &= 0 \\ \mathcal{U}(\ell) &= -\rho_0\ u_\ell/2 \\ \mathcal{U}'(\ell) &= -\rho_0\ u'_\ell/2\ , \end{aligned} \tag{3.6}$$

where ρ_0 is the density of the (cold) gas mixture, and u_ℓ and u'_ℓ are the velocity and velocity gradient at $x = \ell$. Since $u(\ell, r) < 0$ (flow is towards the stagnation plate), the negative signs are chosen for convenience to make the constants u_ℓ and u'_ℓ positive. Two common choices for the upstream boundary conditions are the so-called plug-flow (u_ℓ = specified, $u'_\ell = 0$), and potential flow (u'_ℓ = specified), boundary conditions. In the potential-flow case, the velocity gradient is specified at the domain inlet and this determines the value of the radial-pressure eigenvalue, $\Lambda = -\rho_0\,(u'_\ell)^2/4$. The inlet velocity is found as part of the solution and cannot be specified independently. Simulated flame profiles with the same imposed strain rate (upstream of the flame) exhibit different flame stand-off distances and profile shapes dependent on the upstream boundary condition choice (Davis *et al.* 2001; Kee *et al.* 2003). Thus, appropriate inlet velocity boundary conditions must be prescribed to make meaningful comparison with experiment. In this work, both u_ℓ and u'_ℓ are specified from a fit to the measured velocity data in the cold region of the flow, *i.e.*, neither potential- nor plug-flow

boundary conditions are assumed.

The energy and species equations are also solved with specification of inlet composition, inlet temperature, and stagnation-wall temperature (see Kee *et al.* 2003 for more information). These boundary conditions are all measured in the experiment and the data for each experimental run can be found in Appendix J. A no-flux (multicomponent) boundary condition for species is applied at the wall. This no-flux condition takes into account the full multicomponent species flux, including Soret and Fickian diffusion. The simulations use a multicomponent transport model and the GRI-Mech 3.0 kinetics mechanism (Kee *et al.* 2003; Smith *et al.*). Radiation effects are not currently included, but these have been found to be important only for flames near the lean and rich flammability limits (Egolfopoulos 1994). For example, the inclusion of radiation for Φ greater than 0.6 was found to have practically no effect on extinction behavior of methane-air flames.

3.1.1 Cold flow

For non-reacting (constant-temperature) stagnation flows the density is constant throughout the domain. In this case, Eq. (3.4) can be simplified to yield

$$\nu\, u''' \;-\; u\, u'' \;+\; \frac{1}{2}\, u'^2 \;=\; -\,\frac{2\Lambda}{\rho}\;, \tag{3.7}$$

where $u(x)$ is the axial velocity and we have used $u = 2\mathcal{U}/\rho$. The inviscid ($\nu \to 0$) outer solution to Eq. (3.7) is a parabola. In the inviscid limit, the flow is irrotational if $\Lambda = -\rho\,(u'_\ell)^2/4$, for which the solution reduces to potential stagnation flow with the coefficient of the curvature term identically equal to zero, *i.e.*, linear outer flow ($u'_\ell = u_\ell/\ell$). For more general boundary conditions, the resulting flow will have vorticity, whereas the core of the experimental jet is irrotational. The introduction of vorticity to the flow is necessary to accomodate outer flows with curvature.

3.1.2 Reacting flow

For the simulation of flames in stagnation flows, it is necessary to specify u_ℓ, u'_ℓ, and ρ_0. The inlet density, ρ_0, is calculated within CANTERA from the specified inlet composition and temperature. The boundary conditions for each experimental run are reported in Appendix J. Exploiting the parabolic (cold-flow) solution to Eq. 3.7, a quadratic is fit to the velocity data upstream of the flame. u_ℓ and u'_ℓ are then calculated from the fit, at $x = \ell$, minimizing errors that could be introduced by an inconsistent specification of flow boundary conditions, or from data differentiation. The inlet velocity, u_ℓ, was corrected for the velocity lag of the tracer particles at the inlet velocity gradient, u'_ℓ [see Appendix A, Eq. (A.23)]. This permitted the simulations to be post-processed to determine the particle velocity profile and resulting modeled-PSV profile. Figure 3.1 shows the experimental PSV profile, and the corresponding parabolic fit, for a methane-air flame at $\Phi = 0.9$ and $L/d = 1.2$

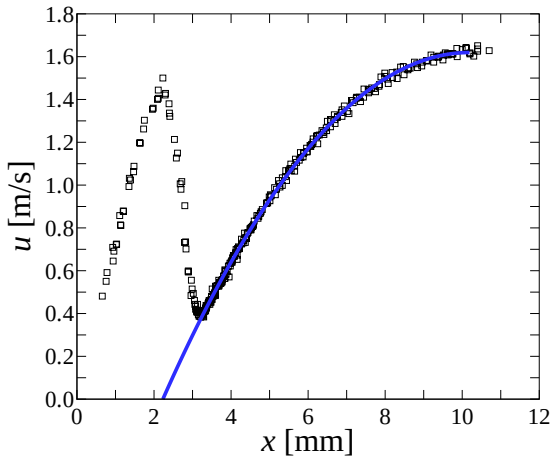

Figure 3.1: Parabolic fit (solid line) to PSV experimental results (□) for a $\Phi = 0.9$ methane-air flame at $L/d = 1.2$.

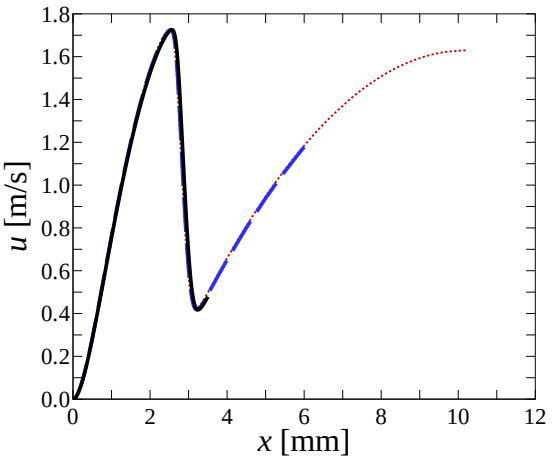

Figure 3.2: Simulated flame profiles for the data in Fig. 3.1 with $\ell = 3.5\,\text{mm}$ (solid), 6 mm (dash), and 10.19 mm (dot).

($L \approx 12\,\text{mm}$). Figure 3.2 shows profiles resulting from different choices of the simulation domain, ℓ. The good agreement for simulations performed with different choices of ℓ validates the use of a parabolic fit in the cold-flow region.

This methodology is similar to that used by Sung *et al.* (1996a; Appendix), where an intermediate flow boundary condition (between the limits of potential- and plug-flow) was used to visually align the velocity profile ahead of the reaction zone. In the work of Sung *et al.* (1996a), an initial simulation utilizing the plug-flow boundary condition was performed. Using a continuation method (see Nishioka *et al.* 1996), the inlet velocity and velocity gradient were adjusted to determine the inlet boundary condition that best matched the experimental data. In the present work, the cold-flow parabolic fit is performed prior to a running a single simulation with no constraint applied to the resulting flame location.

More information on the CANTERA simulations, including a convergence study, sample scripts, and a sensitivity analysis for the various simulation boundary conditions is given in Appendix D. The use of the CANTERA software package for the simulation of strained flames has previously been documented (Bergthorson *et al.* 2004, 2005a).

Chapter 4

Impinging laminar jets

4.1 Introduction

Axisymmetric jets impinging perpendicularly on a wall are encountered in a variety of contexts, from large-scale applications of fully developed turbulent jets impinging on the ground, as in Vertical Take-Off and Landing (VTOL) aircraft (Bradbury 1972; Rubel 1980, 1983), to the small-scale use of laminar jets to determine the shear strength of vascular tissue in the study of atherogenesis (Deshpande & Vaishnav 1982). Impinging jets are also used in Chemical Vapor Deposition (CVD) processes (*e.g.*, Houtman *et al.* 1986; Goodwin 2003) and in the study of laminar flames (*e.g.*, Smith *et al.* 1971; Mendes-Lopes 1983; Bergthorson *et al.* 2005a). Work has also been conducted on opposed-jet stagnation flow, a configuration widely used in combustion experiments (*e.g.*, Kee *et al.* 1988; Rolon *et al.* 1991; Kostiuk *et al.* 1993). Definitive experimental data for laminar impinging jets in the nozzle-to-plate separation distance, L, to nozzle-diameter, d, ratio (see Fig. 2.2) range of $0.5 \leq L/d \leq 1.5$ are not widely available. This range of L/d is useful in the study of strain-stabilized flames in combustion research. Available data in this range do not include detailed axial velocity-profile measurements along the flow centerline, except for the study of Mendes-Lopes (1983). Such measurements are important in assessing one-dimensional flame models. This chapter focuses on the hydrodynamics of non-reacting impinging-jet flow, as a basis for studies of strained flames.

Flow velocities in impinging jets have been measured using Laser-Doppler Velocimetry (LDV) (Rolon *et al.* 1991; Kostiuk *et al.* 1993) and Particle Image Velocimetry (PIV) (Landreth & Adrian 1990). In this study, Particle Streak Velocimetry (PSV: see Appendix B and Bergthorson *et al.* 2005a), is used to obtain instantaneous flow field measurements and, in particular, axial velocities along the flow centerline. A new PSV methodology has been implemented in this work that includes digital imaging, image processing, and new analysis techniques. These improvements allow quantitative velocity data to be obtained throughout the flow field without excessive post-processing. This allows PSV to achieve accuracies that compete with LDV or PIV, while providing many advantages such as much lower particle mass loading, short run-time experiments, and high accuracy

velocity measurement from single Lagrangian particle trajectories. In these experiments, the static (Bernoulli) pressure drop across the nozzle contraction is also measured concurrently, providing measurement redundancy and a valuable independent parameter, as discussed below.

Impinging-jet flows have been described analytically, or simulated numerically, using different formulations and techniques. Schlichting (1960) presents a one-dimensional axisymmetric model for an infinite-diameter jet impinging on a plate. This model was originally used with potential-flow boundary conditions (linear outer flow). The one-dimensional model was extended to allow both the velocity and velocity gradient to be specified at some distance from the stagnation plate, providing a more realistic and flexible boundary condition for finite-nozzle-diameter impinging-jet flows (Kee *et al.* 1988; Dixon-Lewis 1990). Two-dimensional, steady, axisymmetric calculations of viscous (Deshpande & Vaishnav 1982) and inviscid (Schach 1935; Strand 1964; Rubel 1980, 1983; Phares *et al.* 2000a,b) impinging-jet flow have also been performed. Except for the work of Strand (1964), these calculations do not include nozzle-to-wall proximity effects.

In this work, the flow is modeled with varying levels of complexity: by means of an axisymmetric Navier-Stokes simulation, an axisymmetric potential-flow formulation, and a one-dimensional streamfunction model (see Chapter 3 and Bergthorson *et al.* 2005b). The first method is a spectral-element scheme (Henderson & Karniadakis 1995; Karniadakis & Sherwin 1999) that solves the incompressible axisymmetric Navier-Stokes equations. The unsteady spectral-element method is robust, and time- and space-accurate. The second method is a finite-difference potential-flow solution based on the classical ideal-jet approach (Birkhoff & Zarantonello 1957; Gurevich 1965). The potential- and viscous-flow calculations capture wall-proximity effects by including parts of the nozzle and plenum assembly in the computational domain. The viscous simulations are part of the Ph.D. research of K. Sone, and T. W. Mattner performed the potential-flow simulations. A full discussion of the viscous and potential-flow simulations is given in Bergthorson *et al.* (2005b). The one-dimensional model relies on the traditional streamfunction formulation (see Chapter 3).

The experimental results are used to assess the accuracy of the different simulation methodologies. Additionally, new scaling parameters and empirical properties of the centerline axial velocity field are discussed. The new scaling allows the identification of an analytical expression for the axial velocity profile of a laminar impinging jet for Reynolds numbers in the range $200 \leq Re \leq 1400$. The experimental data on impinging jets has been documented previously (Bergthorson *et al.* 2004).

4.2 Results and discussion

Experimental velocity data reported here were recorded at three nominal Reynolds numbers,

$$Re \equiv \frac{\rho\, d\, U_{\mathrm{B}}}{\mu} \cong 400\,,\ 700\,,\ \text{and } 1400\,, \tag{4.1}$$

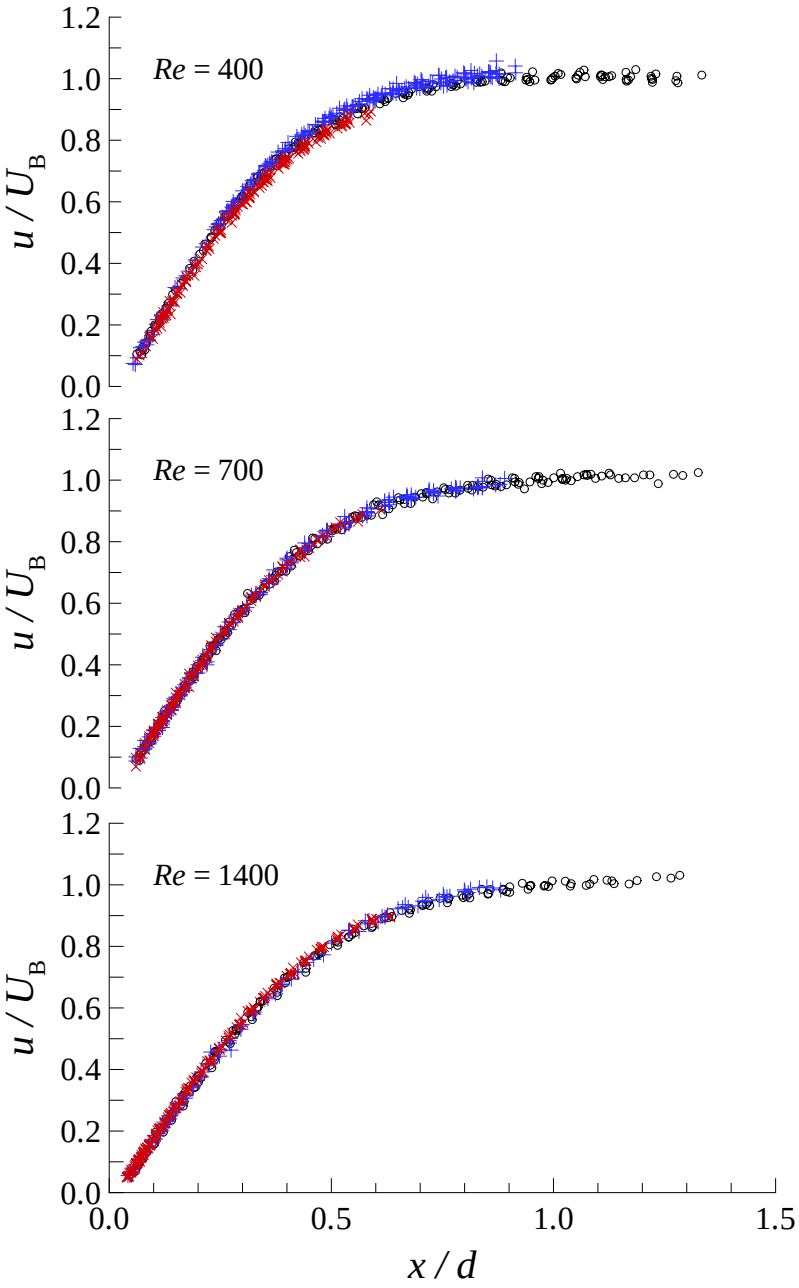

Figure 4.1: Comparison of velocity versus axial distance from plate at three nominal Reynolds numbers. Velocities are scaled by the Bernoulli velocity, U_{B}, and axial distances by the nozzle diameter, d. Experimental results for separation distances of $L/d = 1.4$ ($\circ$), $L/d = 1.0$ ($+$), and $L/d = 0.7$ ($\times$).

with actual values to within ± 35, in each case, and at three nozzle-to-stagnation plate separation distance to nozzle-exit-diameter ratios, $L/d \cong 0.7$, 1.0, and 1.4. In Eq. (4.1), ρ is the gas density, d is the nozzle diameter, U_{B} is the Bernoulli velocity [see Eq. (2.5)], and μ is the gas viscosity. Figure 4.1 compares measured axial velocities, scaled by the Bernoulli velocity, U_{B}, for the three L/d ratios, at

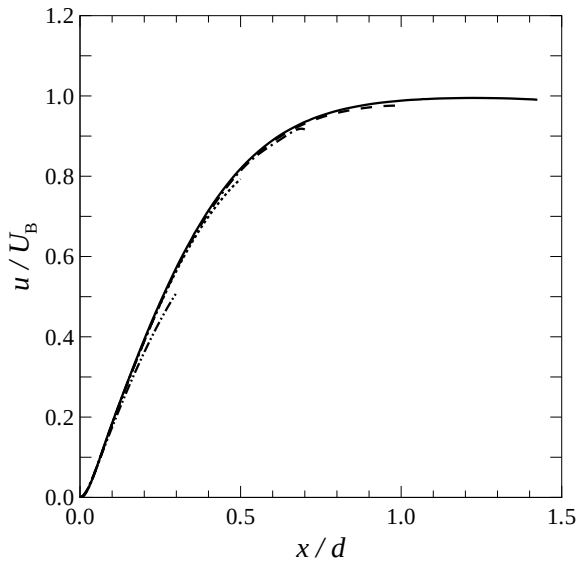

Figure 4.2: Scaled velocity versus axial distance from plate. Viscous calculations at $Re = 700$ and $L/d = 1.4$ (solid), 1.0 (dash), 0.7 (dash-dot), 0.5 (dotted), and 0.3 (dash-dot-dot).

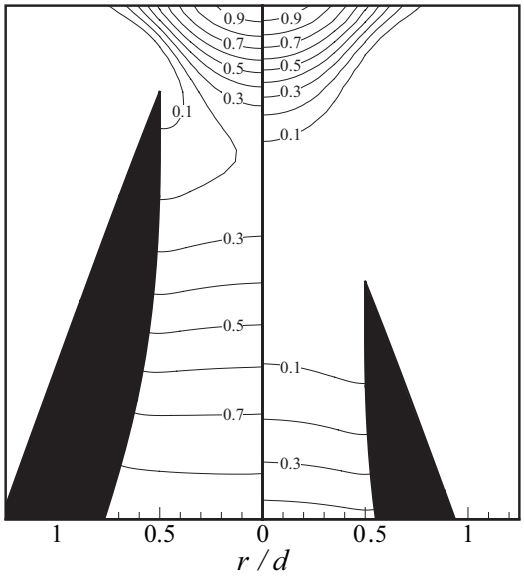

Figure 4.3: Pressure contours, normalized by the Bernoulli pressure, at $L/d = 0.5$ (left) and $L/d = 1.4$ (right).

the three Reynolds numbers. The velocity profiles collapse to a single curve, independent of L/d, if the axial velocity is scaled by the Bernoulli velocity. A centerline axial velocity deficit at the jet-exit develops as the separation distance is decreased due to the influence of the stagnation point on the nozzle flow (Rolon *et al.* 1991; Kurosoy & Whitelaw 2001). Notably, the velocity and its gradient adjust to maintain self-similarity, with the Bernoulli velocity scaling the flow.

Results from the axisymmetric viscous simulations performed by K. Sone (see Bergthorson *et al.* 2005b) are included to confirm the experimental findings. Figure 4.2 shows the axisymmetric viscous simulation results at $Re = 700$ and variable L/d. The inclusion of the nozzle interior in the solution domain permits the study of nozzle-wall proximity effects. The velocity profiles follow a single curve when velocities are scaled by the Bernoulli velocity, consistent with the experimental results. Figure 4.3 gives pressure contours at $L/d = 0.5$ and 1.4, with pressures scaled by the Bernoulli pressure. The near-wall pressure field is not altered by the nozzle position. As the separation distance decreases, the stagnation-point pressure field extends into the nozzle, altering the nozzle flow. Figure 4.4 compares the experimental data with the axisymmetric viscous calculations at $L/d = 1.4$ and $Re = 400$, 700, and 1400. The differences between experimental and numerical results for these three cases are less than $0.015\,U_\mathrm{B}$ root-mean-squared (rms), indicating that the experimental flow field is adequately modeled. Figure 4.5 compares particle-streak-image data and streamlines from the axisymmetric viscous simulations. Good qualitative agreement can be seen, even in the entrainment region where the velocities are low ($< 0.02\,U_\mathrm{B}$).

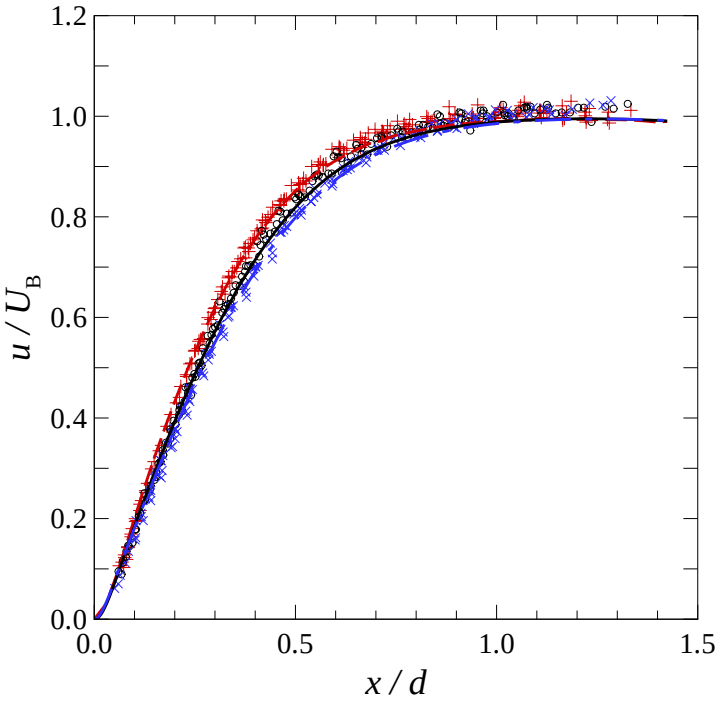

Figure 4.4: Scaled velocity versus axial distance from plate. Viscous calculations (lines) and experimental data (symbols) at $Re = 400$ (dash/+), 700 (solid/$\circ$), and 1400 (dash-dot/$\times$).

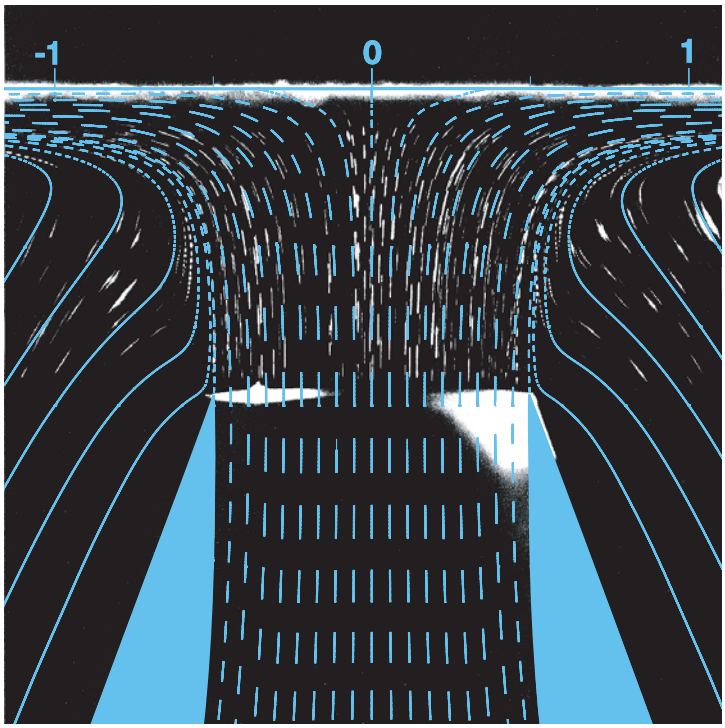

Figure 4.5: Particle streak image detailing entrained flow with superimposed axisymmetric viscous calculation (blue lines) at $Re = 700$ and $L/d = 1.0$.

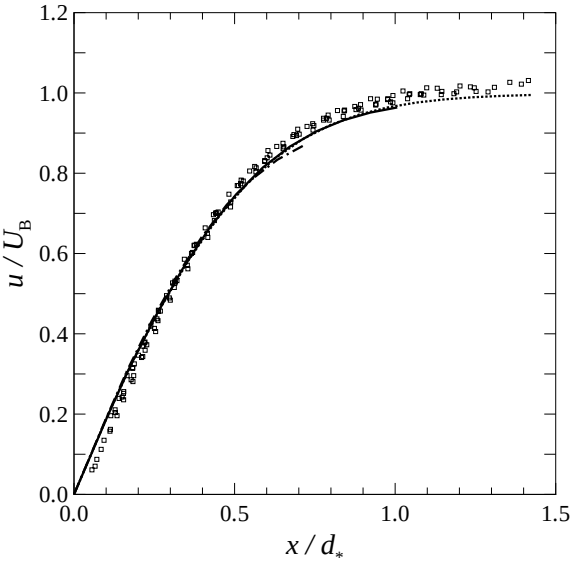

Figure 4.6: Velocity versus axial distance from plate normalized by the effective diameter d_*. Experimental data at $Re = 1400$ (□) and potential-flow simulations (lines) at $L/d_* = 1.4$ (dash), $L/d_* = 1.0$ (solid), and $L/d_* = 0.7$ (dash-dot).

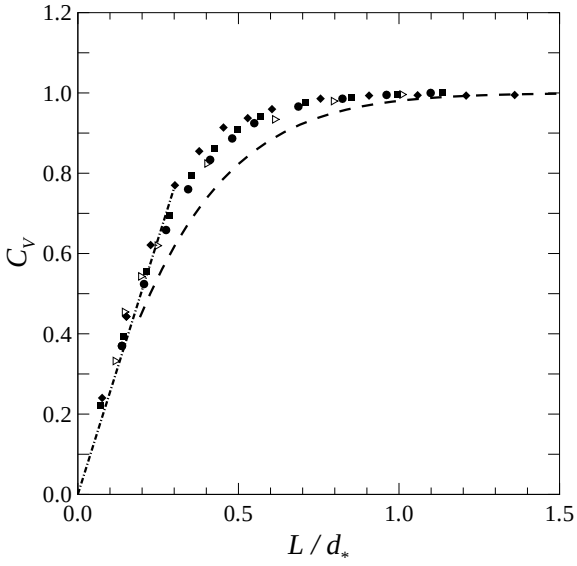

Figure 4.7: Discharge coefficient C_V *vs.* L/d_*. Experimental data at $Re_\infty = 400$ (◇), 1400 (□), and 2800 (○), potential-flow results (dash line), and data (▷) and theoretical curve (dash-dot line) by Strand (1964).

Figure 4.6 compares the experimental data at the highest Reynolds number to the potential flow results obtained by T. W. Mattner (see Bergthorson *et al.* 2005b). Here the axial distance is normalized by the effective diameter d_*, where d_* is the nozzle diameter corrected for the nozzle-wall boundary-layer displacement thickness. One of the main effects of the Reynolds number in this flow is the change in the effective jet diameter through the boundary-layer displacement thickness. This effect should be removed before comparing the experiments to the inviscid potential-flow results, which are approached in the limit of infinite Reynolds number. Boundary layer thicknesses are estimated from axisymmetric viscous simulations of the nozzle flow. The small disagreement close to the wall is attributable to wall boundary layer displacement effects. This discrepancy leads to a difference in the maximum centerline axial velocity gradient. As with the experimental results, the axial velocity profiles collapse independent of L/d. At these relatively low Reynolds numbers, the coupling between the near-potential flow and the viscous boundary layers cannot be accommodated in a simple way.

Experimental values of the discharge coefficient,

$$C_V \equiv \frac{Q}{\pi\, r_*^2\, U_\mathrm{B}}, \tag{4.2}$$

were obtained from concurrent measurements of the Bernoulli pressure (yielding U_B) and the volumetric-flow rate, Q. For large separation distances, the velocity outside the nozzle-wall boundary layers is

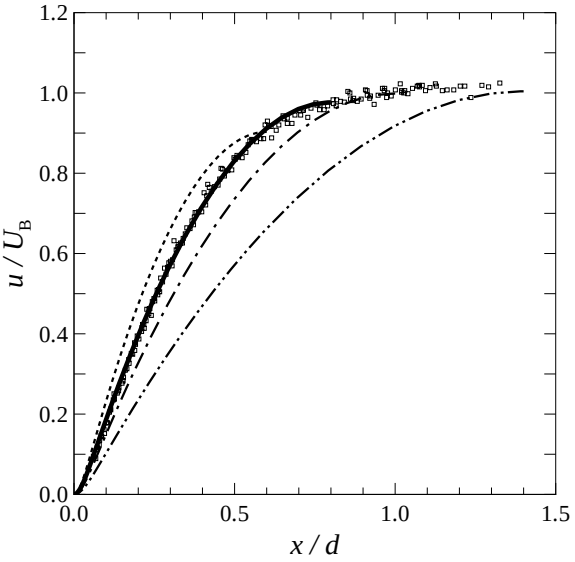

Figure 4.8: Comparison of streamfunction simulations with plug-flow boundary conditions (lines) to experimental results (□) at $Re = 700$, varying ℓ: $\ell/d = 0.6$ (dash), $\ell/d = 0.8$ (solid), $\ell/d = 1.0$ (dash-dot), $\ell/d = 1.4$ (dash-dot-dot).

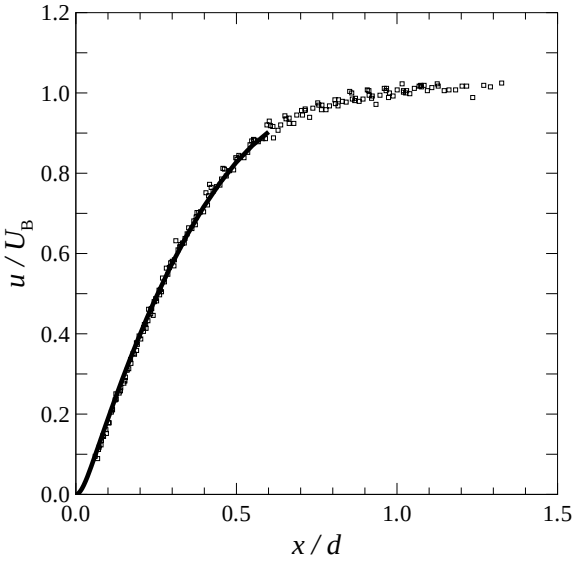

Figure 4.9: Comparison of streamfunction simulation (line) to experimental data (□) at $Re = 700$. Boundary conditions calculated from error-function fit to the data at $\ell/d = 0.6$.

essentially uniform and equal to U_B. The displacement-thickness-corrected radius $r_* = d_*/2$ can be estimated from $Q = \pi r_*^2 U_B$, where the values of U_B and Q are taken at large separation distances, $L/d \cong 1.5$. Figure 4.7 plots experimental values of C_V as a function of the normalized nozzle-wall separation distance L/d_*. Results from the potential-flow simulations performed by T. W. Mattner are included for comparison. These experiments are at constant mass flux and are reported in terms of the Reynolds number, based on the Bernoulli velocity measured at large separation distances, $Re_\infty = Re\,(L/d \gg 1)$. Estimates based on data from Strand (1964), as well as his approximation of $C_V(L/d)$, for $L/d \ll 1$, are also included for comparison. The decrease of the discharge coefficient as the nozzle approaches the stagnation wall is attributable to the decrease in volume flow rate caused by the axial flow deceleration (adverse pressure gradient) near the axis, at fixed Bernoulli pressure.

Figure 4.8 compares the experimental axial velocity data, at $Re = 700$, to four different one-dimensional simulations, with plug-flow boundary conditions and different choices of the interior boundary location, ℓ. Plug-flow boundary conditions capture the flow only for $\ell/d = 0.8$. This is due to the fact that the outer solution to the one-dimensional equations is a parabola and cannot capture the free-jet behavior (zero-gradient region of flow) that is exhibited for $x/d > 1.0$. Finite velocity gradients are evident for $x/d < 0.8$. The value of $\ell/d = 0.8$ is an intermediate case for which plug-flow boundary conditions capture the flow. The approximations invoked in arriving at the one-dimensional streamfunction model are valid in the limit of an infinite-diameter jet impinging on a surface. However, from Fig. 4.8, it appears that the model should be able to capture the flow

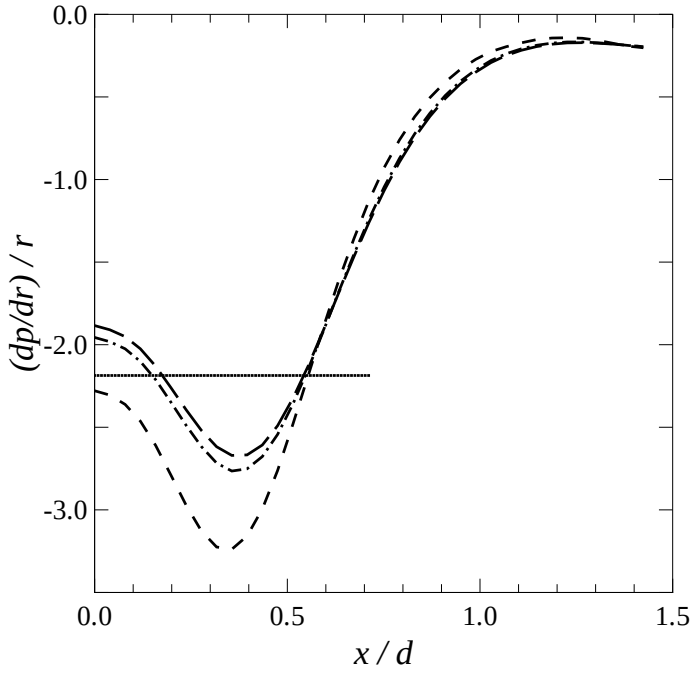

Figure 4.10: Comparison of the pressure eigenvalue function over several radial locations: $r/R = 0$ (long dash), $r/R = 0.2$ (dash-dot), $r/R = 0.5$ (dash), to that of one-dimensional model (solid), which is constant in both x and r.

in the region $0 \leq x/d < 0.8$ if appropriate boundary conditions are specified.

The velocity and velocity-gradient boundary conditions at a given axial location, $u(\ell)$ and $u'(\ell)$, can be specified from an error-function fit to the experimental data [see Eq. (4.3)]. The one-dimensional solution calculated using this method at $Re = 700$, over the range $0.3 \leq \ell/d \leq 0.7$, has a maximum error of less than $0.03\,U_{\rm B}$, when compared to axisymmetric viscous simulations. Figure 4.9 shows the one-dimensional simulation results compared to experimental data at $Re = 700$, with boundary conditions taken from the experimental data at $\ell/d = 0.6$.

In the one-dimensional streamfunction formulation, the radial-pressure eigenvalue, $\Lambda = \frac{1}{r}\frac{dp}{dr}$ [see Eq. (3.5)], is a constant. In their study of cold and reacting opposed-jet flows, Frouzakis *et al.* (1998) find that Λ varies axially with a parabolic inlet velocity profile, while it is close to a constant when a plug-flow boundary condition is used. Figure 4.10 plots Λ as a function of the axial coordinate at several radii from the axisymmetric viscous simulations of K. Sone. Values of the radial coordinate are normalized by the nozzle radius, $R = d/2$. Λ varies considerably between the nozzle and stagnation plate. In addition, the value of $\Lambda =$ constant is plotted from a one-dimensional simulation performed using velocity boundary conditions taken from the two-dimensional simulation results. The one-dimensional value of Λ passes through the direct numerical simulation results.

To further assess the one-dimensional models applicability to finite-nozzle diameter experiments, the axial velocity profiles from the axisymmetric-viscous simulations of K. Sone are presented at

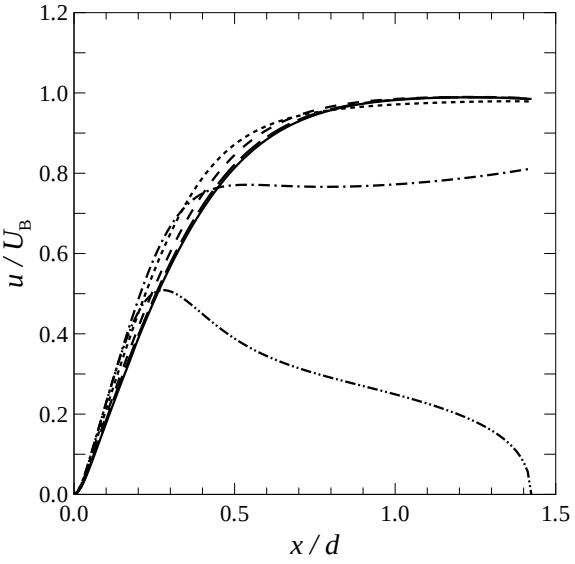

Figure 4.11: Axial velocity versus axial distance from plate at radial locations of $r/R = 0$ (solid), $r/R = 0.2$ (long dash), $r/R = 0.4$ (dash), $r/R = 0.6$ (dot), $r/R = 0.8$ (dash-dot), and $r/R = 1.0$ (dash-dot-dot). $Re = 700$ and $L/d = 1.4$.

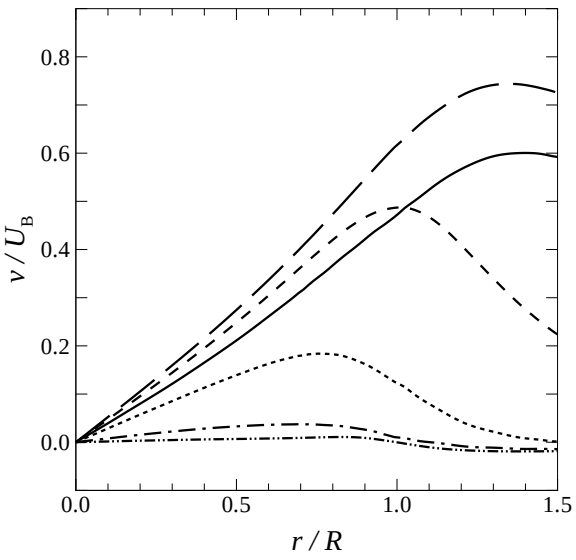

Figure 4.12: Radial velocity versus radial distance at axial locations of $x/d = 0.01$ (solid), $x/d = 0.1$ (long dash), $x/d = 0.2$ (dash), $x/d = 0.4$ (dot), $x/d = 0.7$ (dash-dot), and $x/d = 1.0$ (dash-dot-dot). $Re = 700$ and $L/d = 1.4$.

several radii in Fig. 4.11. The axial-velocity profiles collapse for 20% of the radial domain, with only slight deviations observed at up to 60% of the nozzle-radius. At larger radial locations, the near-wall flow appears to be well-characterized by the one-dimensional model. Radial velocity profiles are given in Fig. 4.12 as a function of the axial distance from the wall. The one-dimensional model assumes a linear variation in the radial velocity with distance from the axis. The profiles are linear for more than 60% of the radial domain.

In their study of turbulent jets, Kostiuk *et al.* (1993) showed that opposed- or impinging-jet velocity data are well-characterized by an error function and used the parameters obtained from the error-function fit to collapse their experimental data. Their error function contained three adjustable parameters, the velocity at infinity, U_∞, a strain-rate parameter, α, and a wall-offset length, δ/d,

$$\frac{u(x)}{U_\infty} \;=\; \mathrm{erf}\left[\,\alpha\,\left(\frac{x}{d} \;-\; \frac{\delta}{d}\right)\right] \;. \tag{4.3}$$

The collapse of the experimental and numerical data discussed above suggests that the appropriate velocity scale for laminar impinging jets is the Bernoulli velocity, *i.e.*, $U_\infty = U_\mathrm{B}$. From one-dimensional viscous stagnation-flow theory (see Section 4.2.1), the scaled-offset length, δ/d, which is proportional to the scaled-wall-boundary-layer thickness, can be related to the strain-rate parameter, α, such that

$$\frac{\delta}{d}(Re,\alpha) \;=\; 0.755\,\sqrt{\frac{1}{Re\,\alpha}} \;. \tag{4.4}$$

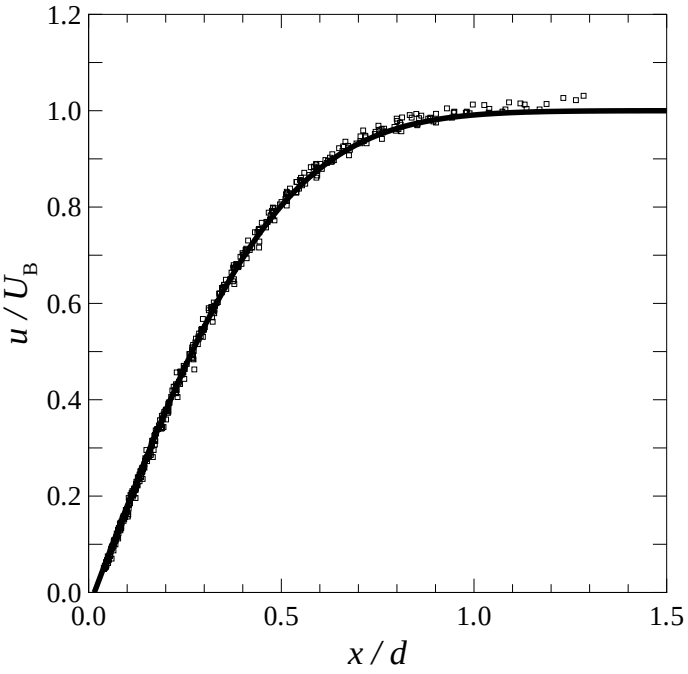

Figure 4.13: Comparison of error-function fit (line) to experimental data (□) at $Re = 1400$.

Re	α	δ/d	Experiment $\epsilon_{\rm rms}/U_{\rm B}$	Simulation $\epsilon_{\rm rms}/U_{\rm B}$
400	2.21	0.027	0.017	0.014
700	2.00	0.020	0.010	0.009
1400	1.88	0.015	0.011	0.010

Table 4.1: Error-function fit parameters and rms error, $\epsilon_{\rm rms}$, of fits to experimental and viscous-simulation data.

Thus, the only free parameter in this error-function fit to the data is the strain-rate parameter, α, which should be a function of Reynolds number alone, *i.e.*, $\alpha = \alpha(Re)$. Therefore, the axial velocity field for an axisymmetric impinging laminar jet is fully specified by the Bernoulli velocity, $U_{\rm B}$, since the Reynolds number is, in turn, derived from it. The error-function fit to the data at $Re = 1400$ is plotted in Fig. 4.13. The error function was fit to each experimental and viscous simulation case by adjusting α such that the root-mean-squared (rms) error was minimized. For each Reynolds number, the strain-rate parameter α was averaged over the range $0.7 \leq L/d \leq 1.4$. This single $\alpha(Re)$ dependence was subsequently used in all error-function fits to determine the resulting rms error, $\epsilon_{\rm rms}$. The fit parameters and $\epsilon_{\rm rms}$ are shown in Table 4.1.

As previously mentioned, the main Reynolds number effect for this flow is through the nozzle-wall boundary-layer thickness. The effect of the nozzle-exit velocity profile is studied in Fig. 4.14 for profiles varying from a top-hat shape, representative of the outflow from a high-contraction ratio nozzle, to a parabolic profile, representative of laminar pipe flow. These axisymmetric viscous

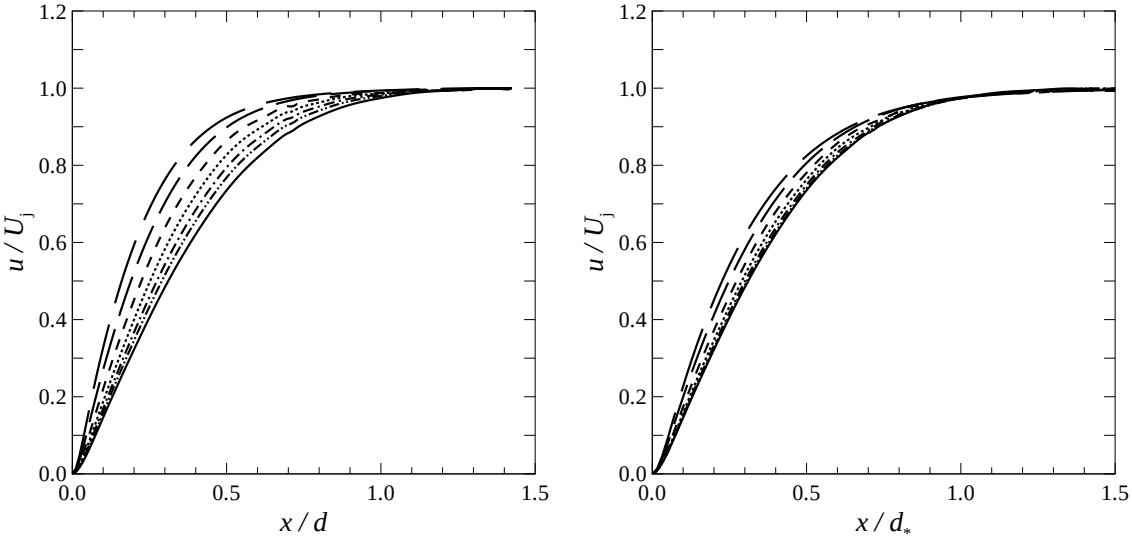

(a) (b)

Figure 4.14: Simulated velocity profiles at $Re = 700$ and $L/d = 1.4$. Axial distance scaled by d (a) and d_* (b), for variable nozzle-exit velocity profiles: Parabolic ($d_*/d = 0.71$, long dash), hyperbolic-tangent profiles with $d_*/d = 0.76$ (medium dash), $d_*/d = 0.82$ (dash), $d_*/d = 0.87$ (dot), $d_*/d = 0.91$ (dash-dot), $d_*/d = 0.95$ (dash-dot-dot), and top-hat ($d_*/d = 1.0$, solid) profiles.

simulations were performed by K. Sone. Real nozzle-exit velocity profiles will lie in between these two extremes (see Fig. 2.3). Intermediate cases are studied by specifying hyperbolic tangent profiles whose coefficients are adjusted to obtain a variation of boundary-layer displacement-thicknesses. The results in Fig. 4.14a,b are obtained by removing the nozzle interior from the axisymmetric-viscous-simulation domain and specifying the velocity profiles at the nozzle exit. Due to the lack of a plenum in the simulations, velocities are scaled by the velocity at the axis of the jet, U_j, instead of the Bernoulli velocity. Figure 4.14a indicates that there is a significant effect of the nozzle-exit velocity profile on the resultant axial velocity field. Figure 4.14b plots the axial velocity profiles with the axial distance normalized by the boundary-layer thickness corrected diameter, d_*. For $d_*/d > 0.87$ this scaling results in a good collapse of the profiles.

From the previous results, the displacement-thickness-corrected diameter, d_*, is an appropriate scaling parameter for axial distances. Figure 4.15 shows the scaled velocity profiles from axisymmetric viscous simulations at four Reynolds numbers. For low Reynolds numbers ($Re = 200$), viscous losses result in a jet-exit velocity that is lower than the Bernoulli velocity. There is an additional weak Reynolds number effect exhibited for $Re = 200$ and 400 that is not fully captured by the current scaling and is manifested in the slope of the profiles. However, the velocity profiles collapse reasonably well using this scaling and this allows the specification of an analytical expression for the

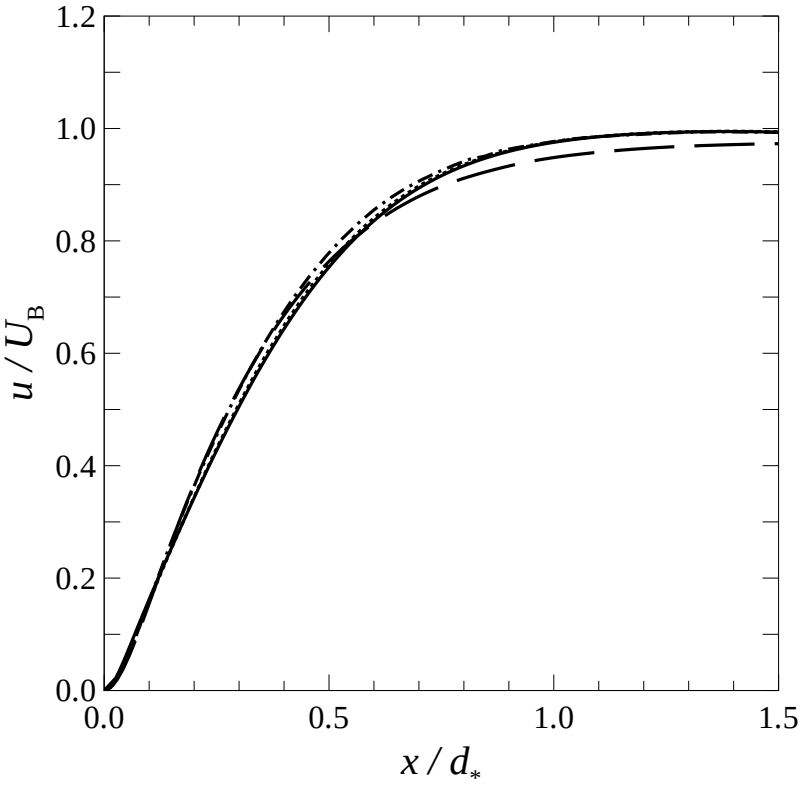

Figure 4.15: Axisymmetric-viscous simulation velocity profiles versus axial distance from plate normalized by the effective diameter, d_*, at $L/d = 1.4$ and $Re = 200$ (long dash), 400 (dash-dot), 700 (dot), and 1400 (solid).

velocity profile of the impinging jet in this Reynolds number range, *i.e.*,

$$\frac{u(x)}{U_{\rm B}} \;=\; \mathrm{erf}\left[\alpha_* \left(\frac{x}{d_*} - \frac{\delta}{d_*}\right)\right] \;, \tag{4.5}$$

where $\alpha_* = 1.7$, and $\delta/d_* = 0.016$ were found from fitting this error function to the axisymmetric-viscous-simulation data. The rms error of the error-function fit is less than 0.5% for $Re = 700$ and 1400 and less than 2% for $Re = 200$ and 400. At high Reynolds number, the wall boundary-layer thickness tends to zero and the potential flow formulation should accurately model the flow. In this limit, the velocity field is given by $u/U_{\rm B} = \mathrm{erf}\left[\alpha_{\rm p}\,(x/d_*)\right]$, with $\alpha_{\rm p} = 1.59$, as found by fitting this error function to the potential flow simulations. These expressions yield the velocity profile for an impinging jet with a measurement of the Bernoulli pressure across the nozzle contraction, the gas density and viscosity, the diameter ratio of the nozzle inlet and outlet, and the boundary layer thickness at the nozzle exit.

Using Eq. (4.3), the strain rate at any point on the axis can be computed using the error-function

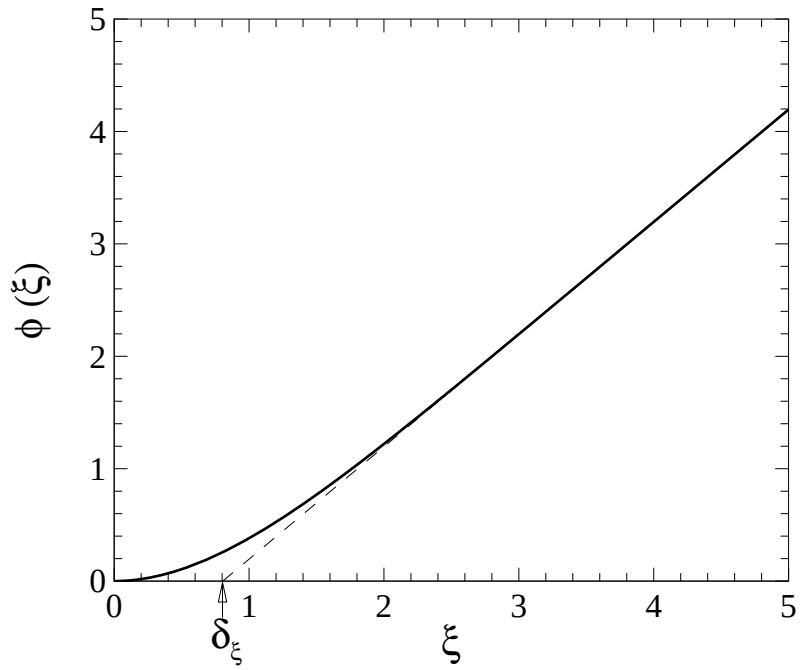

Figure 4.16: One-dimensional stagnation flow solution with potential flow boundary conditions (solid), and linear fit (dash) showing wall-boundary-layer offset δ_ξ.

fit,

$$\sigma(x) \;=\; \frac{\mathrm{d}u(x)}{\mathrm{d}x} \;=\; \frac{2\,U_\mathrm{B}\,\alpha}{\sqrt{\pi}\,d}\,\exp\left[-\alpha^2\left(\frac{x}{d}-\frac{\delta}{d}\right)^2\right]\;. \tag{4.6}$$

This yields a maximum strain rate of $\sigma_\mathrm{max} = 2\,U_\mathrm{B}\,\alpha/\sqrt{\pi}\,d$, at $x = \delta$.

4.2.1 Wall boundary-layer thickness

From one-dimensional stagnation-flow theory, the wall boundary-layer thickness depends only on the velocity gradient in the potential-flow region (Schlichting 1960; Kee *et al.* 2003). The cold-flow solution to the boundary-layer equations is a linear function in the far-field, with a viscous boundary layer close to the wall. The only free parameter in this flow is the far-field velocity gradient u'_∞. In the far-field, the high-order derivatives vanish (u''', $u'' \to 0$) and, from Eq. (3.7), the radial pressure gradient eigenvalue is equal to $\Lambda/\rho = -(u'_\infty)^2/4$. The resulting equation can be nondimensionalized through the transformations $\xi = x\,\sqrt{u'_\infty/\nu}$ and $\phi = u(x)/\sqrt{u'_\infty \nu}$, resulting in the following equation for $\phi(\xi)$:

$$2\phi''' - 2\phi\phi'' + (\phi')^2 = 1\;. \tag{4.7}$$

The boundary conditions are $\phi(0) = \phi'(0) = 0$ and $\phi'(\infty) = 1$. Eq. (4.7) can be solved using a shooting method, where $\phi''(0)$ is adjusted to satisfy the boundary condition at infinity. Figure 4.16 shows the solution to Eq. (4.7). The nondimensionalized wall boundary-layer displacement thickness

δ_ξ can be calculated in the linear region of the flow ($\xi > 5$):

$$\delta_\xi = \xi - \frac{\phi(\xi)}{\phi'(\xi)} = 0.80 \tag{4.8}$$

From Eq. (4.6), the slope of the error function as it approaches the boundary layer is given by $\mathrm{d}u/\mathrm{d}x = 2U_\mathrm{B}\alpha/(\sqrt{\pi}d)$. Equating this to u'_∞ allows the boundary layer thickness to be determined analytically from the other error function parameters, U_B and α. Thus, the wall boundary-layer displacement thickness in physical space is equal to

$$\frac{\delta}{d} = \delta_\xi \, \frac{(\pi)^{1/4}}{(2)^{1/2}} \, \sqrt{\frac{1}{Re\ \alpha}} = 0.755 \, \sqrt{\frac{1}{Re\ \alpha}} \, , \tag{4.9}$$

where $Re = d\,U_\mathrm{B}/\nu$, as defined previously.

4.3 Conclusions

Scaling the centerline axial velocity for an impinging jet by the Bernoulli velocity, calculated from the static pressure drop across the nozzle contraction, collapses centerline axial-velocity data on a single curve that is independent of the nozzle-plate separation distance for separation-to-diameter ratios of $L/d \geq 0.5$. The axisymmetric viscous and potential-flow simulations reported here allow nozzle-wall proximity effects to be investigated by including the nozzle in the solution domain. Using this simulation domain, axisymmetric viscous simulations yield good agreement with experiment and confirm the velocity profile scaling. The potential-flow simulations reproduce the collapse of the data; however, at these Reynolds numbers, viscous effects result in disagreement with experiment. One-dimensional streamfunction simulations can predict the flow in the stagnation region if the boundary conditions are correctly specified. The radial-pressure eigenvalue, Λ, is found to vary throughout the flow field in axisymmetric viscous simulations. The good agreement between the one-dimensional simulations and either experimental data or two-dimensional simulations indicates that the axial velocity is not sensitively dependent on the spatial variation of Λ.

The scaled axial velocity profiles are well-characterized by an error function with one Reynolds-number-dependent parameter α. The error function provides a good fit to both experimental and viscous-simulation data, with root-mean-squared errors of $\epsilon_\mathrm{rms} \lesssim 0.02\,U_\mathrm{B}$. Viscous effects are captured by scaling the axial distance by the effective (displacement-thickness-corrected) diameter d_*. This scaling relies on thin nozzle boundary layers (d_*/d close to unity) and negligible viscous losses through the nozzle. These scalings allow the specification of an analytical expression for the velocity profile of an impinging laminar jet over the Reynolds number range of $200 \leq Re \leq 1400$.

Chapter 5

Strained, premixed flames

5.1 Introduction

The development of detailed, accurate, chemical-kinetic models is one of the most difficult problems in combustion. In the review article by Simmie (2003), he states that the "design of a reaction mechanism is still a black art with the majority being constructed on an ad hoc basis relying heavily on intuition, rules of thumb, etc. and building on previous sub-mechanisms." The combustion of hydrogen is generally considered to be well-understood (Westbrook & Dryer 1984), and the chemistry models require approximately 10 species and 30 reactions to capture the kinetic effects. Even so, Turányi *et al.* (2002) have found that the uncertainty associated with the various reactions and thermodynamic parameters leads to an uncertainty of $\pm$20–30 cm/s in the laminar flame speed for hydrogen-air flames. The addition of carbon chemistry complicates matters. Methane, CH_4, is the simplest hydrocarbon fuel, yet typical mechanisms require 30–40 species and more than 300 reactions (*e.g.*, Smith *et al.*; Hughes *et al.* 2001). As one investigates longer hydrocarbon chains, all reactions associated with smaller hydrocarbons must be included, along with the addition of reactions that account for the breaking up of these chains into C_1 and C_2 fragments. The key to understanding and modeling the combustion of hydrocarbon fuels in flames is obtaining an accurate chemical-kinetic model for the oxidation of C_1 and C_2 hydrocarbon fuels (Miller *et al.* 1990). This is due to the fact that in flames of higher alkanes and alkenes, reactions leading to C_1 and C_2 fragments are too fast to limit the overall rate of combustion (Warnatz 1984a; Miller *et al.* 1990). In order to understand the combustion of gasoline, kerosene, or other long-chain hydrocarbon fuels, the combustion chemistry of methane, ethane, ethylene, etc. must first be understood.

As methane is the simplest hydrocarbon fuel, and because of its importance as a baseline for all other hydrocarbons, it has received the most study (Simmie 2003). Unfortunately, although significant effort has been expended in developing reliable models for methane combustion (*e.g.*, the GRI-Mech initiative, Smith *et al.*), such models have not been tested/validated against sufficient numbers of kinetically independent experiments (Frenklach *et al.* 1992). In fact, no detailed

methane oxidation mechanism has been generally accepted as a reference mechanism (Hughes *et al.* 2001). Indeed, four commonly employed methane mechanisms utilize significantly different rate expressions for some of the most important reaction steps (Hughes *et al.* 2001). These mechanisms all perform similarly when compared to currently available experimental data. The conclusion reached by Hughes *et al.* (2001) is disturbing, that the oxidation chemistry of simple fuels such as carbon monoxide, methane, and ethane is still not well-characterized at the elementary level. Turányi *et al.* (2002) have found that the predicted methane-air laminar flame speed has an associated error of 2–5 cm/s, when uncertainties of the individual reaction rates and thermodynamic data are propagated. These authors also found that in premixed freely propagating flames, the location of the peak concentration of important radicals (H, O, OH, CH, CH_2) had similar associated uncertainties as the laminar flame speed. The calculated maximum concentrations of CH and CH_2 radicals also had high uncertainties. The authors suggest that the excellent concurrence between experimental flame velocities and simulation is essentially a result of fortuitous agreement and "fine tuning" of the mechanisms involved. Their conclusion is that the rate coefficients of the relevant reactions are not yet known with sufficient accuracy for exact methane flame modeling. As the various models "fit" the data, but are significantly different from one another, it is not clear which model one should choose when investigating conditions outside of the validated parameter range. Thus, the kinetic models can be considered to be very large, and complicated, empirical fits to the data. According to Simmie (2003), "the ultimate goal of chemical kinetic modeling is to develop an ideal set of thermodynamic data and a 'perfect' reaction mechanism which will describe all the essential details of the physical reality, specifically the combustion of a hydrocarbon in the gas-phase." The eventual development of a predictive, rather than descriptive, chemistry model motivates this experimental study.

A chemical-kinetic mechanism can be considered adequate only if it can describe all relevant chemical responses over the diverse range of parametric and system variations that are expected to occur (Law *et al.* 2003). One of the fundamental problems in the validation of chemistry models is the lack of kinetically independent experimental data against which the models can be compared (Frenklach *et al.* 1992). The variety of proposed kinetic models should exhibit different behavior in some of the regions of their associated parameter space. If a dataset could be compiled that accessed every region of the space, it would be possible to find conditions where each of the proposed models predict (significantly) different results, allowing comparison with experiment to indicate which model is more physically relevant in that region of the parameter space. Such a dataset would be comprised of experiments performed in a wide range of combustion geometries, using varied diagnostic techniques, etc. This reinforces the notion that cooperative research is essential to advance the understanding of hydrocarbon flame chemistry (Simmie 2003). Chemistry models must also be coupled with thermodynamic and transport models for the simulation of flame propagation,

and these models need to be validated (and perhaps adjusted) along with the kinetics (Simmie 2003).

A chemistry model may be utilized in its full detail in numerical studies of combustion phenomena, usually in simplified fluid flows (laminar flames). It is interesting to note that even 50 years ago, many chemists "dismiss(ed) flames as being too hopelessly complicated for fruitful study in any fundamental way" (Fristrom & Westenberg 1965; preface). The considerable complexity (number of species and reactions) required to describe the flame propagation of simple hydrocarbon fuels such as methane and ethylene, supports this pessimistic view. However, well-designed, "simple" experiments should be able to test these complicated mechanisms. The use of flames and flame structure to investigate chemical kinetic and transport models has a long history, with considerable progress in the field because of these experimental investigations (Fristrom & Westenberg 1965). As both numerical and experimental techniques advance, improved ability to make detailed comparisons between experiment and models should lead to the development of increasingly accurate models. According to Daily, researchers perform measurements for several reasons, one being the validation or testing of a theory or computation. This type of *hypothesis testing* involves carrying out an experiment for the purpose of direct comparison with a theory or calculation, often for the purpose of numerical code validation, and may involve detailed measurements of velocity, temperature, and concentration fields. In this research, various *hypotheses* (chemistry, transport, and flow models) are tested by directly comparing experimental measurements to numerical simulations utilizing these models.

The approach taken here is to study C_1 and C_2 hydrocarbon flames in a stagnation-flow geometry, targeting the various chemistry models proposed for the fuel. These data complement other techniques, such as ignition data in shock tube experiments (*e.g.*, Frenklach & Bornside 1984) and the measurement of species profiles in laminar flames (*e.g.*, Davis *et al.* 1999) and flow reactors (*e.g.*, Davis *et al.* 1999). Typically, laminar flame-speed data are also used to validate the kinetic mechanisms (*e.g.*, Egolfopoulos *et al.* 1990; Vagelopoulos *et al.* 1994), and more recently, extinction strain-rate data are being employed (*e.g.*, Zhang & Egolfopoulos 2000; Dong *et al.* 2003). However, laminar flame-speed and extinction strain-rate data study two extreme values of the range of strain rates that flames can be subject to. To probe the models over a wide variety of conditions (*e.g.*, equivalence ratio, ambient pressure, strain-field) studies of strained laminar flames in a wider range of environments are desirable. The high parametric dimensionality of the kinetic and transport models requires many detailed and accurate experiments over a sufficiently large range of conditions. The experimental burden imposed by these requirements is exacerbated when performing laminar flame-speed measurements, as multiple experimental datasets are required to produce a single optimization target. The approach here is to directly compare measurements of strained premixed flames to simulations, resulting in a possible optimization target for every experiment performed. This methodology could allow for the production of a dataset with sufficient parametric dimensionality to constrain the kinetics optimization. Such strained-flame experiments would be enhanced

by simultaneous diagnostics that permit detailed flow and chemical-species data to be recorded and compared to model predictions. This methodology could be applied to the study of laminar flame speeds by allowing the simulation of the experimental data at each imposed strain rate, in addition to comparing the resulting (extrapolated) laminar flame speed with numerical predictions.

Davis *et al.* (2001) found that the simulated extinction strain rate was sensitive to the choice of upstream boundary conditions (*e.g.*, plug- or potential-flow), with differences in the predicted values that are outside of typical experimental uncertainties. The simulated flowfield must accurately capture the experimental flow if extinction data are to be compared to simulations. One could utilize the methodology outlined in this work to study flames at a variety of imposed strain rates, improving the accuracy of the boundary conditions used in determining the extinction strain rate. This would allow a larger portion of the acquired experimental data to be used in validating the chemistry models, rather than simply comparing a single numerical value (flame speed or extinction strain rate) to simulated results. The approach presented in this work relies on detailed measurements of strained flames in a jet-wall stagnation flow. This setup yields a flow with boundary conditions that can be accurately specified, facilitating simulation and comparison with experiment. This flow can also, with care, be stable to high Reynolds numbers. The diagnostics are optimized for accuracy, minimal flame disturbance, and rapid simultaneous recording of flow velocity and CH radical profiles.

The first comparisons between the predictions of the one-dimensional streamfunction model (utilizing potential-flow boundary conditions, see Chapter 3) and flame experiments in jet-wall stagnation flow is given in a pair of papers by Smith *et al.* (1971) and Fang *et al.* (1971). They remarked that "such comparisons would seem to provide a useful means of studying kinetics of combustion reactions in certain instances and of investigating the basic behavior of combustible mixtures when convection, diffusion and finite-rate chemical kinetics are of interest." Their comparisons to experiment were in the form of a global extinction strain rate (nozzle velocity divided by the diameter) and heat flux measurements. Experiments in jet-wall stagnation flow are also discussed in a series of papers by Mendes-Lopes and coworkers (Daneshyar & Mendes-Lopes 1982; Daneshyar *et al.* 1982; Mendes-Lopes & Daneshyar 1985). Laser Doppler Velocimetry (LDV) was utilized to measure axial and radial velocity profiles in cold and reacting stagnation flames with separation distances between 0.74 and 1 nozzle diameter. The radial profile of the axial velocity was shown to exhibit a velocity defect at the nozzle centerline, while the axial and radial velocity profiles exhibited characteristics typical of stagnation-point flow (Daneshyar *et al.* 1982). They also found that the flow could be approximated by a dual axisymmetric stagnation-point flow, where the first stagnation flow is toward an apparent plane determined by the flame dilatation, and the secondary flow impinges on the stagnation surface (Mendes-Lopes & Daneshyar 1985). The strain rate was found to be independent of the nozzle-plate separation distance, although the flame stability was dependent on this distance (Mendes-Lopes 1983). Experimentally measured velocity profiles, using LDV, and temper-

ature profiles, using thermocouples, were compared to theoretical predictions using several matching parameters, such as the upstream and downstream strain rates, flame thickness, and burning velocity. Good agreement was found between the "fit" profiles and their data, indicating that the model can capture the basic features of the flow. These authors find that increasing strain rate tends to decrease the burning velocity, and that the effect of straining is more pronounced when there is heat loss from the reaction zone to the cold stagnation plate (Daneshyar *et al.* 1982; Mendes-Lopes & Daneshyar 1985). The axial velocity profile was found to contain all of the information required for their analysis and the plate temperature did not exhibit a strong influence on the flame. The experimental data of Mendes-Lopes and Daneshyar is compared to theoretical predictions by Eteng *et al.* (1986) and Kim & Matalon (1988), through fitting of the potential flow model to the strain rate just upstream of the flame. Again, the theoretical model is able to capture the basic flow features, if the input parameters are appropriate. Displacement effects of laminar flames are discussed by Kim *et al.* (1992). They find that the dilatation introduced to the flow by the accompanying heat release can significantly alter the strain rate in the flow external to the flame, and that care must be taken when determining the strain-rate parameter used to compare theoretical predictions and experimental results.

Including full transport and chemistry models along with the one-dimensional hydrodynamic model allows the simulation of realistic (experimental) strained premixed flames (Kee *et al.* 1988; Dixon-Lewis 1990). However, few comparisons of such models, utilizing detailed chemistry, and experimental data have been published. Temperature and concentration measurements made using thermocouples and a microprobe gas chromatograph were compared to numerical simulations using such a model by Smooke *et al.* (1990). Law and coworkers studied methane-air, opposed-jet flames for lean, stoichiometric, and rich mixtures, using LDV and CARS for velocity, temperature, and major-species measurements to quantify the effect of stretch on flame structure (Law *et al.* 1994; Sung *et al.* 1994, 1996a,b; Sun *et al.* 1996). To compare experimental and simulated data, a potential-flow boundary condition with a variable inflow mass flux is used to visually match the profiles (Law *et al.* 1994). The authors report general agreement for temperature and major species profiles when the flame location is adjusted to match the measurements. A consistent comment in these papers is the lack of experimental data on flames in stagnation flows.

The effects of thermophoresis on the measurement of velocity profiles in flames is discussed in a pair of papers by Sung and coworkers (Sung *et al.* 1994, 1996a). They found that considerable lag could result between the measured and computed velocity profiles in the post-flame region, even for the sub-micron sized particles used in those studies. These authors utilized the simulated velocity and temperature profiles to estimate the expected particle velocity profile when thermophoretic effects are included. The effects of thermophoresis are more pronounced for flames close to the stagnation surface (for highly strained flames), due to the comparable magnitudes of the local

flow and thermophoretic velocities (Sung *et al.* 1996a). They found improved agreement between experiment and simulation when the effects of thermophoresis were included. However, the simulated post-flame velocity profile was still found to lie above the experimental data. It should also be noted that Sung *et al.* (1996a; see Appendix) extended the previous work by including an intermediate flow boundary condition (between the limits of potential- and plug-flow) to visually align the velocity profile ahead of the reaction zone. In the work of Sung *et al.* (1996a), an initial simulation utilizing the plug-flow boundary condition was performed. Through a continuation method (see Nishioka *et al.* 1996), the inlet velocity and velocity gradient were adjusted to determine the inlet boundary condition that best matched the experimental data. These studies were aimed at determining the effect of the imposed strain rate on the flame structure and found that the major species profiles were not dependent on the applied strain. The use of stagnation-point flames to study kinetic effects through direct simulation of experiment does not appear to have been attempted previously. In addition, the determination of the inlet boundary conditions from the cold portion of the velocity profile, as employed here, while somewhat similar to the technique of Sung *et al.* (1996a), is unique to the present study.

The setup used in this study consists of a high-contraction ratio nozzle impinging upon a solid, temperature-controlled (and monitored) stagnation plate (see Chapter 2). Premixed flames are stabilized in the resulting stagnation-flow. Egolfopoulos *et al.* (1997) studied the effects of a variable temperature wall on the propagation and extinction of premixed laminar flames. This study showed that radical recombination at the wall is unimportant for wall temperatures below approximately 1000 K. The study also found that extinction is largely controlled by the heat loss to the plate, but that the extinction strain-rate is only weakly dependent on the wall temperature. The reference flame speed, $S_{u,\mathrm{ref}}$, for flames well-separated from the wall was found to be independent of the wall temperature. The authors also note that impinging-jet flows result in more stable flames compared to the opposed-jet configuration (Egolfopoulos *et al.* 1997).

Particle Streak Velocimetry (PSV, see Appendix B), complemented by simultaneous CH Planar Laser Induced Fluorescence (PLIF, see Appendix C) imaging at 10 Hz, allows accurate concurrent measurement of both the velocity and CH radical profiles. Planar Laser Induced Fluorescence (PLIF) (Allen *et al.* 1986; Eckbreth 1996) of the CH radical is used in this study as it is a short-lived radical with a narrow spatial profile within the reaction zone. The experimental CH profile can be directly compared to one-dimensional simulation predictions, and can allow deficiencies in the chemical kinetics to be identified. Simultaneous measurements of air, fuel, and diluent mass fluxes, as well as of stagnation plate temperature, allow an accurate specification of boundary conditions for simulations.

Experimental velocity and CH profiles are compared to one-dimensional simulation predictions using the CANTERA software package developed by Goodwin (2003; see also Chapter 3 and Ap-

pendix D). The simulations utilize a multi-component transport formulation (Kee *et al.* 2003). Various chemical-kinetic models are employed to assess their ability to predict the experimental results. GRI-Mech 3.0 (Smith *et al.*) is a combustion mechanism developed to model natural gas combustion and contains 53 species and 325 reactions. The C_3 mechanism of Davis *et al.* (C_3-Davis, 1999) is developed to describe the combustion of C_1–C_3 hydrocarbons and contains 71 species and 469 reactions. The "San Diego" mechanism (see Bibliography: San Diego mechanism) is developed to model the combustion of C_1–C_3 hydrocarbons. Two releases of the "San Diego" mechanism are utilized in this study, the 2003 version (SD2003) containing 39 species and 173 reactions, and the 2005 version (SD2005) containing 39 species and 175 reactions.

In this study, velocity data in the cold-flow region upstream of the flame are used to specify boundary conditions for simulations by exploiting the quadratic cold-flow solution to the one-dimensional equations. The reader is referred to Chapters 2 and 3 for a more detailed description of the experimental apparatus and the simulation methodology. The diagnostics employed here and some preliminary measurements on methane-air flames have been presented previously (Bergthorson *et al.* 2005a). The experimental data studying the effect of variations in the nozzle-to-stagnation plate separation distance were also previously reported (Bergthorson *et al.* 2004).

Strained, methane-air flames are studied as a function of the nozzle-stagnation plate separation distance, L, to assess the simplified hydrodynamic model. Flame temperature dependence is studied by mixture dilution with excess nitrogen. The diagnostics are applied to methane-air flames, under similar strain-rate conditions, as a function of equivalence ratio, Φ. The effect of strain-rate variations is studied for lean, near-stoichiometric, and rich mixtures. Further studies of hydrocarbon chemistry are made by studying ethane- and ethylene-air flames as functions of the applied strain rate and the mixture fraction. The approach and diagnostics permit an assessment of the numerical simulation predictions of strained-flames for low-carbon-number hydrocarbons. These data are made available to kineticists looking for optimization targets (see Appendix L), following the recommendations of the collaborative data approach (Frenklach *et al.* 2003). The work presented here aims at making direct comparisons between model predictions and detailed experimental data in stagnation-point flows. This methodology allows direct comparison of experimental and simulation results, reducing the experimental burden required to acquire data that can further constrain the chemistry model.

5.2 Methane-air flames

Methane-air flames are studied as a function of the nozzle-to-plate separation distance, L. Subsequently, the effect of variable strain rate is studied for near-stoichiometric ($\Phi = 0.9$), lean ($\Phi = 0.7$), slightly rich ($\Phi = 1.1$), and rich ($\Phi = 1.25$) flames. The effect of varying flame strength is studied for a stoichiometric ($\Phi = 1.0$) flame at varying levels of nitrogen dilution. Kinetic effects are found

to be most sensitive to the inlet composition, and flames are studied at approximately constant flame location for a range of equivalence ratios. A set of experiments is also performed with variable dilution, to study flames at various equivalence ratios with similar imposed strain rates and similar flame locations. Unless otherwise indicated, the flames are simulated with the GRI-Mech 3.0 thermo-chemistry/transport model (Smith *et al.*), and a multi-component transport formulation (see Kee *et al.* 2003). For several flames, the experimental results are also compared to simulations utilizing a C_3 model developed by Davis *et al.* (1999) and two versions of the "San-Diego" mechanism (see Bibliography: San Diego mechanism), indicated here by the years of their revision, SD2003 and SD2005. Comparisons of these three models helps to indicate the level of uncertainty in the various proposed chemistry models. Most of these mechanisms have been "tuned" to accurately predict the burning velocities of atmospheric pressure, methane-air flames (and in some cases, ethane- and ethylene-air). It should be noted that the true uncertainty of the model should be found by propagating the uncertainties associated with individual reactions, thermodynamic data, and transport properties through the solution. This was employed by Turányi *et al.* (2002) who found that an uncertainty in the flame speed of 2–5 cm/s is typical for methane-air flames.

Inlet composition boundary conditions are determined from measurements of the individual mass flow rates. The stagnation-wall temperature is specified from the experimental measurements, and the inlet temperature is assumed to be equal to the measured room temperature. Velocity boundary conditions are specified from a parabolic fit to the cold portion of the profile, as discussed in Chapter 3 and Appendix B. The measured boundary conditions and Bernoulli velocity are given for each experimental run in Appendix J. The run number for each experiment is included in the figure captions to assist in cross-referencing.

To account for the effects of particle inertia and thermophoresis, the particle behavior in the simulated flowfield is solved using a Lagrangian technique as described in Appendix A. This technique allows the particle velocity and position to be found as a function of time. The resulting parametric description of the particle velocity profile is post-processed to account for the finite chopping frequency employed, and results in a modeled-particle-tracking (modeled-PSV) profile (see Appendix A). If the simulated flowfield matches the experimental flow, the modeled-PSV profile should agree with the PSV data, as particle-inertia, thermophoretic, and finite chopping-frequency effects are all accounted for.

The CH PLIF profiles presented for methane-air flames were obtained by measuring the on-resonance fluorescence signal and correcting this by subtracting an averaged image with no flame (see Appendix C). This corrects for Rayleigh scattering and dark noise in the images. As discussed in Appendix C, the true CH signal should be obtained by measuring the CH fluorescence signal both on and off of the resonance line, and taking the difference of the two, as suggested by Sutton & Driscoll (2003). This is important as broadband fluorescence from Polycyclic-Aromatic Hydrocarbon

(PAH) soot precursors can be excited by the laser and results in a background noise signal that can dominate the CH fluorescence in some cases (Norton & Smyth 1991). At the time the measurements were recorded, this had not been appreciated. Fortunately, for methane-air flames the profile shapes are not strongly dependent on which correction method is applied (see Appendix C), except for lean ($\Phi = 0.7$) flames for which the profile thickness is overestimated if the off-resonance subtraction is not used. The CH profile location is not sensitive to the choice of correction utilized. The reason the profiles are not strongly affected for methane-air flames is due to the fact that these PAHs exist only within the reaction zone, and exhibit a profile very similar to that of the CH radical itself. However, for rich C_2 flames, it is essential that this off-resonance "noise" be corrected for, as it alters the profile shapes considerably (see Appendix C). To determine the relative CH concentrations and profile thicknesses as a function of the applied strain rate, a second set of data was recorded using the new PLIF processing technique. The data presented in Figs. 5.30 and 5.32 have been corrected for the off-line signal. The conclusions drawn from the experiments performed without the off-resonance correction would not be altered by repeating the measurements using the new technique. Thus, the data are presented using the "no-flame" correction methodology.

5.2.1 Nozzle-to-plate separation distance

Reacting stagnation flows are studied for a near-stoichiometric, $\Phi = 0.9$, methane-air (CH_4-air) flame to determine the effect of heat release on the fluid mechanics and the ability of the one-dimensional simulations to capture the flow. The nozzle-to-plate separation distance, L, is varied at constant Φ to study the hydrodynamics at constant chemistry. Figure 5.1 shows velocity profiles for a $\Phi = 0.9$ methane-air flame at $L/d = 1.2$ and $Re \cong 1100$. Velocities are scaled by the Bernoulli velocity, $U_{\rm B}$ [see Eq. (2.5)], and axial distances by the nozzle diameter, d. The cold-flow error function profile, with $\alpha = 1.93$ corresponding to $Re = 1100$, is also included for comparison. Simulation boundary conditions are specified from a fit to the cold-flow portion of the profile ($0.35 < x/d < 0.8$) to determine u_ℓ and u'_ℓ, minimizing uncertainty in these values. The measured inlet velocity is corrected for particle inertia effects through the relation

$$\frac{u_{\rm p}}{u_{\rm f}} = \frac{1}{1 + C_{\rm KW}\,\tau_{\rm S}\,\sigma} \ , \tag{5.1}$$

where $u_{\rm p}$ is the measured particle velocity, $u_{\rm f}$ is the (local) fluid velocity, $C_{\rm KW}$ is the Knudsen-Weber slip correction factor [see Eq. (A.10)], $\tau_{\rm S}$ is the Stokes time, and $\sigma = du_{\rm p}/dx \cong du_{\rm f}/dx$ is the (local) velocity gradient [see Appendix A, Eq. (A.23)]. The Stokes time is given by

$$\tau_{\rm S} \equiv \frac{\rho_{\rm p} d_{\rm p}^2}{18\,\mu} \ , \tag{5.2}$$

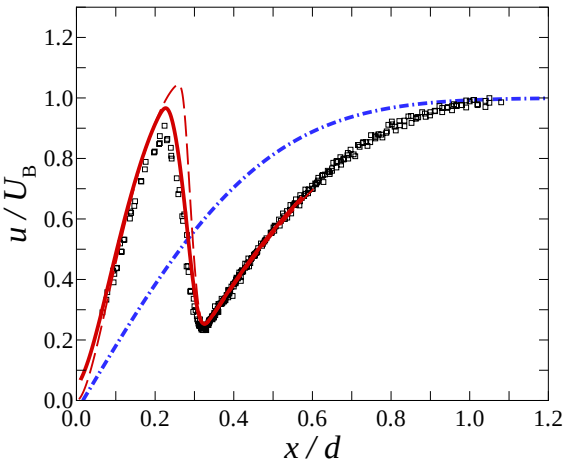

Figure 5.1: CH_4-air flame profiles ($\Phi = 0.9$, $L/d = 1.2$, run196). (□) PSV data, (dashed red line) simulated velocity, u_f, profile (GRI-Mech 3.0), (solid red line) modeled-PSV, u_{PSV}, profile, (dot-dash blue line) cold-flow error function.

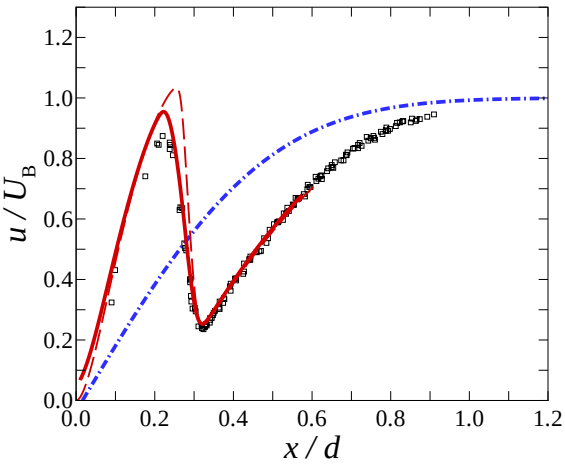

Figure 5.2: CH_4-air flame profiles ($\Phi = 0.9$, $L/d = 1.0$, run197). Legend as in Fig. 5.1.

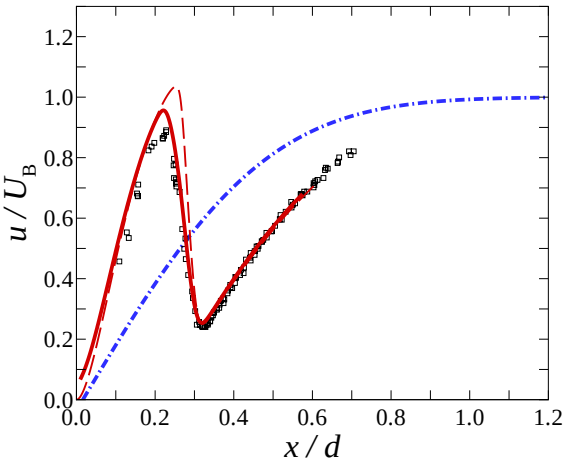

Figure 5.3: CH_4-air flame profiles ($\Phi = 0.9$, $L/d = 0.8$, run199). Legend as in Fig. 5.1.

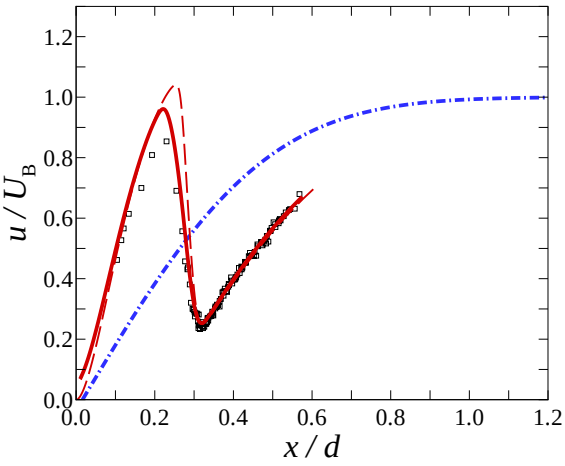

Figure 5.4: CH_4-air flame profiles ($\Phi = 0.9$, $L/d = 0.6$, run200). Legend as in Fig. 5.1.

where ρ_p is the particle density, d_p is the particle diameter, and μ is the (local) fluid viscosity. $U(\ell) = \rho_0\, u_\ell/2$ and $U'(\ell) = \rho_0\, u'_\ell/2$ are then calculated to specify the boundary conditions. In this chapter, ℓ/d is fixed at 0.6, unless otherwise noted.

Numerical simulations are performed using the one-dimensional streamfunction model with multi-component transport and GRI-Mech 3.0. The modeled-PSV profile is also included for comparison (see Appendix A). The simulated fluid velocity is denoted by u_f, and the modeled-PSV profile by u_{PSV}. The particles used in these experiments were 3 μm ceramic microspheres ($\rho_p \cong 2400\,\mathrm{kg/m^3}$; 3M Zeeospheres, W-210), and the chopping frequency was $\nu_c = 2000\,\mathrm{Hz}$. The simulated fluid velocity

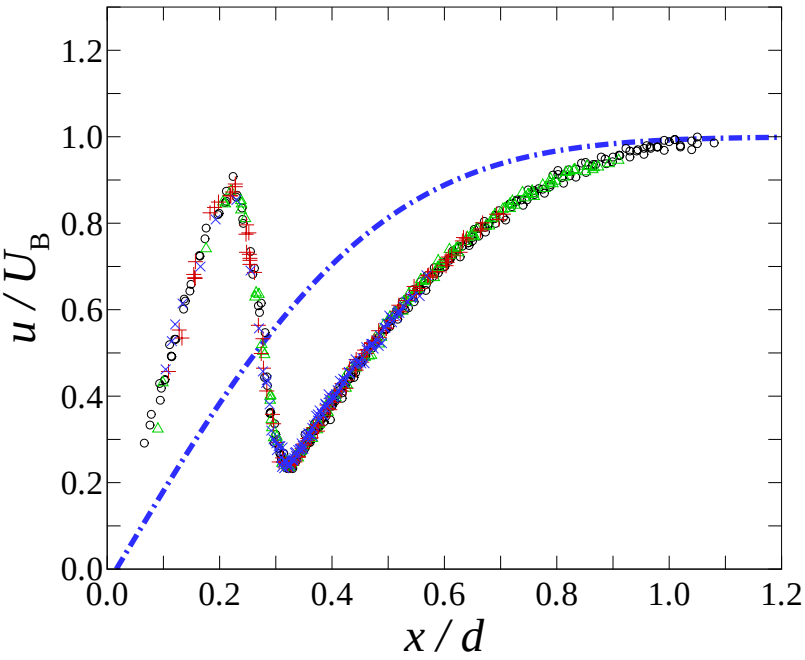

Figure 5.5: CH_4-air flame profiles ($\Phi = 0.9$, run196-200) at: $L/d = 0.6$ ($\times$), $L/d = 0.8$ ($+$), $L/d = 1.0$ ($\triangle$), and $L/d = 1.2$ ($\circ$). Cold-flow error function is also included (dot-dash blue line).

profile is in reasonable agreement with experiment, but predicts a much higher post-flame velocity than measured. Including the particle-inertia, thermophoretic, and finite chopping-frequency effects bring the modeled profiles closer to the experimental data, but the post-flame velocities are still larger than those measured. There is significant improvement in the agreement of the overall shape of the post-flame profiles, indicating that such effects must be accounted for in this high-velocity, high-velocity-curvature region of the flow. The ignition of a flame results in the introduction of a virtual stagnation point that alters the flowfield, although the strain rate, du/dx, experienced by the flame is similar to that of the cold-flow. Figures 5.2, 5.3 and 5.4 detail measured and simulated velocity profiles for a $\Phi = 0.9$ methane-air flame at $L/d = 1.0$, 0.8, and 0.6 at $Re \cong 1100$. The Bernoulli velocity in these experiments was kept constant to within $\pm 0.3\%$. Good agreement is seen for all profiles, except for an overprediction of the post-flame velocities. A nozzle-exit velocity deficit is evident compared to the cold-flow error function for $L/d = 0.6$ and 0.8.

A comparison of velocity profiles at variable L/d is given in Fig. 5.5. At constant U_B, the velocity profiles collapse independent of L/d. This is consistent with the results presented in Chapter 4, where the flowfield of a cold impinging jet was found to be independent of the nozzle-plate separation distance. In the reacting flow, a velocity defect is produced at the nozzle exit such that the velocity and gradient match the cold-flow portion of the profile for large L/d. Thus, the nozzle to plate separation distance, L, is not an important parameter in either nonreacting or reacting stagnation flow. The applied strain rate to the flame, and the resulting flame location, is a function only of

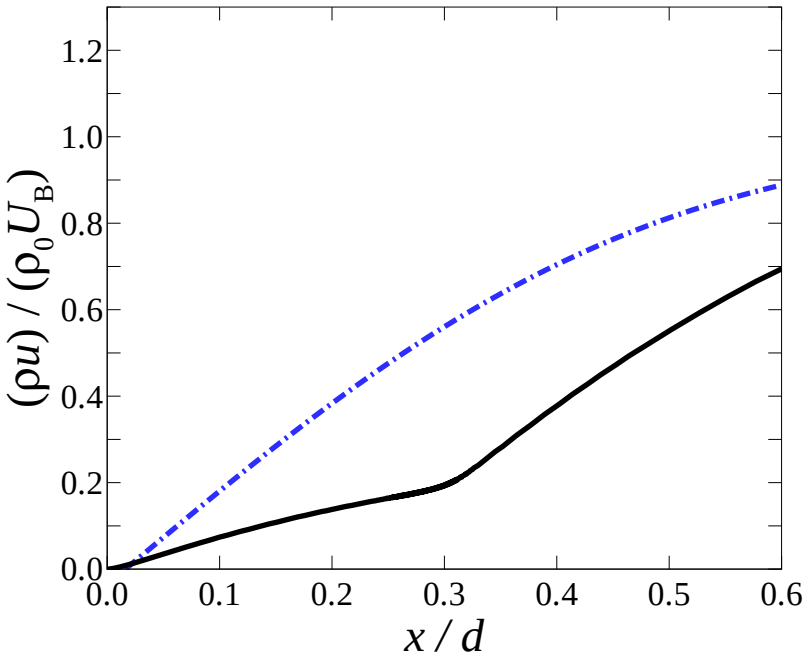

Figure 5.6: CH_4-air flame profiles of ρu ($\Phi = 0.9$). (solid black line) simulation for $L/d = 1.2$, $Re \approx 1100$, (dot-dash blue line) cold-flow error function.

the imposed Bernoulli velocity. It should be noted that this is true only for Bernoulli velocities that result in the stabilization of stagnation flames at all separation distances. At large L/d it can be possible to stabilize flames with low stretch-rates that would be attached to the nozzle for shorter separation-distances. The flowfield in this case will be dependent on where the flame is stabilized.

Figure 5.6 plots the product of the simulated velocity and density, scaled by the cold gas density, ρ_0, and U_B. The profiles of ρu are composed of two nearly linear stagnation flows with different gradients, corresponding to the cold- and hot-flow regions. The large rise in the post-flame velocity profile occurs because of the drop in density resulting from the combustion heat release and attendant temperature rise. The results in this section were reported in Bergthorson *et al.* (2004).

5.2.2 Imposed strain rate

Near-stoichiometric methane-air flames are studied for variable imposed strain rates. The strain rate, $\sigma = \mathrm{d}u/\mathrm{d}x$, is defined as the gradient of the velocity profile upstream of the velocity minimum. The strain rate is calculated by fitting a line to the PSV data in a 1 mm region upstream of the velocity minimum. Results for a weakly stretched flame are presented in Fig. 5.7. The simulated flowfield is post-processed as described in Appendix A to estimate the modeled-PSV profile ($d_p \cong 3\,\mu$m, $\rho_p \cong 2400\,\mathrm{kg/m^3}$; $\nu_c = 2000\,$Hz). Measured and simulated velocity profiles are in reasonable agreement, with the most notable discrepancy observed near the peak of the post-flame velocity profile. The

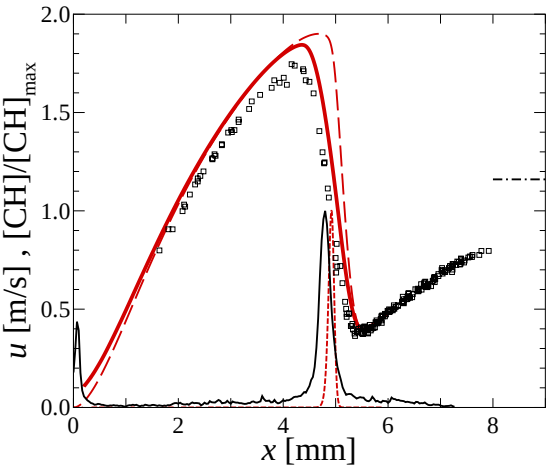

Figure 5.7: CH_4-air flame profiles ($\Phi = 0.9$, $\sigma = 212\,s^{-1}$, $L/d = 0.8$, run205). (dash-dot line) U_B, (□) PSV data, (black line) PLIF data, (long-dash red line) simulated velocity, u_f, profile (GRI-Mech 3.0), (solid red line) modeled-PSV, u_{PSV}, profile (short-dash red line) simulated CH profile.

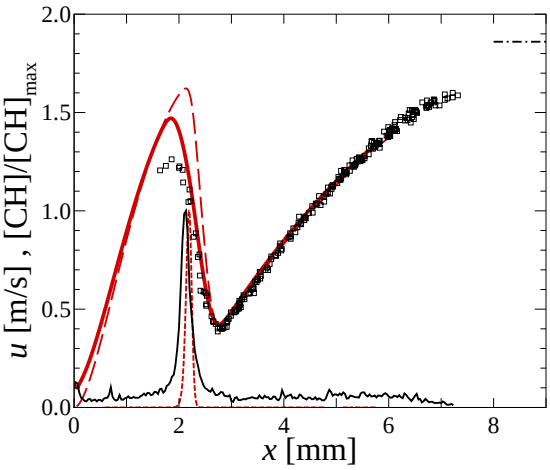

Figure 5.8: CH_4-air flame profiles ($\Phi = 0.9$, $\sigma = 368\,s^{-1}$, $L/d = 0.8$, run209). Legend as in Fig. 5.7.

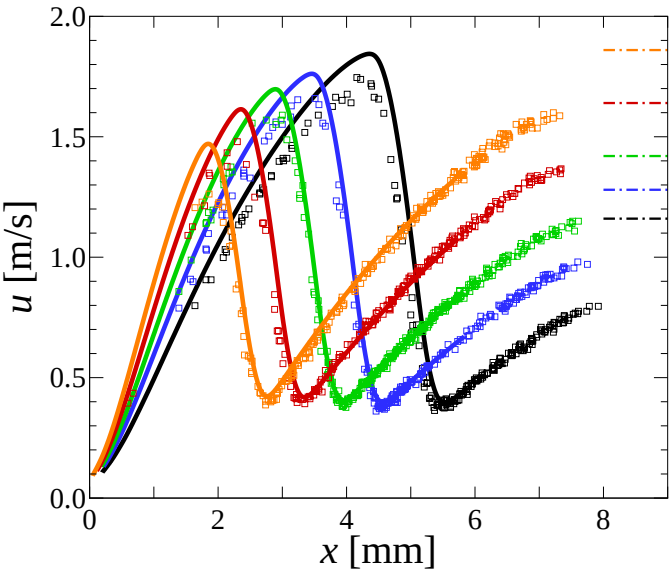

Figure 5.9: CH_4-air flame profiles for variable imposed strain rate ($\Phi = 0.9$, $L/d = 0.8$, run205-209). (dash-dot line) U_B, (□) PSV data, (solid line) modeled-PSV, u_{PSV}, velocity profiles; Maximum imposed strain rates are $\sigma = 212\,s^{-1}$ (black), $236\,s^{-1}$ (blue), $275\,s^{-1}$ (green), $334\,s^{-1}$ (red), and $368\,s^{-1}$ (orange).

minimum of the simulated velocity profile also lies above the minimum of the experimental data. The acceleration zone through the flame and the region of velocity maximum are overpredicted by the simulation as well. Especially noteworthy is the secondary stagnation flow, for which the

fluid and modeled-PSV profiles agree with each other but lie above the experimental data. The agreement of the two profiles indicates that particle-inertia, thermophoretic, and finite chopping-frequency effects are not important in this region, and thus the PSV measurements should agree with the fluid velocities in the secondary stagnation flow. In addition, the CH PLIF measurements allow for an independent assessment of simulation performance. Reasonable agreement is found for the predicted CH profile location, with the simulated profile situated upstream of the experiment, as would be expected if the flame strength (speed) was overpredicted. The independent measurements agree with each other and, collectively, indicate that the flame speed for near-stoichiometric, $\Phi = 0.9$, methane-air flames is slightly overpredicted by GRI-Mech 3.0. It should be noted that the post-flame velocity maximum is dependent on the pre-flame minimum velocity, the density-drop (or temperature-rise) through the flame, and the flame thickness. Thus, for a typical pre- to post-flame density ratio of ≈ 7, a 1.5 cm/s difference in the pre-flame velocity minimum will correspond to an ≈ 10 cm/s discrepancy in the post-flame maximum values. Thus, overpredictions in flame velocity are amplified by the density drop through the flame. Figure 5.8 presents the results for a flame close to extinction. For such stagnation-point flames, the flame will adjust its location such that the flame speed matches that corresponding to the imposed strain rate. As the Bernoulli velocity (or nozzle-exit velocity) is increased, the flame moves towards the stagnation plate. As the flame moves towards the stagnation surface, the heat loss to the plate increases eventually extinguishing the flame because of the combined effects of heat loss and stretch. For this near-extinction flame, the flame speed again appears to be overpredicted. While the simulated CH profile is closer to the experimental one, a larger discrepancy is observed between experiment and simulation in the post-flame region. Figure 5.9 shows the measured and simulated velocity profiles for increasing applied strain rate. The minimum and maximum imposed strain rates correspond to Figs. 5.7 and 5.8, respectively. The minimum imposed strain is chosen to correspond to a free-standing stagnation flame; for lower stretch rates a nozzle-attached "button-flame" can result (Günther & Janisch 1972; Dixon-Lewis & Islam 1982). The maximum imposed strain is close to the extinction conditions for this flame. The combined velocity and CH profile comparison plots for the intermediate cases can be found in Appendix G. As the imposed strain rate is increased, the minimum of the velocity profile increases in both the measurements and simulations, with the simulated minimum lying slightly above the measurements in all cases. In addition, the velocity maximum in the post-flame region decreases with increasing strain rate in both the experiment and simulation. The secondary stagnation flow is also found to increase in slope as the imposed strain rate is increased, as might be expected. Similar agreement in the predicted flame location is found for the range of strain rates studied. The consistent agreement between experiment and simulation in these (subtle) features of the flow profiles lends credibility to both the experimental methodology and the various models employed.

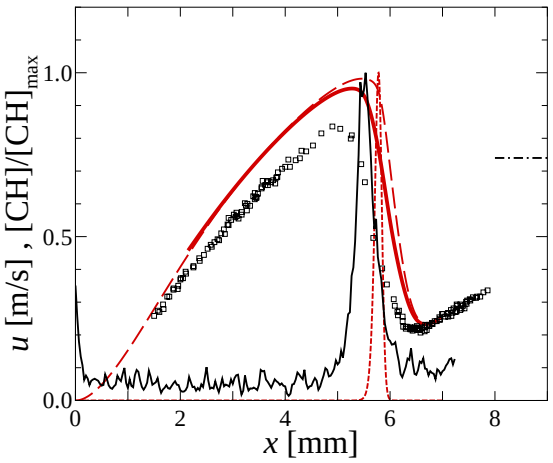

Figure 5.10: CH_4-air flame profiles ($\Phi = 0.7$, $\sigma = 90\,s^{-1}$, $\ell = 7\,mm$, $L/d = 0.8$, $\nu_c = 1600\,Hz$, run210). Legend as in Fig. 5.7.

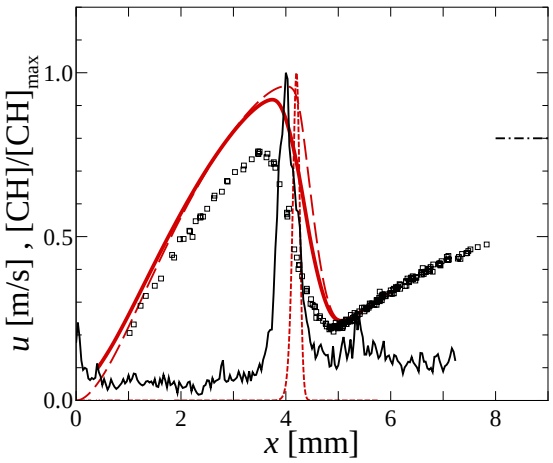

Figure 5.11: CH_4-air flame profiles ($\Phi = 0.7$, $\sigma = 106\,s^{-1}$, $L/d = 0.8$, $\nu_c = 1200\,Hz$, run212). Legend as in Fig. 5.7.

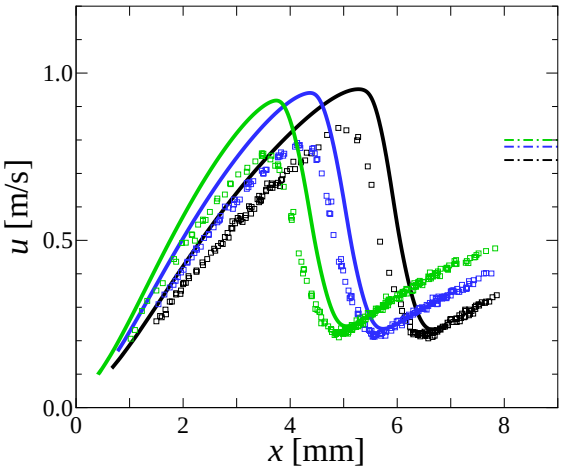

Figure 5.12: CH_4-air flame profiles for variable imposed strain rate ($\Phi = 0.7$, $L/d = 0.8$, run210-212). (dash-dot line) U_B, (□) PSV data, (solid line) modeled-PSV, u_{PSV}, velocity profiles; Maximum imposed strain rates are $\sigma = 90\,s^{-1}$ (black), $99\,s^{-1}$ (blue), and $106\,s^{-1}$ (green), and chopping frequencies are $\nu_c = 1600\,Hz$, $1200\,Hz$, and $1200\,Hz$, respectively.

The effect of variable strain rate was also studied for lean methane-air flames. For lean methane-air flames, the flame speed is much lower than for stoichiometric flames, and the range of strain rates that can be applied is also lower due to the lower extinction strain rate. The minimum strain rate is fixed by the requirement that the flame be freestanding, *i.e.*, not attached to the nozzle, requiring that the nozzle exit velocity be somewhat larger than the flame speed at the corresponding strain rate. Figures 5.10 and 5.11 show the data for flames that are close to the minimum and maximum strain-rate limits at this equivalence ratio. Note that the low signal-to-noise ratio in the CH PLIF profiles is due to the low CH concentration in these flames. The majority of the measured profiles

here will be due to PAH soot precursors, so care is required when comparing the profile shape with simulation. The simulated flowfield (GRI-Mech 3.0) is post-processed to determine the modeled-PSV profile (see Appendix A: $d_p \cong 3\,\mu$m, $\rho_p \cong 2400\,\mathrm{kg/m^3}$; ν_c indicated in figure captions). Figure 5.12 is a comparison of the PSV data and the modeled-PSV profiles for three imposed strain rates. The low and high strain rate cases correspond to the data presented in Fig. 5.10 and Fig. 5.11, respectively. The complete profile for the intermediate case can be found in Appendix G. For these lean-methane flames, the results are consistent for the three different imposed strain rates. The flame speed is overpredicted, with the minimum of the simulated velocity profile upstream of the flame considerably higher than that measured in the experiment. The resulting post-flame velocity profiles are also higher than the measurements, although the overall shape of the modeled-PSV profiles appear to match the shape of the experimental PSV profile. The experimental profiles show a larger decrease in the velocity maximum with increasing strain rate than the corresponding simulations. The predicted CH location is upstream of the measured profile, consistent with an overprediction of the flame speed.

A set of experiments at variable strain rates was also performed for slightly rich methane-air flames at $\Phi = 1.1$. Figures 5.13 and 5.14 show the data for a weakly stretched and strongly stretched flame, respectively. The simulated flowfield is post-processed to determine the modeled-PSV profile (see Appendix A: GRI-Mech 3.0, $d_p \cong 3\,\mu$m, $\rho_p \cong 2400\,\mathrm{kg/m^3}$; $\nu_c = 2400\,$Hz). For these rich flames, the increased chemiluminescence emission from C_2 Swan bands causes interference in the PSV measurements through the reaction zone. The PSV images utilize a 10 nm bandpass filter centered on the (green) laser line; however, the Swan bands also emit in the green portion of the spectrum. Data are not recorded in this region of the flow due to this background-noise source. Figure 5.15 is a comparison of the PSV data and the modeled-PSV profiles for five imposed strain rates. The low and high strain-rate cases correspond to the data presented in Fig. 5.13 and Fig. 5.14, respectively. The complete profiles for the intermediate cases can be found in Appendix G. Again, the results for variable imposed strain rates are consistent with each other. The flame speed is overpredicted, with the minimum of the simulated velocity profile upstream of the flame slightly higher than that measured in the experiment. The resulting post-flame velocity profiles are also higher than the measurements, although the profiles are in closer agreement than for lean methane-air flames. The pre-flame velocity minimum increases in value with increasing strain rate, consistent with the results for lean flames. The predicted CH location is slightly upstream of the measured profile, consistent with a slight overprediction of the flame speed.

The effect of variable strain rate was also studied for rich flames at $\Phi = 1.25$. In our experimental setup, the maximum equivalence ratio for which stable methane-air flames could be established was $\Phi \approx 1.3$. To allow several different strain rates to be studied, a lower value of Φ was chosen. Figures 5.16 and 5.17 show the data for a weakly stretched and strongly stretched flame, respectively.

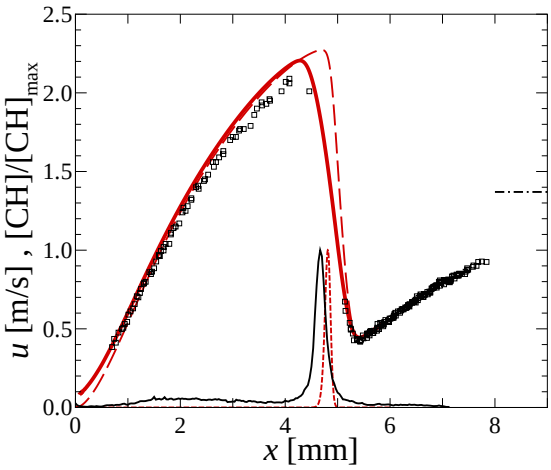

Figure 5.13: CH_4-air flame profiles ($\Phi = 1.1$, $\sigma = 240\,s^{-1}$, $L/d = 0.8$, run220). Legend as in Fig. 5.7.

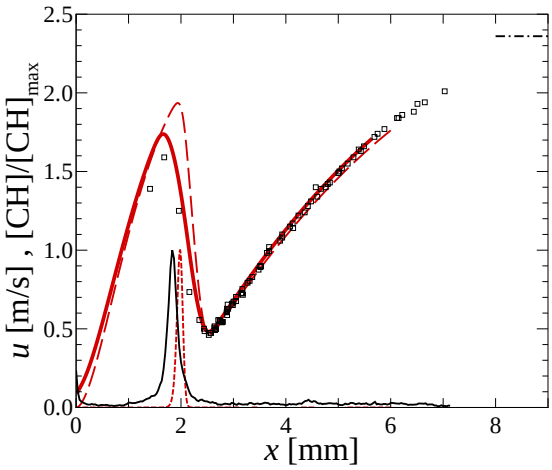

Figure 5.14: CH_4-air flame profiles ($\Phi = 1.1$, $\sigma = 449\,s^{-1}$, $L/d = 0.8$, run224). Legend as in Fig. 5.7.

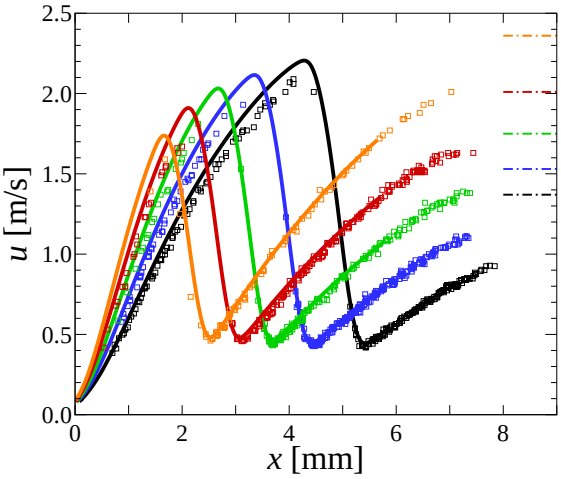

Figure 5.15: CH_4-air flame profiles for variable imposed strain rate ($\Phi = 1.1$, $L/d = 0.8$, run220-224). (dash-dot line) U_B, (□) PSV data, (solid line) modeled-PSV, u_{PSV}, velocity profiles; Maximum imposed strain rates are $\sigma = 240\,s^{-1}$ (black), $279\,s^{-1}$ (blue), $315\,s^{-1}$ (green), $388\,s^{-1}$ (red), and $449\,s^{-1}$ (orange).

The simulated flowfield is post-processed to determine the modeled-PSV profile (see Appendix A: GRI-Mech 3.0, $d_p \cong 3\,\mu m$, $\rho_p \cong 2400\,kg/m^3$; $\nu_c = 1600\,Hz$). Figure 5.18 is a comparison of the PSV data and the modeled-PSV profiles for five imposed strain rates. The low and high strain-rate cases correspond to the data presented in Fig. 5.16 and Fig. 5.17, respectively. The complete profiles for the intermediate cases can be found in Appendix G. Again, the results for variable imposed strain rates are consistent with each other. For the weakly stretched flame, the CH profiles are in close agreement, and the minimum of the simulated profile matches closely with the experimental data. However, the simulated secondary stagnation flow lies above the experimental measurements. For the

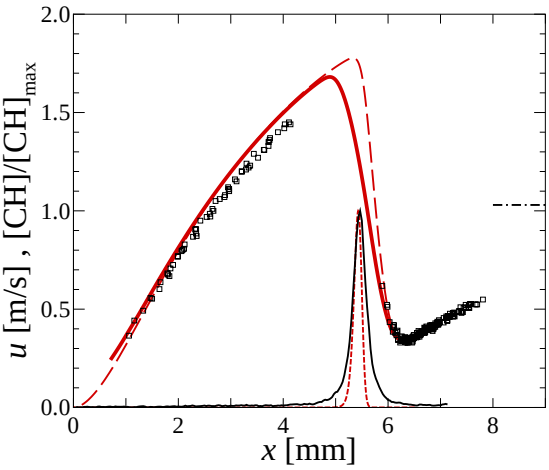

Figure 5.16: CH_4-air flame profiles ($\Phi = 1.25$, $\sigma = 152\,s^{-1}$, $\ell = 7\,mm$, $L/d = 0.8$, run215). Legend as in Fig. 5.7.

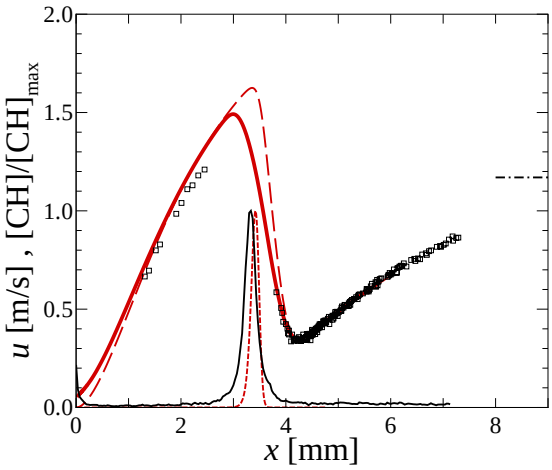

Figure 5.17: CH_4-air flame profiles ($\Phi = 1.25$, $\sigma = 209\,s^{-1}$, $L/d = 0.8$, run218). Legend as in Fig. 5.7.

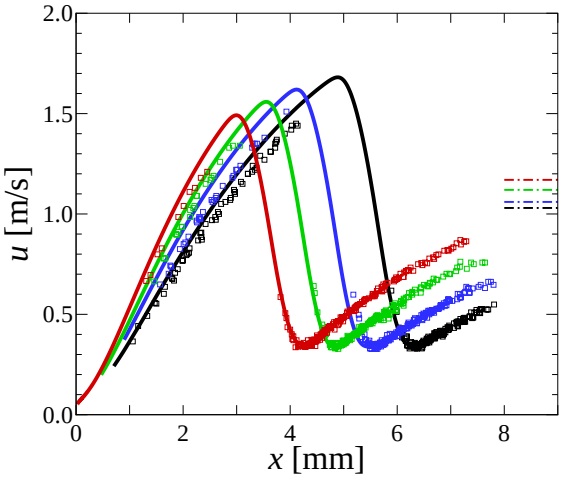

Figure 5.18: CH_4-air flame profiles for variable imposed strain rate ($\Phi = 1.25$, $L/d = 0.8$, run215-218). (dash-dot line) U_B, (□) PSV data, (solid line) modeled-PSV, u_{PSV}, velocity profiles; Maximum imposed strain rates are $\sigma = 152\,s^{-1}$ (black), $175\,s^{-1}$ (blue), $183\,s^{-1}$ (green), and $209\,s^{-1}$ (red).

strongly streched flame, the simulated CH profile is slightly upstream of the PLIF profile, although the minimum of the velocity profile appears to match the experimental data. The variation in the velocity minimum is not large for this range of strain rates. In general, the profiles indicate that the predicted flame speed for methane-air flames using GRI-Mech 3.0 is close to the experimental measurements, but appears to be slightly high for lean flames. In addition, for the range of strain rates that can be applied to flames in a stagnation-flow against a cold plate, the hydrodynamic and chemistry model appear to accurately predict the flow for variations in the imposed strain rate.

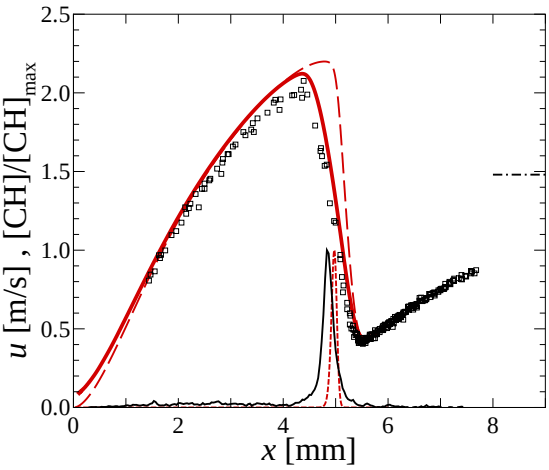

Figure 5.19: CH_4-air flame profiles ($\Phi = 1.0$, 21.0 %O_2:(O_2+N_2), $L/d = 0.8$, run241). Legend as in Fig. 5.7.

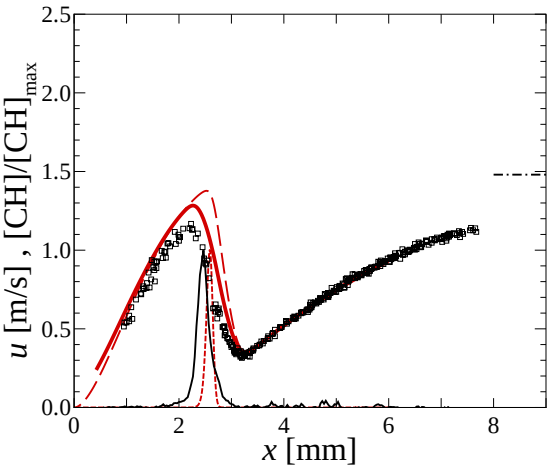

Figure 5.20: CH_4-air flame profiles ($\Phi = 1.0$, 19.0 %O_2:(O_2+N_2), $L/d = 0.8$, run245). Legend as in Fig. 5.7.

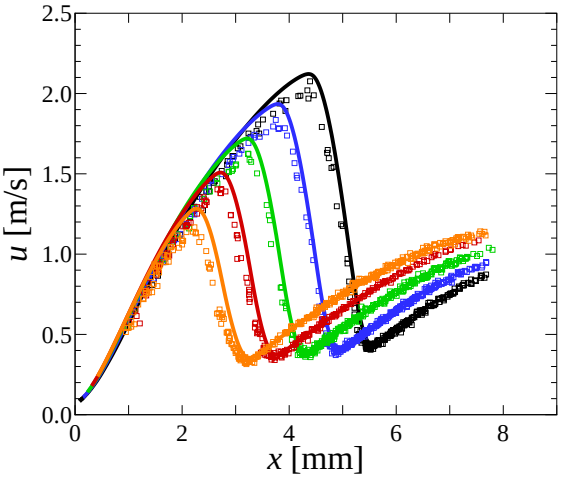

Figure 5.21: CH_4-air flame profiles for variable nitrogen dilution ($\Phi = 1.0$, $L/d = 0.8$, run241-245). (□) PSV data, (solid line) modeled-PSV, u_{PSV}, velocity profiles; %O_2:(O_2+N_2) of 21.0% (black), 20.5% (blue), 20.0% (purple), 19.5% (red), and 19.0% (orange). Bernoulli velocity is constant to within ±1 %.

5.2.3 Nitrogen dilution

Stoichiometric methane-air flames are studied at variable nitrogen dilution to determine the effect of varying flame strength. The simulated flowfields (using GRI-Mech 3.0) are post-processed to determine the modeled-PSV profiles to enable a consistent comparison between experiment and simulation (see Appendix A: $d_p \cong 3\,\mu$m, $\rho_p \cong 2400\,$kg/m^3; $\nu_c = 2000\,$Hz). Dilution is indicated by the percentage of the air (oxygen and nitrogen) that is made up of oxygen molecules, designated by %O_2:(O_2+N_2). The results for a non-diluted flame, for which oxygen makes up 21% of the air composition, %O_2:(O_2+N_2) = 21%, are presented in Fig. 5.19. Figure 5.20 presents the results

for a flame close to extinction, $\%O_2{:}(O_2{+}N_2) = 19\%$. Reasonable agreement in the predicted CH profile location is evident in both cases, with the simulated profile situated slightly upstream of the measured profile, consistent with a slight overprediction of the flame speed. The measured velocity profiles fall beneath the simulated profiles in the post-flame region, and the simulated minimum velocity is slightly higher than that measured by the experiments. The various measurements are again consistent with each other and indicate an overprediction of the flame speed. Figure 5.21 shows the measured and simulated velocity profiles for increasing nitrogen dilution. The non-diluted case corresponds to Fig. 5.19 and the weakest flame (closest to the plate) corresponds to Fig. 5.20. The combined velocity and CH profile comparison plots for the intermediate cases can be found in Appendix G. The Bernoulli velocity was held constant to within $\pm 1\,\%$ over this set of experiments. As the nitrogen dilution is increased, the velocity profile minimum decreases in both the measurements and simulations. The flame adjusts its location to compensate for the decreased flame strength by moving towards the stagnation point. This alters the upstream cold-flow due to the movement of the virtual stagnation point, essentially changing the effective nozzle-to-stagnation point separation distance. The strain rate for these flames is approximately constant, indicating that the Bernoulli velocity determines the imposed strain rate. Notably, the post-flame velocity profiles collapse at variable dilution, indicating that both the pre- and post-flame stretch is controlled by the Bernoulli velocity. Similar agreement in the predicted flame location is found for variable nitrogen dilution. The disagreement in the post-flame velocity maximum is consistent as the dilution increases. The maximum temperature for these flames is 2113 K at $21.0\%O_2{:}(O_2{+}N_2)$ and 1878 K at $19.0\%O_2{:}(O_2{+}N_2)$. This temperature difference corresponds to a 38% change in radiation emission between the maximum and minimum temperature flames. The similar disagreement in the post-flame region for this change of flame temperatures indicates that radiation losses are not responsible for the discrepancy in the post-flame region.

5.2.4 Equivalence ratio

From the study of flames at variable strain rate, it can be concluded that the agreement between measurement and simulation exhibits a larger sensitivity to the mixture composition than to the applied strain rate. Methane-air flames are thus studied as a function of equivalence ratio to further investigate kinetic effects. In the current experimental setup, stable methane-air flames can be established for equivalence ratios in the range $0.7 \leq \Phi \leq 1.3$. Figure 5.22 gives profiles for a lean flame at $\Phi = 0.7$. Profiles are also given for a stoichiometric and rich flame in Figs. 5.23 and 5.24.

Lean methane-air flame speed appears to be overpredicted by GRI-Mech 3.0, as the predicted CH profile is upstream of the experimentally measured one, consistent with the results from the study of variable strain rate (see Figs. 5.10–5.12), indicative of good measurement repeatability. In addition, the minimum of the velocity profile is higher in the simulated profile, as compared to the

experimental data. This is consistent with data obtained from laminar flame speed measurements for lean methane-air flames, for which the laminar flame speed is consistently overpredicted as compared to data obtained from various experimental techniques (*e.g.*, Dong *et al.* 2002; Bosschaart & de Goey 2004). There is better agreement for the stoichiometric flame when the particle behavior in the flame is modeled and the finite resolution of PSV is taken into account. The flame speed does appear to be overpredicted, with both the minimum and maximum points of the velocity profile lying higher than the experimental measurements. In addition, the simulated CH profile is slightly upstream of the measured PLIF profile. GRI-Mech 3.0 was tuned to match laminar flame speed data for methane-air flames, so good agreement is expected for these conditions (Smith *et al.*). For rich methane-air flames ($\Phi = 1.3$), the predicted and experimental profiles show good agreement. In this case, the velocity profiles are almost coincident, and the simulated CH profile is only very slightly upstream of the measurements. A full complement of experiments was performed for equivalence ratios in the range $0.7 \leq \Phi \leq 1.3$ at increments of 0.1 in Φ. The entire set of flame profiles are given in Appendix G in Figs. G.23–G.29. From this suite of experiments, it appears that GRI-Mech 3.0 accurately predicts the flame speed for methane-air flames for a variety of compositions and strain rates. Predicted flame speeds are slightly high, with increasing disagreement for lean mixtures. The overprediction of flame speed is corroborated by the two diagnositic techniques. The minimum and maximum points of the velocity profiles tend to be overpredicted, even when the effects of particle-inertia, thermophoresis, and the finite chopping-frequency are accounted for. In addition,

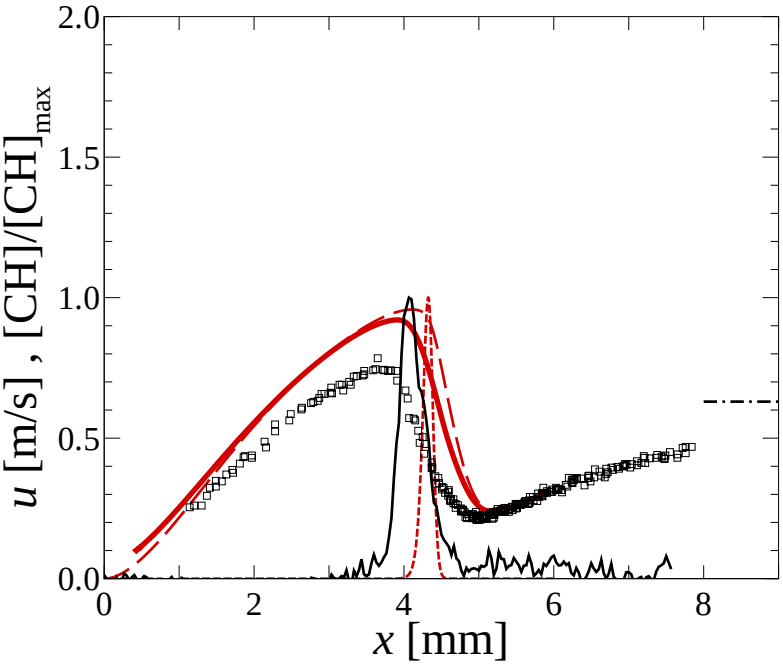

Figure 5.22: Lean CH_4-air flame profiles ($\Phi = 0.7$, run234). Legend as in Fig. 5.7.

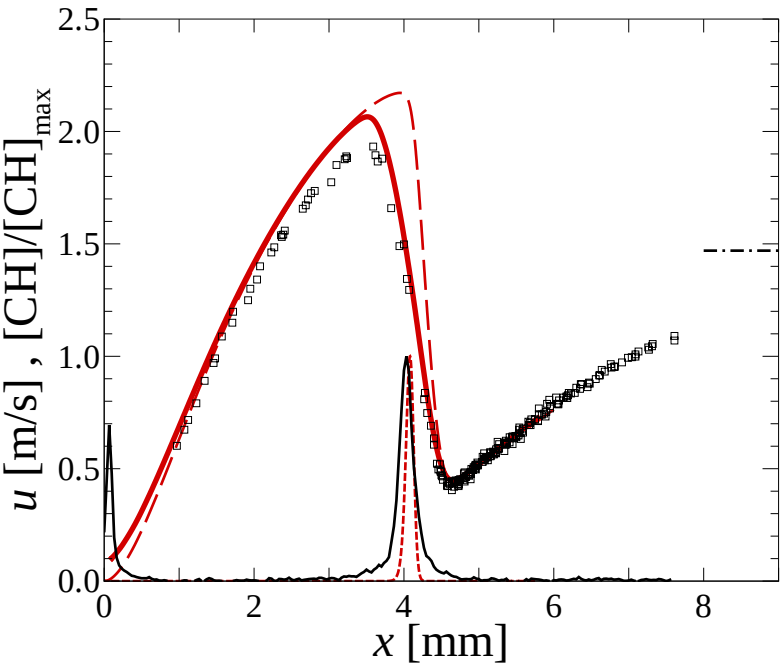

Figure 5.23: Stoichiometric CH_4-air flame profiles ($\Phi = 1.0$, run226). Legend as in Fig. 5.7.

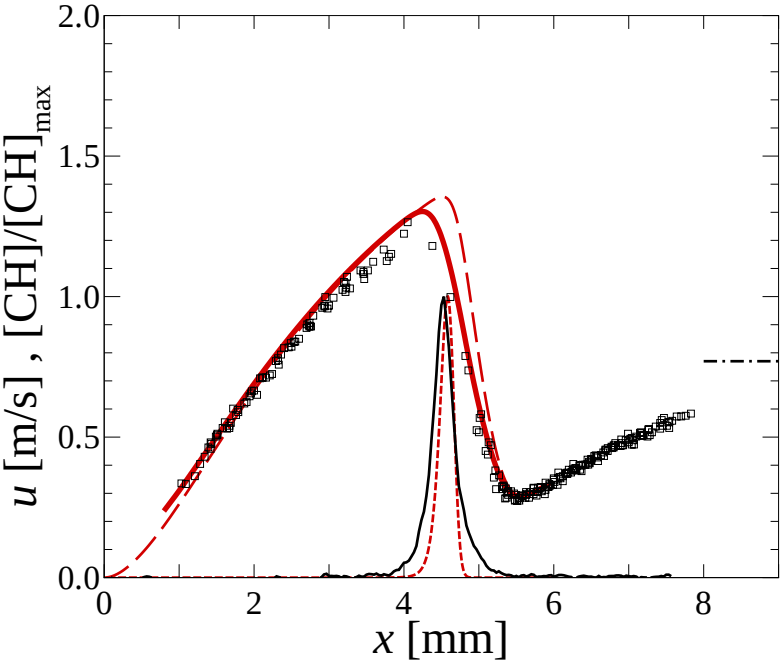

Figure 5.24: Rich CH_4-air flame profiles ($\Phi = 1.3$, run229). Legend as in Fig. 5.7.

the simulated CH profiles tend to lie upstream of the measurements, providing an independent assessment of the simulation performance.

These measurements, along with the simulated results using GRI-Mech 3.0, indicate that the

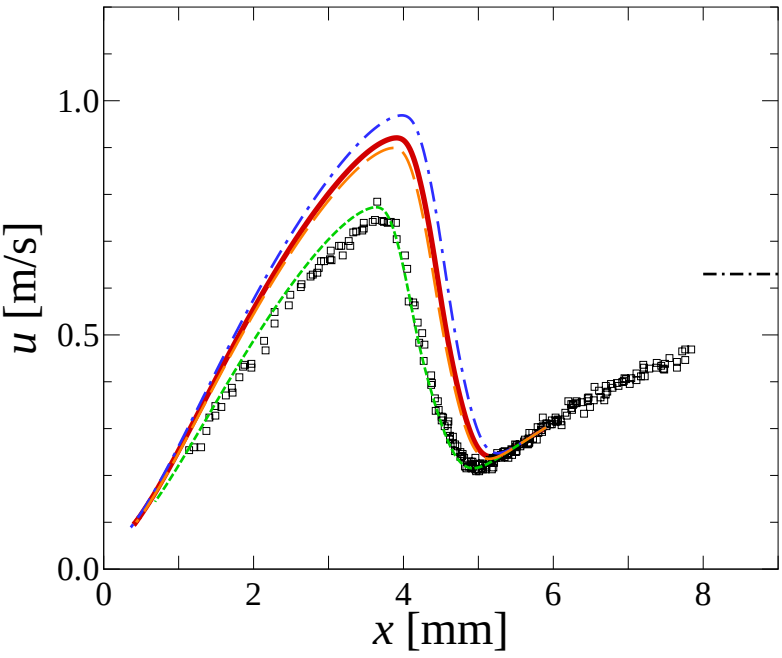

Figure 5.25: Comparison of modeled-PSV, u_{PSV}, profiles to experimental data in a $\Phi = 0.7$, CH_4-air flame (run234). (black dash-dot line) U_{B}, (□) PSV data, (red thick solid line) GRI-Mech 3.0, (green short dash line) C_3-Davis, (blue dash-dot line) SD2003, (orange long dash line) SD2005.

experimental technique is robust and can be applied to a variety of flame conditions, with self-consistent results. The general agreement between experiments and simulation for a wide range of flame speeds (weak lean and rich flames, to strong stoichiometric flames) and a considerable range of imposed strain rates is indicative of the accuracy of the experimental methodology employed and the hydrodynamic, chemistry, thermodynamic, and transport models utilized. It is of interest to compare the predictions utilizing various chemistry models to determine the relative performance of each one.

The lean, stoichiometric, and rich flames presented in Figs. 5.22–5.24 were simulated using the C_3 mechanism of Davis *et al.* (1999), and two releases of the "San Diego" mechanism (see Bibliography: San Diego mechanism), the results are presented in Figs. 5.25–5.27. The modeled-PSV profiles obtained from the simulated flowfield for the experimental-particle properties and tracking time are compared to the PSV data. For lean methane-air flames, the C_3-Davis mechanism (Davis *et al.* 1999) gives the best prediction of the experimental data, while the latest version of the San Diego mechanism, SD2005, is in close agreement with GRI-Mech 3.0. The previous version of the San Diego mechanism, SD2003, shows the largest variance with experiment. Interestingly, while the C_3-Davis mechanism appears to capture the correct flame speed for this mixture, the post-flame velocity profile is still slightly overpredicted. For stoichiometric methane-air flames (see Fig. 5.26), the profiles from the different chemistry models almost collapse onto each other, exhibiting only

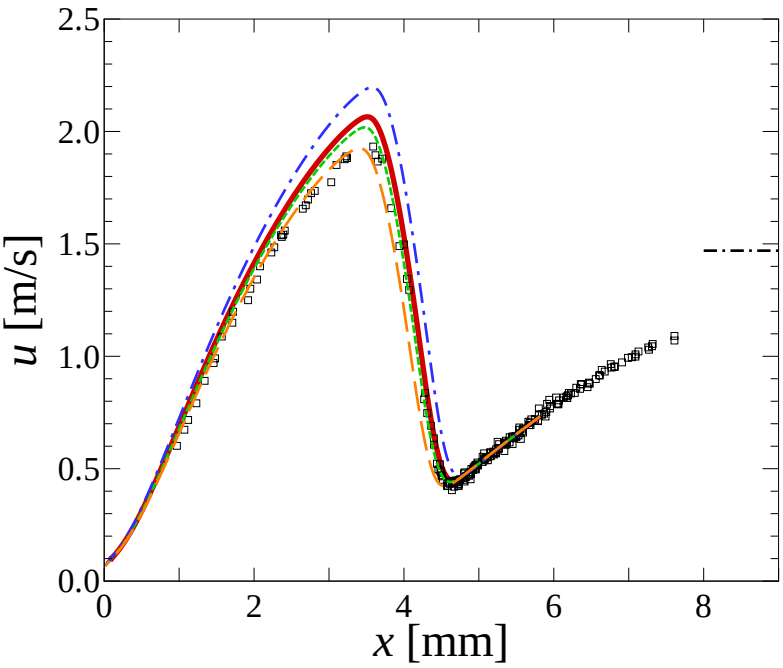

Figure 5.26: Comparison of modeled-PSV, u_{PSV}, profiles to experimental data in a $\Phi = 1.0$, CH_4-air flame (run226). (black dash-dot line) U_{B}, (□) PSV data, (red thick solid line) GRI-Mech 3.0, (green short dash line) C_3-Davis, (blue dash-dot line) SD2003, (orange long dash line) SD2005.

slight differences in the flame speed. The predictions tend to agree with experiment, with a slight overprediction of flame speed in all cases. The effects of particle inertia, thermophoresis, and finite chopping frequency are larger for the stoichiometric case, due to the higher velocities, accelerations, and temperatures associated with these strong-burning flames. Good agreement is also seen for rich methane-air flames (see Fig. 5.27), except for the older version of the San Diego mechanism, SD2003, which overpredicts the flame speed. Corrections for particle inertia, thermophoresis, and finite chopping frequency are not large for this (weak) flame, although there is improved agreement in the slope of the acceleration region when the corrections are applied.

To illustrate the variations between the experiment and the different chemistry models, the difference in CH-layer location between model and simulation is given in Figure 5.28. The predicted location of the CH profile, $x_{\mathrm{CH,sim}}$, is compared to the measured CH profile location, x_{CH}, and the difference between the two is normalized by the simulated CH layer thickness, $\delta_{\mathrm{CH,GRI-3.0,\Phi=1}}$, calculated using the GRI-Mech 3.0 model at stoichiometric conditions ($\Phi = 1$). The CH layer thickness is an appropriate length scale for normalizing the difference in locations. The choice of the stoichiometric CH layer thickness as the reference point was due to the fact that the CH layer thickness varies considerably with equivalence ratio (see Fig. 5.32), and thus two simultaneous variations would be convoluted in the comparison if the CH thickness at the local equivalence ratio was utilized. As the various mechanisms predict very similar CH layer thicknesses (see Fig. 5.31),

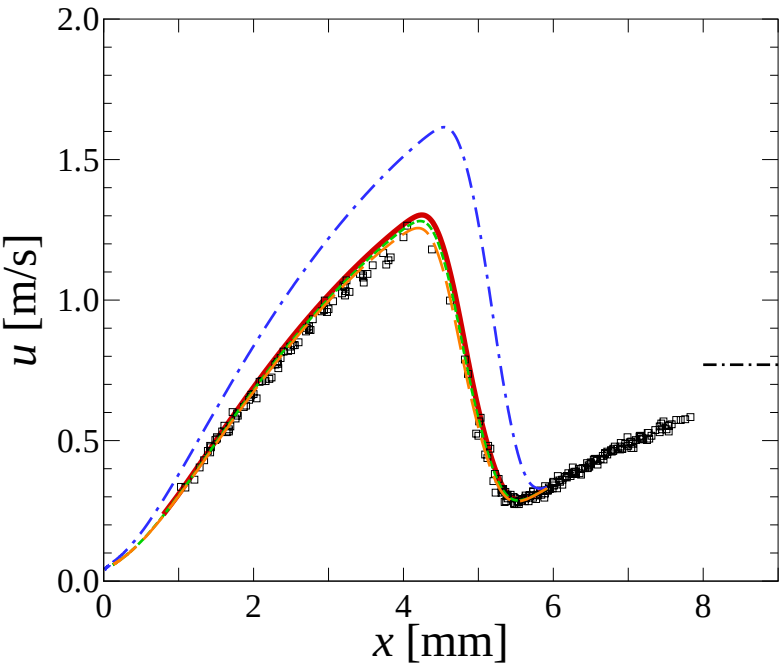

Figure 5.27: Comparison of modeled-PSV, u_{PSV}, profiles to experimental data in a $\Phi = 1.3$, CH_4-air flame (run229). (black dash-dot line) U_{B}, (□) PSV data, (red thick solid line) GRI-Mech 3.0, (green short dash line) C_3-Davis, (blue dash-dot line) SD2003, (orange long dash line) SD2005.

the prediction from GRI-Mech 3.0 was utilized as a reference standard, due to its application to the majority of the flames studied in this chapter. "Two-sided" Lorentzian fits were performed on single-image profiles (see Appendix C), given by

$$S_{\mathrm{CH}}\left(x < x_{\mathrm{CH}}\right) = \frac{S_{\mathrm{CH,max}}\, w_1^2}{(x - x_{\mathrm{CH}})^2 + w_1^2} \quad , \quad S_{\mathrm{CH}}\left(x > x_{\mathrm{CH}}\right) = \frac{S_{\mathrm{CH,max}}\, w_2^2}{(x - x_{\mathrm{CH}})^2 + w_2^2} \; , \tag{5.3}$$

where $S_{\mathrm{CH,max}}$ is the peak intensity, x_{CH} is the peak location, and w_1 and w_2 are the widths corresponding to the half-maximum value on either side of x_{CH}. Thus, the Full-Width at Half-Maximum (FWHM) for the fit profile is given by the sum $w_1 + w_2$. The experimental CH location, x_{CH}, is taken as the mean of the fit values from single-shot profiles, averaging a typical record of 1000 images. The simulated CH location, $x_{\mathrm{CH,sim}}$, was taken to be the location of the peak of the CH profile from the numerical simulations, and the locations of the half-max value on either side of the peak were interpolated from the simulated profiles. The difference in the locations of the two half-max values gave the Full-Width at Half-Maximum (FWHM) for the simulated profile, yielding the CH-layer thickness, δ_{CH}.

In Fig. 5.28, positive values of $(x_{\mathrm{CH,sim}} - x_{\mathrm{CH}})/\delta_{\mathrm{CH,GRI-3.0,\Phi=1}}$ indicate that the simulated CH profile is located *upstream* of the experimental profile and that the flame speed is *overpredicted*. As a reference, the difference between the measured and simulated minimum velocities upstream of

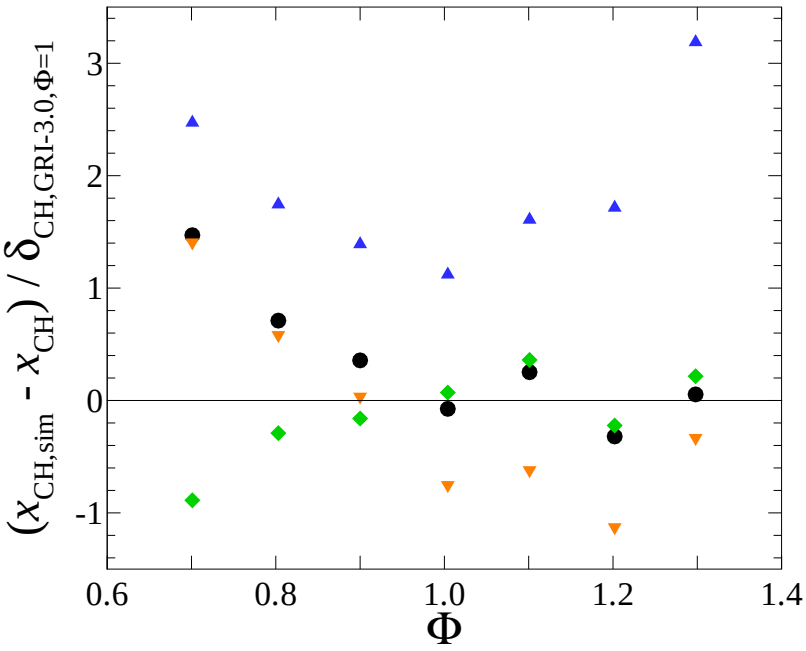

Figure 5.28: Difference between predicted and experimental CH-layer location for various chemistry models: (○) GRI-Mech 3.0, (◇) C_3-Davis, (△) SD2003, (▽) SD2005.

the flame, $\Delta S_{u,ref}$, can be related to the difference between the measured and simulated CH profile locations, Δx_{CH}, through

$$\Delta S_{u,ref} \simeq \sigma \, \Delta x_{CH} \tag{5.4}$$

where $\sigma = du/dx$ is the gradient of the velocity profile near the flame region. For typical strain rates of $\sigma \approx 100$–$200\,s^{-1}$, and a typical flame thickness of $\delta_{CH} \approx 0.1$ mm, a difference in CH locations equal to one flame thickness, $\Delta x_{CH} = \delta_{CH}$, corresponds to a 1–2 cm/s difference in $S_{u,ref}$. The uncertainty in the boundary condition measurements corresponds to a total uncertainty in the predicted flame location of $\approx 0.5\,\delta_{CH}$ (see Chapter 2). The mechanisms tend to agree within one CH-layer thickness near stoichiometry and for rich flames, while GRI-Mech 3.0 appears to overpredict and the C_3-Davis mechanism appears to underpredict flame speeds for lean flames. The earlier version of the San Diego mechanism, SD2003, gives a systematic overprediction of the flame speed for all equivalence ratios. The revised San Diego mechanism, SD2005, produces similar results to GRI-Mech 3.0.

5.2.5 Relative concentration measurements and CH profile thicknesses

The CH PLIF diagnostics allow an assessment of the model performance in predicting relative CH concentrations for variable flame conditions. The predicted peak CH concentrations from the different mechanisms are compared in Fig. 5.29, in units of parts-per-million (ppm). The different mechanisms predict similar trends in the profiles, although the peak concentration varies considerably for

the different mechanisms, with the C_3-Davis mechanism predicting the highest CH concentrations. To measure relative CH concentrations as a function of the mixture-fraction, a set of experiments was performed where the fluorescence signal was measured both on and off of the resonance line of interest. The off-resonance signal was composed of Rayleigh scattering, chemiluminescence, dark-noise, and fluorescence from compounds other than CH, typically attributed to Polycyclic-Aromatic Hydrocarbon (PAH) soot precursors (Norton & Smyth 1991). The CH fluorescence signal is taken as the difference between the on- and off-line components. The CH PLIF data were recorded for this dataset maintaining fixed optics and intensifier gain, as well as fixed laser power. For sufficiently high laser power, the majority of the fluorescence signal can be approximated as being saturated. This allows the relative concentrations of the CH radical to be estimated from the intensity data (see Appendix C). Each PLIF image was corrected for the off-line contribution, the signal from the center 50 columns was averaged, and the resulting profile was fit with a "two-sided" Lorentzian function to determine the peak intensity, peak location, and profile width [see Eq. (5.3) and Appendix C]. These data were then averaged over the dataset (typically 1000 images) to determine the mean and standard deviation of these values. The relative concentrations are normalized to the peak CH concentration at $\Phi = 1.2$.

Figure 5.30 compares the measured relative CH concentration measurements to the four chemistry models employed. The error bars correspond to one standard deviation for the dataset. The data show a similarly shaped profile to the simulations as a function of equivalence ratio, with a weaker drop-off in CH fluorescence as the flame is made increasingly rich or lean. Chen & Mansour (1997) found that their saturated CH fluorescence imaging system had a detection limit of $\Phi = 0.8$ for methane-air flames, corresponding to a CH concentration of 1 ppm. Sutton & Driscoll (2003) found that the CH signal was detectable down to $\Phi = 0.85$ for both methane-air and propane-air (Bunsen) flames. Sutton & Driscoll (2003) found that the maximum CH signal occurs for $\Phi = 1.25$, and that the relative CH concentrations at $\Phi = 1.15$ and 1.35 are comparable. In our case, the signal is considerably lower in the richer $\Phi = 1.3$ case than at $\Phi = 1.1$. However, the numerical predictions using the PREMIX code and GRI-MECH 3.0 follow the data of Sutton & Driscoll (2003), just as the simulated data here using GRI-MECH 3.0 also follow our data. Thus, it may be inferred that the relative CH concentrations (as a function of stoichiometry) are dependent on the experimental configuration, and a direct comparison of our data to that of Sutton & Driscoll may not be valid. The numerical predictions show a stronger variation in the relative CH concentration as a function of Φ than the experimental results both for the data reported here and that of Sutton & Driscoll (2003). In both cases, the predicted relative CH concentrations for lean flames were below that measured using this PLIF technique.

From the CH PLIF data, it is also possible to compare the measured and predicted CH widths as a function of equivalence ratio. Figure 5.31 shows the predicted CH layer thicknesses as a function

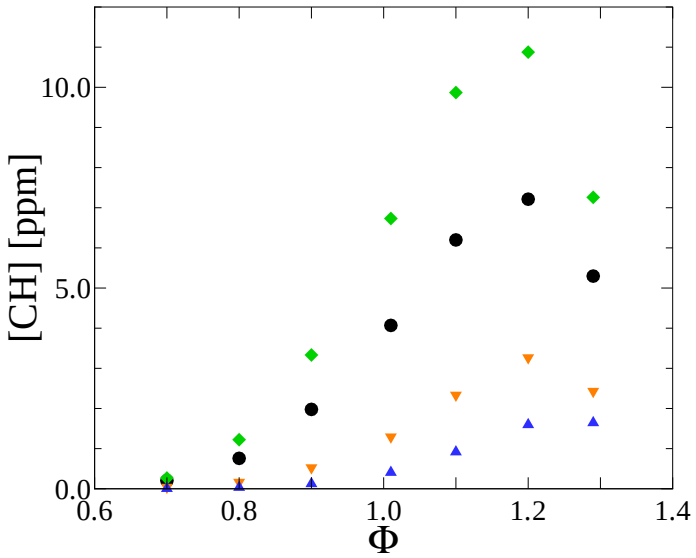

Figure 5.29: Comparison of predicted maximum CH concentrations from various chemistry models: (○) GRI-Mech 3.0, (◇) C_3-Davis, (△) SD2003, (▽) SD2005.

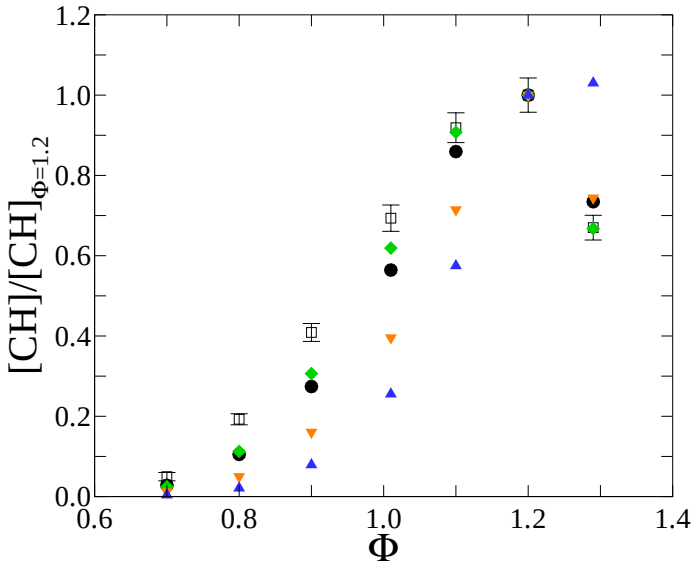

Figure 5.30: Comparison of relative concentration measurements, normalized to the concentration at $\Phi = 1.2$, from various chemistry models to experimental data. (□) CH PLIF data, (○) GRI-Mech 3.0, (◇) C_3-Davis, (△) SD2003, (▽) SD2005.

of the equivalence ratio for the four chemistry models included in this study. The predicted CH layer thicknesses are very consistent for these mechanisms. Figure 5.32 compares experimental and simulated CH profile thicknesses. The measured CH-profile thickness is an ensemble average of the FWHM of individual "two-sided" Lorentzian fits to single-exposure profiles (50-column average over the flat, central portion of the flame [see Eq. (5.3) and Appendix C]. Chen & Mansour (1997)

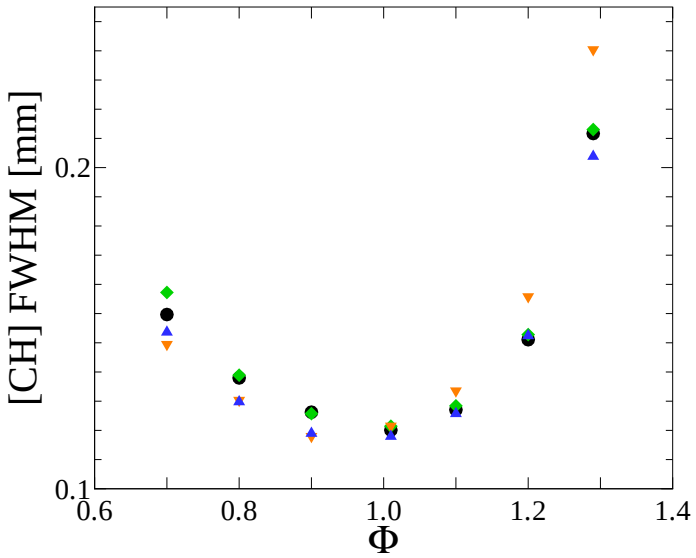

Figure 5.31: Comparison of predicted CH profile thicknesses for various chemistry models: (○) GRI-Mech 3.0, (◇) C_3-Davis, (△) SD2003, (▽) SD2005.

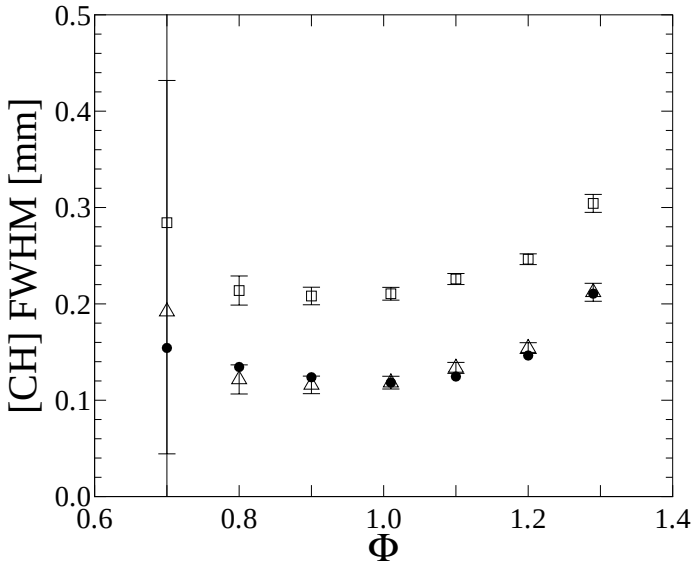

Figure 5.32: Comparison of measured CH profile thickneses to the predictions of GRI-Mech 3.0. (□) uncorrected CH PLIF data, (△) corrected CH PLIF data, (○) GRI-Mech 3.0.

measured the CH layer FWHM to be 0.3 mm, which was larger than the predicted width, but that they claim is "the smallest ever achieved." They attribute the discrepancy to the limiting resolution of the detection system, which was 0.2 mm. For our system, the measured CH profile thickness for a $\Phi = 1.0$ flame is 0.21 mm. However, the resolution of our system is insufficient to fully resolve this profile, and the measured CH profile thicknesses are approximately twice the simulated values. The Point Spread Function (PSF) of the imaging system and the true CH profile can be approximated

by Lorentzians (see Appendix C). A measured PLIF profile will then also be a Lorentzian that is a convolution of the two, with a composite width, δ_{PLIF}, that is the sum of the PSF, δ_{PSF}, and true CH profile, δ_{CH}, widths, *i.e.*, $\delta_{\mathrm{PLIF}} \cong \delta_{\mathrm{PSF}} + \delta_{\mathrm{CH}}$. The PSF width is estimated based on the stoichiometric, $\Phi = 1.0$, flame by subtracting the measured and simulated widths (using GRI-Mech 3.0). This PSF width is systematically applied to study the difference between predicted and measured reference profile thicknesses as a function of equivalence ratio. Figure 5.32 plots the mean FWHM and error bars corresponding to one standard deviation (calculated from ≈ 1000 shots). The large error bars for the $\Phi = 0.7$ flame are due to the low signal level associated with this lean flame. While the CH profile is visible when the on- and off-line images are subtracted, the determination of the profile width is strongly affected by noise in the data. $\Phi = 0.7$ corresponds to the lean detection limit for our setup, for which the estimated concentration of the CH radical is 0.2 ppm, based on the simulation performed with GRI-Mech 3.0. Good agreement is seen between the corrected CH thicknesses and the simulated results as a function of Φ.

5.2.6 Flame temperature

To further isolate the various effects that determine the shape of the velocity and CH profiles, methane-air flames were studied with variable dilution as a function of equivalence ratio. The result is that flames are studied at variable stoichiometry with consistent flame speeds, the stronger flames being diluted with excess nitrogen to reduce their flame speed. The dilution was chosen such that the flames would be situated at the same location between the nozzle and the plate for a similar imposed stretch rate (Bernoulli velocity). The result is that the effects of variable composition (Φ) can be studied at similar strained flame speeds. Figures 5.33–5.36 depict flame profiles for near-stoichiometric flames varying from slightly lean to slightly rich, with variable nitrogen dilution. The minimum of the simulated velocity profile, or reference flame speed, for the four flames is $S_{\mathrm{u,ref}} = 31.5\,\mathrm{cm/s}$, within $\pm 2\%$. Good agreement is seen between experiment and simulation for these flames, indicating satisfactory model performance in this Φ range, independent of mixture strength. The results are consistent with those previously shown for undiluted flames and indicate that GRI-Mech 3.0 overpredicts the flame speed for methane-air flames by a small amount.

5.2.7 Methane-air flame summary

From the previous results, several conclusions can be drawn. The good agreement between model predictions (using GRI-Mech 3.0) and experiment over a wide range of compositions, flame temperature, and imposed strain rate simultaneously validates the experimental methodology and the models employed. In addition, from these data, it is evident that the chemistry models studied here tend to produce better agreement for near-stoichiometric and rich flames, but deviate from the

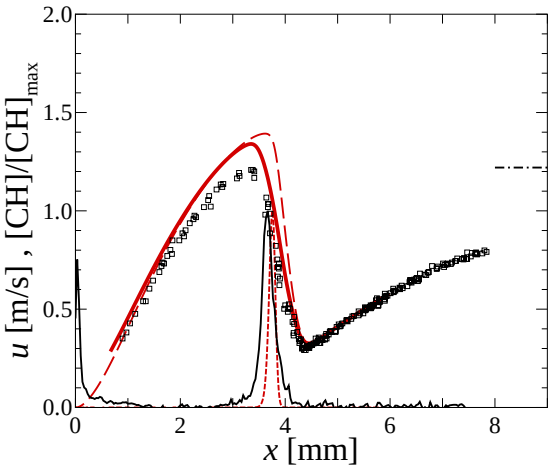

Figure 5.33: CH_4-air flame profiles (Φ = 0.9, 19.5%O_2:(O_2+N_2), run239). Legend as in Fig. 5.7.

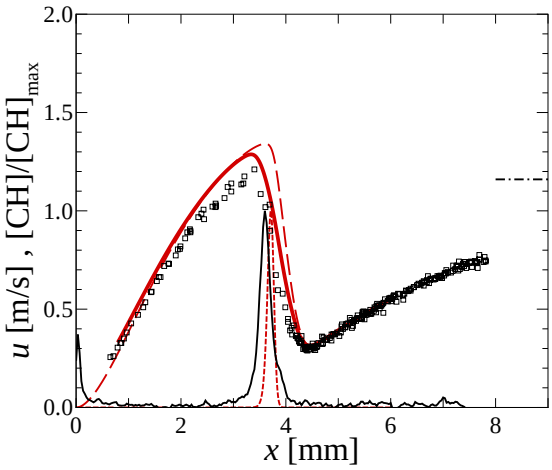

Figure 5.34: CH_4-air flame profiles (Φ = 1.0, 18.5%O_2:(O_2+N_2), run238). Legend as in Fig. 5.7.

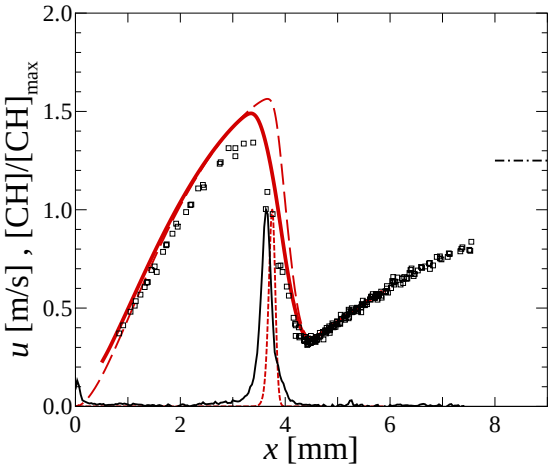

Figure 5.35: CH_4-air flame profiles (Φ = 1.1, 19.0%O_2:(O_2+N_2), run237). Legend as in Fig. 5.7.

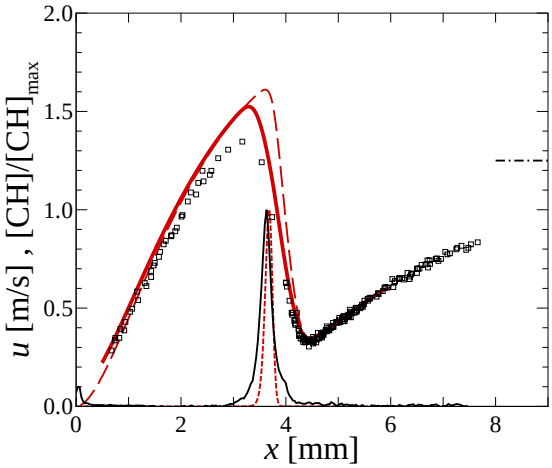

Figure 5.36: CH_4-air flame profiles (Φ = 1.2, 20.0%O_2:(O_2+N_2), run236). Legend as in Fig. 5.7.

experimental results for lean flames. The 2003 version of the San Diego mechanism predicts higher methane-air flame speeds than measured for all equivalence ratios studied. GRI-Mech 3.0 and the 2005 San Diego mechanism both predict higher flame speeds than measured for lean flames, while the C_3-Davis mechanism predicts slightly lower flame speeds than measured for lean flames. CH PLIF measurements provide several interesting conclusions. The variation in flame thickness as a function of stoichiometry is consistent between all of the mechanisms studied here, and the trend is reproduced by the experimental diagnostics when the off-line subtraction methodology is employed. The relative concentration measurements reported here are consistent with the measurements of Sutton & Driscoll (2003), the only other application of this relative fluorescence technique. These

measurements indicate the necessity for performing appropriate off-line correction when estimating relative CH concentrations. The extension of this methodology to planar imaging reported here allows the relative concentration at a large number of points to be measured simultaneously. The experimental techniques employed here are sensitive enough to highlight deficiencies in the various models, indicating areas of the kinetic parameter space that need further study. Even for a relatively simple fuel like methane, further kinetic evaluation and optimization is required.

5.3 Ethane-air flames

Ethane-air flames are studied as a function of the imposed strain rate and mixture fraction. Lean, stoichiometric, and rich flames are studied for variable strain rates to determine the performance of the chemistry models as a function of this parameter. Subsequently, ethane-air flames are studied as a function of stoichiometry to determine the relative performance of the models. The full profiles are presented for a lean, stoichiometric, and rich flame. The particle motion in the simulated flowfield is computed using a Lagrangian technique, and the resulting parametric description of the particle motion is post-processed to yield the modeled-PSV profile (see Appendix A). This modeled-PSV, u_{PSV}, profile accounts for particle inertia, thermophoretic, and finite chopping-frequency effects. The relative performance of the various models is compared to the experimental data by investigating the difference in location of the predicted CH profile location as compared to the experimental measurements. Relative CH concentration measurements are presented as a function of stoichiometry and the width of the CH layers are investigated. All CH profiles presented in this section were obtained by measuring the CH fluorescence on and off of the resonance line and taking the difference between the two (see Appendix C). The full profiles for all ethane-air flames studied are presented in Appendix H.

5.3.1 Imposed strain rate

The effect of varying the imposed strain rate is studied for lean, stoichiometric, and rich flames. Figure 5.37 presents the profiles for a lean ethane-air flame at a low value of the imposed strain rate. The minimum imposed strain rate is determined by the requirement that the flame be free standing, *i.e.*, not attached to the nozzle rim (so-called "button-flame"). The velocity boundary conditions are calculated as discussed previously and the flame simulated using GRI-Mech 3.0. The particle motion in the simulated flow field is solved using a Lagrangian technique. The particles used in this section are $1\,\mu$m alumina particles ($\rho_{\mathrm{p}} \cong 3830\,\mathrm{kg/m^3}$), chosen to minimize particle-inertia effects. The particle velocity profiles are post-processed to determine the modeled-PSV, u_{PSV}, profile, with a chopping frequency for these flames of $\nu_{\mathrm{c}} = 1600\,\mathrm{Hz}$. Figure 5.38 details the profiles for a flame close to the extinction strain rate, and Fig. 5.39 presents the measured velocity and modeled-PSV profiles as a function of the imposed strain rate. The complete profiles for the intermediate cases can be found in Appendix H. For these lean ethane-air flames, the CH concentration is low, resulting in a poor signal-to-noise ratio in the CH profiles. This equivalence ratio is near to the lean detection limit of our system. Including the particle-inertia, thermophoretic, and finite chopping-frequency effects leads to improved agreement in the shape of the simulated and experimental profiles. For lean ethane-air flames, the predicted profiles using GRI-Mech 3.0 closely match the experimental results. The simulated CH layer location is slightly upstream of the PLIF profile, and the minimum

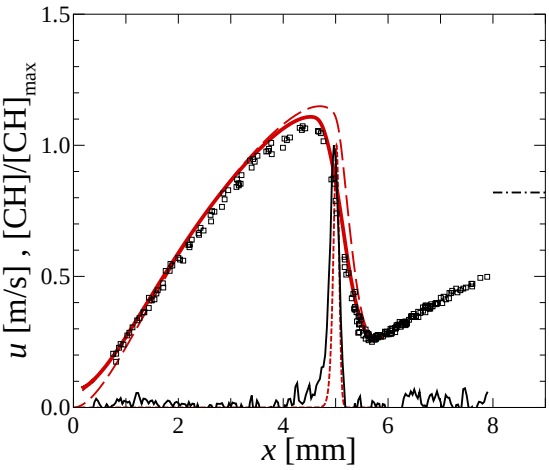

Figure 5.37: Lean C_2H_6-air flame profiles (Φ = 0.7, σ = 121 s^{-1}, L/d = 0.8, run313). (dash-dot line) U_B, (□) PSV data, (black line) PLIF data, (red long dash line) simulated velocity, u_f, profile (GRI-Mech 3.0), (red solid line) modeled-PSV, u_{PSV}, profile, (red short dash line) simulated CH profile.

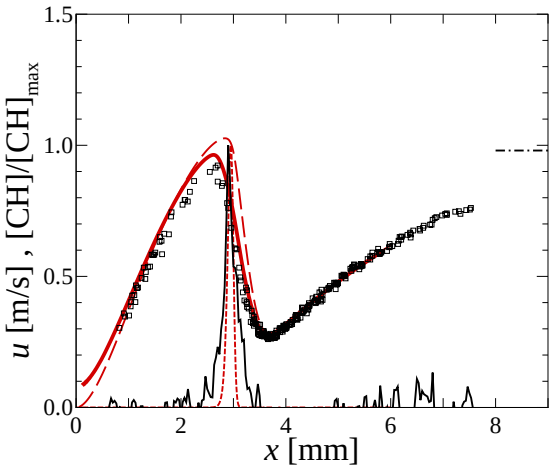

Figure 5.38: Lean C_2H_6-air flame profiles (Φ = 0.7, σ = 171 s^{-1}, L/d = 0.8, run317). Legend as in Fig. 5.37.

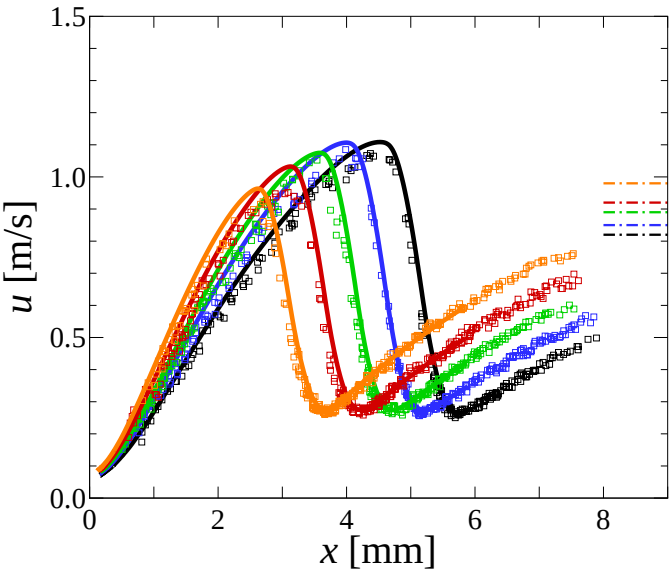

Figure 5.39: Lean C_2H_6-air flame profiles for variable imposed strain rate (Φ = 0.7, L/d = 0.8, run313-317). (dash-dot line) U_B, (□) PSV data, (solid line) modeled-PSV, u_{PSV}, profiles; Maximum imposed strain rates are σ = 121 s^{-1} (black), 127 s^{-1} (blue), 136 s^{-1} (green), 156 s^{-1} (red), and 171 s^{-1} (orange).

and maximum points of the velocity profile are slightly overpredicted. These slight disagreements are within the uncertainty of the measurements and these profiles could be considered to be in good agreement. As the strain rate is increased, the minimum of the velocity profile increases, and

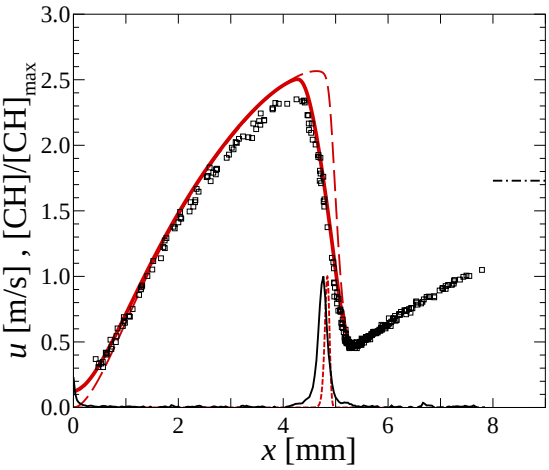

Figure 5.40: Stoichiometric C_2H_6-air flame profiles ($\Phi = 1.0$, $\sigma = 278\,s^{-1}$, $L/d = 0.8$, run319). Legend as in Fig. 5.37.

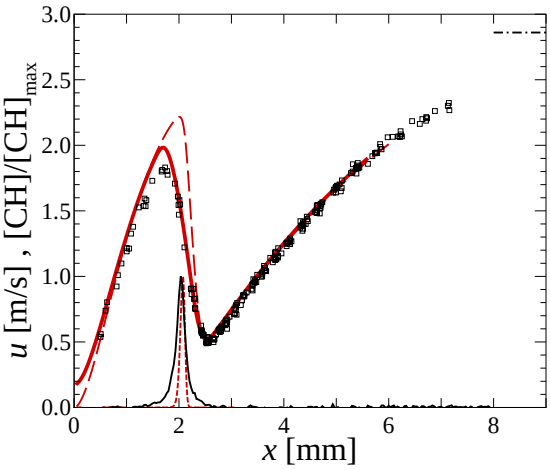

Figure 5.41: Stoichiometric C_2H_6-air flame profiles ($\Phi = 1.0$, $\sigma = 553\,s^{-1}$, $L/d = 0.8$, run323). Legend as in Fig. 5.37.

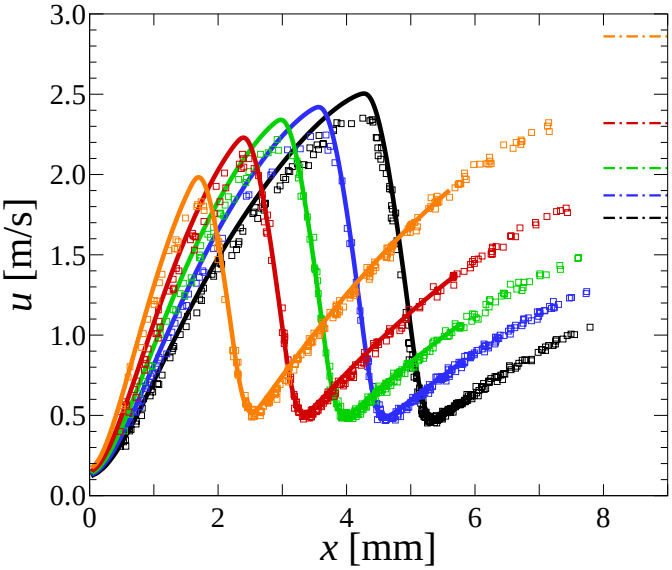

Figure 5.42: Stoichiometric C_2H_6-air flame profiles for variable imposed strain rate ($\Phi = 1.0$, $L/d = 0.8$, run319-323). (dash-dot line) U_B, (□) PSV data, (solid line) modeled-PSV, u_{PSV}, profiles; Maximum imposed strain rates are $\sigma = 278\,s^{-1}$ (black), $317\,s^{-1}$ (blue), $355\,s^{-1}$ (green), $413\,s^{-1}$ (red), and $553\,s^{-1}$ (orange).

the maximum decreases. This trend is accurately captured by both experiment and simulation, indicating good performance of GRI-Mech 3.0 for these lean methane-air flames.

Stoichiometric ethane-air flames are also studied as a function of the imposed strain rate. These strong-burning flames allow a larger variation in the imposed strain rate. Figure 5.40 presents the profiles for a weakly stretched flame and Fig. 5.41 gives the results for a near-extinction flame. The PSV and modeled-PSV profiles are compared as a function of the strain rate in Fig. 5.42.

The burning velocity of these stoichiometric ethane-air flames is quite high, and increased velocities relative to the lean flames are evident. The chopping frequency for these stoichiometric flames was $\nu_c = 2400\,\text{Hz}$, corresponding to the maximum frequency of the chopper employed. Good agreement is seen between experiment and the simulations using GRI-Mech 3.0, with the simulated flame speed slightly overpredicted. The modeled-PSV profiles show significantly better agreement with experiment as compared to the simulated velocity field, again illustrating the importance of modeling both the particle behaviour in the flow and the diagnostic technique. The variation in the value of the velocity minimum and maximum as the strain rate is increased is well-captured by both the experiment and simulations.

Figures 5.43–5.45 present the profiles for rich ethane-air flames at low, high, and variable strain rates. The flame speed for these rich flames is overpredicted by GRI-Mech 3.0, as shown by the CH profile loction and the values of the velocity minimum and maximum. The trend of increasing values of the velocity minimum as a function of strain rate is captured by both the experiment and simulations. A decrease in the velocity maximum value is also seen for increasing strain rate in both experiment and simulation. The chopping frequency in these flames was $\nu_c = 2000\,\text{Hz}$, and improved agreement in the profile shape is seen with the modeled-PSV profile. For methane-air flames, velocity data were not acquired through the reaction zone of rich flames due to chemiluminescence background in this region of the flow. Velocity data are measured through the reaction zone of this rich ethane flame, which has considerably increased emissions of the C_2 Swan bands due to the fact that the fuel contains two carbon atoms. The measurement of particle streaks through this zone is achieved by calculating the (local) background signal around each particle, and removing this before thresholding the streak. A region around each streak is interrogated and the maximum 3 pixels of each row are removed. Particle streak widths are typically 3 pixels for the PSV setup. The remaining pixels in each row are averaged and this average value is removed from each pixel in the corresponding row. The background-intensity variation in the vertical direction through the flame front can be removed in this manner, before processing the streak. Good results can be obtained using this background correction technique even in regions where chemiluminescence is not important, as it accounts for the average dark-noise or Rayleigh-scattering signal in the region around the particle streak. All PSV profiles presented in the remainder of this thesis are processed with this local-background-correction technique. There is an asymmetry in the CH profiles for these rich flames, with a sharper rise on the cold side of the profile as compared to the hot side. This asymmetry is noticeable in both the simulation and the experiment.

5.3.2 Equivalence ratio

As was found for methane-air flames, agreement between measurement and simulation exhibits a larger sensitivity to mixture composition than to the applied strain rate. Ethane-air flames are

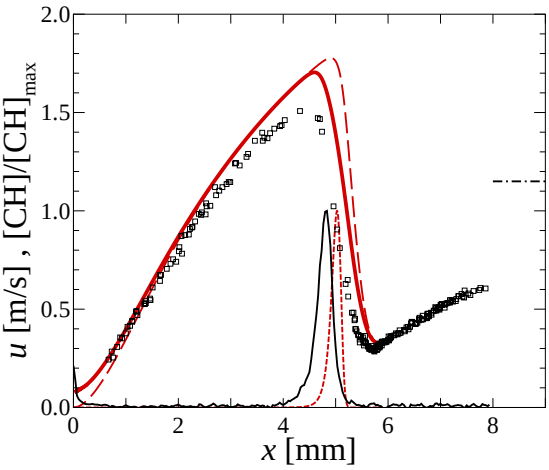

Figure 5.43: Rich C_2H_6-air flame profiles ($\Phi = 1.4$, $\sigma = 167\,s^{-1}$, $L/d = 0.8$, run324). Legend as in Fig. 5.37.

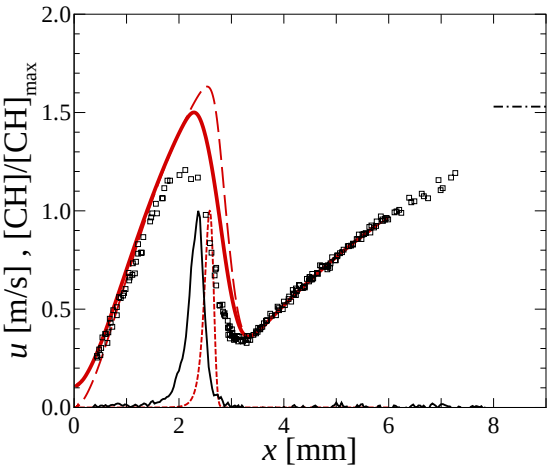

Figure 5.44: Rich C_2H_6-air flame profiles ($\Phi = 1.4$, $\sigma = 256\,s^{-1}$, $L/d = 0.8$, run328). Legend as in Fig. 5.37.

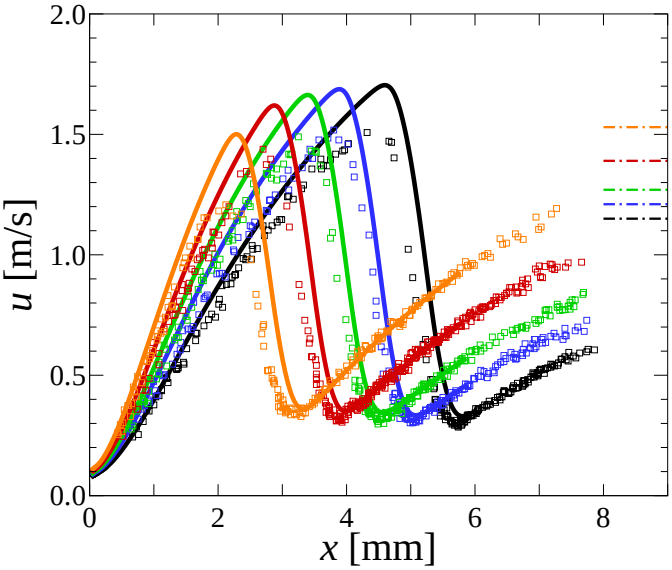

Figure 5.45: Rich C_2H_6-air flame profiles for variable imposed strain rate ($\Phi = 1.4$, $L/d = 0.8$, run324-328). (dash-dot line) U_B, (□) PSV data, (solid line) modeled-PSV, u_{PSV}, profiles; Maximum imposed strain rates are $\sigma = 167\,s^{-1}$ (black), $185\,s^{-1}$ (blue), $201\,s^{-1}$ (green), $220\,s^{-1}$ (red), and $256\,s^{-1}$ (orange).

studied as a function of equivalence ratio to further investigate kinetic effects. In the current experimental setup, stable ethane-air flames can be established for equivalence ratios in the range $0.7 \lesssim \Phi \lesssim 1.5$. The profiles for a lean flame, at $\Phi = 0.7$, are given in Fig. 5.46. Profiles are also given for a stoichiometric and rich flame in Figs. 5.47 and 5.48. The scale of the axes is kept constant for these three flames to illustrate the changing flame speed for lean, stoichiometric, and rich flames. PSV measurements are performed using $1\,\mu m$ alumina particles ($\rho_p \cong 3830\,kg/m^3$),

and the chopping frequencies are ν_c = 1600, 2400, and 1600 Hz for the lean, stoichiometric, and rich flames, respectively. Predictions using GRI-Mech 3.0 are in relatively good agreement with experiment for the lean and stoichiometric ethane-air flames, but the predicted flame speed is higher than experiment for rich flames, as found in the study of variable strain rate. The simulated post-flame velocity profiles consistently fall above the experimental data, even for cases where the CH profile and velocity minimum show close agreement. This is consistent with the results found for methane-air flames. Any overprediction in the reference flame speed (velocity minimum ahead of the flame) is amplified by the order-of-magnitude drop in density through the flame. The modeled-PSV profiles tend to capture the shape of the experimental profiles, again illustrating the importance of accounting for particle inertia, thermophoretic, and finite chopping-frequency effects.

It is of interest to compare the predictions utilizing various chemistry models to determine the relative performance of each one. The lean, stoichiometric, and rich flames presented in Figs. 5.46–5.48 were simulated using the C_3 mechanism of Davis *et al.* (1999), and two releases of the "San Diego" mechanism (see Bibliography: San Diego mechanism). The predictions of these four models are compared to the experimental data in Figs. 5.49–5.51. The modeled-PSV profiles obtained from the simulated flow field for the experimental-particle properties and tracking time are compared to the PSV data. For the lean flame, the C_3-Davis mechanism underpredicts the flame speed, GRI-Mech 3.0 and the SD2005 mechanism are in close agreement and slightly overpredict the flame speed, while the earlier release of the San Diego mechanism predicts a stronger flame speed than

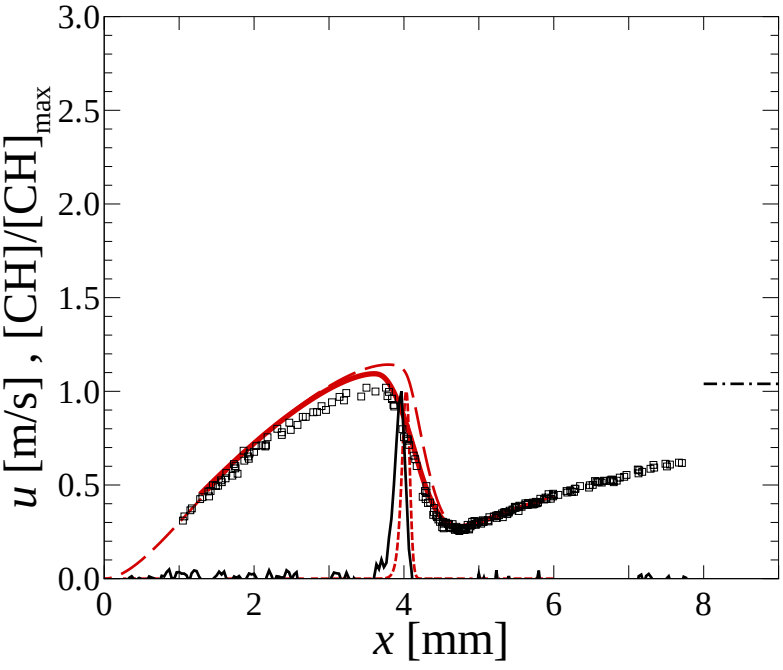

Figure 5.46: Lean C_2H_6-air flame profiles ($\Phi = 0.7$, run337). Legend as in Fig. 5.37.

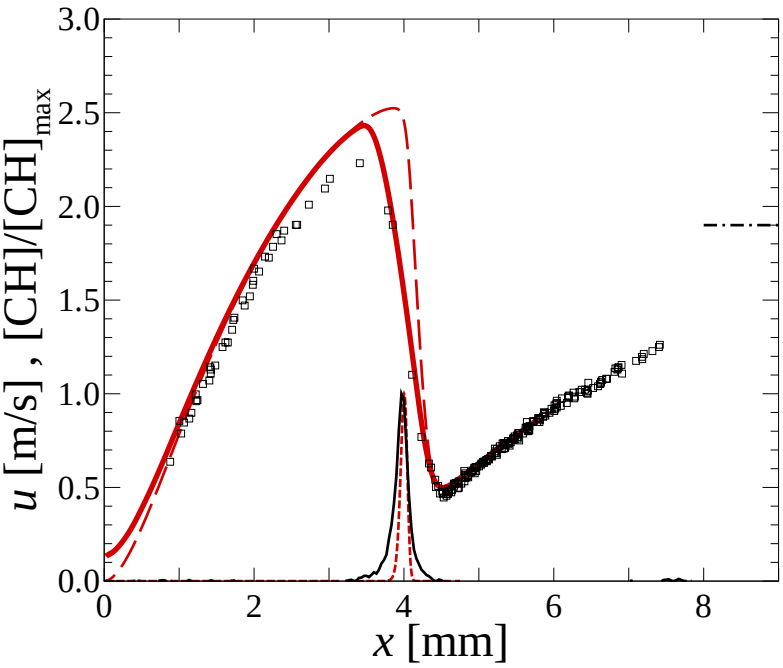

Figure 5.47: Stoichiometric C_2H_6-air flame profiles ($\Phi = 1.0$, run334). Legend as in Fig. 5.37.

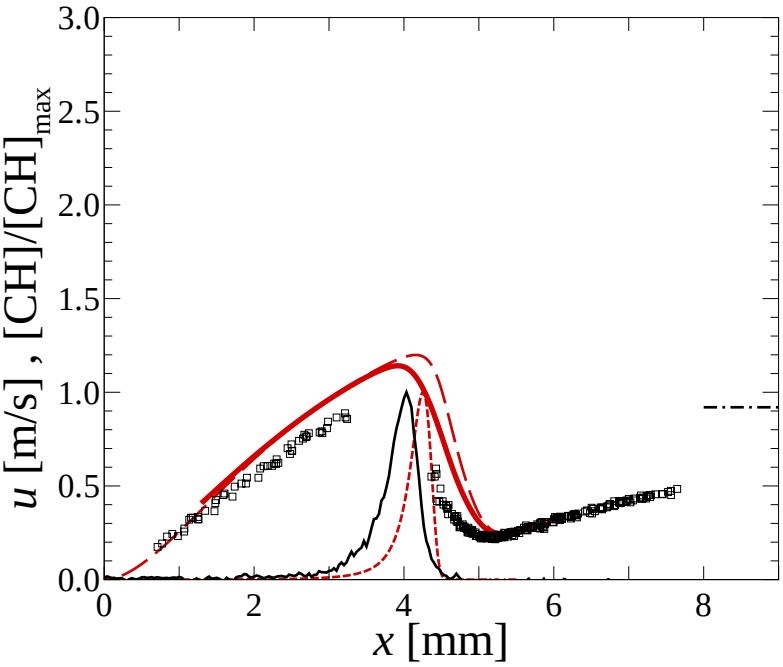

Figure 5.48: Rich C_2H_6-air flame profiles ($\Phi = 1.5$, run329). Legend as in Fig. 5.37.

seen in the experiment. It is interesting to note that the C_3-Davis mechanism predicts a lower value of the reference flame speed and the post-flame profile falls beneath the experimental data. Good agreement is seen for the C_3-Davis, GRI-Mech 3.0, and SD2005 mechanisms for the stoichiometric

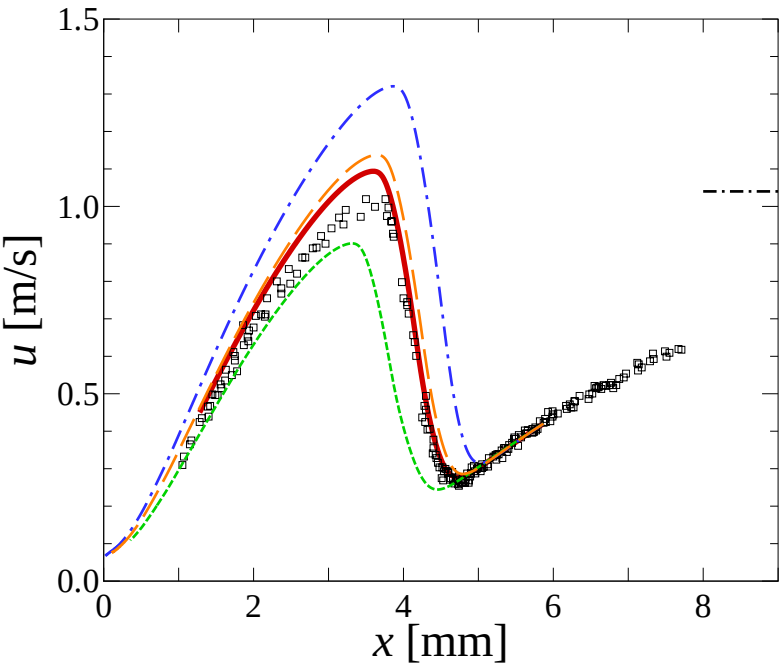

Figure 5.49: Comparison of modeled-PSV, u_{PSV}, profiles to experimental data in a $\Phi = 0.7$, C_2H_6-air flame (run337). (black dash-dot line) U_{B}, (□) PSV data, (red thick solid line) GRI-Mech 3.0, (green short dash line) C_3-Davis, (blue dash-dot line) SD2003, (orange long dash line) SD2005.

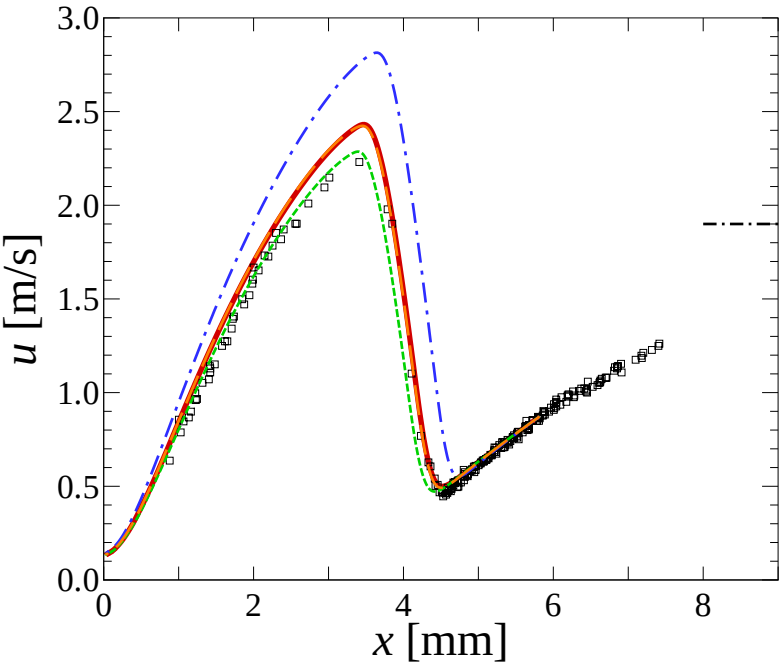

Figure 5.50: Comparison of modeled-PSV, u_{PSV}, profiles to experimental data in a $\Phi = 1.0$, C_2H_6-air flame (run334). (black dash-dot line) U_{B}, (□) PSV data, (red thick solid line) GRI-Mech 3.0, (green short dash line) C_3-Davis, (blue dash-dot line) SD2003, (orange long dash line) SD2005.

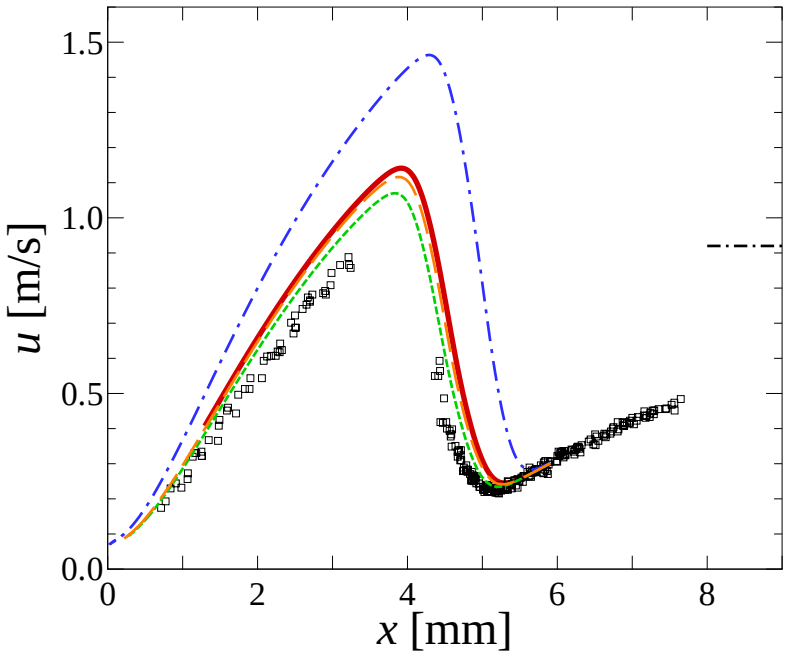

Figure 5.51: Comparison of modeled-PSV, u_{PSV}, profiles to experimental data in a $\Phi = 1.5$, C_2H_6-air flame (run329). (black dash-dot line) U_{B}, (□) PSV data, (red thick solid line) GRI-Mech 3.0, (green short dash line) C_3-Davis, (blue dash-dot line) SD2003, (orange long dash line) SD2005.

flame. For the rich flame, the C_3-Davis, GRI-Mech 3.0, and SD2005 mechanisms give consistent predictions with each other and exhibit stronger flame speeds than observed in the experiment. The SD2003 mechanism overpredicts the flame speed for all ethane-air flames.

The difference between the predicted and experimental CH-layer location is plotted in Fig. 5.52 and allows an assessment of the various chemistry models studied here. The predicted location of the CH profile, $x_{\mathrm{CH,sim}}$, is compared to the measured CH profile location x_{CH}, and the difference between the two is normalized by the simulated CH layer thickness, $\delta_{\mathrm{CH,GRI-3.0,\Phi=1}}$, calculated using the GRI-Mech 3.0 model at stoichiometric conditions ($\Phi = 1$). The models studied here predict very similar CH layer thicknesses for lean to slightly rich flames (see Fig. 5.55). The prediction from GRI-Mech 3.0 was utilized as a reference standard, due to its application to the majority of the flames studied in this chapter, and the generally good agreement of the model. The experimental CH location is taken as the mean of the fit values from single-shot profiles, averaging a typical record of 1000 images. The simulated CH location was taken to be the location of the peak of the CH profile from the numerical simulations, and the locations of the half-max value on either side of the peak were interpolated from the simulated profiles. The difference in the locations of the two half-max values gave the Full-Width at Half-Maximum (FWHM) for the simulated profile, yielding the CH-layer thickness, δ_{CH}. In Fig. 5.52, positive values of $(x_{\mathrm{CH,sim}} - x_{\mathrm{CH}})/\delta_{\mathrm{CH,GRI-3.0,\Phi=1}}$) indicate that the simulated CH profile is located *upstream* of the experimental profile and that the flame speed

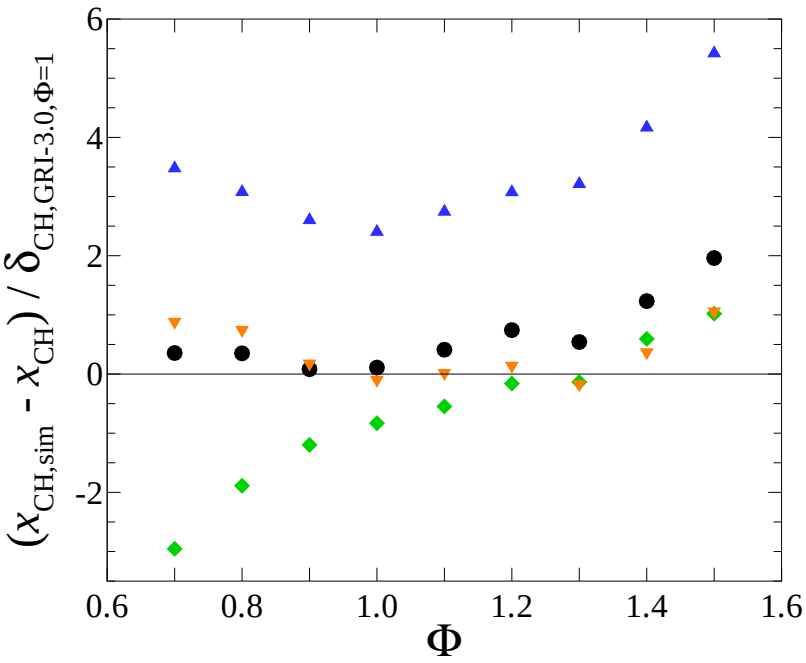

Figure 5.52: Difference between predicted and experimental CH-layer location for various chemistry models: (○) GRI-Mech 3.0, (◇) C_3-Davis, (△) SD2003, (▽) SD2005.

is *overpredicted*. The imposed strain rates for these flames vary between $\approx$ 100–300 s^{-1}, so that a difference in CH locations equal to one flame thickness, $\Delta x_{CH} = \delta_{CH}$, corresponds to a 1–3 cm/s difference in $S_{u,ref}$ [see Eq. (5.4)]. The total estimated uncertainty in the predicted flame location due to the uncertainties in the boundary conditions corresponds to $\approx 0.5\,\delta_{CH}$ (see Chapter 2). The GRI-Mech 3.0 and SD2005 mechanisms show the closest agreement with experiment, with GRI-Mech 3.0 showing better agreement for lean ethane-air flames while the SD2005 mechanism more closely matches experiment for rich conditions. The C_3-Davis mechanism predicts weaker flames than observed for lean conditions, while overpredicting flame speed for rich conditions, following closely the results of the SD2005 mechanism. The SD2003 mechanism again overpredicts the flame speed for all flames studied.

5.3.3 Relative concentration measurements and CH profile thicknesses

The predicted peak CH concentration for the various chemistry models is plotted in Fig. 5.53. All curves exhibit a similar dependence with changing equivalence ratio, with the C_3-Davis mechanism predicting the largest and the SD2003 mechanism the smallest concentrations. The peak concentration for the C_3-Davis mechanism is $\approx$ 15 ppm, as compared to $\approx$ 11 ppm for methane-air flames, with both peaks occurring at $\Phi = 1.2$. Figure 5.54 compares the relative CH concentrations measured with the PLIF technique, as discussed previously and in Appendix C, to model predictions. The

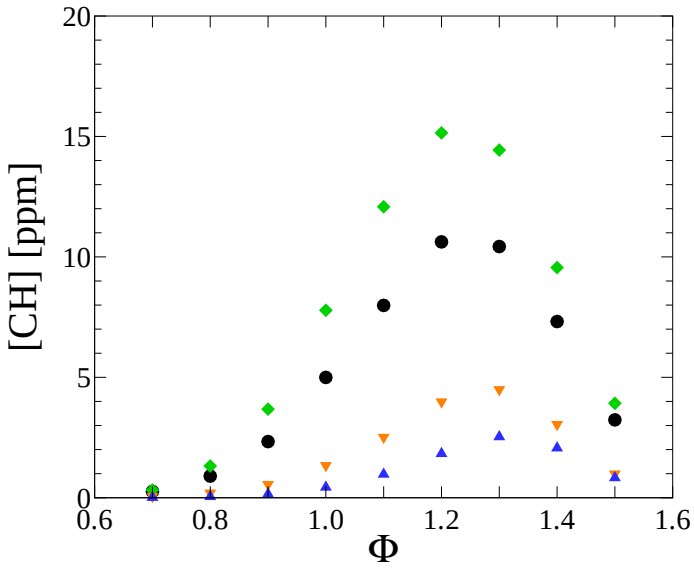

Figure 5.53: Comparison of predicted maximum CH concentrations from various chemistry models: (○) GRI-Mech 3.0, (◇) C_3-Davis, (△) SD2003, (▽) SD2005.

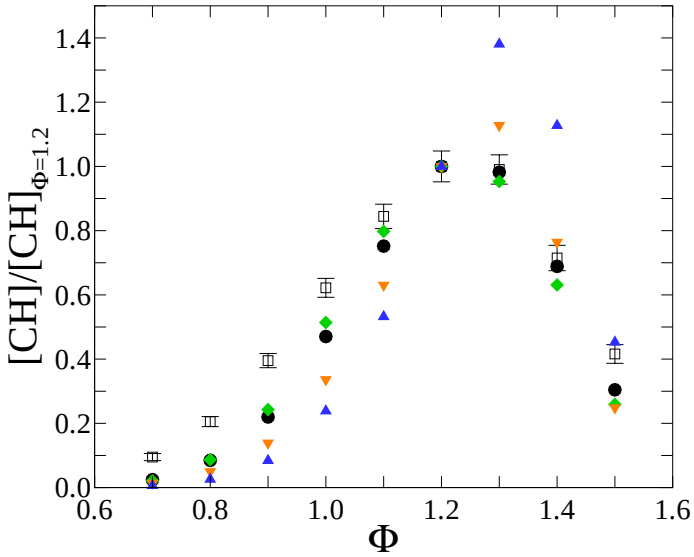

Figure 5.54: Comparison of relative concentration measurements, normalized to the concentration at $\Phi = 1.2$, from various chemistry models to experimental data. (□) CH PLIF data, (○) GRI-Mech 3.0, (◇) C_3-Davis, (△) SD2003, (▽) SD2005.

C_3-Davis measurement shows the best agreement with simulation, while the SD2003 model predicts the peak at $\Phi = 1.3$ and shows a very fast drop-off in concentration for lean conditions, contradictory to the measurements.

The predicted CH-layer thicknesses are presented as the Full-Width at Half-Maximum (FWHM) of the profiles in Fig. 5.55. The GRI-Mech 3.0 and C_3-Davis models are in close agreement with

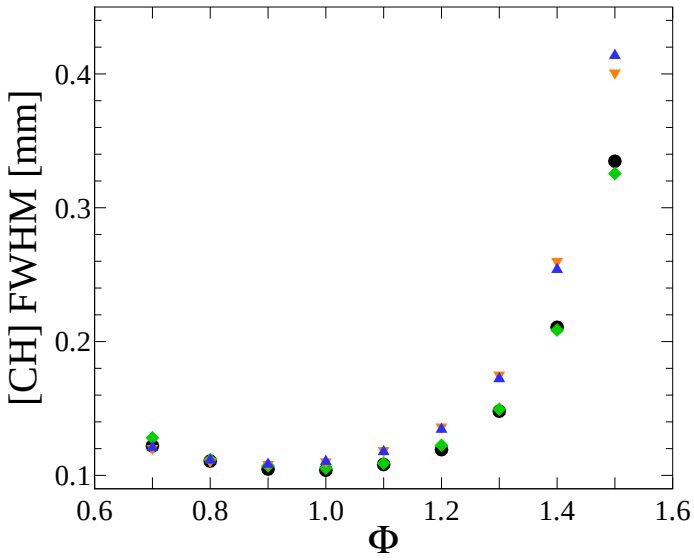

Figure 5.55: Comparison of predicted CH profile thicknesses for various chemistry models: (○) GRI-Mech 3.0, (◇) C_3-Davis, (△) SD2003, (▽) SD2005.

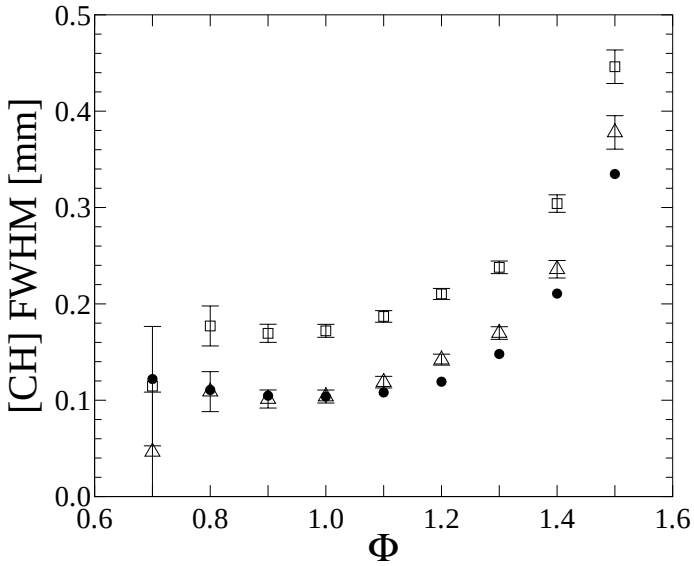

Figure 5.56: Comparison of measured CH profile thickneses to the predictions of GRI-Mech 3.0. (□) uncorrected CH PLIF data, (△) corrected CH PLIF data, (○) GRI-Mech 3.0.

each other, while the two versions of the San Diego mechanism predict larger flame thicknesses for rich flames. Figure 5.56 compares the experimentally measured profiles to those of the GRI-Mech 3.0 model. Good agreement between the experimental and simulated results is seen when the measurements are corrected to match the flame thickness at $\Phi = 1$. However, the required Point-Spread-Function correction factor, δ_{PSF}, is 0.068 mm for these ethane-air flames as compared to 0.092 mm for methane-air flames. As the collection optics were not adjusted, and care was taken

to ensure good focus of the CH profile, this discrepancy points to a misprediction in the relative CH thicknesses for methane- and ethane-air flames. For rich conditions the measured relative CH layer thickness would fall between the predictions of the GRI-Mech 3.0 and San Diego mechanisms.

5.3.4 Ethane-air flame summary

The study of ethane, C_2H_6, the second alkane in order of increasing number of carbon atoms, has revealed some interesting results. Reasonable agreement is seen between GRI-Mech 3.0, C_3-Davis, and the SD2005 mechanisms, although some variance with experiment is evident for each. Dong *et al.* (2002) measured laminar flame speeds in lean ethane air flames, $0.6 < \Phi < 0.8$, and found that GRI-Mech 3.0 overpredicted their results by 5–7 cm/s. This is in contradiction to the current results for which GRI-Mech 3.0 gave good agreement with experiment for lean flames. While the results presented here cannot be directly compared to flame speeds, it is expected that an overprediction of laminar flame speed would coincide with an overprediction of flame speed in these experiments. GRI-Mech 3.0 included the laminar flame speed of ethane at 1 atm as an optimization target, thus the observed agreement could be expected. Data on the GRI-Mech 3.0 Web page (Smith *et al.*) show an underprediction of the flame speed for lean ethane-air flames and an overprediction for rich conditions. The origin of these discrepancies in the reported performance of GRI-Mech 3.0 is unclear. For the other mechanisms, similar comparisons between predicted and measured laminar flame speeds are not available, increasing the importance of the present studies. As all of the mechanisms appear to overpredict flame speed for rich flames, GRI-Mech 3.0 and the SD2005 mechanism could be considered to be more accurate over the entire range of mixture fractions. The SD2003 mechanism substantially overpredicts the flame speed for ethane-air flames, as it did for methane-air. Relative CH concentration measurements exhibit better agreement with the C_3-Davis and GRI-Mech 3.0 mechanisms as compared to the San Diego mechanisms, although the SD2005 model appears to be significantly better than SD2003. These are the only reported relative-concentration measurements of the CH radical in ethane-air flames known to the author.

5.4 Ethylene-oxygen-nitrogen flames

Ethylene-air flames are also studied as a function of the imposed strain rate and the mixture fraction. Lean and rich flames are studied for variable strain rates to determine the performance of the chemistry models as a function of this parameter. Ethylene-air flame speeds are much higher than those for methane and ethane (C_2H_4: $S_u^0(\Phi{=}1) \cong 67\,\mathrm{cm/s}$, C_2H_6: $S_u^0(\Phi{=}1) \cong 41\,\mathrm{cm/s}$, CH_4: $S_u^0(\Phi{=}1) \cong 36\,\mathrm{cm/s}$, *e.g.*, Egolfopoulos *et al.* 1990; Bosschaart & de Goey 2004). For the strong-burning stoichiometric and slightly rich flames, the higher associated velocities resulted in poor performance of the PSV setup employed. Limitations in the chopping frequency of the system ($\nu_{c,max} = 2400\,\mathrm{Hz}$) and the reduced light per pixel associated with the faster moving particles would have resulted in poor accuracy of the velocimetry diagnostic. Rather than perform measurements at these high velocities, ethylene flames were studied with variable dilution to maintain similar flame speeds as a function of stoichiometry, as described in Section 5.2.6 for methane-air flames. Model performance was shown to be independent of flame speed, therefore, dilution can be used to study the kinetic model performance for similar hydrodynamic conditions. The full profiles are presented for lean, stoichiometric, and rich flames. The particle motion in the simulated flow field is computed using a Lagrangian technique, and the resulting parametric description of the particle motion is post-processed to yield the modeled-PSV, u_{PSV}, profile (see Appendix A). This modeled-PSV profile accounts for particle inertia, thermophoretic, and finite chopping-frequency effects. Relative performance of the various models is compared to the experimental data by investigating the difference in location of the predicted CH profile location as compared to the experimental measurements. Relative CH concentration measurements are presented as a function of stoichiometry and the width of the CH layers are investigated. All CH profiles presented in this section were obtained by measuring the CH fluorescence on and off of the resonance line and taking the difference between the two (see Appendix C).

5.4.1 Imposed strain rate

Lean and rich flames are studied at variable imposed strain rates. Figures 5.57 and 5.58 show the profiles for a weakly and strongly stretched flame, respectively. The particle motion is solved through the simulated flow fields and the finite chopping frequency is applied to the profile to yield the modeled-PSV, u_{PSV}, profile ($\nu_c = 2400\,\mathrm{Hz}$: see Appendix A). The particles used in this chapter are $1\,\mu$m alumina particles ($\rho_p \cong 3830\,\mathrm{kg/m^3}$). Figure 5.59 shows the measured and modeled-PSV profiles for variable imposed strain rates. The full profiles for the intermediate cases can be found in Appendix I. GRI-Mech 3.0 predicts significantly higher flame speeds than experimentally measured, as noted previously (Egolfopoulos & Dimotakis 2001). GRI-Mech 3.0 was not developed to model ethylene combustion and was not optimized against ethylene flame speed data. The

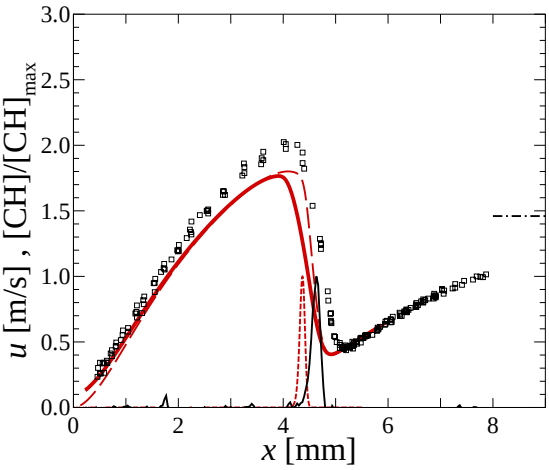

Figure 5.57: C_2H_4-air flame profiles ($\Phi = 0.7$, 21 %O_2:(O_2+N_2), $\sigma = 254\,s^{-1}$, $L/d = 0.8$, run302). (dash-dot line) U_B, (□) PSV data, (black line) PLIF data, (red long dash line) simulated velocity, u_f, profile (C_3-Davis), (red solid line) modeled-PSV, u_{PSV}, profile, (red short dash line) simulated CH profile.

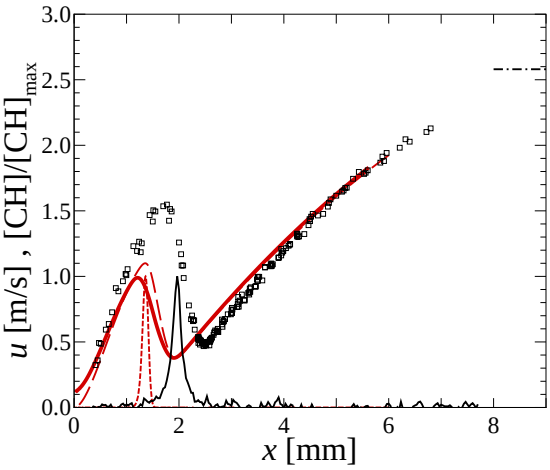

Figure 5.58: C_2H_4-air flame profiles ($\Phi = 0.7$, 21 %O_2:(O_2+N_2), $\sigma = 492\,s^{-1}$, $L/d = 0.8$, run306). Legend as in Fig. 5.57.

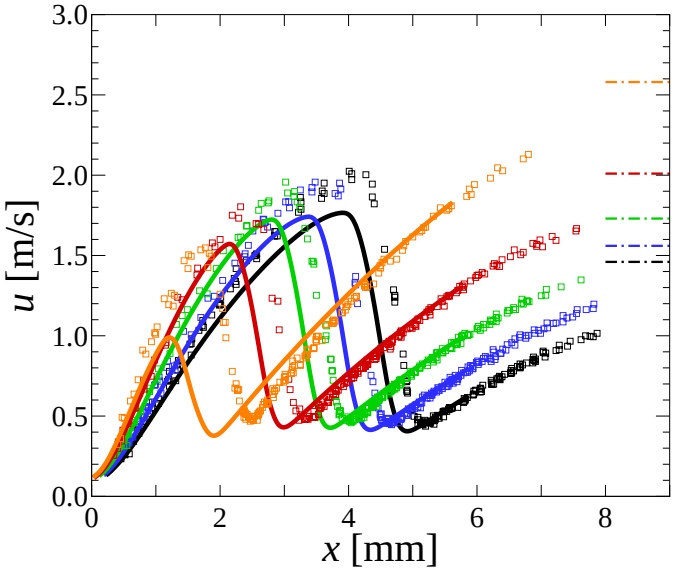

Figure 5.59: C_2H_4-air flame profiles for variable imposed strain rate ($\Phi = 0.7$, 21 %O_2:(O_2+N_2), $L/d = 0.8$, run302-306). (dash-dot line) U_B, (□) PSV data, (solid line) modeled-PSV, u_{PSV}, profiles; Maximum imposed strain rates are $\sigma = 254\,s^{-1}$ (black), $291\,s^{-1}$ (blue), $324\,s^{-1}$ (green), $381\,s^{-1}$ (red), and $492\,s^{-1}$ (orange).

ethylene flames are also simulated using the C_3-Davis mechanism, which was created to model combustion of all hydrocarbons with three or fewer carbon atoms. The C_3-Davis model is compared to experimental data in this section. For these lean ethylene-air flames, the C_3-Davis mechanism is

found to underpredict flame speed. The predicted CH profile is downstream of that measured using PLIF, and the simulated and modeled-PSV profiles fall beneath the data. As strain rate is increased, disagreement between simulation and experiment increases, and for the strongly stretched flame the simulated profile appears to be be much closer to extinction conditions than the experimental flame (see Fig. 5.58). The reference flame speed increases with increasing strain rate in the experiment, with the same trend observed in the simulations for all cases except the flame with the highest imposed strain rate.

The effect of varying the imposed strain rate is also studied for rich ethylene-air flames. Figures 5.60 and 5.61 show the profiles for a weakly and strongly stretched flame, while the modeled-PSV, u_{PSV}, profiles are compared to the data at several strain rates in Fig. 5.62. The weakest and strongest stretched flames in Fig. 5.62 correspond to those detailed in Figs. 5.60 and 5.61, respectively, with the full profiles for the intermediate cases presented in Appendix I. The chopping frequency used to study these flames was $\nu_{\mathrm{c}} = 2400\,\mathrm{Hz}$. The C_3-Davis mechanism overpredicts flame speed for these rich ethylene-air flames. A significant asymmetry is seen in the CH profile shape for these rich flames, similar to that seen for rich ethane-air flames. A comparison shows increased "wings" in the measured profiles, indicative of the approximately Lorentzian point-spread function of the intensified-CCD used to acquire the PLIF data. Similar performance of the model is seen at all imposed strain rates.

5.4.2 Equivalence ratio

For all of the flames studied, results are more strongly dependent on mixture composition than on imposed strain rate. Stable ethylene-air flames can be established in our apparatus for equivalence ratios in the range $0.6 \lesssim \Phi \lesssim 1.8$. The profiles for a lean flame, at $\Phi = 0.6$, are given in Fig. 5.63. Profiles are also given for a stoichiometric and rich flame in Figs. 5.64 and 5.65. The lean and rich flames are not diluted, while the stoichiometric flame was diluted such that the oxygen made up 17 % of the "air." The scale of the axes is kept constant for these three flames to illustrate the changing flame speed for lean, stoichiometric, and rich flames. PSV measurements are performed using $1\,\mu$m alumina particles ($\rho_{\mathrm{p}} \cong 3830\,\mathrm{kg/m^3}$) and chopping frequencies are $\nu_{\mathrm{c}} = 1600$, 2400, and 1600 Hz for the lean, stoichiometric, and rich flames, respectively. Good agreement is seen between the prediction using the C_3-Davis mechanism and experiment for the stoichiometric flame. The simulations, however, underpredict flame speed for the lean case and overpredict the flame speed for the rich case. Our setup has a lean detection limit below $\Phi = 0.6$ for ethylene-air flames, and reasonably good signal-to-noise ratios are achieved for these lean flames, as seen in Fig. 5.63. The CH profile is seen to be quite thin and symmetric for this case. The asymmetry of the CH profile is evident for the $\Phi = 1.8$ flame, for which the signal-to-noise ratio is poor. This is because of the low concentration of CH produced in this rich flame (see Figs. 5.70 & 5.71).

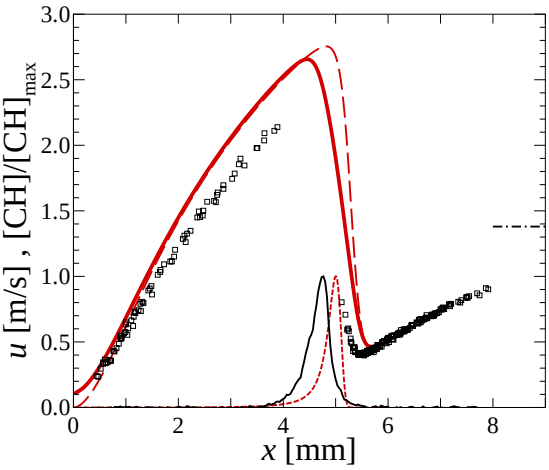

Figure 5.60: C_2H_4-air flame profiles ($\Phi = 1.6$, 21 %O_2:(O_2+N_2), $\sigma = 236\,s^{-1}$, $L/d = 0.8$, run307). Legend as in Fig. 5.57.

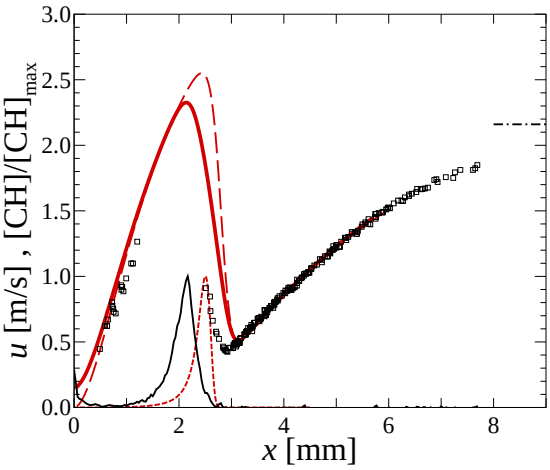

Figure 5.61: C_2H_4-air flame profiles ($\Phi = 1.6$, 21 %O_2:(O_2+N_2), $\sigma = 418\,s^{-1}$, $L/d = 0.8$, run311). Legend as in Fig. 5.57.

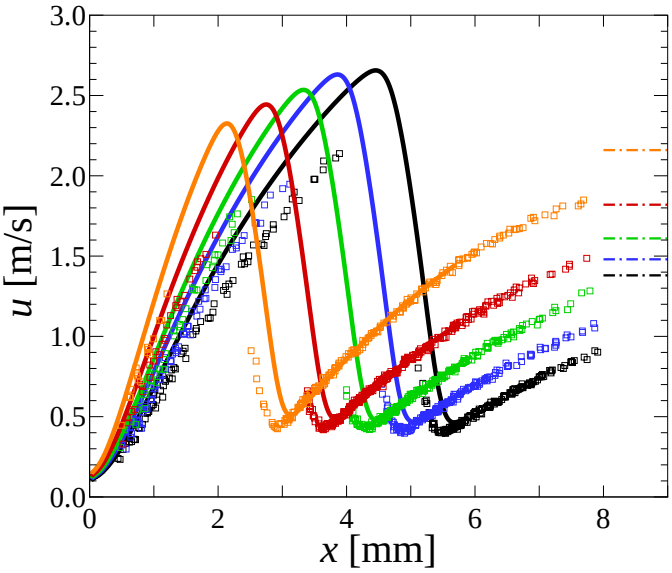

Figure 5.62: C_2H_4-air flame profiles for variable imposed strain rate ($\Phi = 1.6$, 21 %O_2:(O_2+N_2), $L/d = 0.8$, run307-311). (dash-dot line) U_B, (□) PSV data, (solid line) modeled-PSV, u_{PSV}, profiles; Maximum imposed strain rates are $\sigma = 236\,s^{-1}$ (black), $265\,s^{-1}$ (blue), $286\,s^{-1}$ (green), $340\,s^{-1}$ (red), and $418\,s^{-1}$ (orange).

To see the relative performance of the chemistry models included in this study, the modeled-PSV profiles for the lean, stoichiometric, and rich flames are compared to experiment. Figure 5.66 gives the profiles for the lean ethylene-air flame. As noted previously, the C_3-Davis mechanism underpredicts the flame speed, while GRI-Mech 3.0 overpredicts the burning velocity. The SD2003 model closely matches GRI-Mech 3.0, while the newer San Diego mechanism, SD2005, gives closer agreement with experiment, albeit slightly overpredicting the flame speed. For the stoichiometric

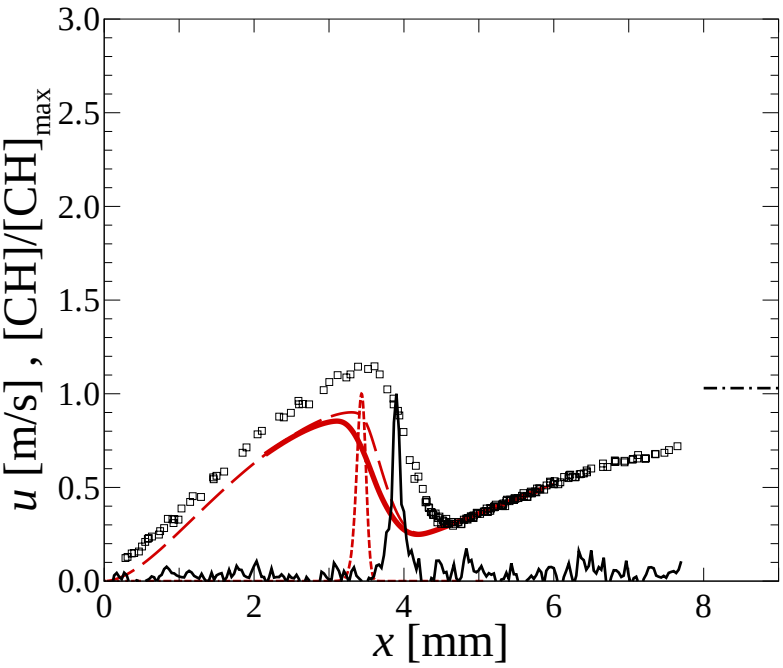

Figure 5.63: Lean C_2H_4-air flame profiles (Φ = 0.6, 21 %O_2:(O_2+N_2), run301). Legend as in Fig. 5.57.

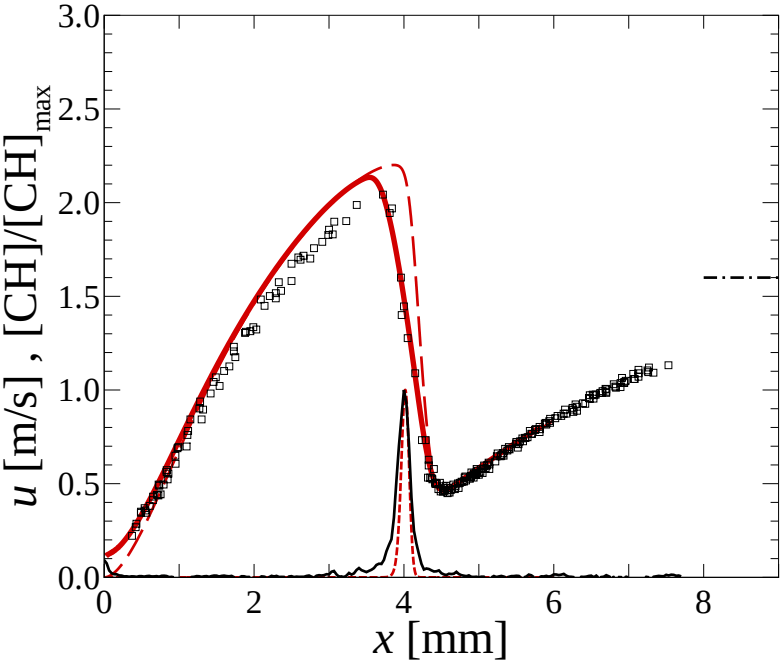

Figure 5.64: Diluted stoichiometric C_2H_4-O_2-N_2 flame profiles (Φ = 1.0, 17 %O_2:(O_2+N_2), run299). Legend as in Fig. 5.57.

flame, the C_3-Davis and SD2005 models are close to each other and accurately predict the flame speed, while the SD2003 and GRI-Mech 3.0 mechanisms overpredict the flame speed (see Fig. 5.67).

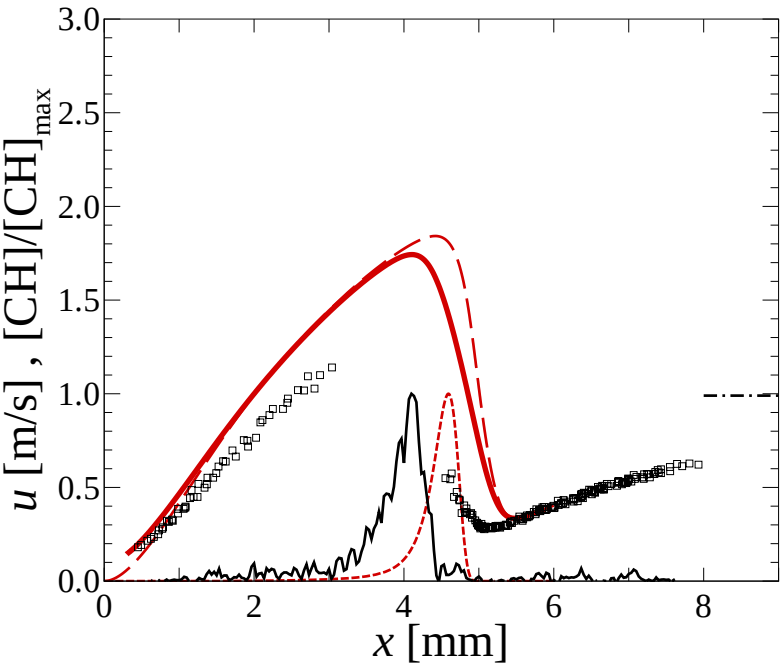

Figure 5.65: Rich C_2H_4-air flame profiles (Φ = 1.8, 21 %O_2:(O_2+N_2), run298). Legend as in Fig. 5.57.

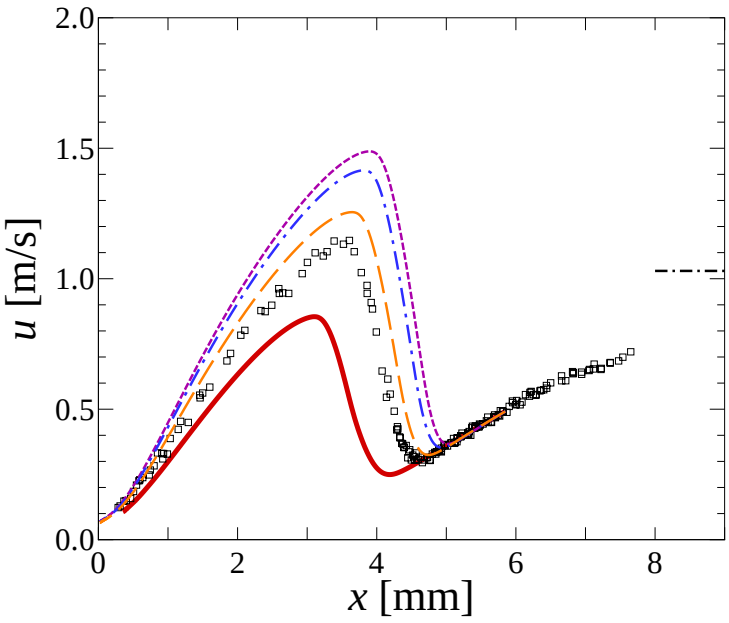

Figure 5.66: Comparison of modeled-PSV, u_{PSV}, profiles to experimental data in a $\Phi = 0.6$, C_2H_4-air flame (21 %O_2:(O_2+N_2), run301). (black dash-dot line) U_B, (□) PSV data, (red thick solid line) C_3-Davis, (purple short dash line) GRI-Mech 3.0, (blue dash-dot line) SD2003, (orange long dash line) SD2005.

Under rich conditions, all of these models overpredict the flame speed; however, the C_3-Davis and SD2005 models give closer agreement to experiment than GRI-Mech 3.0 or the SD2003 mechanism

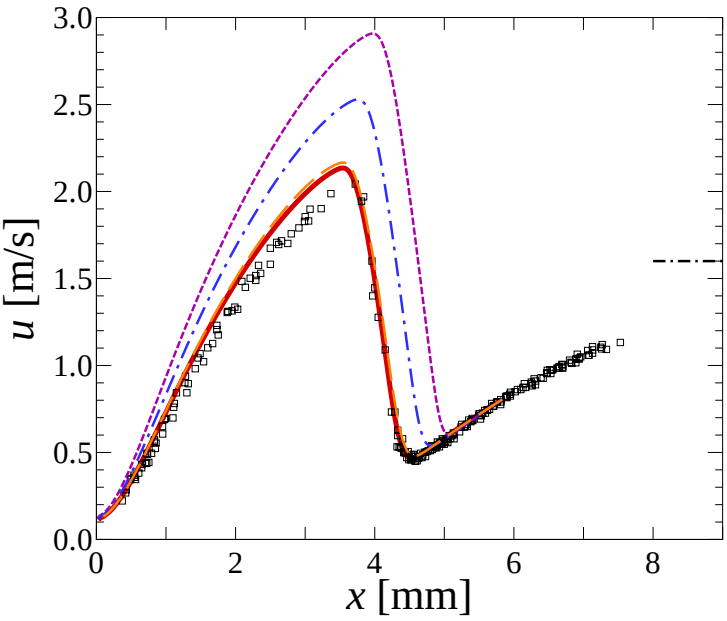

Figure 5.67: Comparison of modeled-PSV, u_{PSV}, profiles to experimental data in a diluted, $\Phi = 1.0$, C_2H_4-O_2-N_2 flame (17 %O_2:(O_2+N_2), run299). (black dash-dot line) U_{B}, (□) PSV data, (red thick solid line) C_3-Davis, (purple short dash line) GRI-Mech 3.0, (blue dash-dot line) SD2003, (orange long dash line) SD2005.

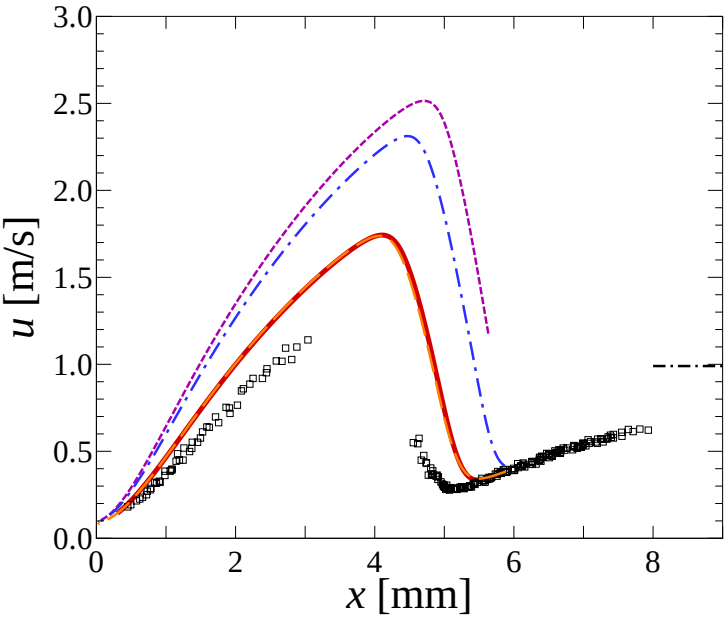

Figure 5.68: Comparison of modeled-PSV, u_{PSV}, profiles to experimental data in a $\Phi = 1.8$, C_2H_4-air flame (21 %O_2:(O_2+N_2), run298). (black dash-dot line) U_{B}, (□) PSV data, (red thick solid line) C_3-Davis, (purple short dash line) GRI-Mech 3.0, (blue dash-dot line) SD2003, (orange long dash line) SD2005.

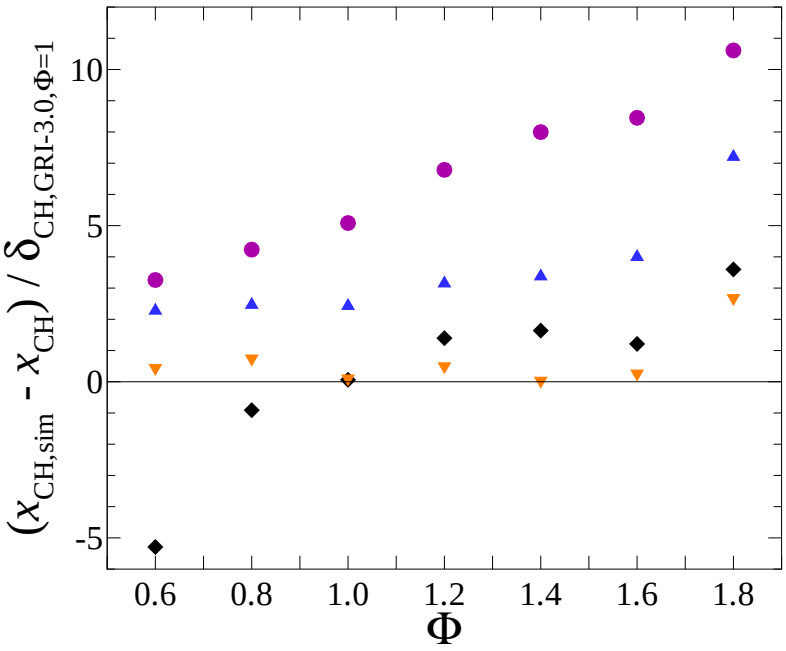

Figure 5.69: Comparison of predicted CH layer location between various chemistry models: (○) GRI-Mech 3.0, (◇) C_3-Davis, (△) SD2003, (▽) SD2005.

(see Fig. 5.68). In both Figs. 5.67 and 5.68 the C_3-Davis and SD2005 velocity profiles almost collapse onto each other, with only slight differences visible for the stoichiometric case.

To compare the relative performance of the chemistry models for the entire suite of experiments performed at variable mixture composition, the difference between the predicted and measured CH profile location, normalized by the predicted flame thickness using GRI-Mech 3.0 at $\Phi = 1$, $(x_{\mathrm{CH,sim}} - x_{\mathrm{CH}})/\delta_{\mathrm{CH,GRI-3.0,\Phi=1}}$, is compared in Fig. 5.69. Again, all of these chemistry models yield similar CH-layer thicknesses at stoichiometric conditions (see Fig. 5.72). The predicted CH-layer thickness of GRI-Mech 3.0 was used for normalizing the difference in location. GRI-Mech 3.0 was used for consistency with the results for methane- and ethane-air flames, even though this model is not as successful in capturing the flame speed for ethylene flames. The imposed strain rates for these flames vary between $\approx$ 100–300 s^{-1}, so that a difference in CH locations equal to one flame thickness, $\Delta x_{\mathrm{CH}} = \delta_{\mathrm{CH}}$, corresponds to a 1–3 cm/s difference in $S_{\mathrm{u,ref}}$ [see Eq. (5.4)]. The total estimated uncertainty in the predicted flame location due to the uncertainties in the boundary conditions corresponds to $\approx 0.5\,\delta_{\mathrm{CH}}$ (see Chapter 2). The SD2005 mechanism shows the best agreement with experiment over this range of mixture fractions, while the C_3-Davis mechanism matches experiment only for stoichiometric conditions and is at variance with experiment for both lean and rich flames. Both the SD2003 and GRI-Mech 3.0 models overpredict the flame speed for all conditions. The GRI-Mech 3.0 predictions exhibit a greater variance with experiment as the flame goes from lean to rich conditions.

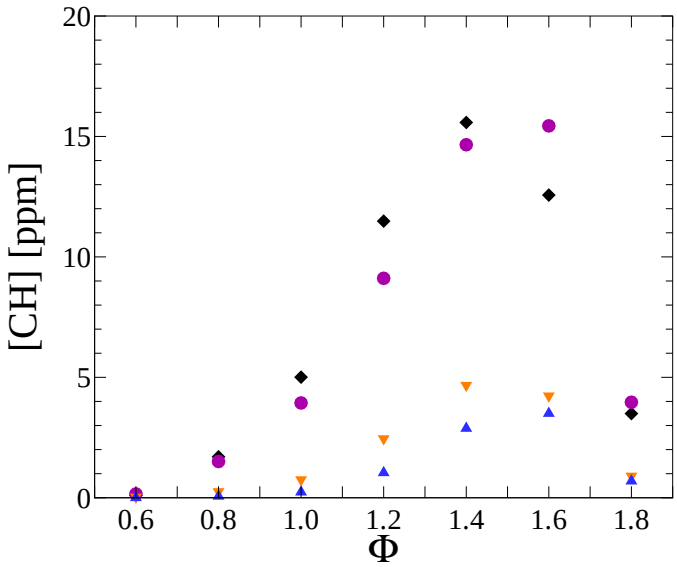

Figure 5.70: Comparison of predicted maximum CH concentrations from various chemistry models: (○) GRI-Mech 3.0, (◇) C_3-Davis, (△) SD2003, (▽) SD2005.

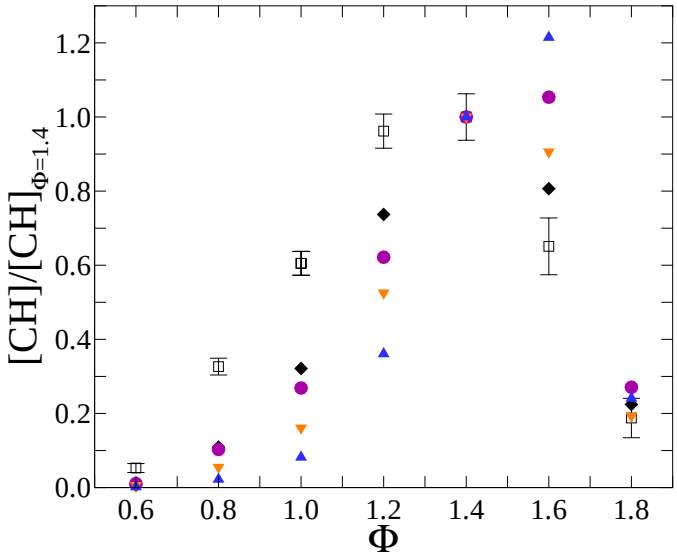

Figure 5.71: Comparison of relative concentration measurements, normalized to the concentration at $\Phi = 1.4$, from various chemistry models to experimental data. (□) CH PLIF data, (○) GRI-Mech 3.0, (◇) C_3-Davis, (△) SD2003, (▽) SD2005.

5.4.3 Relative concentration measurements and CH profile thicknesses

The predicted peak CH concentration for the various chemistry models is plotted in Fig. 5.70. The relative concentration measurements are shown in Fig. 5.71. These models predict similar trends, with the peak CH concentration occuring at $\Phi = 1.4$–1.6. The peak concentration for the C_3-Davis mechanism is ≈ 15 ppm at $\Phi = 1.4$, very close to the maximum concentration for ethane-air flames

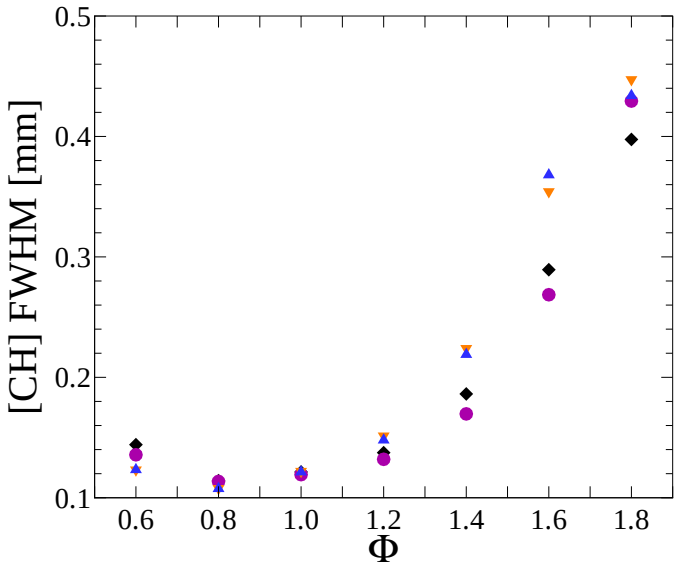

Figure 5.72: Comparison of predicted CH profile thicknesses for various chemistry models: (○) GRI-Mech 3.0, (◇) C_3-Davis, (△) SD2003, (▽) SD2005.

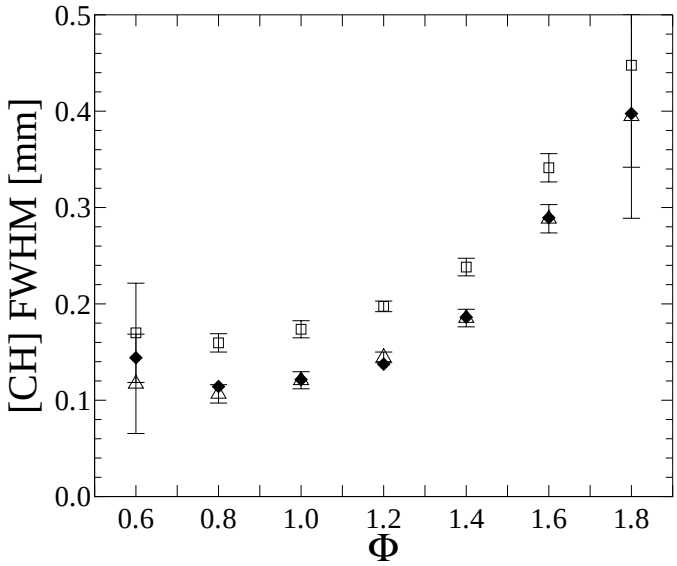

Figure 5.73: Comparison of measured CH profile thickneses to the predictions of C_3-Davis mechanism. (□) uncorrected CH PLIF data, (△) corrected CH PLIF data, (◇) C_3-Davis.

($\Phi = 1.2$). All of these models predict a faster drop-off under lean conditions than measured.

Predicted CH-layer thicknesses are presented as the Full-Width at Half-Maximum (FWHM) of the profiles in Fig. 5.72. Similar results are seen for lean and stoichiometric flames, although variations are observed as the flames become fuel-rich. Figure 5.73 compares the experimentally measured profiles to those of the C_3-Davis model. Good agreement between the experimental and simulated results is seen when the measurements are corrected to match the flame thickness at

$\Phi = 1$. However, the required Point-Spread-Function correction factor, δ_{PSF}, is 0.053 mm for these ethylene-air flames as compared to 0.068 mm for ethane-air and 0.092 mm for methane-air flames. As the collection optics were not adjusted, and care was taken to ensure good focus of the CH profile, this discrepancy points to a misprediction in the relative CH thicknesses for methane-, ethane-, and ethylene-air flames. The uncertainty in the profile widths is largest for lean and rich near-limit flames because of the reduced signal-to-noise ratio due to their low CH concentrations (see Fig. 5.70).

5.4.4 Ethylene-oxygen-nitrogen flame summary

Ethylene, C_2H_4, is the first alkene in the hydrocarbon hierarchy, with a double bond between the two carbon atoms. Of the three fuels investigated, the mechanisms studied here showed the largest variance with ethylene experiments. The SD2005 model was developed to model ethylene combustion and shows the best agreement with experiment. A comparison of measured burning velocities for ethylene-air flames with this mechanism published on the San Diego mechanism Web site (see Bibliography: San Diego mechanism) shows good agreement between model and experiment with a slight overprediction for lean flames, consistent with the results presented here. The SD2003 mechanism overpredicts the flame speed, as for methane- and ethane-air flames. GRI-Mech 3.0 was not developed to simulate ethylene combustion and exhibits the largest variance with experiment. This overprediction of GRI-Mech 3.0 for ethylene-air flames was shown previously by Egolfopoulos & Dimotakis (2001). The large variance between experiment and predictions of the C_3-Davis model is notable, as this mechanism was developed to model C_1, C_2, and C_3 hydrocarbon flames. The C_3-Davis mechanism is found to be in accord with experiment only for stoichiometric conditions. In the work of Hirasawa *et al.* (2002), the laminar flame speeds of ethylene-air flames were measured and compared to the predictions of a mechanism that was composed of the C_3-Davis kinetics and additional reactions for modeling butane combustion. These authors report generally good agreement for all equivalence ratios, with measured flame speeds for lean flames falling above the predictions and predicted flame speeds for stoichiometric and rich flames generally falling above the data. This is consistent with the results presented here and indicates that while the model may predict flame-speed data to within 5 cm/s, the methodology developed for the experiments presented here makes such deviations much more apparent. The measurements reported here are sensitive to the residual between measured and predicted flame speed, rather than the absolute value, which helps to highlight variances with model predictions. To the author's knowledge, other comparisons of the predictions of these models to flame-speed data are not available. Relative CH concentration measurements exhibit better agreement with the C_3-Davis and GRI-Mech 3.0 mechanisms as compared to the San Diego mechanisms, but the drop-off for lean flames appears to be overpredicted in all cases. These are the only reported relative-concentration measurements of the CH radical in ethylene-air flames known to the author.

5.5 Sensitivity analysis

The influence of each model parameter on the simulation prediction can be determined through sensitivity analysis. The sensitivity coefficients may be calculated as part of the simulation or they may be performed using the "brute-force," or explicit method (*e.g.*, Qin *et al.* 2000; Davis & Wang 2002). The CHEMKIN PREMIX package calculates these sensitivity coefficients as part of the solution for freely propagating laminar flames. In the current study, the sensitivity of specific simulation features to variations in the model parameters must be estimated. Specifically, the location of the CH profile is utilized to compare experimental and simulated results, and the sensitivity of this location to the model parameters is required. To determine the sensitivity of the CH profile location to variations in the model parameters, the "brute-force" method is utilized as suggested by Frenklach (1984). Simulations are performed varying a single parameter at a time, and the profiles of each are compared to the original simulation to determine the effect that each parameter has on the predicted output. To minimize errors due to mesh resolution effects, Goldenberg & Frenklach (1995) suggest using quadratic interpolation to find the location of peak concentrations. Rather than interpolating the data, it was decided to utilize the integral CH location for determining parameter sensitivities. The integral CH location is defined as

$$x_{\mathrm{CH,int}} = \frac{\int_0^\ell x\ \chi_{\mathrm{CH}}(x)\ dx}{\int_0^\ell \chi_{\mathrm{CH}}(x)\ dx}\ , \tag{5.5}$$

where x is the axial coordinate, ℓ is the length of the simulation domain, and $\chi_{\mathrm{CH}}(x)$ is the mole fraction of the CH radical. The calculation of the CH-layer location using an integral alleviates difficulties associated with the mesh refinement and is more robust than simply finding the location of peak CH concentration.

The logarithmic sensitivity coefficient for the integral CH location to each model parameter, $\mathcal{V}_j$, can be calculated using

$$L.S.(x_{\mathrm{CH,int}})_j = \frac{d\log x_{\mathrm{CH,int}}}{d\log \mathcal{V}_j} = \frac{\Delta x_{\mathrm{CH,int}}}{x_{\mathrm{CH,int}}}\,\frac{\mathcal{V}_j}{\Delta\mathcal{V}_j} \tag{5.6}$$

or,

$$L.S.(x_{\mathrm{CH,int}})_j = \frac{x_{\mathrm{CH,int}}(\mathcal{V}_j+\Delta\mathcal{V}_j) - x_{\mathrm{CH,int}}(\mathcal{V}_j)}{x_{\mathrm{CH,int}}(\mathcal{V}_j)}\,\frac{\mathcal{V}_j}{\Delta\mathcal{V}_j}\ . \tag{5.7}$$

To find the values of $x_{\mathrm{CH,int}}(\mathcal{V}_j+\Delta\mathcal{V}_j)$, the rate of each reaction is increased by a factor of 50 % and the simulation is resolved, and post-process to find $x_{\mathrm{CH,int}}$. Previous investigators have increased the reaction rates by a factor of 2 (Qin *et al.* 2000), however, a value of 1.5, as used here, is sufficient to observe changes in the simulation output, and results in faster convergence and prevents drastic changes in the simulation output. Increasing the rates by a factor of 1.5 determines the logarithmic

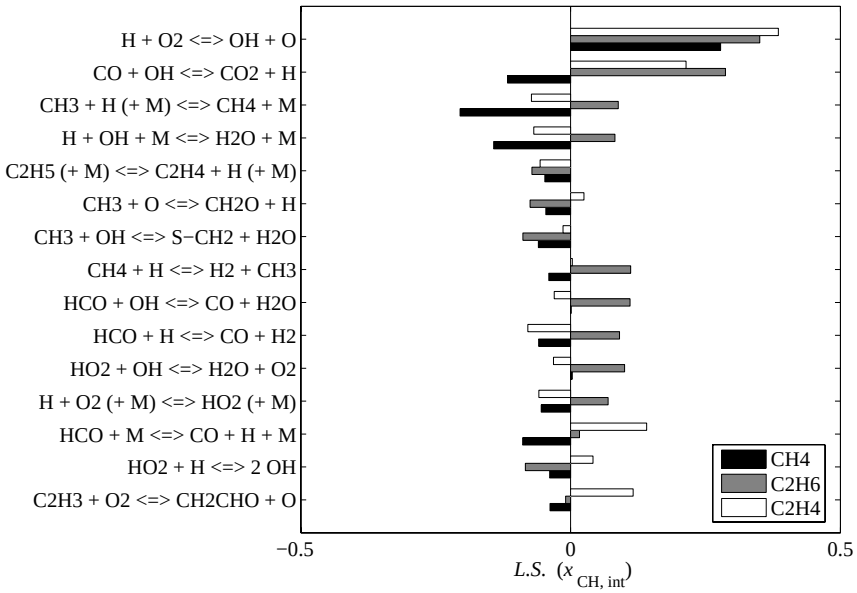

Figure 5.74: Logarithmic sensitivity coefficients of important reactions in stoichiometric methane, ethane, and ethylene flames.

derivative of the variable, $\Delta\mathcal{V}_j/\mathcal{V}_j = 1/2$. A sample "brute-force" sensitivity analysis script is given in Appendix D. Figure 5.74 compares the logarithmic sensitivity coefficients for the most important reactions in stoichiometric methane, ethane, and ethylene flames using the SD2005 mechanism. The main branching reaction H + O_2 → OH + O exerts the largest influence on the flame strength for these hydrocarbon flames. Different reactions are important in the combustion of the three fuels, with some reactions exerting influence only for one of the fuels. In addition, increasing some of the reaction rates increases the flame strength for one fuel, but decreases it for the other fuels. This type of sensitivity analysis can be utilized to find compositions that activate a specific reaction of interest. For example, if the reaction HCO + M → CO + H + M has a high-associated uncertainty, a study of ethylene-air and methane-air flames could be used to evaluate and tune this reaction.

The sensitivity coefficients for the most important reactions in methane-air and ethylene-air flames are given in Figs. 5.75 and 5.76. The relative importance of the various reactions for lean, stoichiometric, and rich flames can be found in this manner. Several of the reactions are only important for lean conditions and such reactions should be investigated to determine if these are responsible for the variance found with experiment. For ethylene, several reactions are only important under rich conditions, while others are only active for lean and stoichiometric flames. These sensitivity analyses indicate the importance of studying flames for a variety of inlet mixture fractions, as the fuel to air ratio is important in determining the relative influence of each reaction. The SD2005 mechanism is made up of 175 individual reactions, here we are comparing 15 of the most important

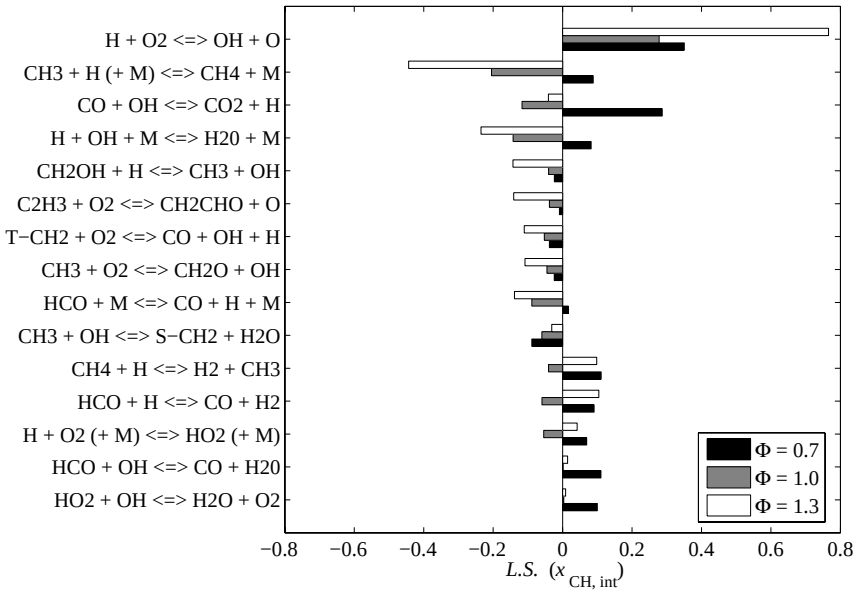

Figure 5.75: Logarithmic sensitivity coefficients of important reactions in methane-air flames.

ones. Even for the 15 reactions presented in these figures, it is difficult to make any conclusions as to why the models may be at variance with experiment. However, by utilizing such sensitivity analyses coupled with a response-surface technique (Frenklach *et al.* 1992), a global optimization could be performed on the reaction mechanism to fit the data. Such an optimization should not be performed on an individual set of experiments, but must make use of as much kinetically independent data as are available. Investigations similar to the one presented here, coupled with studies of ignition delay, flow reactors, etc., could allow the acquisition of a large enough dataset to fully constrain the kinetics models. A global, fully constrained optimization against a large number of experimental targets could result in a predictive mechanism for the combustion of small hydrocarbons.

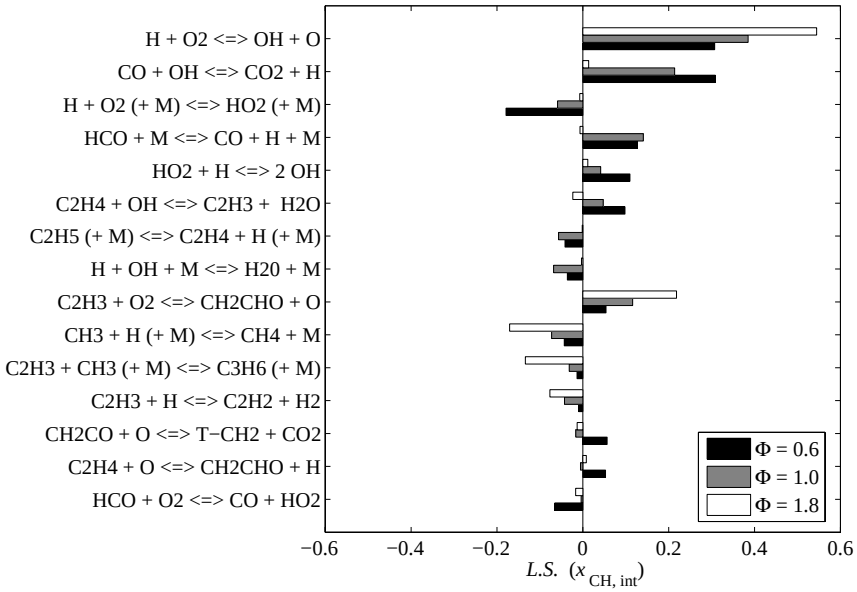

Figure 5.76: Logarithmic sensitivity coefficients of important reactions in ethylene-air flames.

Chapter 6

Conclusions

The goal of the present work is the development of a technique capable of testing chemistry, thermodynamic, and transport models through direct comparison with experiment. The axisymmetric, stagnation-point flame can provide a useful environment for performing such comparisons, because of the sensitivity of the flame location to predicted flame speed and the availability of a one-dimensional hydrodynamic description of the flow. As this model has not been thoroughly validated against experiment, a main goal of the current research is to assess the ability of this hydrodynamic model to capture cold and reacting impinging-jet flows. Subsequently, flames of methane, ethane, and ethylene are studied to assess the relative performance of published kinetics mechanisms.

The impinging laminar jet is important in many contexts, yet almost no experimental measurements have been published, and relatively few theoretical studies have been performed, on this flow. The flowfield of impinging laminar jets was studied through the use of Particle Streak Velocimetry as a function of the nozzle-to-plate separation distance and the Reynolds number. Scaling the centerline axial velocity for an impinging jet by the Bernoulli velocity, calculated from the static pressure drop across the nozzle contraction, collapses centerline axial-velocity data on a single curve that is independent of the nozzle-to-plate separation distance. Axisymmetric viscous calculations performed as part of the Ph.D. research of K. Sone and potential-flow simulations carried out by T.W. Mattner are also included in this report. These axisymmetric viscous and potential-flow simulations allow nozzle-wall proximity effects to be investigated by including the nozzle in the solution domain. Axisymmetric viscous simulations yield good agreement with the current experiments and confirm the velocity-profile scaling. The potential-flow simulations reproduce the collapse of the data; however, at these Reynolds numbers, viscous effects result in disagreement with experiment. One-dimensional streamfunction simulations can predict the flow in the stagnation region if the boundary conditions are correctly specified, although the fundamental assumption of a constant radial-pressure eigenvalue is found to be incorrect from the direct numerical simulations. The velocity boundary conditions must be specified from the local velocity and velocity gradient at an interior point of the flow. The scaled axial velocity profiles are well-characterized by an error function with

one Reynolds-number-dependent parameter. The error function provides a good fit to both experimental and viscous-simulation data. Viscous effects are captured by scaling the axial distance by the effective displacement-thickness-corrected diameter. This scaling relies on thin nozzle boundary layers and negligible viscous losses through the nozzle. These scalings allow the specification of an analytic expression for the velocity profile of an impinging laminar jet over the Reynolds number range of $200 \leq Re \leq 1400$.

The study of laminar flames reveals that the one-dimensional streamfunction model can capture the experimental flow if the boundary conditions are appropriately specifed and the predicted flame speed accurately matches that in the experiment. The inlet velocity boundary conditions can be calculated from a parabolic fit to the cold-flow data, exploiting the inviscid, constant-density solution to the streamfunction equation. The flowfield of reacting impinging jets is also found to be independent of the nozzle-to-plate separation distance, with the Bernoulli velocity determining the flame position and resulting velocity field. By diluting a strong-burning flame with excess nitrogen, the flame strength decreases and the flame is found to move towards the stagnation plate. At constant Bernoulli velocity, the strain rate is found to be consistent both in the cold and hot stagnation flows, with the hot stagnation flows collapsing onto each other. The cold stagnation flows are shifted spatially due to the movement of the flame. This also indicates that the strain field experienced by the flame is well-characterized by the Bernoulli velocity, which is essentially a measure of the jet momentum. The simulations exhibit similar agreement with experiment for variable dilution, and variable resulting flame temperatures, indicating that radiation effects are not responsible for the discrepancies observed in the hot region of the flow. Flames are also studied at variable imposed strain rates at several stoichiometries for each fuel. The simulations tend to predict similar agreement for the range of strain rates that can be supported in this experimental setup. As the flames extinguish largely due to heat loss to the plate, the range of strain rates that can be imposed is less than that for opposed jet flows where twin flames result in a nearly adiabatic flow. However, the improved stability associated with jet-wall flows and the improved accuracy in determining the stagnation-point boundary conditions favor the current implementation.

The approach and diagnostics devloped as part of this research permit an assessment of the numerical simulation predictions of strained flames for low-carbon-number hydrocarbons. GRI-Mech 3.0 is found to give good agreement with experiment for methane- and ethane-air flames, slightly overpredicting the flame speed, and is at variance with experiment for ethylene-air flames. A C_3 mechanism by Davis *et al.* is found to give reasonable agreement for stoichiometric and rich flames, but consistently underpredicts lean flame speeds. The 2005 revision of the San Diego mechanism is found to give the best agreement with experiment for methane, ethane and ethylene flames, while the 2003 version overpredicts the flame speed for all cases studied. The 2005 revision of the mechanism changed several reaction rates to improve burning velocity agreement, resulting in

improved agreement with our results. Specifically, the rates of the H + OH + M → H_2O + M and HO_2 + H → OH + OH reactions were adjusted, and changes were made to the C_3 chemistry.

In the technique reported here, the results are most sensitive to the flame speed predicted by the combustion model at the imposed strain rate. If the predicted flame speed is higher than that measured experimentally, the minimum of the predicted velocity profile will lie above the PSV data, the predicted CH location will be upstream of the PLIF data, and the maximum of the modeled-PSV profile will lie above the PSV data. Discrepancies between predicted and measured flame speeds are amplified by the density drop through the flame. The numerical predictions are quite sensitive to the inlet mixture composition, or the stoichiometry of the flame, for lean and rich conditions. The mass flowrates of all species must be accurately measured, using high-quality mass flowmeters and frequent calibration with the actual gas being metered. In the current experiments, accurate measurement of all boundary conditions results in a total experimental uncertainty that corresponds to approximately one half of the stoichiometric CH layer thickness. This technique can highlight deficiencies in the model performance that may be obscured in laminar flame-speed techniques. The current measurements are sensitive to the residual between the measured and predicted flame speed, rather than the absolute value, which helps to highlight deficiencies in the model predictions. Such discrepancies may be obscured when comparing predicted and measured laminar flame speeds because of the large variation in flame speed as the stoichiometry is varied.

The variation in flame thickness as a function of stoichiometry is consistent between all of the mechanisms studied here, and the trend is reproduced by the experimental diagnostics when the off-line subtraction methodology is employed. The relative concentration measurements in methane reported here are consistent with the measurements of Sutton & Driscoll (2003), the only other application of this relative fluorescence technique. These measurements indicate the necessity for performing appropriate off-line correction when estimating relative CH concentrations. For methane, ethane, and ethylene, predicted relative concentration profiles show a stronger drop-off with changing stoichiometry than observed in the PLIF data.

Overall, the results presented here indicate that further kinetic model evaluation and optimization is required to describe the combustion of C_1–C_2 hydrocarbons. Models that give good agreement with experiment predict the correct strained flame speed for the specified mixture. Discrepancies between experiment and model predictions that lie outside of the uncertainty bounds are attributed to over or under prediction of the flame speed. The results presented in this thesis are made available to kineticists looking for optimization targets (see Appendix L), with the goal of developing a fully constrained, predictive, kinetics model for hydrocarbon fuels. The methodology described here can also allow new optimization targets to be rapidly measured, reducing the experimental burden required to fully constrain the chemistry models.

Appendix A

Particle velocimetry in spatially varying fields

Velocity measurements in fluid systems typically rely on particle techniques. Examples of particle tracking methods are Particle Streak Velocimetry (PSV), Particle Image Velocimetry (PIV), and Particle Tracking Velocimetry (PTV) (see Appendix B & Adrian 1991). These particle tracking techniques rely on measuring the spatial displacement of a particle over a fixed time interval. Another velocity measurement technique, Laser Doppler Velocimetry (LDV), measures the time required to traverse a fixed number of (virtual) fringes in space. LDV utilizes a fixed spatial displacement and measures the time for a particle to traverse that distance. Most implementations of particle tracking techniques assume that the particle velocity is equal to the fluid velocity. However, due to particle-inertia, thermophoretic, and other effects, this assumption may not be valid. In reacting flows, large spatial gradients and curvature exist in the fields of velocity, density, and temperature. Premixed stagnation flames are characterized by two stagnation flows joined through a region of high acceleration owing to the flame-heat-release-induced dilatation. Large temperature gradients exist within the flame front and the wall thermal-viscous boundary layer. In such flows, several difficulties arise in performing particle velocimetry techniques. The particle may lag the flow due to its inertia in regions of high velocity gradient. Large temperature gradients can result in the particle feeling a thermophoretic force in the direction opposite the temperature gradient. In addition, the finite time base utilized in particle tracking techniques can act as a low-pass filter in flows with large velocity curvature.

As particle techniques are ubiquitous in the measurement of velocity fields, errors attributable to particle inertia effects have been widely studied. Gilbert *et al.* (1955) investigated the velocity lag of particles through the reaction zone of a laminar flame. These authors solved the equation of particle motion with the Stokes drag term as the only force, in the case of a linearly varying flowfield. They found that even for small particles, the lag in the reaction zone is appreciable. Haghgooie *et al.* (1986) investigated LDV techniques in turbulent flows and found that particles of 1 or 2 microns in

diameter should adequately follow velocity fluctuations in the flow up to 10 or 2 kHz respectively. These authors also noted that while the flow was seeded with alumina particles with a nominal size of one micron, their LDV setup was not sensitive to these small particles and measurements were recorded only for (agglomerated) particles larger than 5 microns. This indicates that care must be taken when utilizing LDV techniques to verify the minimum particle size that yields valid measurements. Unfortunately, all particles larger than this minimum size will produce valid (larger) Doppler bursts that will dominate the overall signal. Samimy & Lele (1991) studied the behavior of particles in a compressible shear layer, and recommend that the Stokes time [see Eq. (A.24)] be kept below 0.05 for accurate flow visualizations. Melling (1997) discusses tracer particles and seeding for PIV and finds that a maximum particle size of 1 micron is required to achieve a frequency response of 10 kHz, in accord with the findings of Haghgooie *et al.* (1986).

In combustion, additional considerations arise because of large temperature variations in the flow. The high spatial gradients of temperature result in a thermophoretic force that influences the particle motion as it travels through the reaction zone. One can view this thermophoretic (or thermomechanical) force as resulting from the momentum difference between the faster molecules striking the hot side of the particle and the slower molecules colliding with the cold side of the particle. This momentum difference results in a net force that drives the particle away from the higher temperature region of the flow. Sung *et al.* (1994) studied thermophoretic effects on seeding particles in LDV measurements of counterflow premixed flames. They found significant lag between the fluid and particle velocities in the preheat zone of the flame. In a subsequent study, Sung *et al.* (1996a) studied lean methane-air flames and compared measured velocity profiles, using LDV, to simulated velocity profiles. These authors noted discrepancies between measurement and simulation in the reaction zone and in the region of the velocity maximum (high-temperature zone). They also compared their measurements to a velocity profile corrected for the effects of particle inertia and thermophoresis. The corrections bring the simulated and experimental profiles closer together, although the corrected profiles still lie above the experimental measurements in the region of maximum velocity. Egolfopoulos & Campbell (1999) studied dusty reacting flows numerically with thermal coupling between the gas and solid phases. They found that thermophoresis was significant for small particles in regions of large temperature gradients, as one would expect. Gravitational effects were found to be small for particles smaller than 5 microns. Stella *et al.* (2001) investigated the application of PIV to combusting flows. They found that thermophoretic effects were significant for micron-sized particles, but noted that the main effect was a shift between the particle and fluid velocity profiles. These authors also discuss several other important sources of error that need to be considered when investigating turbulent reacting flows. Specifically, non-homogeneity and time-dependence of the refractive-index field was investigated as a source of light-sheet deflection, or "beam steering," as well as image distortion. These authors find that at the laboratory scale, the uncertainty associated

with the beam steering effect can be neglected. The image distortion effect is only experienced in flames with time-dependent index-of-refraction fields, and thus can be neglected in studies of steady laminar flames, such as those reported here.

A.1 Particle motion in spatially varying flowfields

The equation of motion for a particle in one dimension can be expressed using Newton's second law as

$$\Sigma F = m_{\rm p}\, a_{\rm p} = m_{\rm p} \frac{{\rm d}u_{\rm p}}{{\rm d}t} \ , \tag{A.1}$$

where ΣF is the sum of the forces acting on the particle, $m_{\rm p} = 4/3\pi(d_{\rm p}/2)^3\rho_{\rm p}$ is the mass for a spherical particle, $d_{\rm p}$ is the particle diameter, $\rho_{\rm p}$ is the density of the particle, $a_{\rm p}$ is the particle acceleration, and $u_{\rm p}$ is the particle velocity. The most important forces that act on a particle in a typical flow are

$$\Sigma F = F_{\rm PG} + F_{\rm FI} + F_{\rm UD} + F_{\rm G} + F_{\rm SD} + F_{\rm TP} \ , \tag{A.2}$$

where

$$F_{\rm PG} = \frac{\rho_{\rm f}}{\rho_{\rm p}} m_{\rm p} \frac{{\rm d}u_{\rm f}}{{\rm d}t} \tag{A.3}$$

is the pressure-gradient force,

$$F_{\rm FI} = -\frac{1}{2}\frac{\rho_{\rm f}}{\rho_{\rm p}} m_{\rm p} \frac{{\rm d}(u_{\rm p} - u_{\rm f})}{{\rm d}t} \tag{A.4}$$

is the fluid-inertial (or apparent-mass) force,

$$F_{\rm UD} = -\frac{3}{2} d_{\rm p}^2 (\pi\mu\rho_{\rm f})^{1/2} \int_{t_0}^{t} \frac{{\rm d}(u_{\rm p} - u_{\rm f})}{{\rm d}\xi} \frac{{\rm d}\xi}{(t-\xi)^{1/2}} \tag{A.5}$$

is the unsteady-drag force,

$$F_{\rm G} = -m_{\rm p}\, g \tag{A.6}$$

is the graviational force (for a particle traveling upward), $F_{\rm SD}$ is the Stokes-drag force (see Section A.2), and $F_{\rm TP}$ is the thermophoretic force (see Section A.3) (see, for example, Sung *et al.* 1994; Egolfopoulos & Campbell 1999; Stella *et al.* 2001). In these expressions, $\rho_{\rm f}$ and $u_{\rm f}$ are the fluid density and velocity, respectively; μ is the fluid viscosity; and $g = 9.81\,{\rm m/s^2}$ is the gravitational-acceleration constant. For particles in gas-phase flows, the fluid density is typically three orders of magnitude smaller than the particle density, and force terms containing the gas density (pressure-gradient, apparent-mass, and unsteady-drag) are frequently neglected (Sung *et al.* 1994). The gravitational force has been shown to have a small effect for the small particles (≤ 5 microns) used in this study (Egolfopoulos & Campbell 1999). In typical flames, $a_{\rm p} \gg g$, as particles experience accelerations from $a_{\rm p} = 100\,{\rm m/s^2}$ to greater than $a_{\rm p} = 4000\,{\rm m/s^2}$, as compared to $g = 9.81\,{\rm m/s^2}$. For micron-

sized particles in stagnation-point flames, the gravitational force may be neglected. The resulting equation of motion for the particle is

$$m_{\rm p}\frac{{\rm d}u_{\rm p}}{{\rm d}t} = F_{\rm SD} + F_{\rm TP} \ . \tag{A.7}$$

The ability of a particle to accurately track the flow depends on its mass (or inertia) and the local Stokes-drag and thermophoretic forces on the particle.

A.2 Stokes drag

The drag force exerted on a particle in low Reynolds number flow was first described by Stokes in 1851 (see White 1991; p. 177). The Stokes drag is

$$F_{\rm SD} = -3\pi\mu\, d_{\rm p}(u_{\rm p} - u_{\rm f}) \ , \tag{A.8}$$

where μ is the fluid viscosity, $d_{\rm p}$ is the particle diameter, and $u_{\rm p}$ and $u_{\rm f}$ are the particle and (local) fluid velocities, respectively. As the viscosity does not depend on fluid density, Stokes drag is also independent of fluid density. Some authors have also introduced a slip-factor to account for rare-gas (Knudsen number) effects (*e.g.*, Allen & Raabe 1985; Sung *et al.* 1994). The modified Stokes drag is given by

$$F'_{\rm SD} = \frac{-3\pi\mu\, d_{\rm p}(u_{\rm p} - u_{\rm f})}{C_{\rm KW}} \ , \tag{A.9}$$

where

$$C_{\rm KW} = 1 + Kn[\alpha + \beta\exp(-\gamma/Kn)] \tag{A.10}$$

is the Knudsen-Weber slip-correction factor, Kn is the Knudsen number, and $\alpha = 1.142$, $\beta = 0.558$, and $\gamma = 0.999$ are empirical (fit) constants (Allen & Raabe 1985). Equation (A.9) with the (A.10) slip-correction factor is also known as the Millikan drag formula (Talbot *et al.* 1980), and appears to be a good representation for the available data (*e.g.*, Allen & Raabe 1985). The Knudsen number is defined as the ratio of the mean-free path, λ, to the length scale of the flow, $r_{\rm p} = d_{\rm p}/2$ (particle radius), *i.e.*, $Kn = 2\lambda/d_{\rm p}$ (*e.g.*, Talbot *et al.* 1980; Allen & Raabe 1985). In this study, we will follow Talbot *et al.* (1980) and utilize the viscosity-based value for the mean-free path (*e.g.*, Vincenti & Kruger 1965):

$$\lambda = \frac{2\,\mu}{\rho_{\rm f}\,\overline{c}} \ , \tag{A.11}$$

where $\rho_{\rm f}$ is the fluid density and

$$\overline{c} = \sqrt{\frac{8\,\mathcal{R}_{\rm g}\,T}{\pi}} \tag{A.12}$$

is the mean molecular speed of the gas mixture (Talbot *et al.* 1980). In this expression, T is the fluid temperature, $\mathcal{R}_\mathrm{g} = \mathcal{R}_\mathrm{u}/\overline{\mathcal{M}}$ is the specific gas constant, $\mathcal{R}_\mathrm{u} = 8314$ J/(kmol K) is the universal gas constant, and $\overline{\mathcal{M}}$ is the mean molar mass of the gas mixture. For a gas mixture with K species, the mean molar mass is given by

$$\overline{\mathcal{M}} = \sum_{\mathrm{k}=1}^{\mathrm{K}} \chi_\mathrm{k}\, \mathcal{M}_\mathrm{k} \ , \tag{A.13}$$

where the $\mathcal{M}_\mathrm{k}$ are the single-component molar masses and χ_k is the mole-fraction of the kth species. In the work of Egolfopoulos & Campbell (1999), a reduced molecular mass was used to calculate the mean molecular speed,

$$\overline{c}_\mathrm{EC} = \sqrt{\frac{8\, k_\mathrm{B}\, T}{\pi\, m_\mathrm{R}}} \ , \tag{A.14}$$

where k_B is the Boltzmann constant and the reduced molecular mass, m_R, is given by

$$\frac{1}{m_\mathrm{R}} = \sum_{\mathrm{k}=1}^{\mathrm{K}} \frac{1}{m_\mathrm{k}} \ , \tag{A.15}$$

where m_k is the molecular mass of species k. It is not clear why a reduced mass should be utilized in place of the mean mass for the molecular speed (mean-free path) calculation. Most authors do not provide details on how they calculated the mean molecular speed. In this work we utilize the mean molar mass [Eq. (A.13)] to calculate the mean molecular speed and resulting mean-free path.

A particle in a flow with a linear velocity gradient will have an acceleration of

$$\frac{\mathrm{d}u_\mathrm{p}}{\mathrm{d}t} = \frac{\mathrm{d}u_\mathrm{p}}{\mathrm{d}x_\mathrm{p}} \frac{\mathrm{d}x_\mathrm{p}}{\mathrm{d}t} \tag{A.16}$$

$$\frac{\mathrm{d}u_\mathrm{p}}{\mathrm{d}t} \cong \frac{\mathrm{d}u_\mathrm{f}}{\mathrm{d}x} u_\mathrm{p} \tag{A.17}$$

$$a_\mathrm{p} \cong \sigma\, u_\mathrm{p} \ , \tag{A.18}$$

where $x_\mathrm{p}(t)$ is the particle position and $\sigma = \mathrm{d}u_\mathrm{f}/\mathrm{d}x$ is the fluid velocity gradient.

In cold regions of the flow, the Stokes drag is the only active force. Thus, for a particle in a flow with a constant velocity gradient, the ratio of particle to fluid velocity can be estimated as

$$m_\mathrm{p}\, a_\mathrm{p} = F_\mathrm{SD} \tag{A.19}$$

$$m_\mathrm{p}\, a_\mathrm{p} = \frac{-3\pi\mu\, d_\mathrm{p}(u_\mathrm{p} - u_\mathrm{f})}{C_\mathrm{KW}} \tag{A.20}$$

$$\frac{4}{3}\pi \left(\frac{d_\mathrm{p}}{2}\right)^3 \rho_\mathrm{p}\, a_\mathrm{p} = \frac{-3\pi\mu\, d_\mathrm{p}(u_\mathrm{p} - u_\mathrm{f})}{C_\mathrm{KW}} \tag{A.21}$$

$$-\frac{\rho_\mathrm{p} d_\mathrm{p}^2}{18\,\mu}\, C_\mathrm{KW}\, \sigma\, u_\mathrm{p} = (u_\mathrm{p} - u_\mathrm{f}) \tag{A.22}$$

$$\frac{u_\mathrm{p}}{u_\mathrm{f}} = \frac{1}{1 + C_\mathrm{KW}\, \tau_\mathrm{S}\, \sigma} \ , \tag{A.23}$$

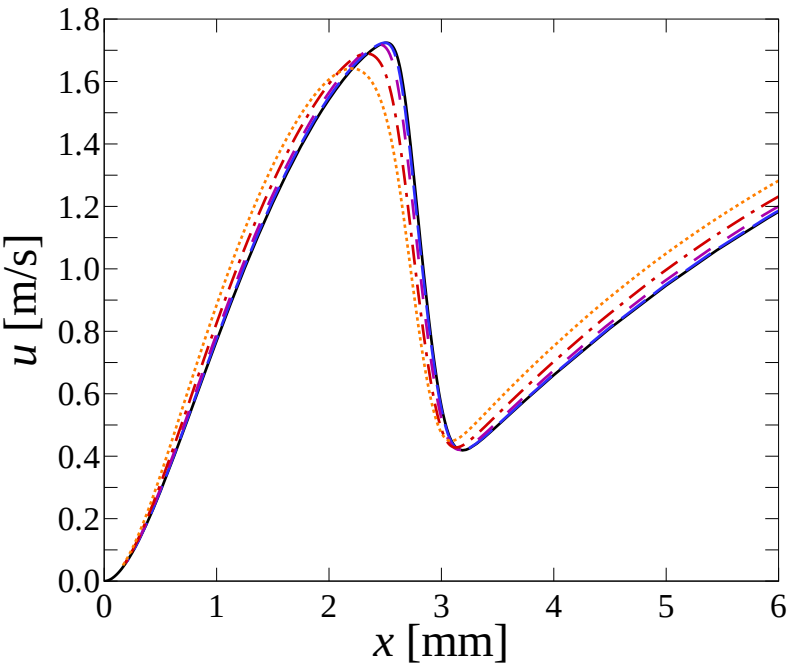

Figure A.1: Particle size effects considering Stokes drag force only. Fluid velocity profile shown as black solid line. Particle velocity profiles are included for: $d_\mathrm{p} = 1\,\mu$m alumina (Al_2O_3) particle (blue long dash), and for ceramic microspheres of size $d_\mathrm{p} = 3$, 5, and $7\,\mu$m (purple dash, red dash-dot, orange dot, respectively).

where

$$\tau_\mathrm{S} \equiv \frac{\rho_\mathrm{p} d_\mathrm{p}^2}{18\,\mu} \tag{A.24}$$

is the Stokes time for the particle. For a particle decelerating in a stagnation flow, $\sigma < 0$, and thus the particle velocity is larger than that of the fluid. Good particle tracking requires $C_\mathrm{KW}\,\tau_\mathrm{S}\,\sigma \ll 1$, for which the first-order estimate of the percent difference between the particle and fluid velocities is $100 \times C_\mathrm{KW}\,\tau_\mathrm{S}\,\sigma\,\%$. From a measured (particle) velocity and velocity gradient at any point in the flow, it is possible to calculate the fluid velocity using Eq. (A.23). It should be noted that the velocity lag has a d_p^2 dependence on increasing particle size. Figure A.1 shows the velocity profile for a particle in a near-stoichiometric $\Phi = 0.9$ methane-air flame, for three different representative particles. In this figure, the Stokes drag was the only force included, and the initial particle velocity and acceleration were calculated using Eqs. (A.23) and (A.18), respectively.

A.3 Thermophoretic force

The thermophoretic force, or thermophoresis, results when a particle travels through a region of high-temperature gradient, as occurs in a premixed flame front where temperature gradients can reach 10^6 K/m. The molecules on the high-temperature side of the particle are more energetic

than those on the low-temperature side, resulting in a net force in the direction of decreasing temperature. Thermophoresis is analogous to the Soret transport mechanism, where the diffusion of large-molecular-mass species results in a direction opposite the temperature gradient. The CANTERA package includes a multi-component transport formulation that accounts for the Soret effect. Several theories have been proposed to model the thermophoretic force. However, due to the difficulty in measuring the effect and the limited experimental data with which to validate theory, data and theories remain controversial (*e.g.*, Loyalka 1992; Santachiara *et al.* 2002).

The theory for the free-molecule limit, $Kn \gg 1$, was developed by Waldmann. In this regime, the thermophoretic force can be expressed as (*e.g.*, Talbot *et al.* 1980; Zheng 2002)

$$F_{\mathrm{TP,FM}} = -\frac{8}{15} d_{\mathrm{p}}^2 \frac{\kappa_{\mathrm{tr}}}{\overline{c}} \nabla T \ , \tag{A.25}$$

where κ_{tr} is the translational part of the thermal conductivity (Talbot *et al.* 1980; Zheng 2002),

$$\kappa_{\mathrm{tr}} = \frac{15}{4} \mathcal{R}_{\mathrm{g}} \mu \ . \tag{A.26}$$

Using this expression for the thermal conductivity, Eq. (A.25) may be rewritten in terms of bulk gas quantities,

$$F_{\mathrm{TP,FM}} = -\pi \, \mu \, \nu \, \frac{d_{\mathrm{p}}^2}{2\lambda} \frac{\nabla T}{T} = -\frac{\pi \, \mu \, \nu \, d_{\mathrm{p}}}{Kn} \frac{\nabla T}{T} \ , \tag{A.27}$$

where $\nu = \mu/\rho_{\mathrm{f}}$ is the gas kinematic viscosity, $\lambda = 2\,\mu/\rho_{\mathrm{f}}\,\overline{c}$ is the mean-free path, $\overline{c} = \sqrt{8\mathcal{R}_{\mathrm{g}}T/\pi}$ is the mean molecular speed of the gas, and $Kn = 2\lambda/d_{\mathrm{p}}$ is the Knudsen number (Talbot *et al.* 1980). Waldmann's equation is found to give good agreement with experimental results (Zheng 2002). In the free-molecule limit, the thermophoretic force increases inversely with Knudsen number, tending to zero as the mean-free path becomes much larger than the particle size, *i.e.*, $Kn \to \infty$. We note, however, that Waldmann's equation diverges in the continuum limit, $Kn \to 0$.

In the near-continuum (or slip-flow) limit, $Kn < 1$, Brock (1962) derived an expression for the thermophoretic force using a hydrodynamic analysis with appropriate slip boundary conditions. In this (slip-flow) regime, the thermophoretic force can be given as

$$F_{\mathrm{TP,T}} = -\frac{6\,\pi\,\mu\,\nu\,d_{\mathrm{p}}\,C_{\mathrm{s}}\,(\kappa_{\mathrm{f}}/\kappa_{\mathrm{p}} + C_{\mathrm{t}}Kn)}{(1+3\,C_{\mathrm{m}}Kn)\,(1+2\,\kappa_{\mathrm{f}}/\kappa_{\mathrm{p}} + 2\,C_{\mathrm{t}}Kn)} \frac{\nabla T}{T} \ , \tag{A.28}$$

where κ_{f} and κ_{p} are the fluid and particle thermal conductivities, and C_{s}, C_{m}, and C_{t} are the thermal slip, momentum exchange, and thermal exchange coefficients specified by the kinetic theory of gases (Talbot 1980; Talbot *et al.* 1980). In the case of polyatomic gases, one should use the translational component of the thermal conductivity, $\kappa_{\mathrm{f}} = \kappa_{\mathrm{tr}}$ [see Eq. (A.26)]. In the original analysis by Brock (1962), a value of $C_{\mathrm{s}} = 3/4$ was used and yielded poor agreement with experiment

(Talbot *et al.* 1980). Talbot *et al.* (1980) postulated that Eq. (A.28) can be utilized as a "fitting formula" throughout the entire range of Knudsen numbers, and suggest $C_{\rm s} = 1.17$, $C_{\rm m} = 1.14$, and $C_{\rm t} = 2.18$ as the best values from kinetic theory. In the free-molecular limit, $Kn \rightarrow \infty$, this expression [Eq. (A.28)] reduces to

$$F_{\rm TP,T} = \frac{-6\,\pi\,\mu\,\nu\,d_{\rm p}\,C_{\rm s}\,(C_{\rm t}Kn)}{(3\,C_{\rm m}Kn)\,(2\,C_{\rm t}Kn)}\frac{\nabla T}{T} = \frac{C_{\rm s}}{C_{\rm m}}\,F_{\rm TP,FM} \tag{A.29}$$

[see Eq. (A.27)]. As $C_{\rm s}/C_{\rm m} = 1.03$, this result is also in close agreement with the Waldmann result (Talbot *et al.* 1980). The fact that the Brock formulation reduces to the Waldmann result in the free-molecular limit is fortuitous but provides justification for utilizing it as an interpolation formula over the entire Knudsen-number range. Talbot *et al.* (1980) found that the modified Brock theory gave the best agreement with their experimental results for low Knudsen number, with the above values of $C_{\rm s}$, $C_{\rm m}$, and $C_{\rm t}$.

A "rival" theory to the Talbot fitting-formula is that by Derjaguin & Yalamov (1965, 1966a,b). These authors utilized an application of irreversible thermodynamics and found a result that is similar to that given by Eq. (A.28), with $C_{\rm s} = 1.5$ and the factor $(1 + 3\,C_{\rm m}\,Kn)$ omitted. The corrected Derjaguin & Yalamov (1966b) formula was found to agree with the experimental data of Derjaguin *et al.* (1976) if the constant is revised to $C_{\rm s} = 1.1$, while that of Brock (1962) substantially underpredicted the thermophoretic velocities. Their formulation is expressed as the thermophoretic velocity, rather than thermophoretic force. Ignoring inertial effects, the thermophoretic velocity is the difference between the particle and the fluid velocities, $U_{\rm TP} = u_{\rm p} - u_{\rm f}$, induced by the temperature gradient. Thus, the thermophoretic force can be obtained from the thermophoretic velocity,

$$F_{\rm TP,DY} = -F_{\rm SD} \tag{A.30}$$

$$F_{\rm TP,DY} = \frac{3\,\pi\,\mu\,d_{\rm p}}{C_{\rm KW}}\,U_{\rm TP} \tag{A.31}$$

$$F_{\rm TP,DY} = \frac{3\,\pi\,\mu\,d_{\rm p}}{C_{\rm KW}}\,\frac{-2.2\,\nu\,(\kappa_{\rm f}/\kappa_{\rm p} + C_{\rm t}Kn)}{(1 + 2\,\kappa_{\rm f}/\kappa_{\rm p} + 2\,C_{\rm t}Kn)}\,\frac{\nabla T}{T} \tag{A.32}$$

$$F_{\rm TP,DY} = -\frac{6.6\,\pi\,\mu\,\nu\,d_{\rm p}\,(\kappa_{\rm f}/\kappa_{\rm p} + C_{\rm t}Kn)}{C_{\rm KW}(1 + 2\,\kappa_{\rm f}/\kappa_{\rm p} + 2\,C_{\rm t}Kn)}\,\frac{\nabla T}{T}\ . \tag{A.33}$$

These authors are critical of the work of Brock and other previous investigators (without justification, according to Talbot 1980). Talbot (1980) disagrees with their (implied) use of the Bassett drag formula, which is inaccurate for the moderate values of Knudsen number of interest here. Here we utilized the Millikan drag formula as suggest by Talbot (1980) when converting their thermophoretic velocity into a force. In addition, Talbot (1980) shows that the thermophoretic velocity data of Derjaguin *et al.* (1976) limit to a value above the Waldmann result, while their theory (with $C_{\rm s}$ adjusted to 1.1 to better fit the data) predicts forces twice the Waldmann limit, as $Kn \rightarrow \infty$. These

are perhaps indications of difficulties in the formulation of Derjaguin & Yalamov (1965, 1966b).

In the review article by Zheng (2002), he reports that the majority of reliable experimental measurements (*e.g.*, Li & Davis 1995a), for particles of high thermal conductivity (such as the ceramic particles typically used as tracers in combustion experiments) are bracketed from above by Eq. (A.28) and from below by several different solutions to the linearized Boltzmann equations (*e.g.*, Loyalka 1992) for $0.1 < Kn < 10$. However, Toda *et al.* (1996, 1998) recently found that the Talbot *et al.* (1980) formula underpredicted their experimentally measured thermophoretic velocities by a factor of 5 for large particles ($d_\mathrm{p} = 20\,\mu\mathrm{m}$) and by a factor of 3 for smaller particles ($d_\mathrm{p} = 2.7\,\mu\mathrm{m}$). These experiments were performed in a microgravity environment (thus eliminating thermal-buoyancy-induced flow) and the methodology appears to be sound, so the reason for this disagreement is unclear. Santachiara *et al.* (2002) found that the Talbot *et al.* (1980) formula gave reasonable agreement for particles with high thermal conductivity but overpredicted results for particles with low thermal conductivity. These authors suggested a best-fit formula for the thermophoretic velocity of particles of variable thermal conductivity, which can be converted into a thermophoretic force using the Stokes drag [see Eq. (A.30)],

$$F_\mathrm{TP,S} = \frac{3\,\pi\,\mu\,d_\mathrm{p}}{C_\mathrm{KW}}\,U_\mathrm{TP} \tag{A.34}$$

$$F_\mathrm{TP,S} = -\frac{3\,\pi\,\mu\,d_\mathrm{p}}{C_\mathrm{KW}}\,\left[0.781\,\nu\exp\left(-0.144/Kn\right)\right]\frac{\nabla T}{T} \tag{A.35}$$

$$F_\mathrm{TP,S} = -\frac{2.343\,\pi\,\mu\,\nu\,d_\mathrm{p}}{C_\mathrm{KW}}\,\exp\left(-\frac{0.144}{Kn}\right)\,\frac{\nabla T}{T}\,, \tag{A.36}$$

such that the thermophoretic force is independent of the particle thermal conductivity. This is in disagreement with Li & Davis (1995b), who find that the thermophoretic force is dependent on both the gas and particle thermal conductivities.

These three different formulations appear to be the leading theories in the literature, although all of them could be considered, in some sense, to be empirical fits due to the adjustment of the constants involved. The various solutions to the linearized Boltzmann equation look promising (*e.g.*, Loyalka 1992), although they do appear to underpredict available data and do not allow variations in gas/particle thermal conductivity to be included. Such numerical methods may be useful in discriminating between the various analytic formulations, or may lead to the development of improved theories. The analytic formulations for the thermophoretic force due to Talbot *et al.*, Derjaguin & Yalamov, and Santachiara *et al.*, as well as that of Waldmann, are plotted in Fig. A.2. Here the nondimensionalized thermophoretic force is presented, as all of the theories scale like $F_\mathrm{TP} \propto -\pi\,\mu\,\nu\,d_\mathrm{p}\;\nabla\log(T)$, where $\nabla\log(T) = (\nabla T)/T$. The (Waldmann) free-molecular limit is seen to diverge as the Knudsen number is decreased ($1/Kn$ dependence). This theory is only valid in the limit of $Kn \gg 1$. The theories of Talbot *et al.* and Derjaguin & Yalamov exhibit similar

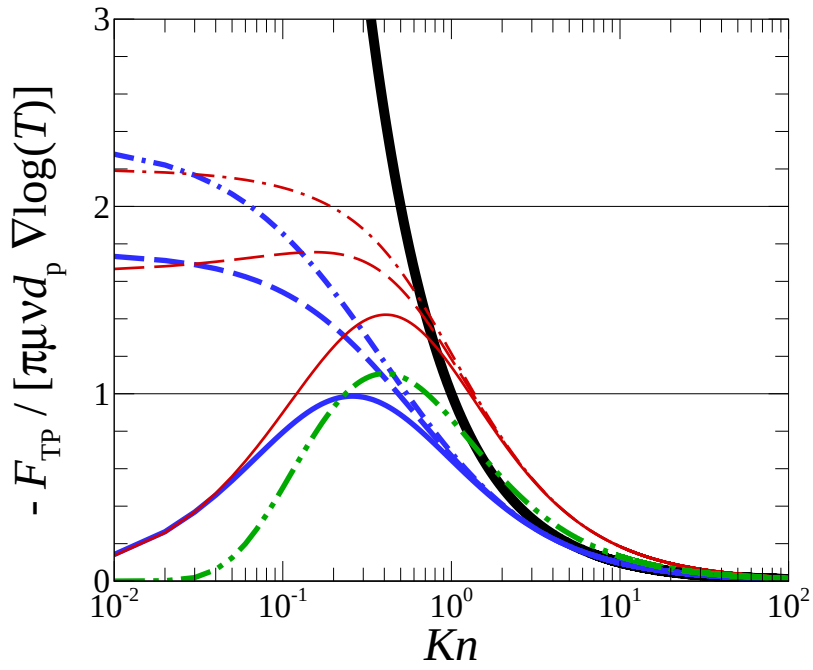

Figure A.2: Scaled thermophoretic forces as a function of Knudsen number. Line colors indicate authors: (thick black line) Waldmann, (medium blue lines) Talbot, (thin red lines) Derjaguin, and (green dash-dot-dot line) Santachiara. For Talbot and Derjaguin relations, line style indicates the ratio κ_f/κ_p: (solid) 0, (dash) 0.5, and (dash-dot) 1.0.

trends, with the Derjaguin & Yalamov formulation typically predicting a higher thermophoretic force. For high-thermal-conductivity particles ($\kappa_f/\kappa_p \ll 1$), the thermophoretic force has a peak between $0.1 < Kn < 1$, while it plateaus for low Knudsen number when conductivities are closely matched ($\kappa_f/\kappa_p \approx 1$). For the alumina particles used in these experiments, $\kappa_f/\kappa_p \lesssim 0.01$, and calculated forces will closely match the curves for $\kappa_f/\kappa_p = 0$. The correlation of Santachiara *et al.* predicts a similar dependence on Kn as the Talbot *et al.* and Derjaguin & Yalamov relations for $\kappa_f/\kappa_p = 0$, although it predicts a much faster drop-off for low Kn.

Typically, the thermophoretic forces are plotted scaled by the Waldmann limit, $F_{TP,FM}$. The three relations are plotted in Fig. A.3, using this scaling and setting $\kappa_f/\kappa_p = 0$. As the Waldmann limit diverges for small Kn, these curves all tend to zero at this limit. The three different formulations presented here all become proportional to the Waldmann limit for large Knudsen numbers, however both the Derjaguin & Yalamov and Santachiara *et al.* expressions asymptote to values above 1. This is perhaps indicative of difficulties in these formulations, although both relations were not designed to be utilized for large Knudsen number. The agreement between the Talbot *et al.* result and the Waldmann limit for large Knudsen number is perhaps fortuitous and is the reason that it was suggested as an appropriate interpolation formula (Talbot *et al.* 1980). Although significant controversy exists in both the published theory and data for the thermophoretic force, all proposals

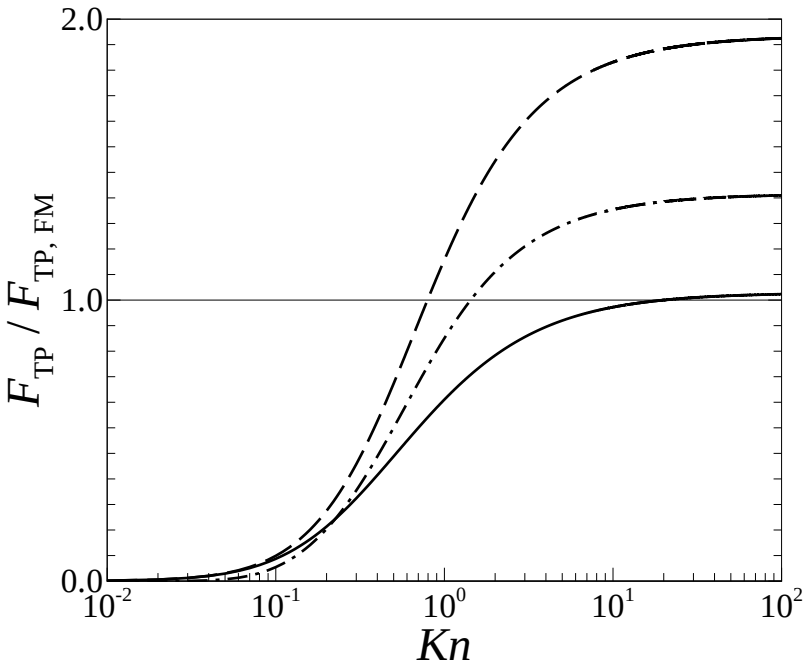

Figure A.3: Thermophoretic forces scaled by the (Waldmann) free-molecular limit for $\kappa_f/\kappa_p = 0$. Line style indicates author: (solid) Talbot *et al.* (1980), (dash) Derjaguin & Yalamov (1965, 1966b), (dash-dot) Santachiara *et al.* (2002).

basically predict similar behavior and vary only in the (constant) scaling factors. Here we will follow previous combustion investigators and utilize the Talbot *et al.* formulation for the estimation of the thermophoretic force (*e.g.*, Sung *et al.* 1994; Egolfopoulos & Campbell 1999). The Talbot interpolation formula seems to provide the most consistent prediction for the thermophoretic force over a wide range of Knudsen numbers. In the results that follow, Eq. (A.28) is utilized to estimate the thermophoretic force, using the translational part of the gas thermal conductivity as given by Eq. (A.26).

In combustion, thermophoresis has been studied by several investigators. Kim & Kim (1991) investigated the deposition of particles in reacting stagnation-point flows and found good agreement between experiment and their numerical results utilizing the formula of Talbot *et al.* (1980), with slightly modified constants C_s, C_m, and C_t. Sung and coworkers studied the effects of thermophoresis on LDV results in premixed and diffusion flames (Sung *et al.* 1994, 1996a). They found improved, but not perfect, agreement between the corrected simulation profiles and the measurements, using the modified Brock (1962) expression for the thermophoretic force by Talbot *et al.* (1980). Sung *et al.* (1994) also noted that particle nonsphericity could play a role in determining thermophoretic properties (*e.g.*, Keh & Ou 2004). However, as the orientation of the spheroids would be random with respect to the temperature gradient, such an effect would most likely result in increased data scatter, rather than a systematic error. In their study of dusty reacting flow, Egolfopoulos &

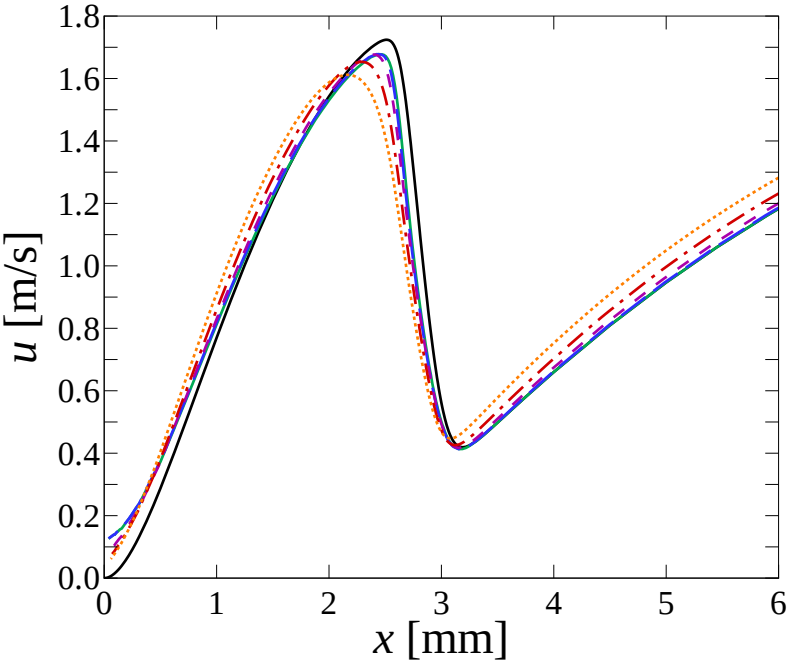

Figure A.4: Particle size effects including both Stokes-drag and thermophoretic forces. Fluid velocity profile included as solid black line. Particle velocity profile for a massless particle is included as solid green line. Particle velocity profiles are included for: $d_{\mathrm{p}} = 1\,\mu$m alumina (Al_2O_3) particle (blue long dash), and for ceramic microspheres of size $d_{\mathrm{p}} = 3$, 5, and $7\,\mu$m (purple dash, red dash-dot, orange dot, respectively).

Campbell (1999) utilized the same thermophoretic expression as Sung *et al.* (1994). However, in calculating the mean-free path of the multi-component mixture, they utilized the reduced molecular mass rather than the mean molecular mass [see Eq. (A.14) & (A.15)].

The thermophoresis of soot particles is also an interesting topic in combustion. Gomez & Rosner (1993) utilized counterflow laminar diffusion flames to study the thermophoresis of small soot aggregates and found the results to be in quantitative agreement with the predictions from kinetic theory in the free-molecule (Waldmann) limit [Eq. (A.25)]. Ono *et al.* (2002) measured thermophoretic velocities of soot particles in microgravity. They found that the thermophoretic velocity did not depend on aggregate soot particle size and matched closely that predicted by the free-molecular limit, in accordance with the results of Gomez & Rosner (1993). Soot aggregates exhibit an open structure, and drift at the same velocity as the individual (small) soot particles.

The particle velocity profiles resulting from the influence of the Stokes drag and thermophoretic forces for several representative particles is depicted in Fig. A.4. The particle profiles in Figs. A.1 and A.4 were calculated by integrating the equation of motion [Eq. (A.7)] in time, evaluating the location, velocity, and acceleration of the particle at each time step. The slip-corrected form of the Stokes drag [Eq. (A.9)] and the Talbot expression for the thermophoretic force [Eq. (A.28)] were utilized in evaluating the particle motion. The temperature, temperature gradient, fluid viscosity, mean

molar mass, and other profiles are interpolated from the CANTERA simulated profiles at the particle location at each time step. The gas translational thermal conductivity is calculated from the viscosity and the mean molar mass according to Eq. (A.26). The thermal conductivity of the aluminum-oxide (Al_2O_3) particles, κ_p, is taken from standard tables (Incropera & De Witt 1990; Table A.2). Due to the small size and high thermal conductivity of the particles, their temperature is assumed equal to the local gas temperature. The initial particle velocity was given by Eq. (A.23) at the inlet to the simulation domain ($x = 0$), using the simulated fluid velocity and velocity gradient values. In the cold-flow region the thermophoretic force does not contribute, and the initial acceleration can be estimated from the Stokes drag to be $a_p\,(t = 0) = -3\pi\,\mu\,d_p(u_p - u_f)/m_p$. Increased lag is evident for the larger particles. A temperature gradient exists between the hot post-flame products and the cooled stagnation surface. The particle velocity profiles do not go to zero in the near-wall region because of the thermophoretic force imposed on the particles in the direction of the wall as they traverse the thermal wall boundary layer.

A.4 Spatial resolution effects in regions of velocity curvature

The velocities measured by a particle tracking technique may not be equal to the fluid velocity, even for cases in which the particle accurately tracks the flow. This is especially true if there are large spatial variations (high-gradient and high-curvature regions) in the velocity field, such as in reacting flow/flame experiments. The following discussion will quantify this effect in one spatial dimension. Using Eq. (A.7), the particle position, velocity, and acceleration can be integrated in time from the initial conditions (stated above) using the simulated fluid properties to determine the local forcing. The resulting parametric description of the particle location, $x_p(t)$, and velocity, $u_p(t)$, as a function of time allows the experimental diagnostic to be modeled.

Particle tracking techniques utilize a fixed time and measure the distance traveled by the particle in that time. Depending on the time interval chosen, this can act as a low-pass filter on measured profiles. Choosing a time interval, τ, allows the particle tracking velocity field, $u_{PSV}\,(x_{PSV})$, to be modeled as

$$u_{PSV}\,(x_{PSV}) = \frac{x_p(t+\tau) - x_p(t)}{\tau}\ , \tag{A.37}$$

where

$$x_{PSV} = \frac{x_p(t+\tau) + x_p(t)}{2} \tag{A.38}$$

is the position at which the particle-tracking velocity estimate is placed, in this case taken as the average location of the start and end of the particle trajectory over the Lagrangian time interval, τ. As the Lagrangian time interval, τ, is made arbitrarily small, $u_{PSV}\,(x_{PSV})$ will converge to $u_p\,(x_p)$. However, for longer Lagrangian times, the particle-tracking velocity will not match the particle

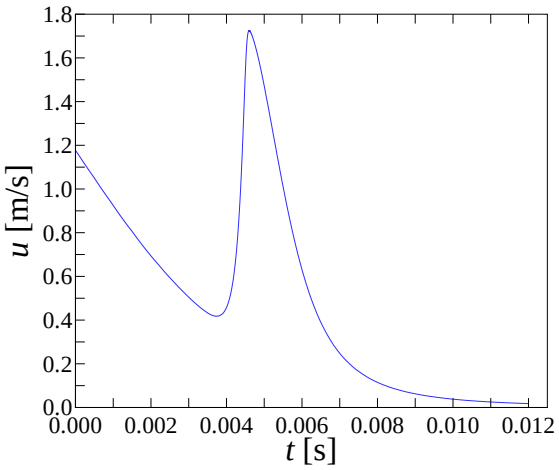

Figure A.5: Particle velocity profile versus time.

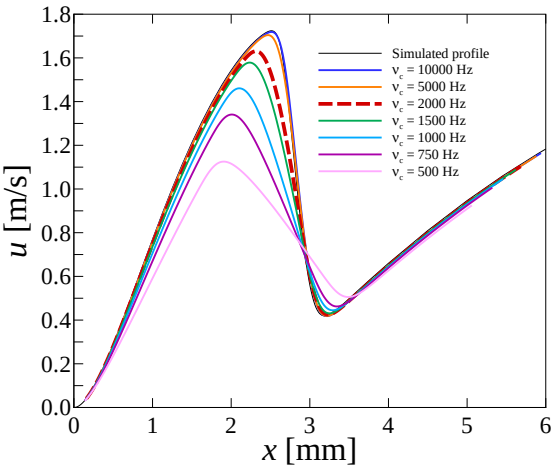

Figure A.6: Modeled-PSV velocity profiles, u_{PSV}, as a function of the chopping frequency.

velocity field due to spatial averaging of the velocity profiles. Unfortunately, it is not possible in practice to make τ arbitrarily small, because the particle displacement, Δx, in the time τ must be sufficient with respect to the spatial resolution of the detector. Typically, one chooses τ to ensure that the minimum velocities of interest can be accurately measured.

To illustrate the effect of finite chopping frequency, a (massless) particle is tracked through the same flame profiles as utilized in Figs. A.1 and A.4, such that the particle velocity as a function of x is identical to the fluid velocity (F_{TP} is set to zero). The velocity profile, for a particle following the flow, as a function of time for this flame is given in Fig. A.5. Various chopping frequencies are applied to this velocity-time profile and yield the results in Fig. A.6. As τ increases, the measured velocity field deviates from the true velocity field in the post-flame region. This region of the flow is characterized by large velocities and large curvature of the velocity field, both of which contribute to the reduced accuracy of the particle technique in this zone. The particle tracking technique acts similarly to a low-pass spatial filter that performs a moving-average of the velocity field over an axial distance proportional to the fluid velocity at that point. Figure A.7 compares the experimental PSV profile to the simulated fluid velocity profile, $u_{\mathrm{f}}\,(x)$, the modeled particle trajectory, $u_{\mathrm{p}}\,(x_{\mathrm{p}})$, and the resulting modeled-PSV velocity profile, $u_{\mathrm{PSV}}\,(x_{\mathrm{PSV}})$, for a 3 micron ceramic microsphere ($\rho_{\mathrm{p}} = 2400\,\mathrm{kg/m^3}$) and a chopping frequency of $\nu_{\mathrm{c}} = 2000\,\mathrm{Hz}$. This example includes the effects of particle inertia, Stokes-drag, thermophoretic forces, and finite chopping frequency. Improved agreement is seen between the modeled and measured velocity profiles in the post-flame region. However, the modeled-PSV profile is still found to lie above the experimental measurements, consistent with the findings of Sung *et al.* (1996a).

In Fig. A.7, the predicted velocity profile lies above the PSV data when particle-inertia, thermophoretic, and finite-chopping-frequency effects are included. To address the source of the remain-

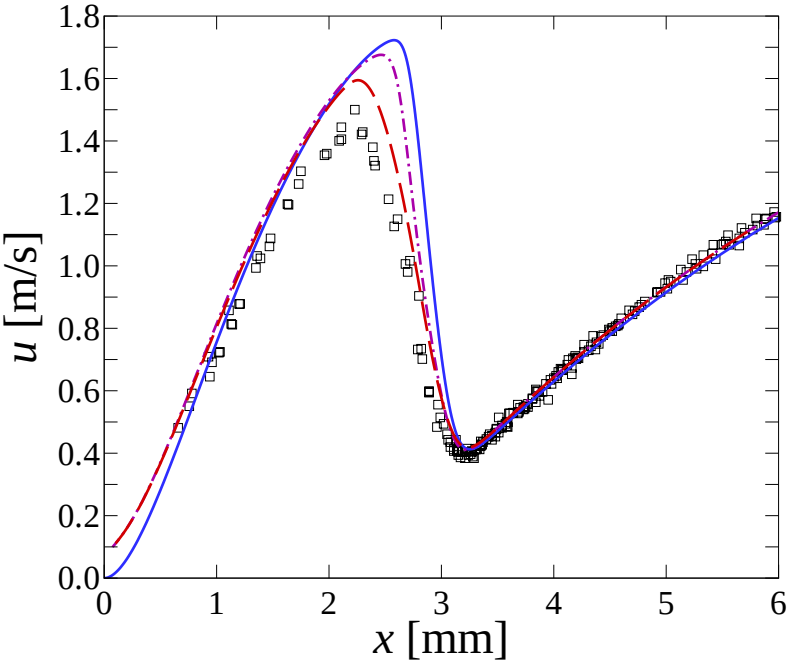

Figure A.7: $\Phi = 0.9$ methane-air flame profiles at $L/d = 1.2$. (□) PSV data, (blue solid line) simulated fluid profile, $u_{\mathrm{f}}(x)$, (purple dash-dot line) modeled particle profile, $u_{\mathrm{p}}(x_{\mathrm{p}})$, (red long-dash line) modeled-PSV profile, $u_{\mathrm{PSV}}(x_{\mathrm{PSV}})$. $d_{\mathrm{p}} = 3\,\mu$m, $\rho_{\mathrm{p}} = 2400\,\mathrm{kg/m^3}$, and $\nu_{\mathrm{c}} = 2000\,$Hz.

ing discrepancy, simulations were performed at increasing levels of nitrogen dilution to artificially lower the predicted flame speed. Figure A.8 presents profiles at varying levels of oxygen content. As the effective oxygen content of the "air" is reduced from 21.0%O_2:(O_2+N_2) to 20.4%O_2:(O_2+N_2), the reference flame speed varies from 0.417 m/s to 0.388 m/s, a change of 7%. These two levels of dilution give values of the reference flame speed both above and below the experimentally measured minimum of 0.399 m/s. The maximum simulated-PSV velocity, for this dilution range, varies from 1.588 m/s to 1.393 m/s, a relative change of 12%. The resulting velocity maxima are seen to span the experimental data. Dilution will reduce the flame speed and the flame temperature simultaneously, making comparison of the diluted profiles and experiment difficult. From Fig. A.8 it is seen that if the predicted flame speed is slightly higher than experiment, a large discrepancy will be evident in the region of the velocity maximum. Velocity differences in the cold-flow region are amplified by the density drop through the flame.

A.5 Summary

To perform detailed comparisons between simulations and experiment, the uncertainty in the diagnostic technique must be estimated. In particle-tracking velocimetry techniques, the particle may not accurately track the fluid velocities due to the combined effects of thermophoresis and particle in-

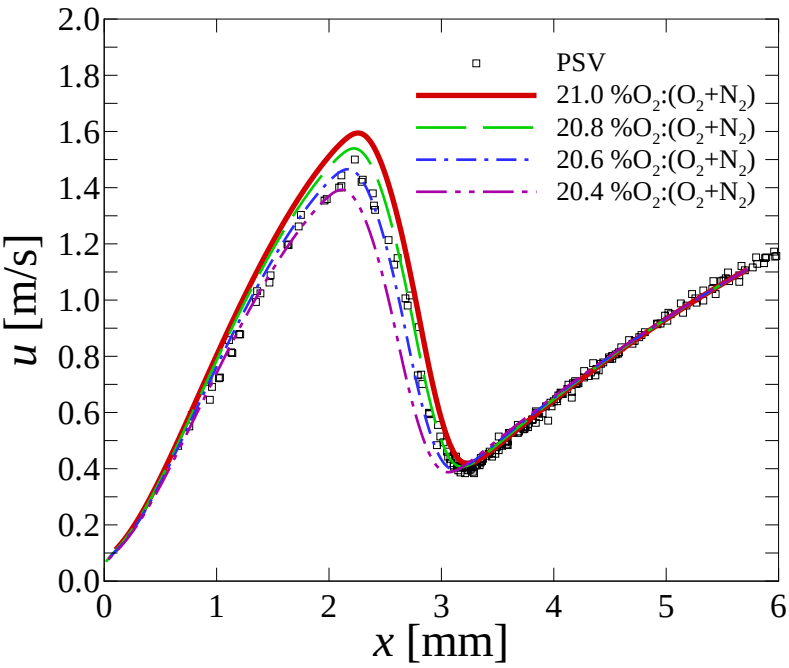

Figure A.8: Modeled-PSV profiles compared to experimental data for a $\Phi = 0.9$ methane-air flame. Simulations are performed for varying levels of nitrogen dilution to artificially adjust the predicted flame speed. $d_\mathrm{p} = 3\,\mu\mathrm{m}$, $\rho_\mathrm{p} = 2400\,\mathrm{kg/m^3}$, and $\nu_\mathrm{c} = 2000\,\mathrm{Hz}$.

ertia. In addition, the finite time interval in particle tracking techniques can act as a spatial low-pass filter. However, these systematic measurement errors and uncertainties can be accounted for using the techniques presented in this Appendix. The motion of a particle through a simulated flowfield is modeled using the equation of motion, Eq. (A.7). A particle is released at the inlet of the simulation domain at $t = 0$, and the particle position, $x_\mathrm{p}(t)$, and velocity, $u_\mathrm{p}(t)$, are solved as a function of time using a Lagrangian technique. By appropriately choosing the initial values of $u_\mathrm{p}(t = 0)$ and $a_\mathrm{p}(t = 0)$, transient effects can be removed. Modeling the particle motion can remove the systematic errors that result from assuming the particle accurately tracks the flow. The resulting description of the particle position as a function of time can be used to model the particle-tracking technique, using Eq. (A.37) and Eq. (A.38) and the experimental particle-track time τ. The modeled-PSV profile, $u_\mathrm{PSV}\,(x_\mathrm{PSV})$, accounts for the systematic errors and uncertainties in the diagnostic and should be used when comparing predictions to experimental data. The implementation presented here is general and may be applied to any modeled flowfield to permit direct comparisons to experimental results.

Appendix B

Particle Streak Velocimetry

Flow velocities in this work are measured using Particle Streak Velocimetry (PSV). PSV is one of a family of flow-measurement techniques that rely on measuring particle locations at several instances to estimate local fluid velocities. An excellent review of the family of particle-tracking techniques, including Particle Image Velocimetry (PIV), Particle Tracking Velocimetry (PTV), and PSV, and their relative benefits and disadvantages is given by Adrian (1991). In PIV, the flow is relatively heavily seeded with particles and two images are recorded sequentially, a short-duration light pulse providing the illumination in each image. The change in particle position is divided by the delay between exposures to estimate the local fluid velocity. To obtain velocity estimates at each spatial location typically requires many particles within each interrogation window. In PTV and PSV, a long-exposure image is recorded and the light source is pulsed multiple times. As a particle moves through the image plane, its position is "marked" at each time step, allowing the velocity field to be estimated from the position and time record. PTV relies on a light source of short pulse duration and high repetition frequency, resulting in a series of "dots" marking the particle trajectory. PSV relies on a continuous (or long pulse) light source and shuttering or "chopping" it in time to produce a series of particle "streaks." PSV has seen more widespread application than PTV because of the historically limited availability of high-power, high-repetition-rate light sources.

An early example of PSV can be found in the flow visualization work of Prandtl & Tietjens (1954), originally published in 1934. In combustion, particle-tracking techniques have long been used to study reacting flow fields. Particle-streak images were utilized by Smith (1937) to investigate the flow field of a Bunsen burner. The illumination was interrupted by a slotted disc rotating at known speed to produce the particle streaks. This same technique was applied in a more systematic study of burner-stabilized flames by Lewis & von Elbe (1943; see also 1961, Ch. V.7). These authors utilized MgO dust for the tracer particles and noted that some of the particle trajectories appeared to be affected by particle inertia. They attempted to correct the flow lines using conservation-of-mass arguments. This "stroboscopically illuminated particle method" was utilized by Andersen & Fein (1949) to study propane-air Bunsen flames. The nozzle was contoured to produce a flat

nozzle-exit-velocity profile, resulting in a straight-sided Bunsen cone. These authors utilized the particle streak tracks to determine the velocities on both sides of the flame front, and applied the equation of continuity and equation of state to estimate the flame temperature. They noted that the tracks of some particles appeared to lag the flow and corrected this effect by extrapolating the far-field trajectory back to the flame front. The use of particle-tracking visualizations of streamlines (and streamtubes) was also used by Fristrom *et al.* (1953) to determine the density as a function of position in a propane-air Bunsen flame, which was then converted into a temperature profile. These authors note that the changing gas composition within the flame introduces uncertainty to the temperature determination and utilized mixtures that minimized this effect. They also noted that the accuracy of the technique is limited by the ability of the particles to follow the flow and concluded that their maximum particle size of 5 microns was sufficient to track the streamlines to within 2%. In addition, they noted that if the flame was overloaded with particles, the burning velocity would decrease. With the particle loading utilized in their study, no change in burning velocity was detected (Fristrom *et al.* 1953). In a subsequent work, these authors further discuss temperature measurements using particle tracking and estimate that the correction required due to the thermophoretic effect was, at maximum, a quarter of a percent for a flame at one quarter atmosphere pressure (Fristrom *et al.* 1954; see also Fristrom 1954). Interestingly, Fristrom *et al.* (1954) utilized a ballistic switch, where a series of spark gap switches are aligned in the path of a rifle bullet, to fire the flash lamps successively (see Fristrom & Westenberg 1965; Ch. VII). This resulted in a 5 microsecond illumination at a repetition rate of 20 kHz. The text by Fristrom & Westenberg (1965; see Ch. VII & VIII) contains a summary of aerodynamic (velocity) measurements in flames, including sources of error and examples of the required apparatus for PSV. Pandya & Weinberg (1964) utilized PSV to measure velocity profiles in an ethylene diffusion flame, and found a particle-free zone around the flame when the velocities of the two jets were equal and the rates of supply of fuel and oxygen were in the stoichiometric ratio. These authors attribute this to the flame acting as a "weak gas source," although thermophoresis (see Appendix A) would be important in this flow region, contrary to their statement that "possible deviations of particle velocities and directions from those of the corresponding stream lines, due to both lag in acceleration and thermo-mechanical effects, were considered. . .and found to be unimportant under present conditions." Tewari & Weinberg (1967) studied flame quenching by a cold suface and measured the burning velocity of a lean ethylene-air flame in the vicinity of the heat sink using PSV. The structure of a counterflow diffusion flame of ethanol was studied using particle tracking (Pandya & Srivastava 1975), and laminar burning velocities have also been measured in "button flames" using particle-tracking techniques (*e.g.* Günther & Janisch 1972; Dixon-Lewis & Islam 1982). Andrews & Bradley (1972) provide a critical review of burning velocity measurements in simple hydrocarbon flames. Many of the measurements contained in their review were performed using particle-tracking techniques and a large subset of

these has been cited above.

The particle-tracking technique is reviewed in a paper by Kumar & Pandya (1970). The following is an excerpt from their review:

> The [particle-tracking] technique thus seems to be versatile. . .no elaborate equipment is needed; a reasonably good camera, a high intensity source of light and a few laboratory grade lenses are all that is required to make it a success. In principle the flow pattern to be visualized is illuminated from the side and the tracer particles suspended in the gas stream are photographed from a direction perpendicular to the illuminating beam. For making quantitative measurements of the local flow velocities, the illuminating beam is interrupted at a regular frequency. The tracks recorded on the plate then correspond to the length travelled by the tracer particles during a known time period and are, therefore, a direct measure of the flow velocity. In practice if reliable results are desired, the technique has to be evolved to a high level of sophistication.

These authors also discuss the practical issue of illumination requirements, which increase as flow velocity increases as a result of the reduced particle residence time at any location in the flow. They also suggest that lasers may provide a good source of light, although they utilize flash lamps in this study. Kumar & Pandya (1970) also discuss thermomechanical and diffusional lag between the particles and the gas stream, and the ability of the tracer particles to track changes in flow velocity. They find that particles about 5 microns in diameter give good results in atmospheric flames. It is also noted that temperature measurement using particle tracks can result in large errors when applied to flows with large stream-tube curvature, such as stagnation or opposed-jet flows. In these early studies, images were recorded onto photographic film and then processed to determine velocity fields by performing measurements (by hand) on prints made from the negatives (typically at several times magnification).

PSV flow velocity measurements were made in a shear layer by Dimotakis *et al.* (1981). In this work, particle-streak images were taken with a photographic camera and a positive transparency was made from the negative. This transparancy was digitally scanned using a 1024-element linear detector to digitize the image data. The resulting digital data was processed to calculate the velocity vectors in the flow. Another example of PSV is the work of Rimai and coworkers (Marko & Rimai 1985; Adamczyk & Rimai 1988), where the flow field of an engine cylinder and throttle body was studied using a SIT vidicon to record the image data digitally, allowing the flow field to be processed without handling photographic film. Agüí & Jiménez (1987) discuss sources of error in particle-tracking techniques, specifically in turbulent flows, and provide a good example of the required experimental apparatus. PTV was utilized for flame-speed measurements at the tip of a slot burner in the work of Echekki & Mungal (1990), using a 20 W copper vapor laser at 5882 Hz. In this incarnation

of particle tracking, the high-pulse-rate laser exposes the particle track as a series of "dots" on the imaging device due to the short pulse duration. PSV has also been utilized in combustion for qualitative flow visualization (*e.g.* Sugiyama 1994). The Ph.D. thesis of Vagelopoulos (1999) provides a description of a PSV technique that was the starting point for this work. Vagelopoulos discusses several sources of error in the application of the technique and provides some measurements for both cold and reacting impinging-jet flows.

In the work presented here, extensions and improvements to existing PSV techniques were implemented. This PSV methodology yields low fractional-error axial velocity data, with the technique optimized for measurements in axisymmetric stagnation flow. In axisymmetric, steady flow, the axial velocity component along the centerline of the flow field can be reliably measured. Particle paths do not cross or overlap, and out-of-plane particle displacements are small and easily discernible when they occur (in-focus/out-of-focus streaks). The high sensitivity of the scattering cross section to particle size, in the size range employed, allows easy identification of agglomerates that may not track high spatial-gradient regions in the flow. Streaks used for PSV processing were from in-plane, non-agglomerated particles.

A single PSV image can capture the entire velocity field, making it ideal for short-run-time experiments. The resulting accuracy is comparable to that obtained with LDV or Particle Image Velocimetry (PIV), while offering relative advantages in flame environments. The reduced particle loading required for PSV minimizes flame disturbances introduced by particle seeding that can alter the effective thermal/heat-capacity environment, or the chemical kinetic/catalytic environment by providing surface-chemistry sites. Ancimer *et al.* (1999) state that "high concentrations of refractory seed particles might affect combustion through their added heat capacity, acting as thermal radiation sources, or by altering knock tendencies." In their numerical study of dusty reacting flows, Egolfopoulos & Campbell (1999) observed flame cooling and eventual extinction for increased values of the particle number density. They note that the much higher thermal capacity of the solid phase can result in a reduction in the thermal response of the gas phase. Low PSV particle loading also reduces Mie-scattering interference in CH Planar Laser Induced Fluorescence (PLIF) image-data, improving CH profile statistics. In PIV, the higher required particle number densities and the high spectral intensity of the Nd:YAG laser pulses can cause interference (Carter *et al.* 1998). Particle loading required for accurate velocity measurements with PSV is an order of magnitude lower, or more, than required for LDV or PIV. In a single PSV image frame, one or two particles traversing the vertical extent of the image suffice. In contrast, PIV measurements require a dispersion of particles throughout the domain in any one (short-time) exposure. The large reduction in density that accompanies the temperature rise through the reaction zone results in an order of magnitude reduction in the particle number density. To obtain good particle dispersion in the hot region of the flow, it must be seeded with 10 times the number of particles required to obtain good statistics

in the cold region. Early PIV measurements in flames resulted in valid data only in the pre-flame zone due to this correlated drop in particle density through the flame front (Stella *et al.* 2001). By heavily seeding the cold gases, subsequent authors were able to measure the velocity in the post-flame region. With LDV, high particle number densities are required to obtain converged statistics in a reasonable time. Thus, when measuring the high-temperature regions of the flow, the particle loading must be increased by an order of magnitude to obtain similar performance as that in the cold-flow region. Altman (1991) investigated the optimal seeding density for particle-streak photography. For a one-dimensional flow, the optimum particle seed density per unit length is given by $\lambda = 2/L_s$, where L_s is the streak length. This analysis is for the case where the image-exposure time is equal to the illumination time. However, in the methodology employed here, a single particle may traverse the entire domain during the exposure, being illuminated multiple times. Thus, it can be argued that the optimal seeding density for this PSV implementation is $\lambda = 2/L_i$, where L_i is the image extent, in this case the nozzle-plate separation distance, L.

An important consideration when performing any particle tracking technique is the ability of the tracer particles to accurately follow the flow (see Appendix A). In a one-dimensional, variable-velocity field, particles will follow the flow if the dimensionless product of the local strain rate $\sigma = \partial u/\partial x$, and the Stokes time, $\tau_\mathrm{S} \equiv \rho_\mathrm{p} d_\mathrm{p}^2/(18\,\mu)$, is small, *i.e.*, if

$$\sigma\,\tau_\mathrm{S} \;\equiv\; \sigma\,\frac{\rho_\mathrm{p}\,d_\mathrm{p}^2}{18\,\mu} \;\ll\; 1\;. \tag{B.1}$$

In this work, several particle types were utilized. In the cold-flow work and for measurements in ethane and ethylene flames, alumina particles were used (Al_2O_3; median size, $d_\mathrm{p} \cong 0.8\,\mu$m, $\rho_\mathrm{p} \cong 3830\,\mathrm{kg/m^3}$; Baikowski Malakoff, RC-SPT DBM). Some methane-flame experiments utilized ceramic microspheres to increase the scattered-light intensity of the particle streaks (median size, $d_\mathrm{p} \cong 3\,\mu$m, $\rho_\mathrm{p} \cong 2400\,\mathrm{kg/m^3}$; 3M Zeeospheres, W-210). Particle motion in spatially varying velocity and temperature fields is discussed in Appendix A.

A schematic of the experimental setup is given in Fig. B.1. A Coherent I-90 Ar-ion (CW) laser, operated at 2–3 W, acts as the illumination source. Two cylindrical lenses generate a thin laser sheet ($\approx 200\,\mu$m) in the field of view. An Oriel chopper system (Model 75155), with a 50 % duty-cycle wheel, modulates the laser beam. The chopper was placed at a horizontal waist in the laser beam to minimize on-off/off-on transition times. Chopping frequencies were in the range, $0.5\,\mathrm{kHz} \le \nu_\mathrm{c} \le 2.4\,\mathrm{kHz}$, with ν_c optimized depending on flow velocity, in each case.

Image data were recorded with the in-house-developed "Cassini" (Shan & Dimotakis 2001) and "KFS" (Kern *et al.* 2001) digital-imaging systems. They are based on low-noise, 1024^2-pixel CCDs, on a 12 μm pitch. The Cassini camera is based on a CCD developed for the NASA *Cassini* mission. The KFS CCD was designed by M. Wadsworth and S. A. Collins of JPL. The camera heads and

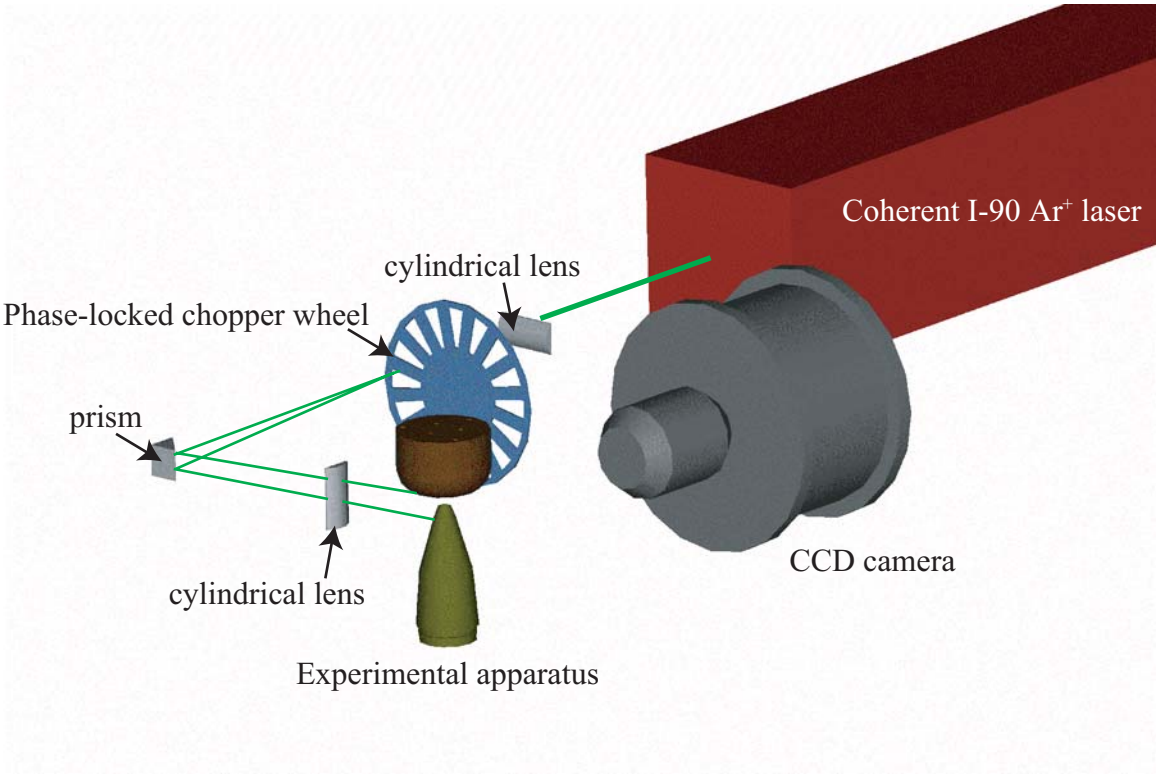

Figure B.1: PSV experimental apparatus.

data-acquisition systems were designed and built by D. Lang at Caltech. Output for both is digitized to 12 bits/pixel. Magnification ratios were in the range of 1:1–1:1.5, using a Nikon 105 mm, $f/2.8$ macro lens. In the reacting flow experiments, a bandpass filter (514.5 nm center wavelength, 10nm bandpass, Thermo-oriel P10-515-R) was used to block chemiluminescence emissions, along with thermal radiation from the particles (see Stella *et al.* 2001). Exposure-time control in the Cassini camera was implemented with a built-in computer-controlled Uniblitz shutter, with opening and closing times of 7 ms and 6 ms, respectively. Exposure times were varied for optimum particle-streak density in the images, with framing rates for these experiments in the range of 4–10 fps.

A single image of a cold-jet flow with particle streaks is reproduced in Fig. B.2, for a nozzle-plate separation to nozzle-diameter ratio of $L/d = 1.0$. In this flow, the jet-nozzle centerline velocity is $U = 106$ cm/s, yielding a Reynolds number, $Re \cong 700$. The top and bottom portions of the laser sheet are masked to minimize scattering from the solid plate and nozzle surfaces. A corresponding example of a PSV image in a reacting flow is given in Fig. B.3, for a methane-air flame at an $L/d = 0.8$ and equivalence ratio of $\Phi = 0.9$.

Small-particle streaks approximate Lagrangian trajectories of the flow (see Fig. B.2). Local velocities $u(x)$, are estimated from streak pairs as $u(x) \cong \Delta X(x)/\Delta t$, yielding $u_{\rm I} = L_{\rm I}/\tau_{\rm c}$ and $u_{\rm II} = L_{\rm II}/\tau_{\rm c}$, where $\tau_{\rm c} = 1/\nu_{\rm c}$ (reciprocal of chopper frequency) and $L_{\rm I} = x_{2{\rm s}} - x_{1{\rm s}}$ and $L_{\rm II} = x_{2{\rm e}} - x_{1{\rm e}}$

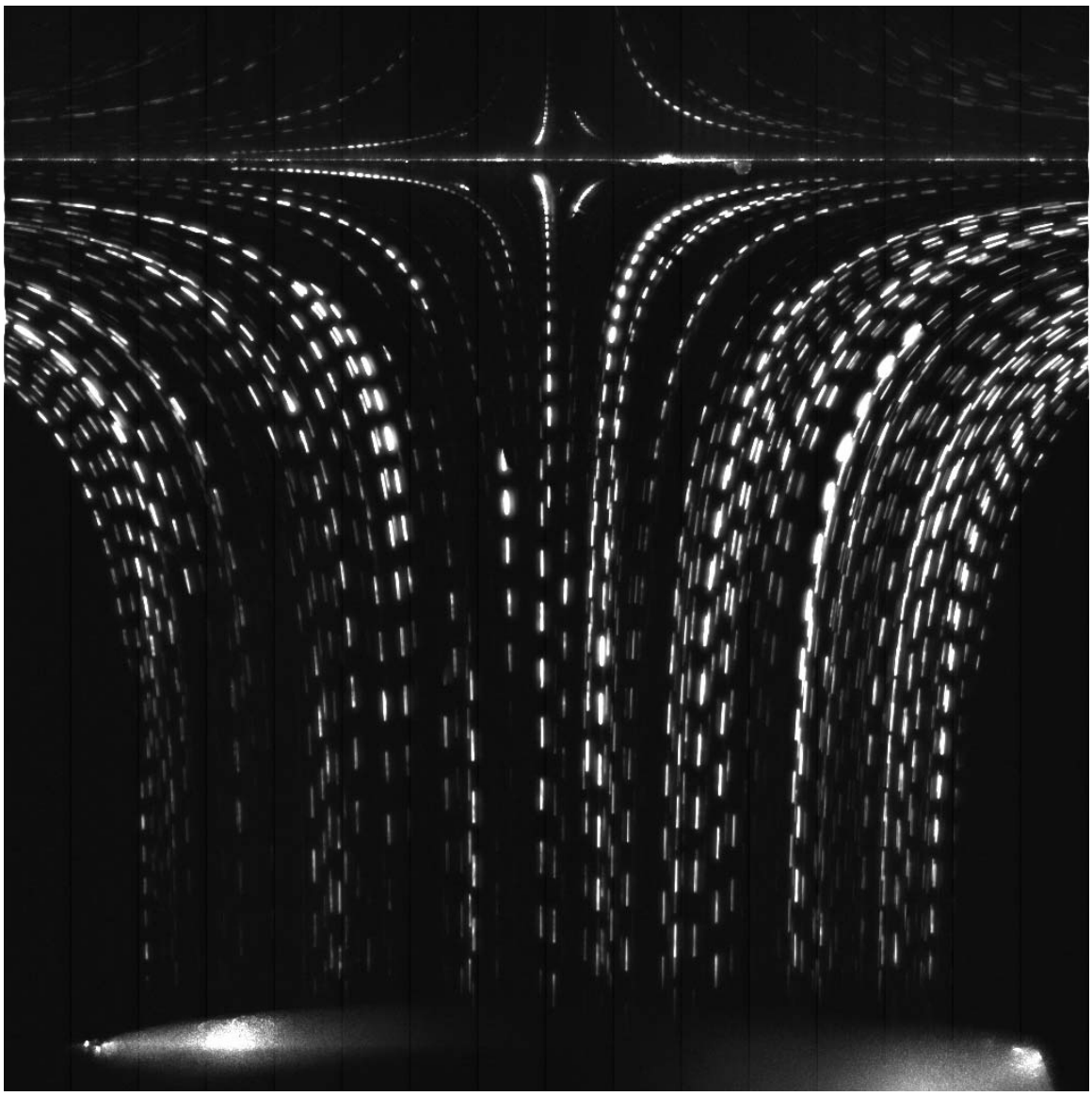

Figure B.2: Impinging-jet flow. $Re_{\mathrm{j}} = 700$, $U_{\mathrm{j}} = 105\,\mathrm{cm/s}$, $L/d = 1.0$. Stagnation plate and nozzle exit are visible.

are the distances from the start/end of one streak to the start/end of the next, respectively (see Fig. B.4). The velocity estimate, u_{I}, is located at $x_{\mathrm{I}} = (x_{1\mathrm{s}} + x_{2\mathrm{s}})/2 + (w_1 + w_2)/4$, where $x_{i\mathrm{s}}$ is the spatial location of the start of the ith streak and w_i is the width of the ith streak (see Fig. B.4). Similarly, u_{II} is located at $x_{\mathrm{II}} = (x_{1\mathrm{e}} + x_{2\mathrm{e}})/2 - (w_1 + w_2)/4$, where $x_{i\mathrm{e}}$ is the location of the end of the ith streak. Using the same intensity threshold on a streak pair removes systematic errors in applying the Lagrangian time interval τ_{c} to the spatial extent of a streak pair. This methodology produces good agreement between velocity values derived from each streak pair. Streak lengths are estimated using bicubic fits on the 2-D streak-intensity image data, sampled to a 0.1-pixel resolution in both dimensions. An intensity threshold of approximately 0.4 of the maximum intensity of each

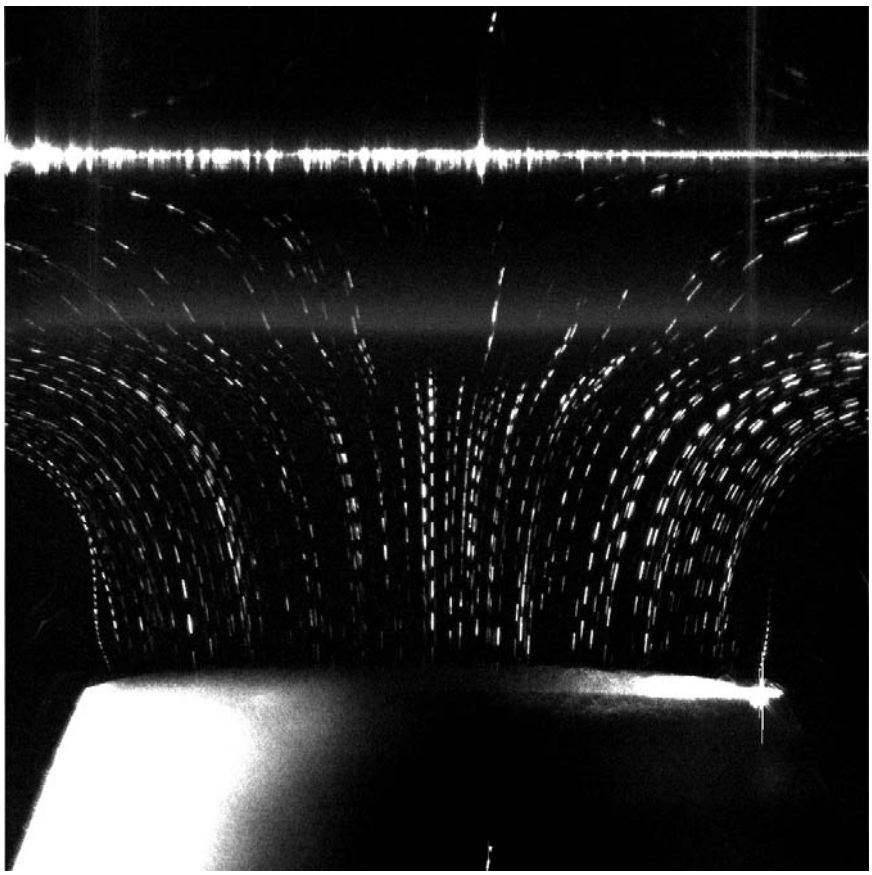

Figure B.3: PSV in a strained premixed methane-air flame, chemiluminescence is visible. $\Phi = 0.9$, $L/d = 0.8$.

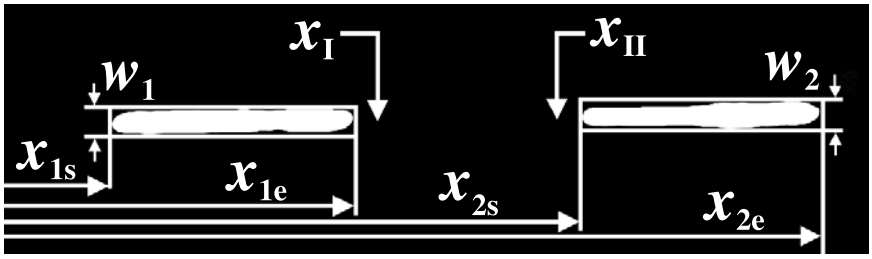

Figure B.4: PSV measurement implementation.

streak is used to determine streak dimensions to this sampling resolution. The resulting procedure is accurate, with an overall PSV error of $< 0.01\,U_{\mathrm{B}}$.

Previous analyses relied on measuring the length of the streak and dividing by the illumination time (*e.g.* Vagelopoulos 1999). The streak image is a result of a particle image (spot) being convolved with the particle motion during the exposure time. The appropriate particle displacement distance is thus the streak length minus the particle-image diameter, typically the streak width (see Vagelopoulos 1999). In such a processing methodology, a single measurement is made from each (illuminated) streak. In the present implementation, a particle trajectory is illuminated half the time,

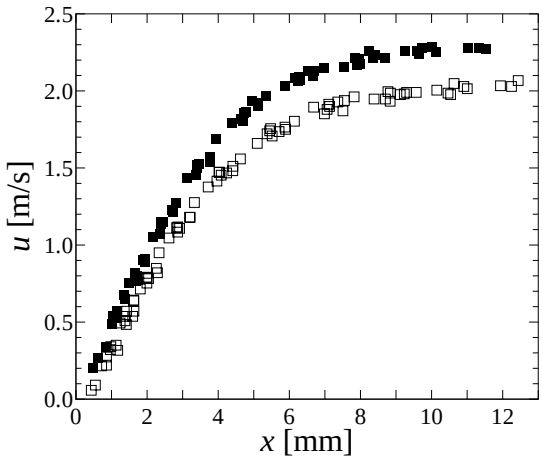

Figure B.5: Cold impinging-jet profile utilizing light (open squares) and dark (filled squares) streaks.

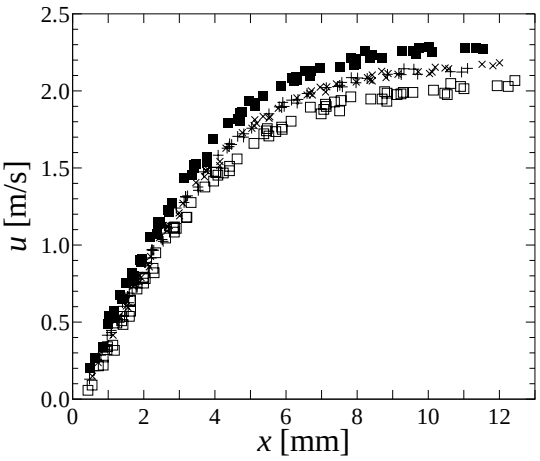

Figure B.6: Cold impinging-jet profile showing results of new methodology compared to light (open squares) and dark (filled squares) streak results. (+) Start-to-start, (×) end-to-end processing techniques.

resulting in a series of "light" and "dark" streaks. The end of one streak and the start of the next correspond to a hypothetical "dark" streak. From a single particle track, such a methodology would result in twice the number of data points. This methodology was applied to a cold impinging jet flow, and the results are presented in Fig. B.5. There is a systematic discrepancy between the light- and dark-streak velocity profiles. The source of this systematic error is attributed to the difficulty in assigning the illumination time to the thresholded streak length. To improve the accuracy of the PSV processing methodology, two locations at the same point of the illumination cycle are utilized, as discussed above. The use of the same point in the cycle reduces the uncertainty in the time base, and results in a pair of profiles that give good agreement with one another. This methodology produces two data points from each streak pair, resulting in the same spatial sampling as the traditional processing technique. The results of the new methodology are included in Fig. B.6 and are seen to split the difference between the light/dark-streak profiles.

PSV spatial resolution is comparable to that of other particle velocimetry techniques, *e.g.*, PIV, LDV, that rely on comparable spatial displacements (*e.g.*, 10–30 pix, or $\approx$ 100–300 μm, for this flow). These methods measure the distance traveled by a particle along a particle path in a fixed time (PIV, PSV), or the time required to traverse a fixed number of fringes in space (LDV). Particle methods require care in regions of high fractional change in speed along individual particle track segments, here limited to measurements very close to the wall, or in regions of high velocity curvature. PIV or PSV measurements in regions of high spatial gradients, or curvature, are subject to systematic errors in the assigned velocity value and spatial location. For PIV and PSV, these errors scale with the fractional variation of the velocity in the measurement interval, $\Delta u/u$, which is small except

near the wall, or the square-root of the velocity curvature, $\sqrt{\overline{u''}/\bar{u}}$, and the sampling extent. For particle tracking techniques, the sampling extent is the particle displacement, $\Delta x = \bar{u}\tau_c$, and for finite-probe-volume techniques, *e.g.*, LDV, it is the probe volume size. Appendix A discusses the application of particle velocimetry techniques to spatially varying flow fields.

B.1 Stagnation flame velocity profile fit

A functional form was developed that can capture the features of stagnation flame velocity profiles. The fit is based upon two parabolic fits to the cold and hot regions of the flow, joined through the use of two unit-step functions with a specified width (error functions). Inclusion of the error functions accommodates the transition between the cold and hot flow regions. The measured velocity at any position in the flow is approximated by

$$u(x) = p_1(x) \times e_1(x) + p_2(x) \times e_2(x) \tag{B.2}$$

where $p_1(x)$ and $p_2(x)$ are parabolas fitting the hot and cold regions, respectively, and given by

$$p_1(x) = a_{1,p_1} \times (x - x_{0,p_1}) + a_{2,p_1}(x - x_{0,p_1})^2 \tag{B.3}$$

$$p_2(x) = a_{1,p_2} \times (x - x_{0,p_2}) + a_{2,p_2}(x - x_{0,p_2})^2 \ , \tag{B.4}$$

and $e_1(x)$ and $e_2(x)$ are unit-step functions (range from 0 to 1) given by

$$e_1(x) = \frac{1}{2}\left\{1 - \mathrm{erf}\left[b_{e_1}\left(x - x_{0,e_1}\right)\right]\right\} \tag{B.5}$$

$$e_2(x) = \frac{1}{2}\left\{1 + \mathrm{erf}\left[b_{e_2}\left(x - x_{0,e_2}\right)\right]\right\} \ . \tag{B.6}$$

In these expressions, x_{0,p_i} is the x-axis intercept of the ith parabola, a_{1,p_i} and a_{2,p_i} are the slope and curvature parameters of the ith parabola, x_{0,e_i} is the location where $e_i = 1/2$, and b_{e_i} is the slope parameter (1/width) for the ith error function. The fit parameters were determined, for each PSV dataset, to minimize the root-mean-squared error of the fit. Figures B.7–B.15 give example profiles for methane, ethane, and ethylene flames at lean, stoichiometric, and rich conditions. Under rich conditions (see Figs. B.12 and B.15), there may be a region within the chemiluminescence zone where PSV data was not obtained. The fit is unconstrained in this region and should not be compared to predictions. The proposed function relies on 10 parameters and is able to adequately capture the PSV profile features for all experiments reported here.

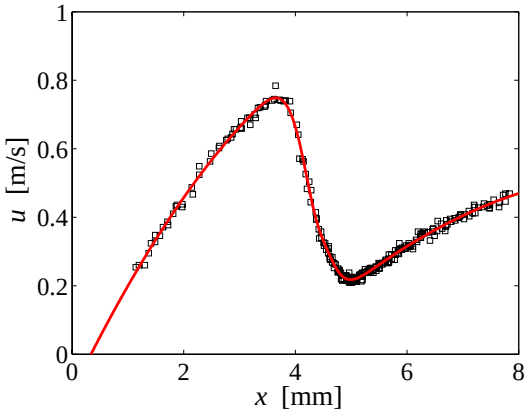

Figure B.7: PSV data (□) and fit (solid red line) for a $\Phi = 0.7$ methane-air flame (run234).

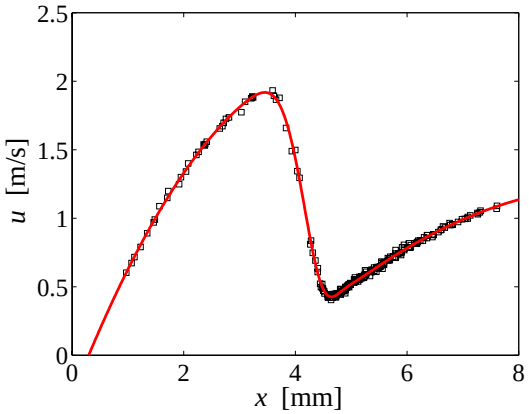

Figure B.8: PSV data (□) and fit (solid red line) for a $\Phi = 1.0$ methane-air flame (run226).

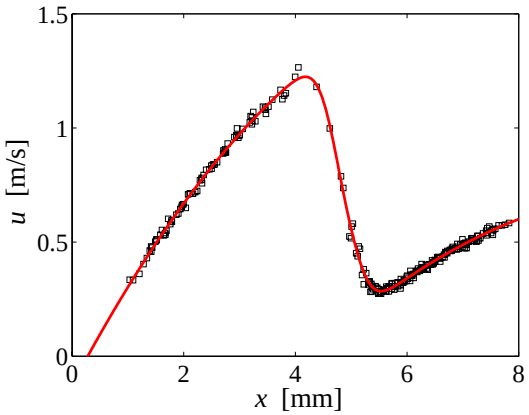

Figure B.9: PSV data (□) and fit (solid red line) for a $\Phi = 1.3$ methane-air flame (run229).

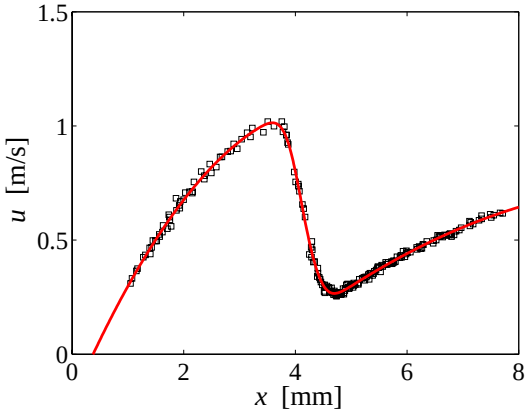

Figure B.10: PSV data (□) and fit (solid red line) for a $\Phi = 0.7$ ethane-air flame (run337).

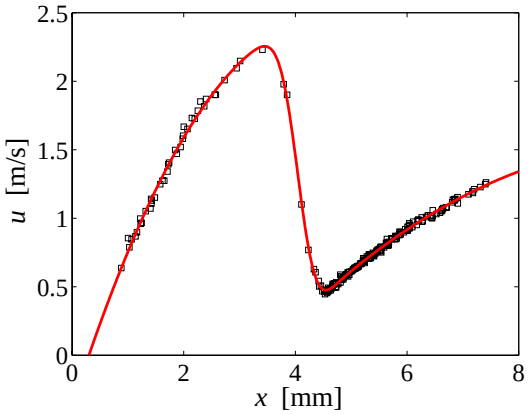

Figure B.11: PSV data (□) and fit (solid red line) for a $\Phi = 1.0$ ethane-air flame (run334).

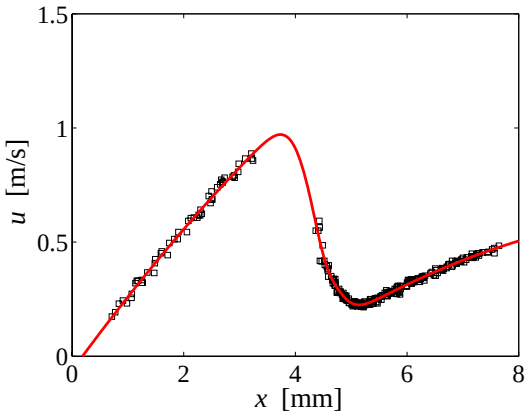

Figure B.12: PSV data (□) and fit (solid red line) for a $\Phi = 1.5$ ethane-air flame (run329).

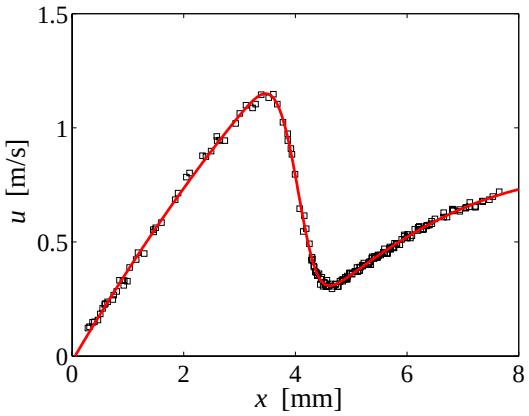

Figure B.13: PSV data (□) and fit (solid red line) for a $\Phi = 0.6$ ethylene-air flame (run301).

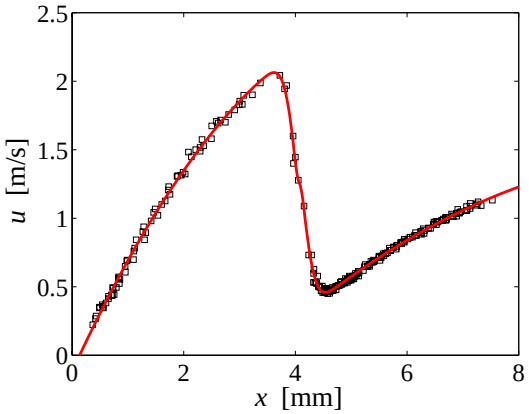

Figure B.14: PSV data (□) and fit (solid red line) for a $\Phi = 1.0$ ethylene-oxygen-nitrogen flame, 17.0%O_2:(O_2+N_2) (run299).

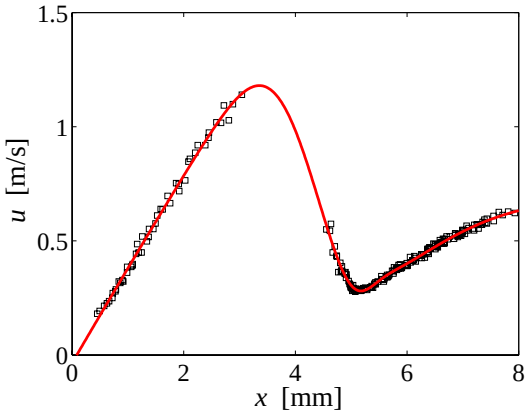

Figure B.15: PSV data (□) and fit (solid red line) for a $\Phi = 1.8$ ethylene-air flame (run298).

B.2 PSV profile fit sample script

The following script corresponds to the contents of `velocityfit.m` which defines the function that is fit to each experimental velocity profile.

```
function [u_fit] = velocityfit(fit,xdata)


x0p1=fit(1);
a1p1=fit(2);
a2p1=fit(3);
x0p2=fit(4);
a1p2=fit(5);
a2p2=fit(6);
x0e1=fit(7);
be1=fit(8);
x0e2=fit(9);
be2=fit(10);


p1=a1p1.*(xdata-x0p1)+a2p1.*(xdata-x0p1).^2;
p2=a1p2.*(xdata-x0p2)+a2p2.*(xdata-x0p2).^2;
e1=0.5*(1-erf(be1.*(xdata-x0e1)));
e2=0.5*(1+erf(be2.*(xdata-x0e2)));


u_fit=p1.*e1+p2.*e2;
```

B.3 PSV uncertainty

The availability of an analytical expression for the velocity data allows the root-mean-squared (rms) uncertainty of the PSV technique to be estimated. The rms uncertainty of the PSV technique is estimated to be $\approx 1.5\,\%\,U_{\mathrm{B}}$ for experiments reported here. The velocity and velocity-gradient boundary conditions specified in the simulations have an associated uncertainty due to the scatter in the PSV data. Linear regression analysis of the parabolic fits to the velocity data in the cold flow region is used to determine the 95 % confidence bounds on the fit. The uncertainty in the velocity boundary condition, u_ℓ, is taken as the average difference between the 95 % bounds and the fit value at the specified location, ℓ. To determine the uncertainty in the velocity gradient at the simulation inlet, parabolas were fit to the max (min) bound at the start of the fit domain, the fit value at ℓ, and the min (max) bound at the end of the fit domain. These two parabolas represent the minimum

and maximum possible slope at ℓ for the given confidence bounds. The average difference in the slope between these two fits and the optimal fit represent a maximum uncertainty in the measured velocity gradient. It should be noted that CANTERA requires the spreading rate, V_ℓ, be specified, which is equal to one half of the axial velocity gradient in cold regions of the flow. The uncertainty in V_ℓ is the same as that in the velocity gradient. The estimated uncertainty in the velocity boundary condition, u_ℓ, is $\pm 0.8\,\%$, and the estimated uncertainty in the velocity gradient, or V_ℓ, is $\pm 5\,\%$.

Appendix C

Planar Laser Induced Fluorescence

The measurement of minor species concentrations in flames typically relies upon Laser-Induced Fluorescence (LIF, *e.g.*, Eckbreth 1996). Daily (1997) states that "for appropriate species, mainly those with strong UV and visible radiative transitions and relatively simple structure, LIF remains the most sensitive and straight forward method for concentration measurements." The excellent review article on LIF spectroscopy in flames by Daily (1997) provides a thorough introduction to spectroscopy, including discussions on energy levels, state distributions, line shapes, etc. According to Daily, researchers perform measurements for several reasons, one being the validation or testing of a theory or computation. This type of *hypothesis testing* involves carrying out an experiment for the purpose of direct comparison with a theory or calculation, often for the purpose of numerical code validation, and may involve detailed measurements of velocity, temperature, and concentration fields. In this research, various *hypotheses* (chemistry, transport, and flow models) are tested by directly comparing experimental measurements to numerical simulations utilizing these models. Daily (1997) also points out the usefulness of LIF in imaging, a technique typically labeled Planar Laser Induced Fluorescence (PLIF). With PLIF, simultaneous species measurements may be made at thousands, or even millions, of points. Two reviews of the PLIF technique in combustion are provided by Hanson (1988,1990).

In combustion, PLIF measurements are typically performed on the OH radical. Crosley (1989) points out that while the OH molecule is one of the most important molecular radicals in typical flames, its measurement provides little information on the chemistry. The OH concentration rises slowly through the reaction zone and remains high far into the burned gases, essentially marking where reactions have occured, rather than where reaction is occuring. According to Crosley, intermediate species whose concentrations rise and fall within the reaction zone are much more revealing. The methylidyne radical, CH, is found to exist near the flame front and reveals where the combustion chemistry is taking place (Crosley 1989). For this reason, the reaction zones of hydrocarbon-air flames have been imaged using CH PLIF (Allen *et al.* 1986; Paul & Dec 1994). CH has also been suggested as being an important participant in prompt-NO production (Crosley 1989; Norton &

Smyth 1991). Accurate modeling of CH production is essential for the prediction of these important pollutant emissions, especially for low-temperature flames where the prompt mechanism can dominate (Renfro *et al.* 2001). Luque *et al.* (1996) state that "our experience with flame chemistry models has shown that the correct prediction of absolute CH concentration and position in a one-dimensional laminar flame forms a key test of the relevant part of the chemical mechanism." CH LIF provides an excellent way to identify and analyze the primary reaction zones, as the CH radicals only exist in these thin regions (Sutton & Driscoll 2003). In addition, the electronic states are accessible using available dye lasers, and it is possible to excite the radicals to the second excited state (B–X excitation) and record the fluorescence from the first excited state (A–X emission). The resulting large wavelength shift between excitation and emission allows the Rayleigh and Mie scattering of the excitation beam to be rejected using optical filters. For these reasons, the CH radical was studied in this work. CH is a reactive intermediate species whose spatial distribution is sharp and can be directly compared to simulations. Succesful predictions of CH profiles can help validate the chemistry and transport models utilized in detailed numerical simulations, while disagreement with experiment can indicate regimes where further investigation of the kinetic/transport models is required.

The measurement of species concentrations using LIF has been performed using several strategies. The first requires knowledge of the rates of the various transitions involved, the second involves measuring these rates *in situ*, the third uses a scheme that does not require rates (saturation and/or using special detection strategies) and the fourth relies on calibration or relative measurement (Daily 1997). In the limit of weak excitation, the fluorescence signal is directly proportional to pumping power, or spectral intensity. In this regime, the LIF signals need to be corrected for variations in the collisional quenching rate, which depends on the concentration of several major and minor species and the temperature (Sutton & Driscoll 2003). Luque *et al.* have performed quantitative CH measurements in low-pressure flames (Luque & Crosley 1996; Luque *et al.* 1996), and subsequently extended this methodology to atmospheric pressure flames (Luque *et al.* 2002). The point-wise measurements of Luque *et al.* were performed in the linear regime (low-laser power), and required calibration of the optical collection efficiency using Rayleigh scattering, and measurements of the peak LIF signal at multiple laser powers to determine the absolute number density. In addition, to obtain spatial profiles, the burner had to be translated relative to the excitation and collection optics. Renfro *et al.* (2001) performed point-wise relative CH LIF concentration measurements in counterflow-diffusion flames, at atmospheric-pressure, using picosecond laser excitation in the linear regime (weak excitation). These authors state that a robust technique is not presently available for measuring quantitative, spatially resolved, CH (absolute) concentrations in atmospheric-pressure flames. Their approach for measuring relative concentrations relies on the use of a picosecond excitation source, and measuring the fluorescence lifetime (quenching) of the CH signal at each

point.

To avoid the issues associated with collisional quenching, the diagnostics can be operated in the saturated mode by ensuring that the laser power is sufficiently high to saturate the LIF signals (Daily 1977). When the fluorescence is saturated, the fluorescence signal is directly proportional to the number density of the species of interest and is relatively independent of variations in the quenching rate coefficient or laser irradiance (Daily 1977; Sutton & Driscoll 2003). The saturation behaviour of CH fluorescence has been studied by Bonczyk & Shirley (1979) and Takubo *et al.* (1983). Verdieck & Bonczyk (1981) studied concentrations of trace radicals (CH, CN and NO) in flames using saturated LIF point measurements. Thes authors found concentrations of CH that were within a factor of 2–3 of those obtained using absorption techniques. Kohse-Höinghaus *et al.* (1983, 1984) utilized saturated single-point LIF measurements to estimate absolute number densities for OH and CH in a low-pressure acetylene/oxygen flame. These authors found good agreement between measured and predicted OH profiles, but significant disagreement in the relative profiles of CH. The use of saturated fluorescence imaging was demonstrated by Chen & Mansour (1997). Point measurements of relative CH concentrations in Bunsen flames using saturated LIF were performed by Sutton & Driscoll (2003).

Even for large excitation powers, there will always be some portion of the fluorescence signal that is still in the linear regime due to the "wings" of the laser sheet in space and in time (Daily 1978). In single-point spectroscopic measurements, a focused laser beam typically acts as the excitation source. The fluorescence signal is detected using a monochrometer/spectrometer oriented perpendicularly to the laser beam propagation direction. The slit of the monochrometer/spectrometer is aligned either along the direction of the laser beam, or perpendicular to it. The latter arrangement can result in a higher spatial resolution, while the parallel arrangement has the advantage that the signal would be saturated along the slit axis. The "wing" effects result in a square-root dependence of the fluorescence signal on the laser spectral intensity for the perpendicular case, with a slightly less than square-root dependence for the parallel case (Daily 1978, 1997). In PLIF measurements, the fluorescence should exhibit a nearly square-root dependence on the pumping intensity in the saturation regime. In spite of the fact that no pure saturation of the fluorescence signal is detected, there are two advantages to operating at higher laser irradiances. The first advantage is that larger signals are obtained, improving signal-to-noise ratios. The second is that due to the logarithmic dependence of the fluorescence signal on the laser intensity, there is a rapid decrease in the dependence of the signal on the laser power for large spectral irradiances (Daily 1978, 1997). This results in reduced uncertainty due to shot-to-shot variations in laser power.

The low signal level associated with operating in the linear regime makes imaging of the CH radical very difficult. Saturated fluorescence imaging results in increased signal along with a reduced sensitivity to variations in collisional quenching rates and laser power. In this work, the goal is to

study flames for a variety of fuels, stoichiometries, and strain rates. The technique of Sutton & Driscoll (2003) can provide accurate relative measurements of the CH radical and is also fairly simple to implement. The flexibility afforded by this technique permits short run-time experiments and allows for the study of multiple flame environments. Sutton & Driscoll (2003) performed single-point saturated LIF measurements of the CH radical in Bunsen flames burning methane- and propane-air. These authors measured the fluorescence signal on and off the resonance line of interest, and took the difference between the two values as the CH signal. In this study, the methodology of Sutton & Driscoll (2003) has been extended to planar imaging of the fluorescence. Chen & Mansour (1997) demonstrated saturated PLIF imaging and measured relative CH concentration profiles within single images without offline subtraction. The work presented here extends the preliminary measurements reported in Bergthorson *et al.* (2005a) and is the first application of saturated PLIF imaging for the measurement of relative CH concentrations and concentration profiles over a wide variety of flame conditions. The theory supporting this saturated PLIF technique follows.

The fluorescence signal power, S_{F}, for a two-level system is given by

$$S_{\mathrm{F}} = \epsilon_{\mathrm{opt}}\,\epsilon_{\mathrm{q}}\,h\nu\,\frac{\Omega_{\mathrm{c}}}{4\pi}\,V_{\mathrm{c}}\,\frac{B_{12}}{B_{12}+B_{21}}\,\frac{A_{21}}{1+I_{\nu,\,\mathrm{sat}}/I_{\nu}}\,N_1^0\ , \tag{C.1}$$

where ϵ_{opt} is the efficiency of the collection optics, ϵ_{q} is the quantum efficiency of the detector, $h\nu$ is the photon energy, h is Planck's constant, ν is the optical frequency of the transition, Ω_{c} is the solid angle of the collection optics, V_{c} is the focal (collection) volume, and N_1^0 is the initial population in the lower (ground) state (*e.g.*, Eckbreth 1996). In Eq. (C.1), B_{12} & B_{21} are the Einstein coefficients for stimulated absorption and emission, respectively, A_{21} is the Einstein coefficient for spontaneous emission, I_{ν} is the laser excitation irradiance,

$$I_{\nu,\,\mathrm{sat}} \equiv \frac{(A_{21}+Q_{21})\,c}{B_{12}+B_{21}}\ , \tag{C.2}$$

is the saturation spectral irradiance, Q_{21} is the collisional quenching rate constant, and c is the speed of light. For a system in thermal equilibrium with the radiation field, it can be shown that

$$g_1 B_{12} = g_2 B_{21}\ , \tag{C.3}$$

where g_i is the degeneracy of the ith state (Eckbreth 1996). The interpretation of the LIF signal requires a model for the excitation dynamics and this modeling usually has the largest source of systematic errors associated with it (Daily 1997). The most serious concern is the dependence of the signal on the collisional quenching rate constant, Q_{21}, which is dependent on the local composition and temperature (Crosley 1989). If the laser irradiance is increased until $I_{\nu} \gg I_{\nu,\,\mathrm{sat}}$, Eq. (C.1)

reduces to (Daily 1977; Bonczyk & Shirley 1979)

$$S_{\mathrm{F,sat}} = \epsilon_{\mathrm{opt}}\,\epsilon_{\mathrm{q}}\,h\nu\,\frac{\Omega_{\mathrm{c}}}{4\pi}\,V_{\mathrm{c}}\,\frac{A_{21}}{1+g_1/g_2}\,N_1^0\ , \tag{C.4}$$

where we have also used the result of Eq. (C.3). In this regime, the fluorescence signal is independent of both the laser irradiance and the quenching rate. Physically, in this regime the rates of laser absorption and emission are so large that they dominate the state-to-state energy transfer into and out of the levels (Eckbreth 1996). This model relies on several assumptions whose applicability need to be discussed. The first is that the system must be described as a two-level system, which is not the case for the CH radical, as we are relying on the use of three states (A, B, and X) in our excitation-detection scheme. However, if the transfer rates out of levels 1 and 2 are balanced by transfer in from other states, this model will also hold. In addition, it may also be valid when broadband fluorescence detection is used, if the rotational transfer in the upper state is fast (Hanson *et al.* 1990). Fast rotational transfer in the upper state is a good approximation for the atmospheric flames studied here. The second assumption that must be satisfied is that the laser's spectral bandwidth must be broad compared to the bandwidth of the molecular transition, satisfied here as the laser line width is $\approx 0.5\,\mathrm{cm}^{-1}$ as compared to the $0.3\,\mathrm{cm}^{-1}$ absorption line width of the CH molecule at 2300 K (Sutton & Driscoll 2003). The third requirement is that the system reaches steady state, which requires that the time to reach steady state be much shorter than both the fluorescence decay time and the laser pulse length. According to Verdieck & Bonczyk (1981), a few picoseconds are sufficient for these transitions to saturate, and a 10 ns pulse length is sufficient for the system to reach steady state. Chen & Mansour (1997) found that both the fluorescence decay time and the laser pulse length (6 ns) were much larger than the time to reach steady state for atmospheric flame conditions. However, Chen & Mansour (1997) also found that collisional quenching effects can be important, even under saturated conditions, if the decay time is not less than the laser pulse length. Various estimates for the CH decay time give values close to 2 ns (Sutton & Driscoll 2003), which is smaller than our ≈ 10 ns laser pulse length.

The ratio of the fluorescence signal, S_{F}, to that at a reference state, $S_{\mathrm{F,ref}}$, is given by [see Eq. (C.4)]

$$\frac{S_{\mathrm{F}}}{S_{\mathrm{F,ref}}} = \frac{C_{\mathrm{opt}}}{C_{\mathrm{opt,ref}}}\,\frac{C_{\mathrm{L}}}{C_{\mathrm{L,ref}}}\,\frac{f_{\mathrm{B},J}(T)}{f_{\mathrm{B},J}(T)_{,\mathrm{ref}}}\,\frac{N_{\mathrm{CH}}}{N_{\mathrm{CH,ref}}}\ , \tag{C.5}$$

where C_{opt} is a constant that depends on the collection efficiency of the optics, C_{L} accounts for the laser pulse shape and the overlap of the laser line and the absorption line, $f_{\mathrm{B},J}(T)$ is the Boltzmann fraction that defines the fractional population of the lower laser-coupled state J, and N_{CH} is the number density of the CH radical (Sutton & Driscoll 2003). Here we have utilized the fact that the

number density of CH radicals in the lower rotational state is given by a Boltzman distribution,

$$N_1^0(T;J) = f_{\mathrm{B},J}(T)\, N_{\mathrm{CH}} \ . \tag{C.6}$$

In the case where

$$\frac{C_{\mathrm{opt}}}{C_{\mathrm{opt,ref}}} = \frac{C_{\mathrm{L}}}{C_{\mathrm{L,ref}}} = \frac{f_{\mathrm{B},J}(T)}{f_{\mathrm{B},J}(T)_{,\mathrm{ref}}} = 1 \tag{C.7}$$

the relative CH number density is directly obtained from the measurement of the relative CH fluorescence signal alone.

In our study, the measurements were performed with the same collection optics and similar flame location, so $(C_{\mathrm{opt}}/C_{\mathrm{opt,ref}}) = 1$. The ratio $(C_{\mathrm{L}}/C_{\mathrm{L,ref}})$ is dependent on the Doppler-broadening of the absorption line and is proportional to $(T/T_{\mathrm{ref}})^{1/2}$ for different flame temperatures. Sutton & Driscoll (2003) find that for their methane- and propane-air experiments, where the temperature varies from 1950–2300 K, $(C_{\mathrm{L}}/C_{\mathrm{L,ref}})$ is equal to 1.0 ± 0.04. The Boltzmann distribution determines the fraction of molecules in the J^{th} rotational state at a temperature, T,

$$f_{\mathrm{B},J}(T) = B_{\mathrm{R}}\,(2J+1)\,\frac{hc}{k_{\mathrm{B}}T}\,\exp\left[-B_{\mathrm{R}}J(J+1)\frac{hc}{k_{\mathrm{B}}T}\right] \ , \tag{C.8}$$

where k_{B} is the Boltzmann constant and B_{R} is the rotational constant for the molecule, given by $B_{\mathrm{R}} = h/(8\pi^2 c\, I_{\mathrm{R}})$ with I_{R} the moment of inertia for the molecule. The rotational constant for the ground state of the CH radical is $B_{\mathrm{R}} = 14.2\,\mathrm{cm}^{-1}$ (Eckbreth 1996). The $J = 7$ state is a transition that is relatively insensitive to temperature variations while still providing a large fluorescence yield, and results in $(f_{\mathrm{B},J}(T)/f_{\mathrm{B},J}) = 1.0 \pm 0.04$ for the range of temperatures reported above (Sutton & Driscoll 2003). Sutton & Driscoll find that

$$\frac{C_{\mathrm{opt}}}{C_{\mathrm{opt,ref}}}\frac{C_{\mathrm{L}}}{C_{\mathrm{L,ref}}}\frac{f_{\mathrm{B},J}(T)}{f_{\mathrm{B},J}(T)_{,\mathrm{ref}}} = 1 \tag{C.9}$$

to within $\pm 5\,\%$.

The result given by Eq. (C.5) would hold if the fluorescence signal was fully saturated both in time and space. However, both spatial and temporal "wing" effects result in some portion of the fluorescence signal arising from non-saturated fluorescence (Daily 1997). Due to the low value of the saturation spectral intensity for CH, the majority of the laser pulse will saturate, allowing a large collection gate time and a significant increase in the collected fluorescence signal (Sutton & Driscoll 2003). Sutton & Driscoll find that the temporal and spatial non-saturation effects contribute to approximately 5 % additional uncertainty each. Thus, the relative concentration of CH radicals in a specific experiment to that at the reference state can be estimated by directly comparing the ratio

of the fluorescence signals,

$$\frac{N_{\mathrm{CH}}}{N_{\mathrm{CH,ref}}} = \frac{S_{\mathrm{F}}}{S_{\mathrm{F,ref}}} \ , \tag{C.10}$$

to within an experimental uncertainty of $\approx \pm 10\,\%$.

Equation (C.10) relies on multiple assumptions regarding saturation, achievement of steady-state conditions, etc. If some of these assumptions are not fully satisfied, the largest source of error would be the dependence of the fluorescence signal on the (local) quenching environment. Fortuitously, the fluorescence-decay rate (collisional quenching) is found to be insensitive to the CH position within low-pressure flames; *i.e.*, the quenching is not strongly sensitive to variations of species concentration and flame temperature (Rensberger *et al.* 1988; Chen & Mansour 1997). Rensberger *et al.* (1988) find that at constant pressure, the collisional quenching varies by less than 50 % for different flames (methane-, propane-, and acetylene-air), positions and excitation transitions, and suggest that quantitative measurement of CH using either the A or B state may be much easier than initially anticipated. As the energy transfer from the B to the A state is relatively independent of the flame conditions, excitation to the B state and measurement of the A–X fluorescence provides good measure of the ground state population while eliminating almost all scattered light problems (Rensberger *et al.* 1988). Renfro *et al.* (2001) showed that the fluorescence lifetime varies significantly for different fuels, and they found it necessary to take this into account in performing relative concentration measurements. However, for a specific fuel, the quenching rate should not vary significantly, and thus by using a different reference state for each fuel, quenching effects can be minimized further. In summary, although many assumptions have been made in the derivation of Eq. (C.10), it should provide reasonably accurate results for the conditions utilized in this study.

A schematic of the PLIF apparatus is given in Fig. C.1. CH fluorescence measurements are obtained by exciting the $\mathrm{Q}_1(7)$ transition of the $B^2\Sigma - X^2\Pi(0,0)$ CH band at 390.30 nm, in the UV (*e.g.*, Carter *et al.* 1998; Sutton & Driscoll 2003). Excitation to the B state yields a higher signal than excitation to the A state (Luque *et al.* 2000) and a large wavelength shift between excitation and fluorescence, facilitating filtering of Mie- and Rayleigh-scattering interference, important in particle-seeded flames. The $\mathrm{Q}_1(7)$ band provides a high signal level and low temperature sensitivity. This excitation scheme has previously been used in several studies of the CH radical (Carter *et al.* 1998; Ratner *et al.* 2000; Sutton & Driscoll 2003; Han & Mungal 2003). The UV beam is obtained from a tripled Nd:YAG (355 nm)-pumped dye laser operating at 10 Hz (Spectra-Physics PRO-290 & Sirah PrecisionScan). Pulse duration is ≈ 10 ns with a line width of $\approx 0.5\,\mathrm{cm}^{-1}$ (8 pm).

The output of the dye laser is passed through a pair of cylindrical lenses (CVI; 150 mm and 500 mm at right angles) and yields a laser sheet with a Rayleigh range centered on the jet axis. Laser-sheet nonuniformity on a shot-to-shot and mean basis could lead to a systematic error (Hanson

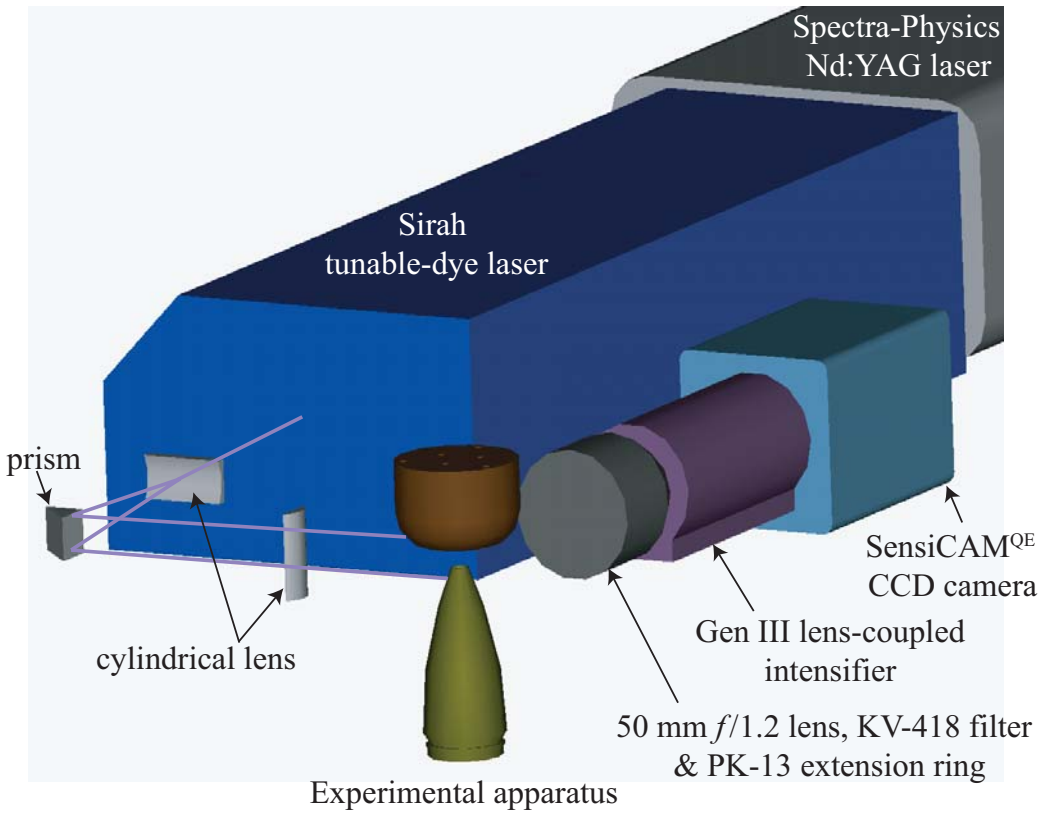

Figure C.1: PLIF experimental apparatus.

et al. 1990). Daily (1997) points out that typical laser systems produce beams that are composed of a variety of transverse modes that can focus to an Airy distribution, which has multiple peaks in the transverse direction, rather than a Gaussian (single-peaked) distribution. These pulsed lasers are also typified by significant shot-to-shot variability of pulse energy and temporal behavior. Daily notes that such variabilty could contribute to uncertainty in the measurement quantity. To minimize such effects, several steps were taken. The laser sheet was spatially filtered into a uniform beam using a set of knife-edges (Coherent 61–1137), and focused tightly near the axis. A second spatial filtering was performed as close to the experiment as possible to block the extra transverse modes. The resulting laser sheet cross-sectional area was typically $A_\mathrm{b} \approx 6\,\mathrm{mm} \times 0.5\,\mathrm{mm} = 0.03\,\mathrm{cm}^{-1}$. Laser sheet uniformity was monitored using laser burn paper (Zap-IT Z–25). Secondly, relative concentration measurements were performed with the CH layer located at the same axial location (or as close as possible for some near-limit flames), resulting in a similar illumination field for flames of variable stoichiometry. In addition, the data from multiple shots (typically of the order of 1000 images) are processed individually and the statistics are determined by finding the mean and standard deviation of the single-shot data. The average laser power was monitored and maintained constant for all experiments for a specific fuel, thus the shot-to-shot variation of laser power should only lead to an increase in the uncertainty of the quantity, rather than a systematic variation. The

laser spectral intensity is given by

$$I_\nu = \frac{E_\mathrm{p}}{\tau_\mathrm{p}\, A_\mathrm{b}\, SW} \ , \tag{C.11}$$

where E_p is the pulse energy, τ_p the pulse length, A_b the laser beam cross-sectional area, and SW the laser spectral width, typically specified in units of cm^{-1} (Daily & Rothe 1999). The saturation behavior (spectral intensity) of the CH radical has been studied by several authors. Bonczyk & Shirley (1979) find a value of $I_{\nu,\,\mathrm{sat}} = 10^5 - 10^6\,\mathrm{W/(cm^2\,cm^{-1})}$, while Takubo *et al.* (1983) found a value of $I_{\nu,\,\mathrm{sat}} = 10^4\,\mathrm{W/(cm^2\,GHz)} = 10^5\,\mathrm{W/(cm^2\,cm^{-1})}$. Here we will utilize the more conservative estimate of $I_{\nu,\,\mathrm{sat}} = 10^6\,\mathrm{W/(cm^2\,cm^{-1})}$. For the PLIF profiles presented here, a typical laser power of $\approx 15\,\mathrm{mJ/pulse}$ results in a saturated laser spectral intensity of $I_\nu \approx 10^8\ \mathrm{W/(cm^2\,cm^{-1})}$. This laser intensity is two orders of magnitude higher than that required for saturation. Due to the high laser intensity used in this study, the portion of the signal in the linear regime should be much lower than the saturated portion.

Fluorescence was collected with a Nikon 50 mm, $f/1.2$ lens at magnifications near 1:1. These magnifications were achieved through the use of a 27.5 mm extension ring (Nikon PK-13). A Schott KV-418 long-pass filter is used to reject Mie and Rayleigh scattering (Carter *et al.* 1998). This filter transmits approximately 90% of the fluorescence near 430 nm, while having a large extinction ratio at the excitation wavelength. Fluorescence is recorded from the A–$X(1,1)$, A–$X(0,0)$, and B–$X(0,1)$ bands in the 420–440 nm range. By utilizing a high-transmission long-pass filter that rejects the excitation wavelength, the system detects the broadband emission from multiple lines and results in maximum signal. The use of broadband detection minimizes bias due to rotational-energy transfer in the upper (A) state (Garland & Crosley 1985), as the fluorescence is collected from all of the rotational bands of the A–X transition. Detection relies on a lens-coupled intensifier (Ultra-Blue Gen-III, Cooke Corp. VS-364) with a cooled CCD (Cooke Corp. SensiCAM$^{\mathrm{QE}}$, binned to $344 \times 260\,\mathrm{pix}^2$; a binned pixel = 46 μm in the flow). Images were recorded at 10 Hz, as dictated by the laser pulse rate. A sample CH PLIF (single-exposure) image is depicted in Fig. C.2(a), and an average of 1000 exposures is shown in Fig. C.2(b). Daily (1997) points out that the most significant advantage to using intensifiers for LIF detection is the ability to gate the detector in time. In this study, a 70 ns gate time rejects the background light (chemiluminescence, etc.) at very high ratios, while retaining the fluorescence signal. The main disadvantage to the use of such intensifier tubes is their reduced spatial resolution (Hanson *et al.* 1990). The intensifier limits the spatial resolution of the detection system, and thus the CCD may be binned by a factor of 16 (1 binned pixel = 4×4 CCD pixels), without loss of spatial resolution. This binning is also required to achieve an adequate signal, and reduces the storage requirements for the CH PLIF data.

PLIF excitation spectroscopy helps to confirm the CH excitation and helps determine the dye-laser wavelength that results in optimum signal-to-noise ratio. Figure C.3 shows an experimentally

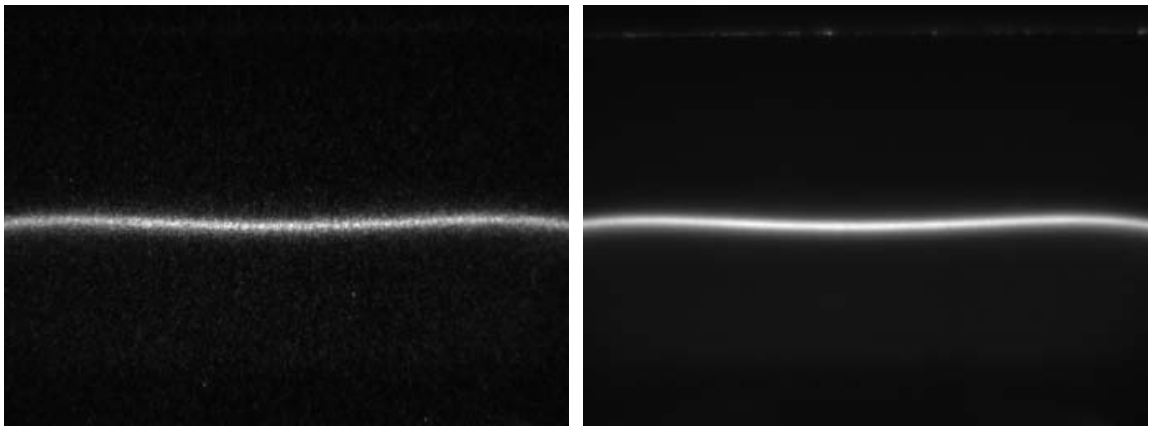

(a) Single image (b) 1000-exposure average

Figure C.2: Example PLIF images for a methane-air flame ($\Phi = 1.0, L/d = 0.8$) at a resolution of $344 \times 260\,\mathrm{pix}^2$. Stagnation plate is visible in averaged image.

measured CH excitation scan, at a resolution of 0.5 pm. To obtain this scan, a series of images were recorded as the laser was scanned over the indicated wavelength range. Each image corresponds to a single excitation wavelength and was processed to determine the fluorescence intensity at this wavelength. The fluorescence (or flame) region was extracted by thresholding an image obtained by averaging over the entire dataset and multiplying each image by the resulting binary mask. Typical scans recorded series of more than 5000 images. Spectrum simulations are performed with LIFBASE (Luque & Crosley 1999). The scan depicted in Fig. C.3 was performed with a laser power of 0.2 mJ/pulse, in a 1mm×2cm sheet, producing a laser spectral intensity of $I_\nu \approx 2 \times 10^6 \approx I_\nu^{sat} \approx 10^6$ W/(cm^{2}cm^{-1}). This scan is thus in the partially saturated regime. An average image with no laser excitation was used to remove the average chemiluminescence and dark noise. The output of the Excalite 389 dye used in this study is from 382–392 nm, leading to the fall-off noted in the 391–393 nm range. Comparisons to simulation show that the location of the lines is in excellent agreement. Figure C.4 shows a narrow-band spectrum obtained at a higher laser power of 5 mJ/pulse and a resolution of 0.2 pm. This scan is in the saturated regime, and the line width of the laser can be estimated to be 8 pm (0.5 cm^{-1}) from the measured CH lineshapes. This spectrum shows the off-resonance signal that must be subtracted to obtain the pure CH fluorescence signal when the diagnostics are operated in the saturated regime.

To determine the CH fluorescence signal, the fluorescence was detected with the laser tuned to the absorption wavelength (390.3 nm), and then subsequently measuring the signal with the laser tuned off of the absorption line (390.5 nm). The off-resonance signal consists of broadband fluorescence from soot precursors (Norton & Smyth 1991), Rayleigh scattering of the laser sheet, a small amount of chemiluminescence, and the dark noise of the detection system (Sutton & Driscoll 2003). In laminar

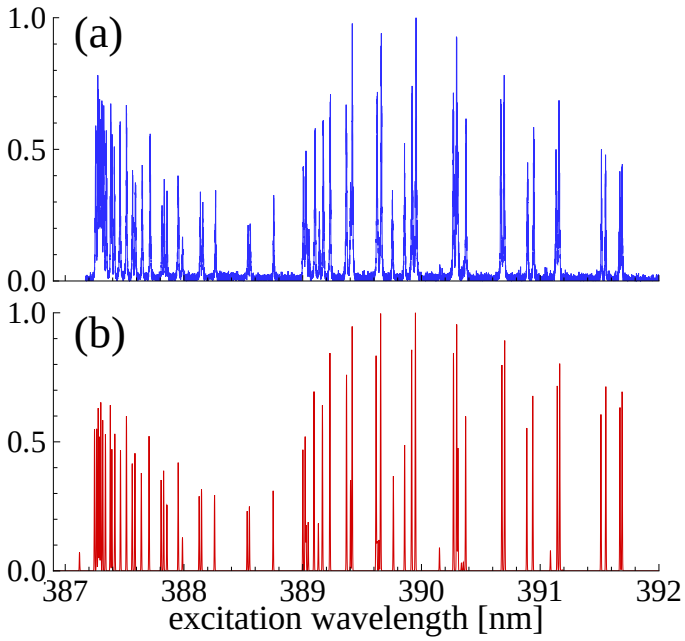

Figure C.3: Experimental (a) and simulated (b) CH spectra in a methane-air flame ($\Phi = 0.9, L/d = 0.8$) at a laser power of 0.2 mJ/pulse. Spectral simulation performed using LIFBASE (Luque & Crosley 1999).

methane-air diffusion flames, Norton & Smyth (1991) found that broadband fluorescence attributed to polycyclic aromatic hydrocarbons can often be stronger than the CH signal when fluorescence is detected with a narrow bandpass filter rather than a monochromator. When broadband detection is utilized, such as in the work reported here, this background "noise" source can be even more significant. Thus, the fluorescence signal is taken as

$$S_{\mathrm{CH}} = S_{390.3\,\mathrm{nm}} - S_{390.5\,\mathrm{nm}} \ , \tag{C.12}$$

where $S_{390.3\,\mathrm{nm}}$ and $S_{390.5\,\mathrm{nm}}$ are the on- and off-resonance signals, respectively. A typical experiment consisted of recording a set of images of the laser sheet with no flame (typically 200 images), then recording the data with the flame (1000 PLIF images). Following the recording of the on-resonance PLIF data a set of 200 off-resonance images was recorded. The off-resonance and no-flame images were averaged and provided two different background images, the no-flame images recorded the Rayleigh scattering, chemiluminescence, and dark-noise only, while the off-resonance signal also included fluorescence from species in the flame other than CH. In preliminary methane-air experiments the off-resonance images were not recorded, and the no-flame images were used to correct the profiles for the background noise (Bergthorson *et al.* 2005a). Figure C.5 shows a profile obtained from the centerline column of an average of 1000 exposures on-resonance, the centerline profile from the no-flame images, and the corrected profile. These preliminary results were used to measure the

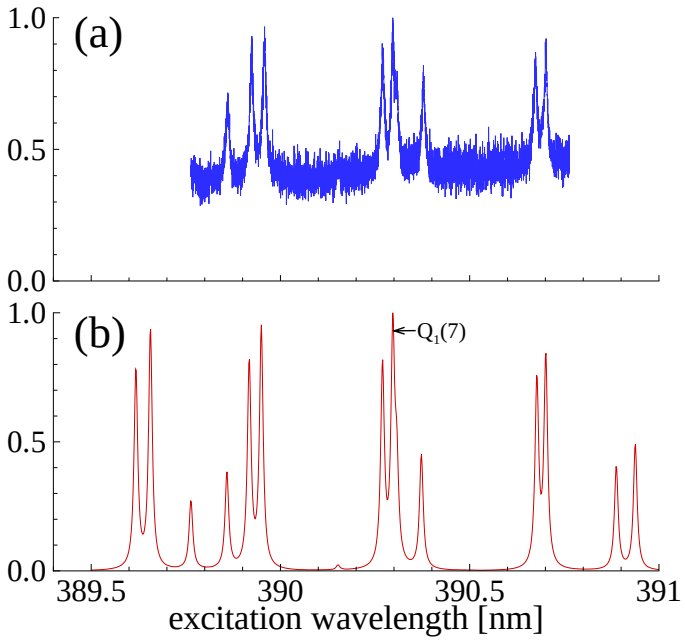

Figure C.4: Experimental (a) and simulated (b) CH spectra in a methane-air flame ($\Phi = 0.9$, $L/d = 0.8$) at a laser power of 5 mJ/pulse. Spectral simulation performed using LIFBASE (Luque & Crosley 1999) with an instrumental resolution of 8 pm (0.5 cm^{-1}). The $Q_1(7)$ transition used in this study is indicated for reference.

spatial profiles of CH and were not used to estimate CH concentrations. Figure C.6 depicts on- and off-resonance profiles, obtained from the center column of the averaged images, and the extracted CH profile. For methane-air flames, the profiles obtained do not vary significantly in shape or location if the no-flame image is used to correct the data rather than the off-resonance image. However, for very lean flames ($\Phi = 0.7$), the measured profile is mostly due to off-resonance signal, and the CH profile width will be overestimated if the off-resonance signal is not subtracted. Removing the off-resonance signal is very important in rich C_2 flames, where soot precursors are more prevalent. Figure C.7 shows the averaged on- and off-resonance profiles, as well as the extracted CH fluorescence signal. The averaged no-flame profile is also included for reference, and represents the Rayleigh scattering, chemiluminescence, and dark-noise signals. The contribution from non-CH fluorescence is evident if the off-resonance and no-flame profiles are compared. The corrected CH profile has a more asymetric shape than the uncorrected profile, a result consistent with numerical simulations of these rich C_2 flames. The average off-resonance image was subtracted from each on-resonance image to extract the CH signal when performing relative CH concentration measurments. CH profiles are obtained from (corrected) single-shot images by summing across the (flat) central portion of the flame. 50-column averaging, about the jet axis, yields good (single-frame) profile statistics.

Renfro *et al.* (2001) showed that the spatial profiles of CH radicals in counterflow diffusion flames of methane and ethane were well-characterized by Gaussians. Three parameters were necessary to

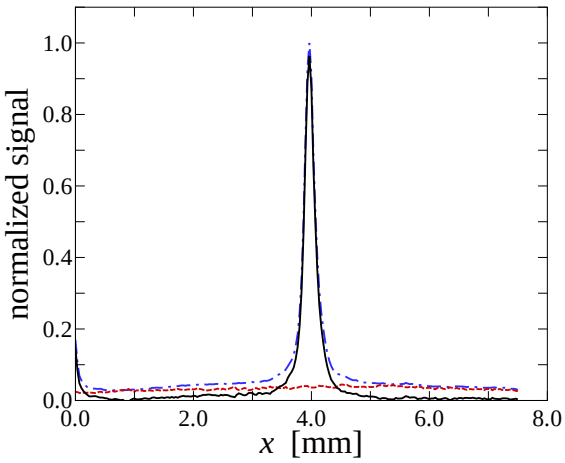

Figure C.5: Preliminary CH PLIF processing technique in a $\Phi = 1.0$ methane-air flame. On-resonance data (dash-dot) are corrected by subtracting the average no-flame images (dash) to yield the corrected profile (solid). The on-resonance profile is extracted from the center (single) column of an average of 1000 single exposures for clarity.

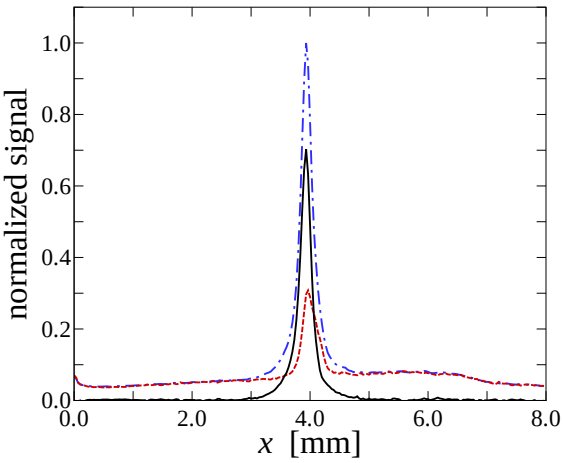

Figure C.6: PLIF processing technique in a $\Phi = 1.0$ methane-air flame. On-resonance data (dash-dot) are corrected by subtracting an average of the off-resonance images (dash) to yield the CH fluorescence signal (solid). The on-resonance profile is extracted from the center (single) column of an average of 1000 single exposures for clarity.

fit the data, the peak (relative) concentration, the axial location, and the profile width. Early work used Gaussian fits to the profiles to extract these three parameters from each image. However, in some of the rich ethane- and ethylene-air flames studied here, the CH profiles were found to be asymmetric (see Fig. C.7). Typically the profiles showed a sharp rise on the "cold" side of the profile and a longer tail on the "hot" side of the flame. In addition, the profiles were found to be better represented by Lorentzian fits in the tail region of the profile. Therefore, "two-sided" Lorentzian fits were performed on the single-image profiles, given by

$$S_{\mathrm{CH}}\left(x < x_{\mathrm{CH}}\right) = \frac{S_{\mathrm{CH,max}}\, w_1^2}{(x - x_{\mathrm{CH}})^2 + w_1^2} \quad , \quad S_{\mathrm{CH}}\left(x > x_{\mathrm{CH}}\right) = \frac{S_{\mathrm{CH,max}}\, w_2^2}{(x - x_{\mathrm{CH}})^2 + w_2^2} \, , \tag{C.13}$$

where $S_{\mathrm{CH,max}}$ is the peak intensity, x_{CH} is the peak location, and w_1 and w_2 are the widths corresponding to the half-maximum value on either side of x_{CH}. Thus, the Full-Width at Half-Maximum (FWHM) for the fit profile is given by the sum $w_1 + w_2$. Performing a fit on each image allows the full information content of the profile to be utilized in calculating the four parameters. As a consistency check, the peak value and location were also extracted from the raw data for each image. The FWHM was found by interpolating the profile to sub-pixel accuracy to find the locations of the half-maximum on each side of the peak and taking the difference between the two. These three parameters (peak intensity, peak location, and FWHM) were plotted as a function of image number from both the fit and the raw data. Typically, the peak intensity of the fit was slightly

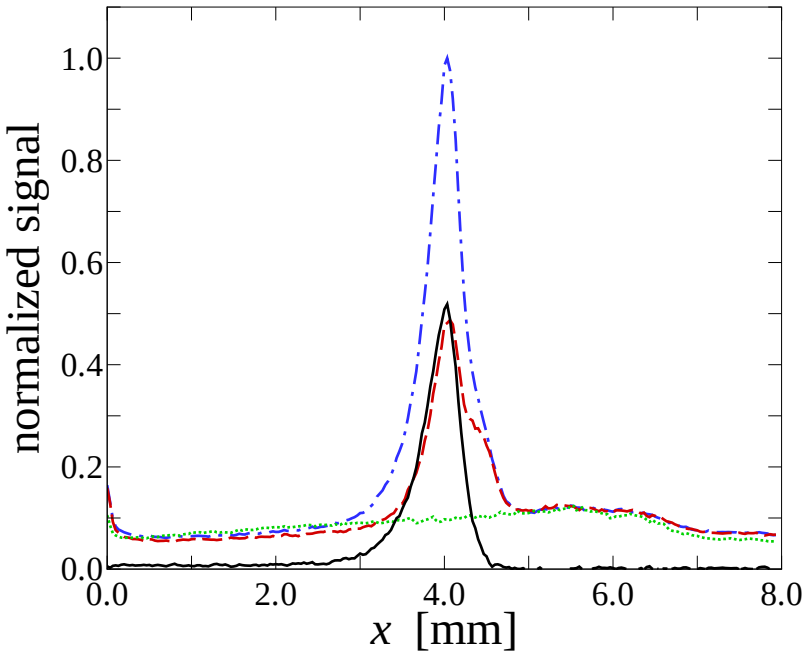

Figure C.7: PLIF processing technique in a $\Phi = 1.5$ ethane-air flame. On-resonance data (dash-dot) are corrected by subtracting an average of the off-resonance images (dash) to yield the CH fluorescence signal (solid). An averaged no-flame profile is included for reference (dot). The on-resonance profile is extracted from the center (single) column of an average of 1000 single exposures for clarity.

higher than that obtained from the raw data, as the peak could reside spatially between two pixels. The peak location was consistent between the fit and raw data, although there was less scatter in the fit data (sub-pixel stability in flame location). The FWHM from the fit was also typically smaller than that found from the raw data. The lower peak intensity in the raw data results in a lower half-maximum value and thus a resulting larger profile width. These trends were consistent across the various flames studied here. Relative concentration, profile width, and profile location data are reported from fit values, as the use of multiple data points in performing the fit results in reduced uncertainty. The mean and standard deviation for the fit parameters were calculated for each 1000 image record. Figure C.8 gives several CH profiles, obtained from a single image (50-column averaging), the average profile (single column, 1000-image average) and a "two-sided" Lorentzian using the average fit parameters. Good agreement between the single-image and average profiles indicates that the flame is quite stable over the 100 second experiment (1000 images at 10 Hz), and that the flame is quite flat over the 50 columns used to extract the single-image profiles. Flame stability is necessary as any flame movement between the recording of the PLIF data and the off-resonance signal could lead to uncertainty in the CH profile. Using this technique, the CH profile in $\Phi = 0.7$ methane-air flames was detected, below the minimum detection limit of $\Phi = 0.8$ found by Chen & Mansour (1997), and $\Phi = 0.85$ found by Sutton & Driscoll (2003). The lower

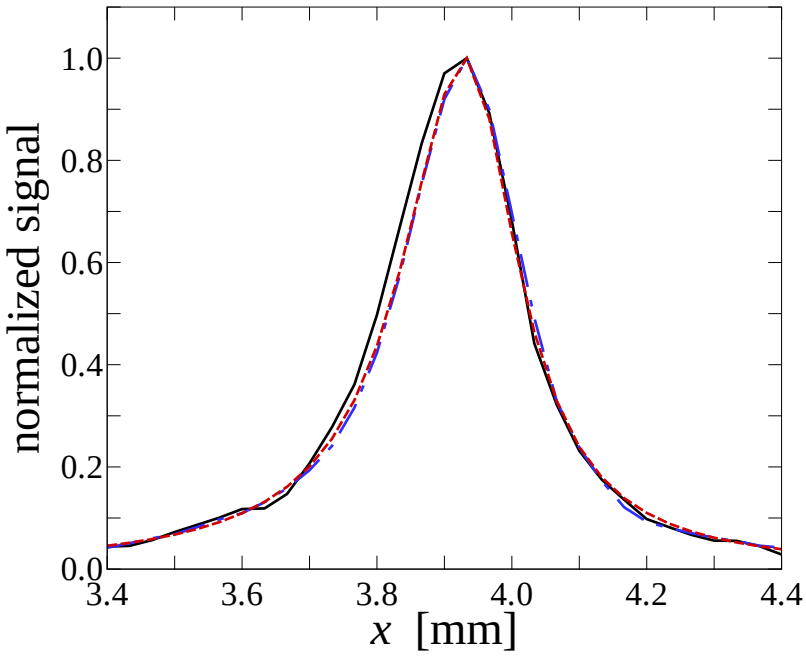

Figure C.8: Comparison between profiles obtained from a single image (solid), an average of 1000 exposures (dash-dot), and the Lorentzian function obtained with the mean fit values (dash).

detection limit found in this study is most likely attributable to a higher signal-to-noise ratio. The high signal-to-noise ratio is evident in the comparison of the single-image profile to that obtained with an average of 1000 images in Fig. C.8.

C.1 "Two-sided" Lorentzian sample script

Single-shot PLIF profiles were fit using a "two-sided" Lorentzian using MATLAB. The following sample script corresponds to the contents of the file `doublelorentzian.m` which defines the function that is fit to each single image profile.

```
function [y_fit] = doublelorentzian(fit,xdata)
S_CH=fit(1)*100; %Factor of 100 maintains similar order of magnitude for fit parameters
x_CH=fit(2);
w1=fit(3);
w2=fit(4);
for i=1:1:size(xdata,2)
    if xdata(i) < x_CH;
        y_fit(i)=S_CH*w1^2./((xdata(i)-x_CH).^2+w1^2);
    else
        y_fit(i)=S_CH*w2^2./((xdata(i)-x_CH).^2+w2^2);
    end
end
```

Appendix D

CANTERA stagnation flame simulations

Simulations of stagnation point flames were performed using the CANTERA software package developed by Goodwin (2003). To demonstrate how the flame simulations reported in this thesis were performed using CANTERA, example PYTHON input scripts are presented. The first script specifies the boundary conditions and input parameters, creates a gas and a stagnation flame object, provides a guess for the solution using a profile obtained from the thermodynamic equilibrium concentrations, and solves the stagnation-flow problem. The solution is obtained first using a mixture-averaged transport formulation without the energy equation, and then with the energy equation. The second solution is refined further, typically to greater than 300 grid points to ensure good convergence, as discussed below. The multicomponent transport formulation is then employed to find the final solution. Note that additional programming, such as alterations to the CANTERA STAGNATIONFLOW.PY script are not described here. As well, simple scripts such as WRITE.PY were also written to allow the flame solution to be written to comma-delimited files. These simple scripts are not provided here, for brevity.

D.1 CANTERA stagnation-flame script

```
from Cantera import *
from Cantera.OneD import *
from Cantera.OneD.StagnationFlow import StagnationFlow
import write
########################parameter values#########################
p          =   1*OneAtm # pressure
tburner    =   295.0    # burner temperature
tsurf      =   335.9    # plate temperature
```

```
uinlet     =   0.7636   # m/s
spreadrate =   118.4    # 1/s
comp       =  'CH4:1.00, O2:2.00, N2:7.52'  # premixed gas composition
filnam     =  'run226_'
flameloc   =   0.25     # initial guess for flame location
slopemix   =   0.05     # refinement criteria
slopemulti =   0.10
curvemix   =   0.8
curvemulti =   0.8
###############################################################
# Set the solution domain:
initial_grid = [0.0, 0.0005, 0.001, 0.002, 0.003, 0.004, 0.005, 0.0055, 0.006]  # m
tol_ss    = [1.0e-5, 1.0e-13]       # [rtol atol] for steady-state problem
tol_ts    = [1.0e-2, 1.0e-5]        # [rtol atol] for time stepping
loglevel  = 1                       # amount of diagnostic output (0-5)
refine_grid = 1                     # 1 to enable refinement, 0 to disable
ratio = 3.0
prune = 0.0
mechanisms  = ['gri30', 'C3_Davis', 'SDmech_20050218', 'SDmech_20030830']
gasid = ['gri30_mix', 'C3-Davis', 'SDmech_20050218', 'SDmech_20030830']
###############################################################
for i in range(len(mechanisms)):
        print 'Starting solution with mechanism: '+mechanisms[i]
        ################ create the gas object ########################
        gas = IdealGasMix(mechanisms[i]+'.cti', gasid[i])
        gas.addTransportModel('Multi')
        # set its state to that of the unburned gas at the burner
        gas.setState_TPX(tburner, p, comp)
        mdot = gas.density()*uinlet            # kg/m^2/s
        ################ create stagnation flame object ##################
        f = StagnationFlow(gas = gas, grid = initial_grid)
        # set the properties at the inlet
        f.inlet.set(massflux = mdot, mole_fractions = comp, temperature = tburner)
        f.inlet.setSpreadRate(spreadrate)
        # set the surface state
        f.surface.setTemperature(tsurf)
```

```
# set the simulation properties
f.set(tol = tol_ss, tol_time = tol_ts)
f.setMaxJacAge(100, 200)
f.setTimeStep(1e-5, [1,2,5,10,20])
f.setRefineCriteria(ratio = 10.0, slope = 1.0, curve = 1.0, prune = 0.0)
f.set(energy = 'off')
# initialize and solve the problem
f.init(products='equil', flame=flameloc) # assume adiabatic equilibrium products
f.solve(loglevel, refine_grid)
# change refinement criteria for full simulation
f.setRefineCriteria(ratio=ratio, slope=slopemix, curve=curvemix, prune=prune)
f.set(energy = 'on')
f.solve(loglevel,refine_grid)
f.save(filnam+mechanisms[i]+'_mix.xml','energy','methane')
write.csvwrite(filnam+mechanisms[i]+'_mix',f,gas)
print 'finished mixture-averaged solution with mechanism: '+mechanisms[i]
# Switch to Multicomponent model
gas.switchTransportModel('Multi')
f.flow.setTransportModel(gas)
f.setTimeStep(1.0e-5, [10,50,100,100,200])
f.set(energy = 'off')
f.solve(loglevel, 0)
f.set(energy = 'on')
f.solve(loglevel, 0)
f.save(filnam+mechanisms[i]+'_multi_norefine.xml','energy','methane')
write.csvwrite(filnam+mechanisms[i]+'_multi_norefine',f,gas)
print 'finished multicomponent solution (no refinement) with mechanism: '+mechanisms[
f.setRefineCriteria(ratio=ratio, slope=slopemulti, curve=curvemulti, prune=prune)
f.solve(loglevel, refine_grid)
f.save(filnam+mechanisms[i]+'_multi_refine.xml','energy','methane')
write.csvwrite(filnam+mechanisms[i]+'_multi_refine',f,gas)
print 'finished multicomponent solution (refined) with mechanism: '+mechanisms[i]
f.showStats()
```

The second script provided here shows how the logarithmic-sensitivty coefficients were calculated using the "brute-force" method. A flame simulation that had previously been saved is restored, using the same boundary conditions and input parameters as used in the previous simulation. The solution is restored by solving the flame with the energy equation off, then again with the energy equation enabled. Flames are solved changing one of the reaction rates at a time by a factor of 1.5. This is performed for all of the reactions in the mechanism. The resulting flame profiles are processed using a MATLAB script to calculate the integral CH-layer location, $x_{\mathrm{CH,int}}$.

D.2 "Brute-force" sensitivity coefficient script

```
from Cantera import *
from Cantera.OneD import *
import write
########################parameter values#########################
p          =   1*OneAtm      # pressure
tburner    =   295.0         # burner temperature
tsurf      =   336.94        # plate temperature
uinlet     =   0.3390        # m/s
spreadrate =   82.8919       # 1/s
comp       =  'CH4:1.298, O2:2, N2:7.52'  # premixed gas composition
filnam     =  'run229_'
tol_ss     = [1.0e-5, 1.0e-13]  # [rtol atol] for steady-state problem
tol_ts     = [1.0e-2, 1.0e-5]   # [rtol atol] for time stepping
loglevel   = 1                  # amount of diagnostic output (0-5)
mechanisms = ['SD2005']
gasid      = ['SD2005']
i=1
gas = IdealGasMix(mechanisms[i]+'.cti', gasid[i])
gas.addTransportModel('Multi')
# set its state to that of the unburned gas at the burner
gas.setState_TPX(tburner, p, comp)
mdot = gas.density()*uinlet                # kg/m^2/s
#
f = StagnationFlow(gas = gas, grid = initial_grid)
# set the properties at the inlet
f.inlet.set(massflux = mdot, mole_fractions = comp, temperature = tburner)
```

```
f.inlet.setSpreadRate(spreadrate)
# set the surface state
f.surface.setTemperature(tsurf)
# initialize the simulation
f.init()
# set the simulation properties
f.set(tol = tol_ss, tol_time = tol_ts)
f.setMaxJacAge(100, 200)
f.setTimeStep(1e-5, [1,2,5,10,20,50,100,100,200])
gas.switchTransportModel('Multi')
f.flow.setTransportModel(gas)
f.restore('run229_SD2005_multi.xml','energy')
gas.setMultiplier(M,i)
f.set(energy = 'off')
f.solve(loglevel,0)
f.set(energy = 'on')
f.solve(loglevel,0)
prefix='run229_SD2005_sens_'
write.csvwriteshort(prefix+'init',f,gas)
#Adjust parameters and loop through solutions:
M=1.5 #M is the multiplier adjustment
for i in range(0,174): #SD2005 has 175 reactions
        f.restore('run229_SD2005_multi.xml','energy')
        gas.setMultiplier(M,i)
        f.set(energy = 'off')
        f.solve(loglevel,0)
        f.set(energy = 'on')
        f.solve(loglevel,0)
        write.csvwriteshort(prefix+str(i),f,gas)
        gas.setMultiplier(1,i)
        print 'finished solution '+str(i)
        f.showStats()
```

D.3 Sensitivity analysis

The influence of each model parameter on the simulation prediction can be determined through sensitivity analysis. The sensitivity coefficients may be calculated as part of the simulation or they may be performed using the "brute-force," or explicit method (*e.g.*, Qin *et al.* 2000; Davis & Wang 2002). The CHEMKIN PREMIX package calculates these sensitivity coefficients as part of the solution for freely propagating laminar flames. In the current study, the sensitivity of specific simulation features to variations in the model parameters must be estimated. Specifically, the location of the CH profile is utilized to compare experimental and simulated results, and the sensitivity of this location to the model parameters is required. To determine the sensitivity of the CH profile location to variations in the model parameters, the "brute-force" method is utilized, as suggested by Frenklach (1984). Simulations are performed varying a single parameter at a time, and the profiles of each are compared to the original simulation to determine the effect that each parameter has on the predicted output. To minimize errors due to mesh resolution effects, Goldenberg & Frenklach (1995) suggest using quadratic interpolation to find the location of peak concentrations. Rather than interpolating the data, it was decided to utilize the integral CH location for determining parameter sensitivities. The integral CH location is defined as

$$x_{\mathrm{CH,int}} = \frac{\int_0^\ell x\ \chi_{\mathrm{CH}}(x)\ \mathrm{d}x}{\int_0^\ell \chi_{\mathrm{CH}}(x)\ \mathrm{d}x}\ , \tag{D.1}$$

where x is the axial coordinate, ℓ is the length of the simulation domain, and $\chi_{\mathrm{CH}}(x)$ is the mole fraction of the CH radical. The calculation of the CH-layer location using an integral alleviates difficulties associated with the mesh refinement and is more robust than simply finding the location of peak CH concentration.

The logarithmic sensitivity coefficient for the integral CH location to each model parameter, $\mathcal{V}_j$, can be calculated using

$$L.S.(x_{\mathrm{CH,int}})_j = \frac{\mathrm{d}\log x_{\mathrm{CH,int}}}{\mathrm{d}\log \mathcal{V}_j} = \frac{\Delta x_{\mathrm{CH,int}}}{x_{\mathrm{CH,int}}}\,\frac{\mathcal{V}_j}{\Delta \mathcal{V}_j}\ , \tag{D.2}$$

or

$$L.S.(x_{\mathrm{CH,int}})_j = \frac{x_{\mathrm{CH,int}}(\mathcal{V}_j + \Delta\mathcal{V}_j) - x_{\mathrm{CH,int}}(\mathcal{V}_j)}{x_{\mathrm{CH,int}}(\mathcal{V}_j)}\,\frac{\mathcal{V}_j}{\Delta \mathcal{V}_j}\ . \tag{D.3}$$

This formulation for the calculation of sensitivity coefficients allows the influence any model parameter to be evaluated. An important consideration in the current experiments is the sensitivity of the model output to the boundary conditions. The boundary conditions are measured experimentally and each have a corresponding uncertainty. Figure D.1 shows the simulation sensitivity to the boundary conditions for a lean, stoichiometric, and rich methane-air flame. In Fig. D.1, the bound-

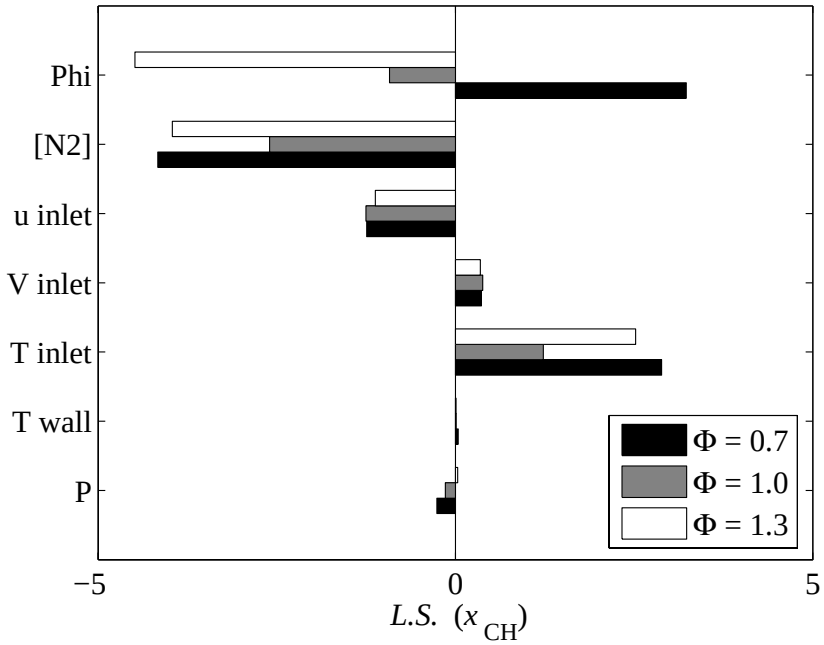

Figure D.1: Logarithmic sensitivity coefficients for the simulation boundary conditions.

ary conditions are the specified equivalence ratio, Phi, the concentration of nitrogen, [N2], the inlet velocity, u inlet, the inlet spreadrate, V inlet, the inlet temperature, T inlet, the wall temperature, T wall, and the pressure, P. The simulations are most sensitive to the inlet mixture composition, which is characterized by the equivalence ratio and the concentration of nitrogen. Thus, the mass flux of each component must be accurately measured, as discussed in Appendix F. For lean flames, increasing the equivalence ratio increases the flame strength, while for stoichiometric and rich flames the flame strength is reduced when the equivalence ratio is increased. The sensitivity to the equivalence ratio is larger for lean and rich flames due to the large variation in flame speed with equivalence ratio. As the flame speed is relatively constant near the stoichiometric point, the sensitivity to Φ is reduced for the stoichiometric flame. As the nitrogen concentration is increased, the flames become weaker and move towards the stagnation plate, indicated by a negative value of the logarithmic sensitivity. Increasing the value of the inlet velocity pushes the flames closer to the stagnation surface, with similar sensitivities seen for all cases. As the spreading rate, or inlet velocity gradient, is increased, the flames move toward the nozzle resulting in a positive sensitivity. The inlet temperature is also an important parameter, increasing the flame strength considerably for lean and rich conditions. The results are almost independent of the wall temperature, as evidenced by the low sensitivity to this boundary condition. The system pressure also exhibits a minor influence on the results.

The logarithmic sensitivity coefficients for each reaction in the mechanism can also be determined using Eq. (D.3). The rate of each reaction is increased by a factor of 50 % and the simulation is

resolved. Previous investigators have increased the reaction rates by a factor of 2 (Qin *et al.* 2000); however, a value of 1.5 as used here is sufficient to observe changes in the simulation output, and results in faster convergence and prevents drastic changes in the simulation output.

D.4 Convergence study

The convergence of the simulations was studied as a function of the number of grid points in the solution. The grid points are determined by an adaptive-mesh refinement script that refines the solution based on three parameters, `ratio`, `curve`, and `slope`. The `ratio` parameter defines the maximum cell-length ratio between adjacent cells. With a uniform initial grid, a value of `ratio` = 3.0 allows the cell size to double between adjacent cells, allowing for adaptive refinement. A value of `curve` = 0.8 was found to give good convergence, and places additional grid points in the regions of high-curvature that exist in these flame simulations. The value of `slope` is reduced to add more grid points to the solution. As the number of grid points gets large, convergence takes excessive amounts of time when using the multicomponent transport model, and the time-integration tends to fail. Figure D.2 shows the convergence properties of the maximum temperature, $T_{\max,i}$, maximum velocity, $u_{\max,i}$, and maximum of the CH profile, $x_{\mathrm{CH},i}$. The values from the ith profile are compared

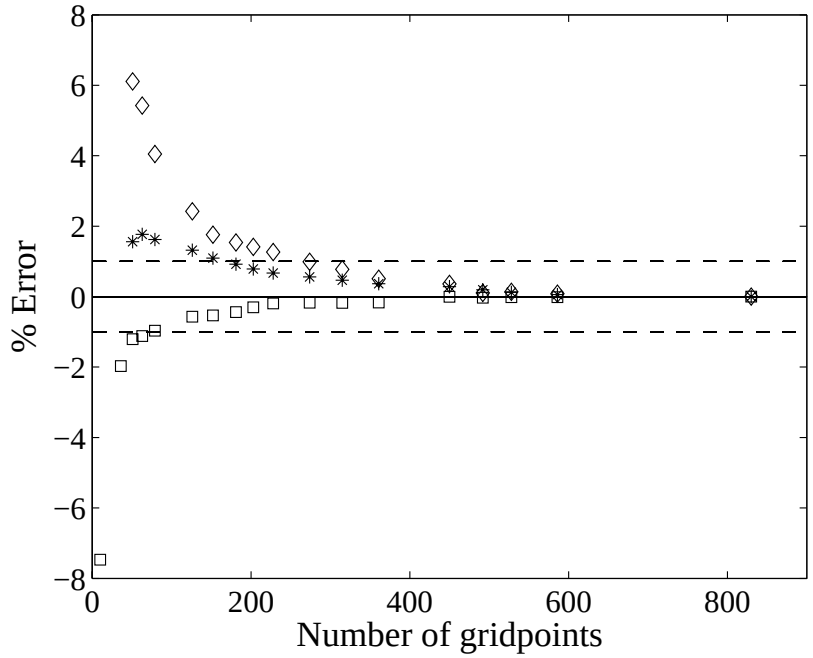

Figure D.2: Convergence study in a $\Phi = 1.0$ methane-air flame. The percent error relative to the solution with the maximum number of grid points, N, is calculated for simulations at varying resolution, i. (□) $100 \times (T_{\max,i} - T_{\max,\mathrm{N}})/T_{\max,\mathrm{N}}$, (◇) $100 \times (u_{\max,i} - u_{\max,\mathrm{N}})/u_{\max,\mathrm{N}}$, (∗) $100 \times (x_{\mathrm{CH},i} - x_{\mathrm{CH,N}})/x_{\mathrm{CH,N}}$.

to the values in the simulation with the maximum number of grid points, N ≈ 800, and expressed as the percent difference. The values are seen to asymptote with a difference of less than 1 % when the number of grid points exceeds 300. This number of grid points was used as a minimum value when flame simulations were performed, the actual number of points determined by the adaptive-refinement technique and the stability of the solution.

D.5 Sample flame profiles

Sample profiles of the temperature and density fields are given in Fig. D.3, where the wall is located at $x = 0$ and the inlet to the simulation domain is at $x = 6\,\text{mm}$. The temperature and density are essentially conjugate variables. This is due to the assumption of constant thermodynamic pressure in the simulations, and the relative constancy of the mean molar mass. Figure D.4 plots the spreading-rate,

$$V(x) = \frac{v(x)}{r} \,, \tag{D.4}$$

where $v(x)$ is the radial velocity and r is the radial coordinate.

Figures D.5 and D.6 plot the concentration profiles for some of the major and minor species

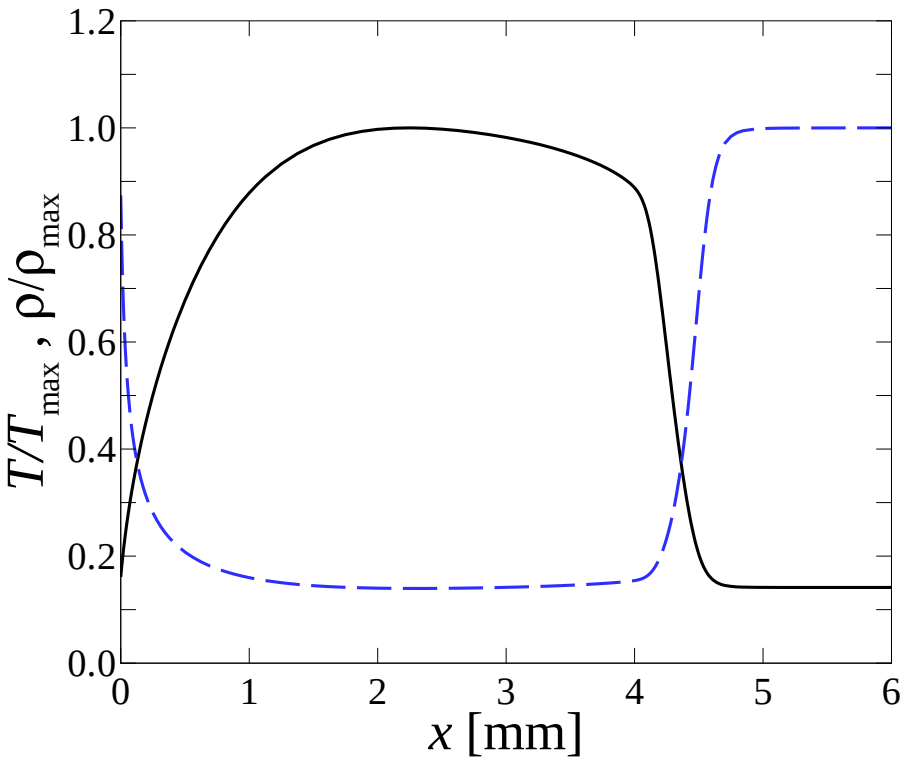

Figure D.3: Temperature (solid) and density (dashed) profiles normalized by the maximum value in the solution domain, in a $\Phi = 1.0$ CH_4-air flame.

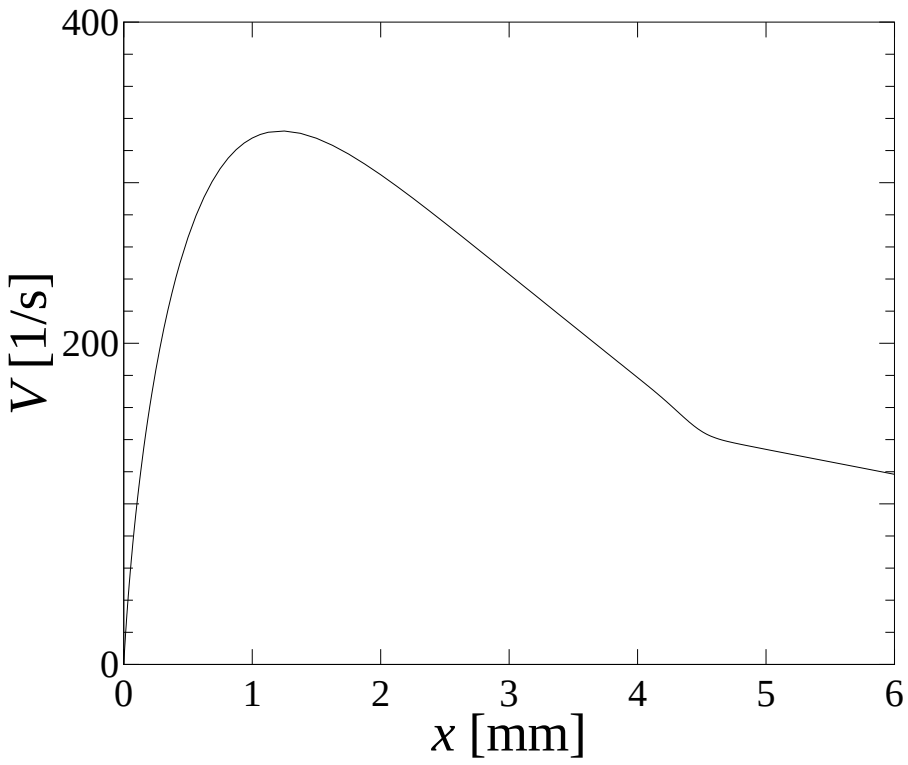

Figure D.4: Plot of spreading-rate, $V(x)$, in a $\Phi = 1.0$ CH_4-air flame.

involved in the combustion of methane. The oxygen and methane are converted into water and carbon dioxide through the flame. Some carbon monoxide is seen to remain in the post-flame gases, resulting in an excess of oxygen in the post-flame region even for this stoichiometric flame. A comparison of four minor species of interest in combustion are given in Fig. D.6. CH is an important intermediate due to its use as a reaction-zone marker, as discussed in Appendix C. OH has commonly been employed for laser-induced fluorescence measurements due to its large concentration (1500-times the concentration of CH), but is seen to have a broad spatial profile. The H radical is one of the most important flame radicals; however, it is also seen to exhibit a rather broad spatial profile. Studies measuring H radical profiles in such flames would provide a sensitive test of the transport models employed due to the high-mobility of this species. HCO has been used as a marker for the flame heat-release zone or the reaction zone. It is seen to provide similar information to the CH radical.

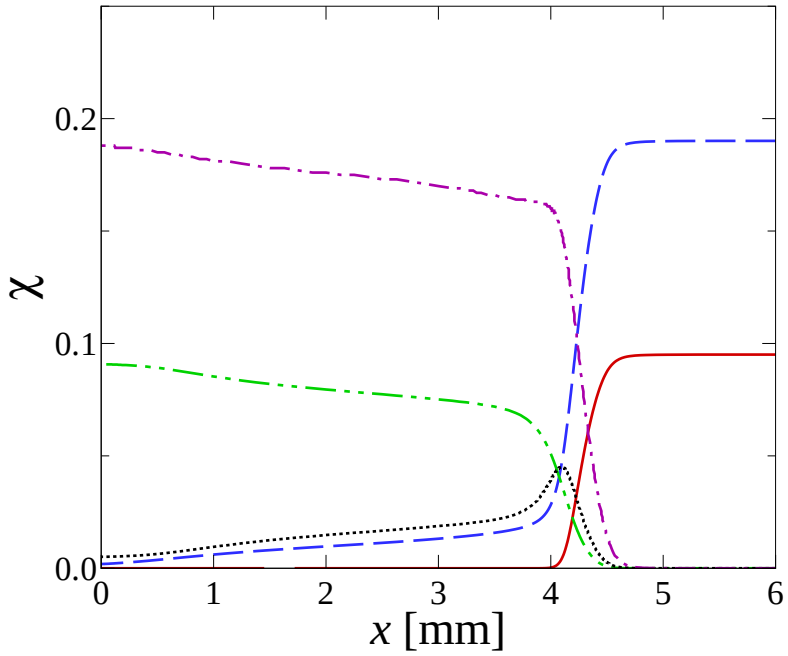

Figure D.5: Major-species mole-fraction, χ, profiles in a $\Phi = 1.0$ CH_4-air flame. (solid) CH_4, (dash) O_2, (dash-dot) H_2O, (dash-dot-dot) CO_2, (dot) CO.

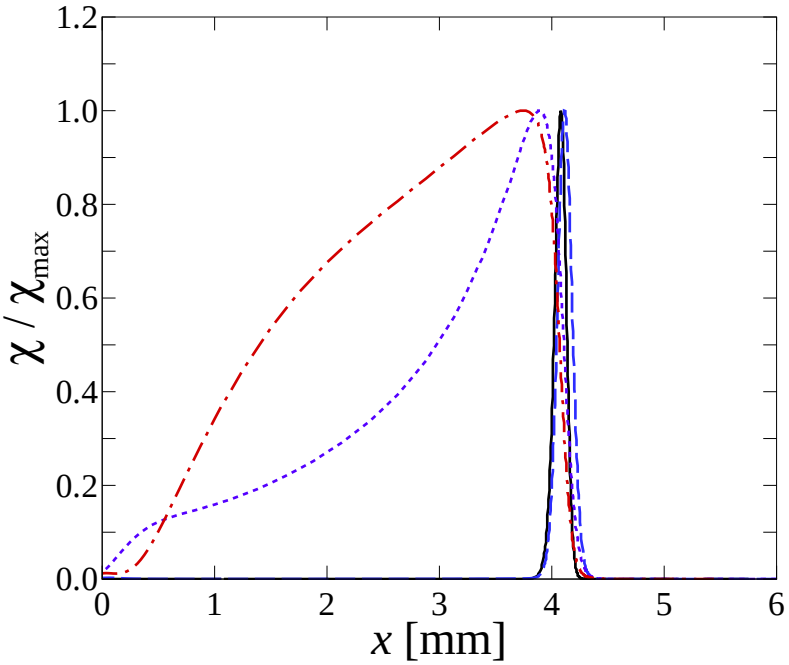

Figure D.6: Minor-species mole-fraction profiles normalized by the peak concentration of the radical, χ/χ_{max}, in a $\Phi = 1.0$ CH_4-air flame. (solid) CH, $\chi_{CH,max} \approx 4$ ppm, (dash-dot) OH, $\chi_{OH,max} \approx 7100$ ppm, (short dash) H, $\chi_{H,max} \approx 5800$ ppm (long dash) HCO, $\chi_{HCO,max} \approx 38$ ppm.

Appendix E

Nozzle design

Care was taken to design a nozzle and plenum system that would produce a jet with a uniform velocity profile and be stable for high Reynolds numbers. A series of screens (coarse to fine mesh) and honeycomb were utilized in the plenum system to create a uniform, stable flow upstream of the nozzle contraction. The nozzle contraction was designed to minimize the formation of Taylor-Görtler vortices (Drazin & Reid 1981) in the concave section. A similar methodology was utilized by Dowling (1988) to design contraction nozzles for studies of turbulent-jet mixing. Here the methodology of Dowling (1988) is extended by utilizing a 7th-degree polynomial to describe the contraction, rather than a 6th-degree polynomial, to obtain an additional degree of freedom in the design. The nozzle exterior was designed such that the shape approximately conforms to the streamlines for the entrainment-induced flow of a point source jet (Landau & Lifshitz 1987).

E.1 Design methodology for nozzle interior

The interior profile of the nozzle was designed to minimize the formation of Taylor-Görtler vortices in the concave section. These vortices are produced by an instability in boundary layers experiencing concave curvature. The Görtler parameter, G, used by Liepmann (1943) in his study of the transition of a boundary layer on a curved surface is defined as

$$G = -Re_\theta^2 \, \theta \, r'' \; . \tag{E.1}$$

This parameter should be minimized and kept below 50 to prevent Taylor-Görtler vorticies from forming. The boundary conditions and parameters used to define the nozzle contour are

$$r(0) = r_0 \quad r(x_\mathrm{e}) = r_\mathrm{e} \tag{E.2}$$

$$r'(0) = 0 \quad r'(x_\mathrm{e}) = 0 \tag{E.3}$$

$$r''(0) = 0 \quad r''(x_\mathrm{e}) = 0 \tag{E.4}$$

$$r(x_1) = r_1 \quad r(x_2) = r_2 \ , \tag{E.5}$$

where r_0 and r_e are the radii of the inlet and outlet of the nozzle, respectively, and x_e is the length of the contraction section. These three parameters were determined prior to the optimization. The radii at two different locations along the contraction length, r_1 and r_2, were varied to alter the contraction profile. Adjusting these two free parameters allows the Görtler parameter to be minimized over the nozzle length.

To perform this optimization, an iterative process is undertaken to ensure that an accurate estimate of the boundary-layer growth is made. An axisymmetric Thwaites approximation (White 1991) is used to estimate the momentum thickness at any point along the nozzle. An initial "guess" to the momentum thickness at the inlet is made, $\approx 0.5\,\mathrm{mm}$, and an inlet velocity is chosen such that conservation of mass through the contraction yields an exit velocity that is approximately the maximum expected exit velocity of $3\,\mathrm{m/s}$. This value was chosen as it is the estimated exit velocity that will be required to extinguish a very strong flame. The momentum thickness is given (White 1991) by the equation

$$\theta^2 = \frac{0.45\nu}{r^2U^6}\int_0^z r^2U^5 dz \ . \tag{E.6}$$

Using the velocity, radius and approximate momentum thickness at the nozzle inlet the integral on the right-hand side of Eq. (E.6) is estimated. This integral is kept as a constant and represents the history of the flow prior to the nozzle inlet, which is very complex due to the honeycombs, screens and other turbulence management systems in place. Equation (E.6) is calculated along the nozzle contraction, estimating the local flow velocity using conservation of mass and the radius of the nozzle. From the initial estimates of the momentum thickness the displacement thickness, δ^*, is calculated along the nozzle. It is calculated using

$$\delta^* = H(\lambda)\,\theta \ , \tag{E.7}$$

where $H(\lambda)$ was approximated by the polynomial fit for $\lambda \leq 0.25$,

$$H(\lambda) \approx 2.0 + 4.14z - 83.5z^2 + 854z^3 - 3337z^4 + 4576z^5 \tag{E.8}$$

$$z = (0.25 - \lambda) \ , \tag{E.9}$$

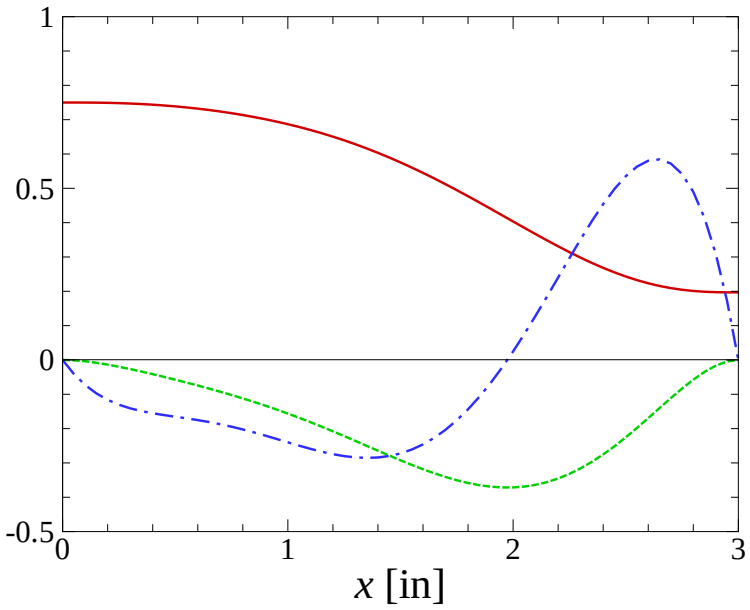

Figure E.1: Optimized nozzle-contraction profile. solid line: r, dashed line: r', and dash-dot line: r''.

and was set equal to 2 for $\lambda > 0.25$. In these equations, the Holstein-Bohlen correlation parameter is calculated using

$$\lambda = \frac{\theta^2}{\nu}\frac{dU}{dx} \ . \tag{E.10}$$

The flow area at each location along the nozzle length is corrected for the local displacement thickness and the velocity is recalculated using conservation of mass. An iterative process is then undertaken in which the momentum and displacement thicknesses are recalculated from the new velocity values and the velocity is corrected again. After about four iterations, the estimates converge.

Figure E.1 shows the optimized radius and the first and second derivatives of the radius as a function of the nozzle axial coordinate. The Görtler parameter depends on the local curvature of the contraction, r'', and the optimized contour essentially keeps this parameter fairly constant over the contraction section. Figure E.2 give the profiles for the Görtler parameter both prior to and after the iteration. The optimized profile yields a fairly constant value of the Görtler parameter along the contraction.

E.2 Nozzle exterior

The outer contour of the nozzle was designed such that the contour matches closely with the streamlines of the potential flow solution presented in Landau & Lifshitz (1987; see §23). The equation for the streamlines of the entrainment-induced flow from a point-source jet is given in polar coordinates

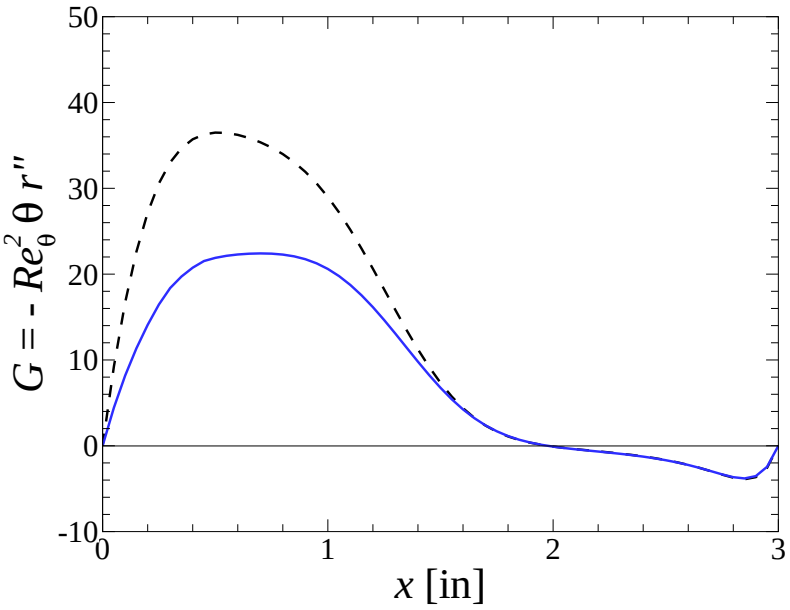

Figure E.2: Görtler parameter as a function of the nozzle axial coordinate. (dashed line) preliminary calculation (solid line) post iteration.

by

$$\frac{r\sin^2\theta}{A-\cos\theta} = \text{constant} \tag{E.11}$$

where the constant A is determined from the jet momentum, P, using

$$P = 16\pi\nu^2\rho A\left[1+\frac{4}{3(A^2-1)}-\frac{1}{2}A\log\frac{A+1}{A-1}\right] \ . \tag{E.12}$$

The jet momentum is given by

$$P = \rho\,\pi\,\left(\frac{d}{2}\right)^2 U_{\rm j}^2 \ . \tag{E.13}$$

where d is the jet diameter and $U_{\rm j}$ is the jet-exit velocity. In these equations, ρ is the fluid density and ν is the kinematic viscosity. From the specified jet momentum, the constant A is calculated. By choosing an appropriate value for the constant in Eq. (E.11) an entrainment streamline close to the desired outer-nozzle contour can be calculated. Converting the polar expression into Cartesian coordinates allows the nozzle-exterior profile to be fit to this streamline. The resulting outer profile is depicted in Fig. E.3.

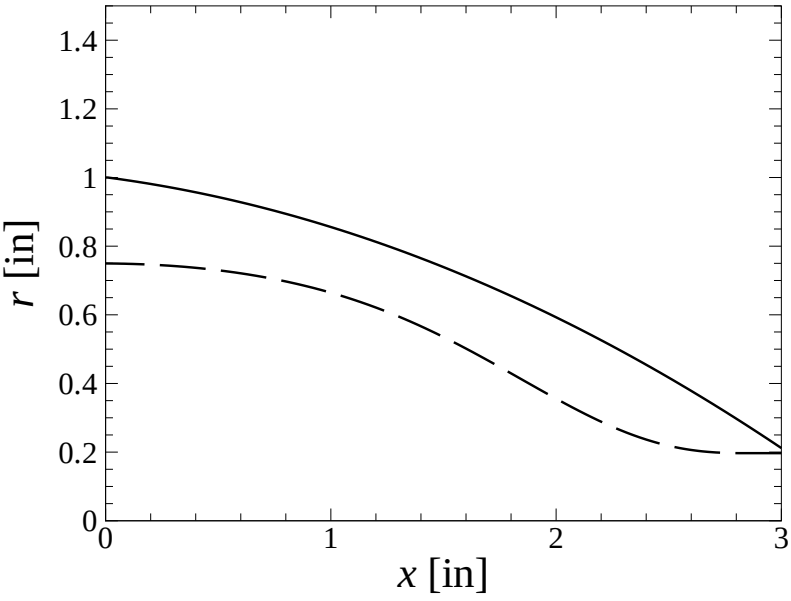

Figure E.3: Nozzle exterior (solid) and interior (dashed) contours.

Appendix F

Mass flow meter calibration

Flame simulation results are found to be extremely sensitive to the inlet mixture fraction (equivalence ratio) for very lean and rich flames. The inlet composition is measured using thermal mass flow meters with a specified accuracy of ±1% full scale. Omega FMA868-V, FMA869-V and FMA872-V flow meters were utilized, one was a 20 standard-Liter-per-minute (sLpm) flow meter calibrated for air, the second was a 5 sLpm nitrogen meter, and the third was a 2 sLpm flow meter used for the fuel-stream measurements and calibrated for methane. The air and methane flow meters were recalibrated at a flow calibration facility (Graftel), and it was discovered that the air flow meter was reading ≈ 3% high at the top end of its range. The methane flow meter was found to be within its specified accuracy when recalibrated. These thermal mass flow meters have two intrinsic errors associated with them. The first is the error due to nonlinearity in the voltage-flow response and the second is due to random (or repeatability) error. The flow meters are specified to be repeatable within ±0.2% F.S. The error due to nonlinearity can be removed by calibrating the thermal flow meter against a device of sufficient accuracy over the entire range of the device. Such a calibration can result in up to a five-fold reduction of the flow-measurement uncertainty. A piston prover device (Bios International DryCal ML-500) was obtained to be used as a calibrator for the thermal flow meters. This device operates by measuring the time that a graphite piston, moving in a borosilicate glass cylinder, takes to travel a known distance. By measuring the bore of the cylinder, the distance between the two sensors, and the time between tripping of the first and second sensor, the volumetric flow is obtained. The volume flow is corrected to standard conditions (1 atm and user-specified temperature) through a measurement of the gas temperature and pressure in the cylinder. This device is quoted to have an uncertainty of ±0.25% of reading for volumetric measurements and ±0.40% of reading for standardized measurements. This can be compared to uncertainties of ±0.5% of reading for a wet-test meter (volume flow), ±0.25% of reading for volume flow using a mercury sealed piston-prover device (Brooks Vol-U-Meter), or ≈ ±0.2% for the NIST bell-prover primary calibration standards. Thus, the DryCal approaches the accuracy achievable by the traditional primary flow standards. As volume or mass flow are necessarily derived quantities

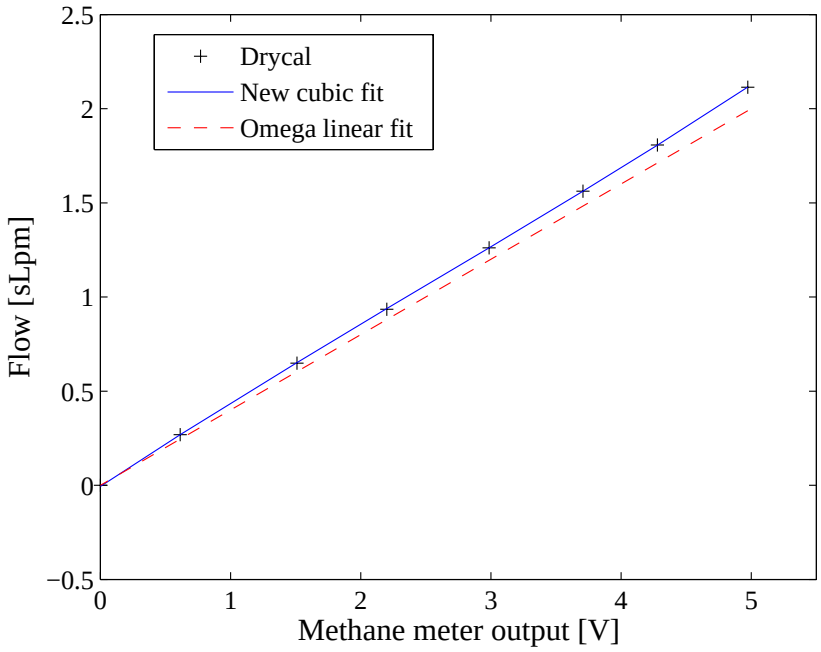

Figure F.1: Comparison of methane flow rate measured using DryCal ML-500 (+) to the manufacturer specified flow-voltage relation (dashed line) and the new cubic fit to the data (solid line).

relying on measurements of length, time, temperature, and pressure, coupled with gas properties, the minimum uncertainty of such measurements is intrinsically higher than measurements of direct quantities such as temperature or pressure.

The methane flow meter was found to be in specification when recalibrated by Graftel. The industry-standard practice for such calibrations is to utilize nitrogen as the calibration gas and apply an empirical gas-correction factor to determine the flow rate of the actual process gas. Calibrating this device against the DryCal ML-500 and using nitrogen as the surrogate gas also gave good agreement when the manufacturer specified flow equation and gas-correction factor were utilized. Figure F.1 plots the flow rate of methane, as measured by the DryCal ML-500, against a line representing the manufacturer-specified flow equation and a third-order fit performed to the data. The ability of the in-house piston prover to utilize the actual process gas (methane), revealed a systematic error in the mass-flow measurement that is attributable to the empirical gas-correction factor. Thus, a cubic polynomial was utilized to represent the flow-voltage relationship of the thermal mass flow meter. The fit constants were found by fitting pairs of flow-rate data, as measured by the DryCal ML-500, to the corresponding voltage output of the thermal flow meter. Figure F.2 plots the error between the flow-rate measured by the DryCal ML-500 and the thermal mass flow meter, using the manufacturer-specified flow-voltage relationship, and the new cubic representation. Error is expressed as the % full-scale error, the industry-accepted way of reporting performance on these

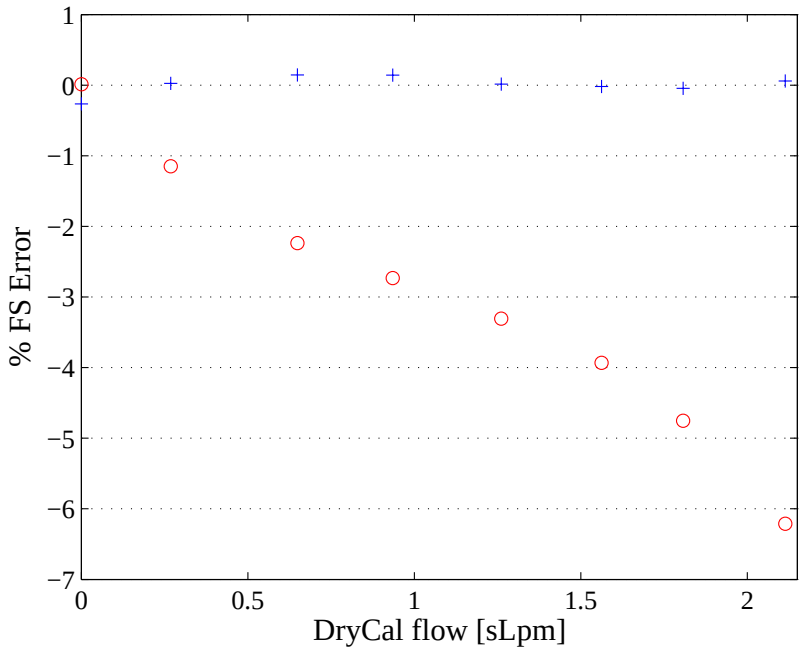

Figure F.2: Full-scale error compared to DryCal ML-500 flow rate for the manufacturer specified calibration (∘) and the new cubic fit (+).

devices. The % full-scale error is calculated as

$$\%\,\text{FS error} = 100 \times \frac{Q_\text{t} - Q_{\text{ML}-500}}{Q_{\text{t,FS}}}\ , \tag{F.1}$$

where Q_t is the volume flowrate measured by the thermal mass flow meter, $Q_{\text{t,FS}}$ is the maximum, or full-scale, flowrate for the thermal mass flow meter, and $Q_{\text{ML}-500}$ is the volume flowrate measured by the DryCal ML-500 piston-prover. Q_t is calculated from the measured voltage output of the flow meter using the appropriate calibration function (linear or cubic). A systematic error of up to 6% is evident in the manufacturer-specified flow-voltage relationship. This systematic error went undetected in calibrations performed by both the manufacturer and an independent company, indicating the need to calibrate these devices against a high-accuracy piston-prover using the actual gas being metered. Figures F.3–F.7 plots both the full-scale and relative error between the DryCal ML-500 measurements and the calibrated thermal flow meters for methane, air, nitrogen, ethane and ethylene. Note that only a select number of calibration datasets have been included in these plots for clarity. The relative error is defined as

$$\%\,\text{REL error} = 100 \times \frac{Q_\text{t} - Q_{\text{ML}-500}}{Q_{\text{ML}-500}}\ , \tag{F.2}$$

where the value of the flowrate at the current setting is utilized to normalize the difference, rather

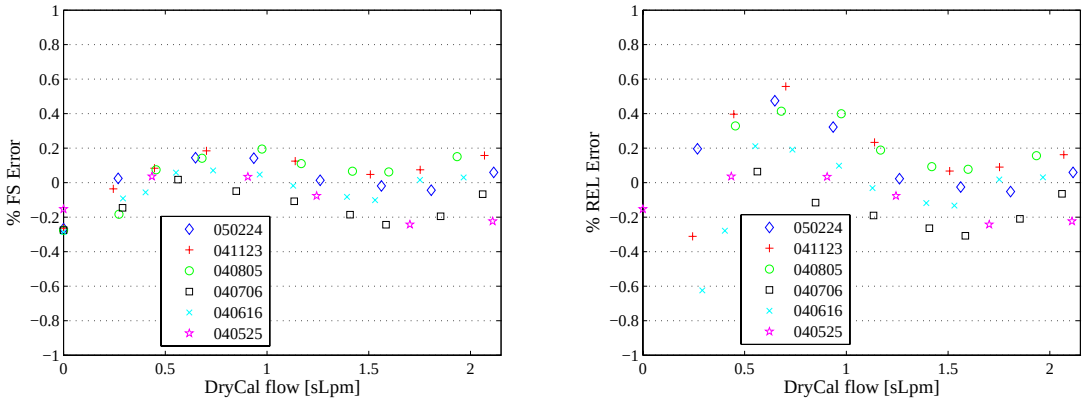

(a) Full-scale error

(b) Relative error

Figure F.3: Full-scale and relative error for methane flow meter compared to DryCal ML-500 measurements. Calibrations from several dates are included to indicate the stability of the devices over extended periods of time.

than the full-scale flowrate. The relative error better measures the uncertainty in a given measurement. The full-scale error tends to be less than $\pm 0.2\%$, in accord with the manufacturer specified repeatability of the instrument. As the flow meters are typically used in the top-half of their flowrange, the estimated uncertainty in the flow measurements relative to the DryCal ML-500 is ± 0.2–0.4%. The DryCal has an associated uncertainty of $\pm 0.4\%$ in the mass-flow measurements, yielding an estimated uncertainty of $\pm 0.6\%$ in the measured flowrates of each gas stream. This yields an estimated uncertainty in the equivalence ratio, Φ, of $\pm 0.8\%$. The estimated uncertainty in the oxygen percentage, $\%O_2{:}(O_2{+}N_2)$, is $\pm 0.2\%$, calculated for the maximum dilution case studied, $16.5\%O_2{:}(O_2{+}N_2)$. Standard error propagation techniques are utilized to determine the uncertainty in the derived quantities from the flow meter uncertainties.

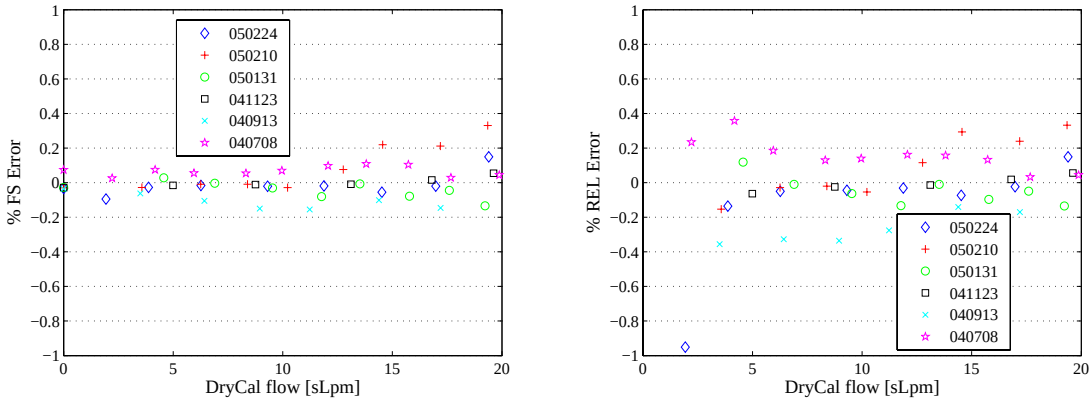

(a) Full-scale error

(b) Relative error

Figure F.4: Full-scale and relative error for air flow meter compared to DryCal ML-500 measurements.

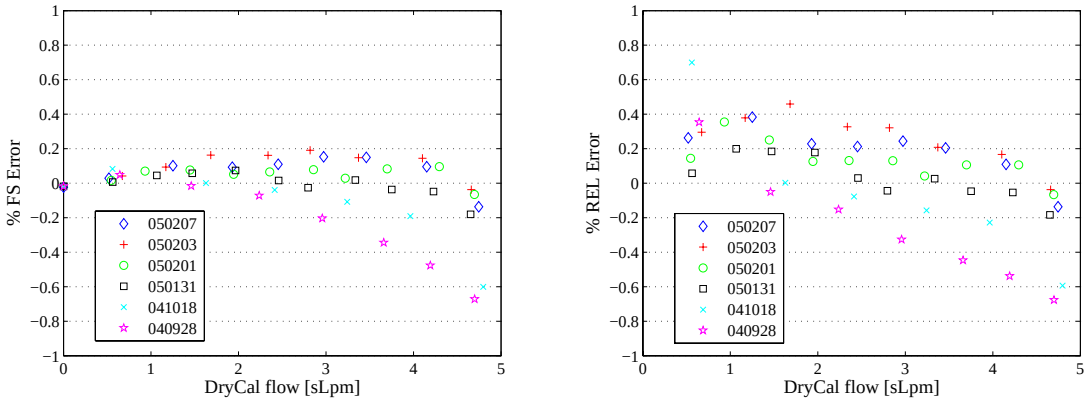

(a) Full-scale error

(b) Relative error

Figure F.5: Full-scale and relative error for nitrogen flow meter compared to DryCal ML-500.

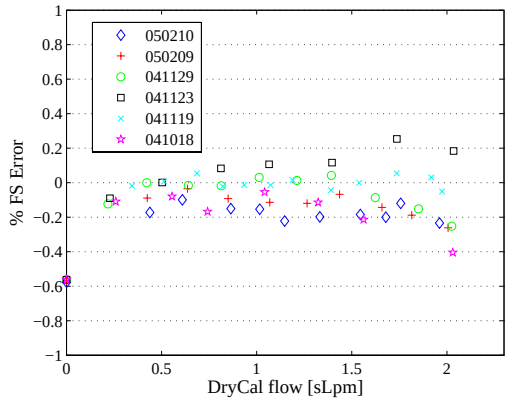

(a) Full-scale Error

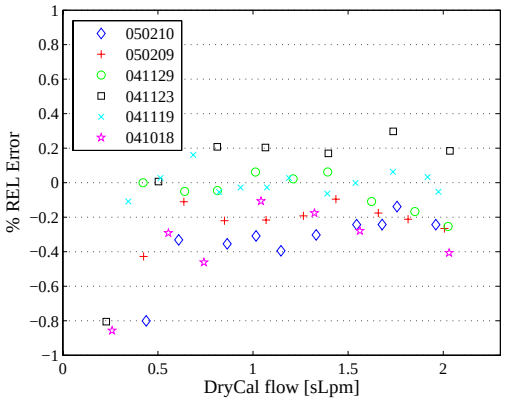

(b) Relative Error

Figure F.6: Full-scale and relative error for ethane flow meter compared to DryCal ML-500.

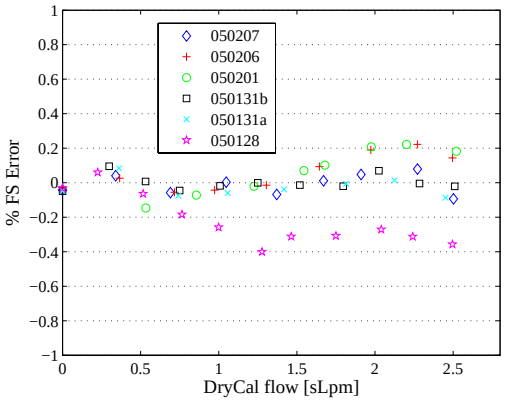

(a) Full-scale error

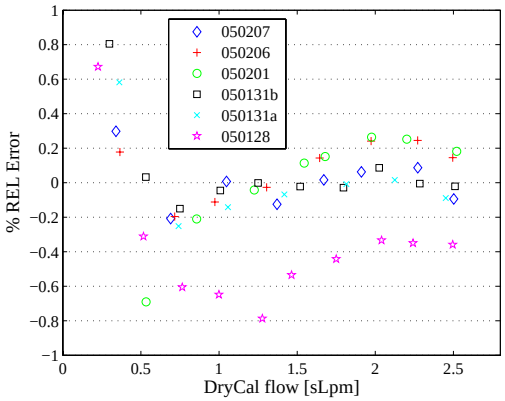

(b) Relative error

Figure F.7: Full-scale and relative error for ethylene flow meter compared to DryCal ML-500.

Appendix G

Methane flame profiles

Methane-air flames are studied as a function of the imposed strain rate at stoichiometries of $\Phi = 0.9$, 0.7, 1.1, and 1.25. Experiments are presented for stochiometric flames at variable levels of nitrogen dilution. The inlet mixture fraction is varied at a consistent flame location for methane-air flames and diluted methane-oxygen-nitrogen flames. All flames in this Appendix were simulated using GRI-Mech 3.0, and were post-processed to determine the modeled-PSV profiles as discussed in Appendix A. The full profiles are presented here for reference.

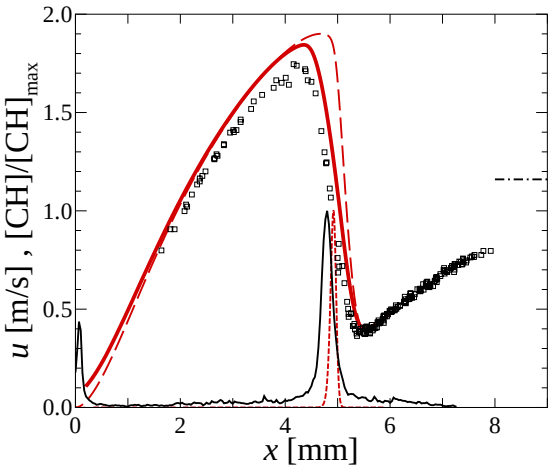

Figure G.1: CH_4-air flame profiles ($\Phi = 0.9$, $L/d = 0.8$, $\sigma = 212\,s^{-1}$, run205). (dash-dot line) U_B, (□) PSV data, (black line) PLIF data, (long-dash red line) simulated velocity profile (GRI-Mech 3.0), (solid red line) modeled-PSV profile, (short-dash red line) simulated CH profile.

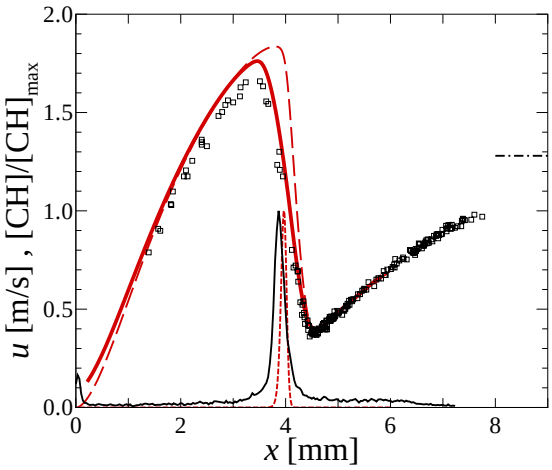

Figure G.2: CH_4-air flame profiles ($\Phi = 0.9$, $L/d = 0.8$, $\sigma = 236\,s^{-1}$, run206). Legend as in Fig. G.1.

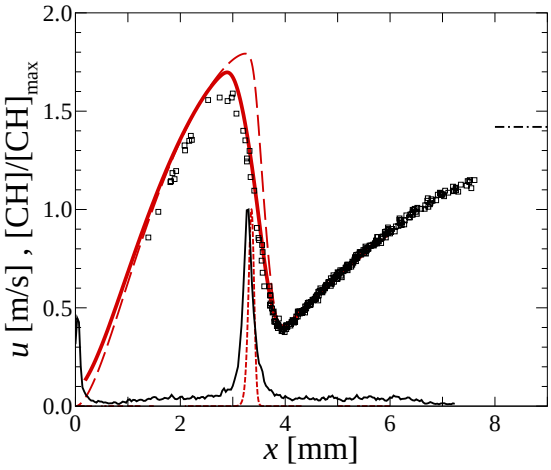

Figure G.3: CH_4-air flame profiles ($\Phi = 0.9$, $L/d = 0.8$, $\sigma = 275\,s^{-1}$, run207). Legend as in Fig. G.1.

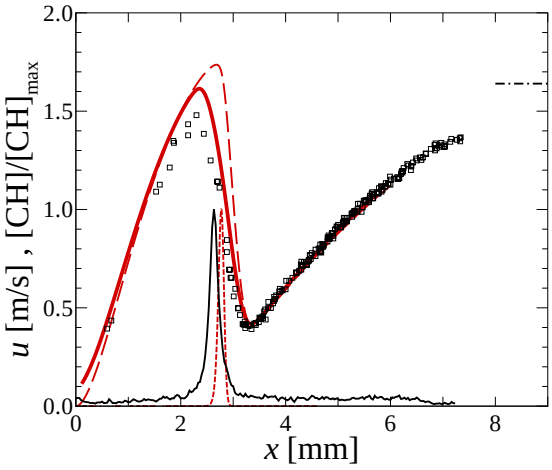

Figure G.4: CH_4-air flame profiles ($\Phi = 0.9$, $L/d = 0.8$, $\sigma = 334\,s^{-1}$, run208). Legend as in Fig. G.1.

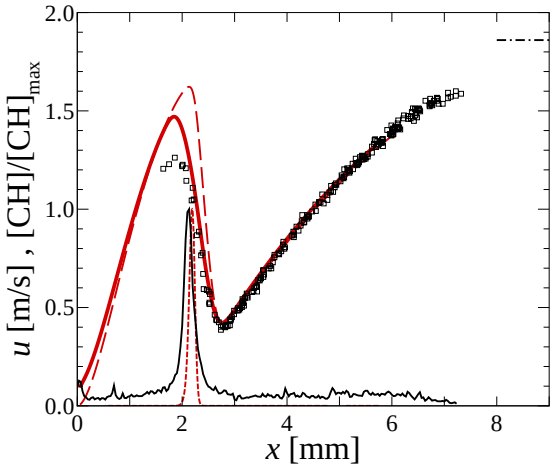

Figure G.5: CH_4-air flame profiles ($\Phi = 0.9$, $L/d = 0.8$, $\sigma = 368\,s^{-1}$, run209). Legend as in Fig. G.1.

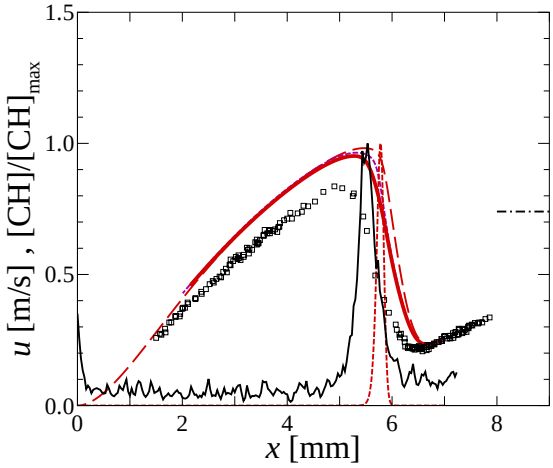

Figure G.6: CH_4-air flame profiles ($\Phi = 0.7$, $L/d = 0.8$, $\sigma = 90\,s^{-1}$, run210). Legend as in Fig. G.1.

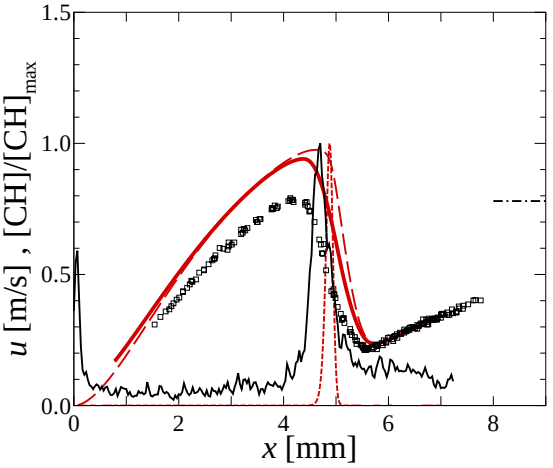

Figure G.7: CH_4-air flame profiles ($\Phi = 0.7$, $L/d = 0.8$, $\sigma = 99\,s^{-1}$, run211). Legend as in Fig. G.1.

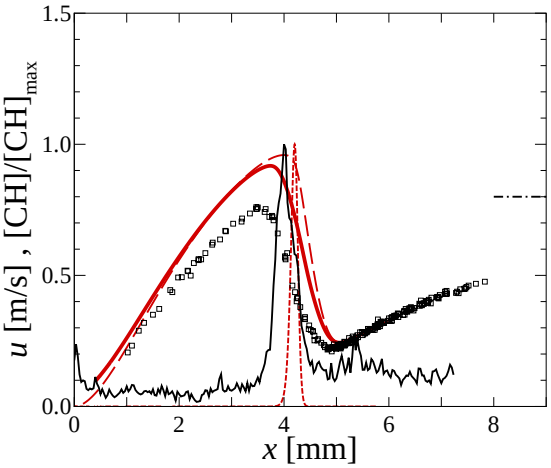

Figure G.8: CH_4-air flame profiles ($\Phi = 0.7$, $L/d = 0.8$, $\sigma = 106\,s^{-1}$, run212). Legend as in Fig. G.1.

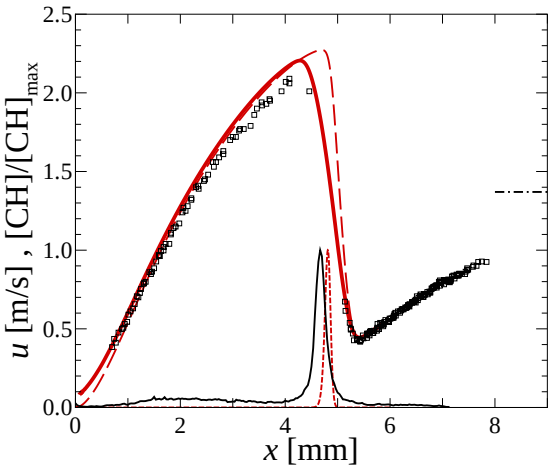

Figure G.9: CH_4-air flame profiles ($\Phi = 1.1$, $L/d = 0.8$, $\sigma = 240\,s^{-1}$, run220). Legend as in Fig. G.1.

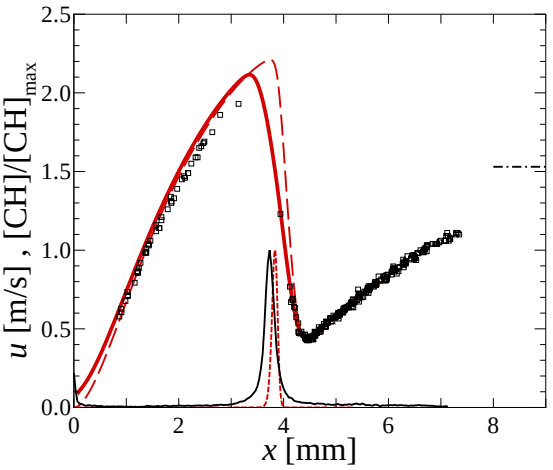

Figure G.10: CH_4-air flame profiles ($\Phi = 1.1$, $L/d = 0.8$, $\sigma = 279\,s^{-1}$, run221). Legend as in Fig. G.1.

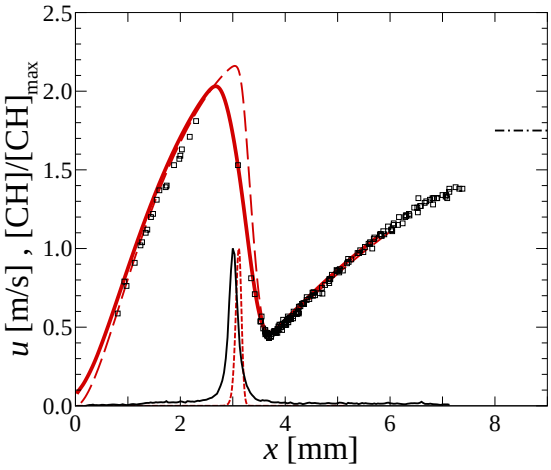

Figure G.11: CH_4-air flame profiles ($\Phi = 1.1$, $L/d = 0.8$, $\sigma = 315\,s^{-1}$, run222). Legend as in Fig. G.1.

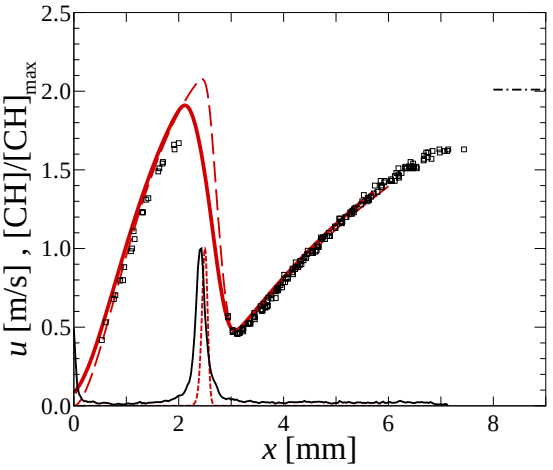

Figure G.12: CH_4-air flame profiles ($\Phi = 1.1$, $L/d = 0.8$, $\sigma = 388\,s^{-1}$, run223). Legend as in Fig. G.1.

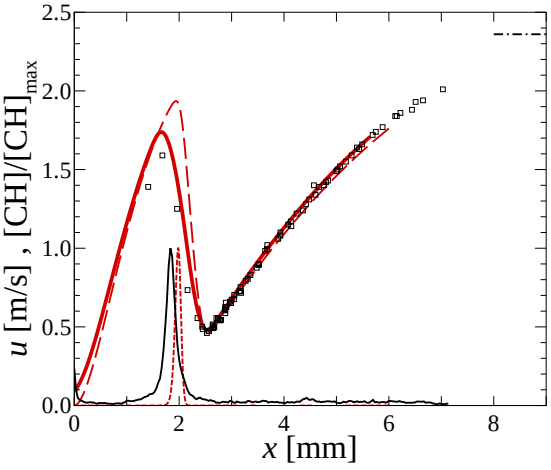

Figure G.13: CH_4-air flame profiles ($\Phi = 1.1$, $L/d = 0.8$, $\sigma = 449\,s^{-1}$, run224). Legend as in Fig. G.1.

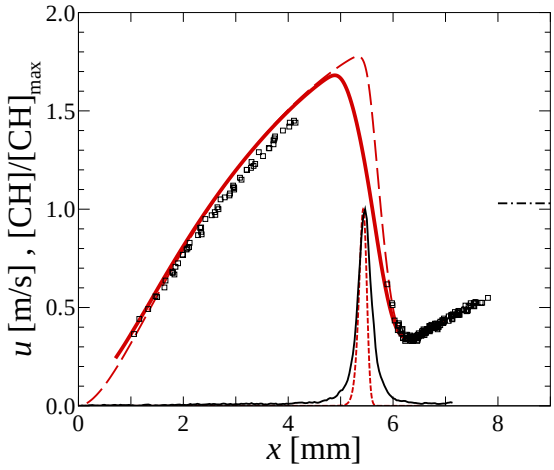

Figure G.14: CH_4-air flame profiles ($\Phi = 1.25$, $L/d = 0.8$, $\sigma = 152\,s^{-1}$, run215). Legend as in Fig. G.1.

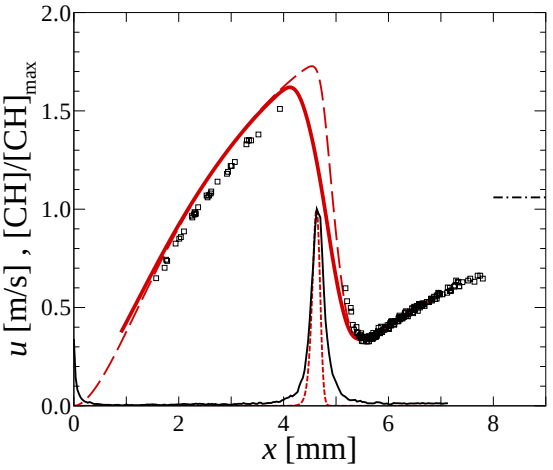

Figure G.15: CH_4-air flame profiles ($\Phi = 1.25$, $L/d = 0.8$, $\sigma = 175\,s^{-1}$, run216). Legend as in Fig. G.1.

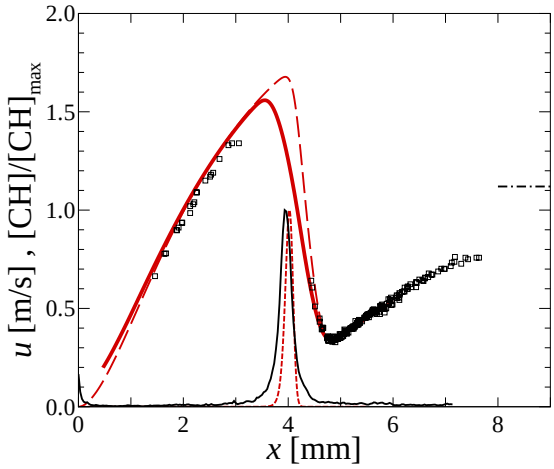

Figure G.16: CH_4-air flame profiles ($\Phi = 1.25$, $L/d = 0.8$, $\sigma = 183\,s^{-1}$, run217). Legend as in Fig. G.1.

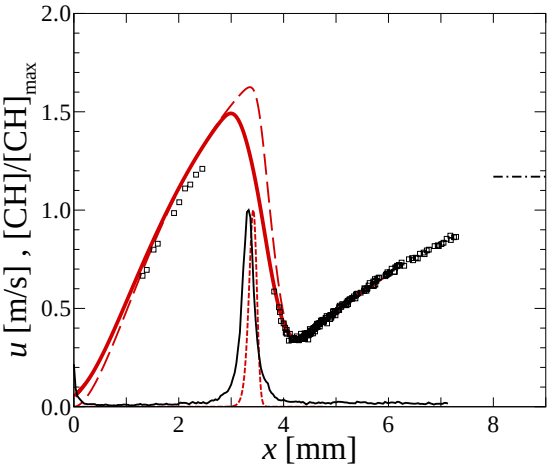

Figure G.17: CH_4-air flame profiles ($\Phi = 1.25$, $L/d = 0.8$, $\sigma = 209\,s^{-1}$, run218). Legend as in Fig. G.1.

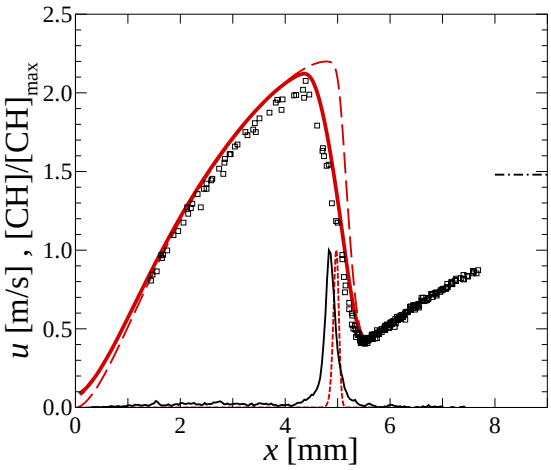

Figure G.18: CH_4-air flame profiles ($\Phi = 1.0$, 21.0%O_2:(O_2+N_2), $L/d = 0.8$, run241). Legend as in Fig. G.1.

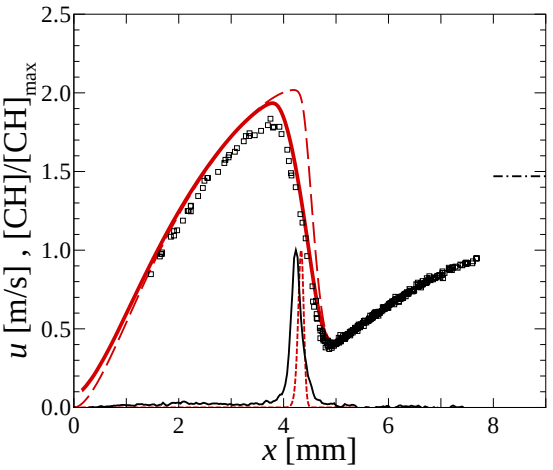

Figure G.19: CH_4-air flame profiles ($\Phi = 1.0$, 20.5%O_2:(O_2+N_2), $L/d = 0.8$, run242). Legend as in Fig. G.1.

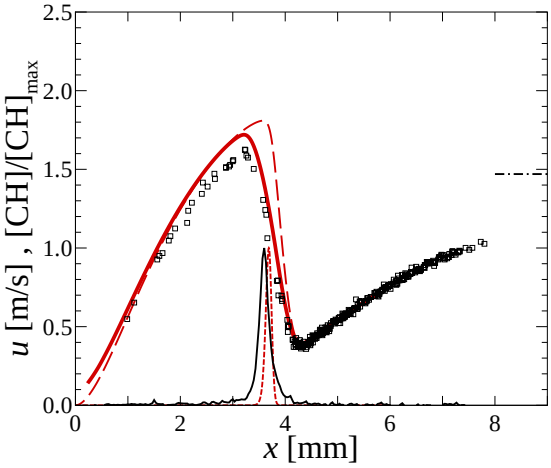

Figure G.20: CH_4-air flame profiles ($\Phi = 1.0$, 20.0%O_2:(O_2+N_2), $L/d = 0.8$, run243). Legend as in Fig. G.1.

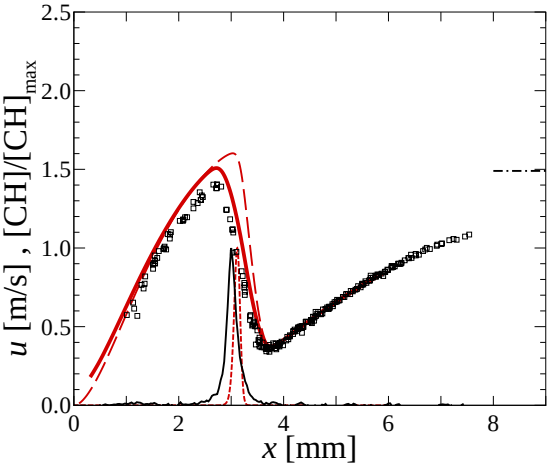

Figure G.21: CH_4-air flame profiles ($\Phi = 1.0$, 19.5%O_2:(O_2+N_2), $L/d = 0.8$, run244). Legend as in Fig. G.1.

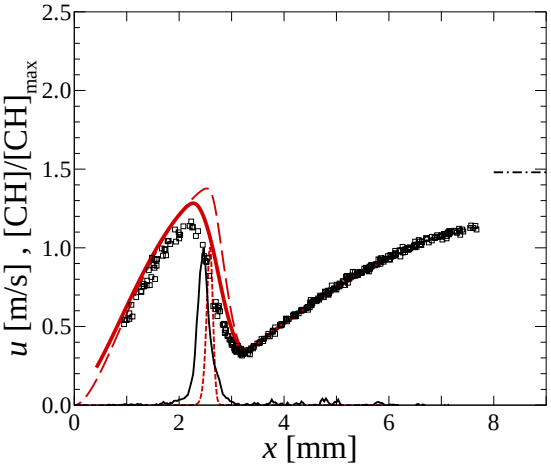

Figure G.22: CH_4-air flame profiles ($\Phi = 1.0$, 19.0%O_2:(O_2+N_2), $L/d = 0.8$, run245). Legend as in Fig. G.1.

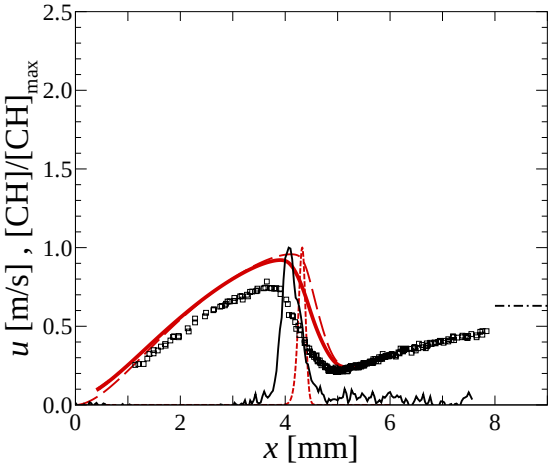

Figure G.23: CH_4-air flame profiles ($\Phi = 0.7$, run234). Legend as in Fig. G.1.

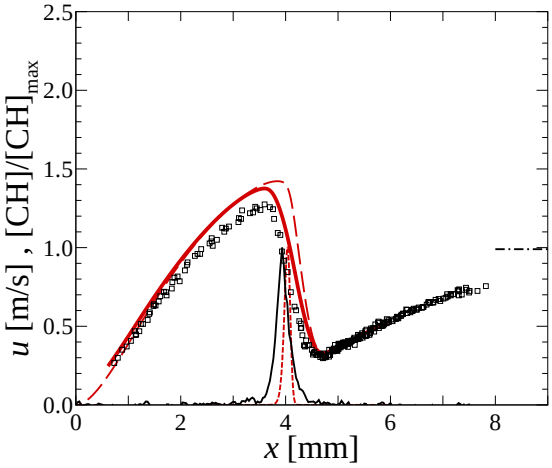

Figure G.24: CH_4-air flame profiles ($\Phi = 0.8$, run231). Legend as in Fig. G.1.

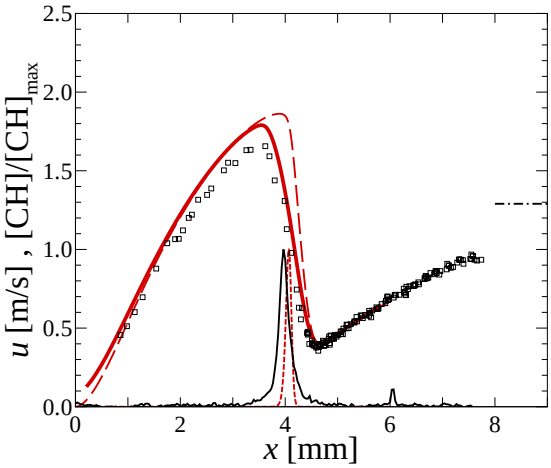

Figure G.25: CH_4-air flame profiles ($\Phi = 0.9$, run225). Legend as in Fig. G.1.

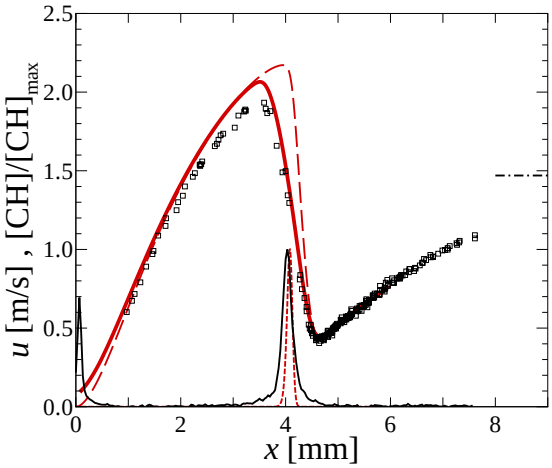

Figure G.26: CH_4-air flame profiles ($\Phi = 1.0$, run226). Legend as in Fig. G.1.

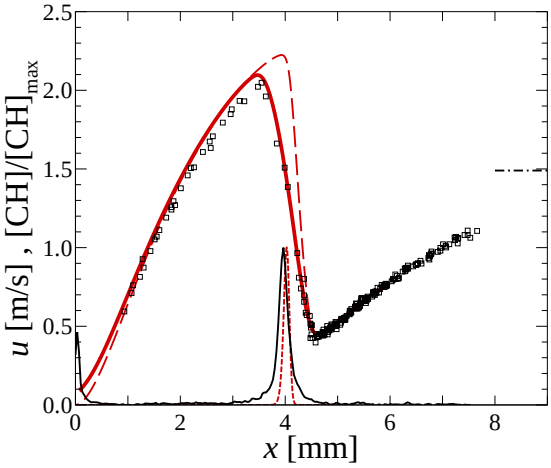

Figure G.27: CH_4-air flame profiles ($\Phi = 1.1$, run227). Legend as in Fig. G.1.

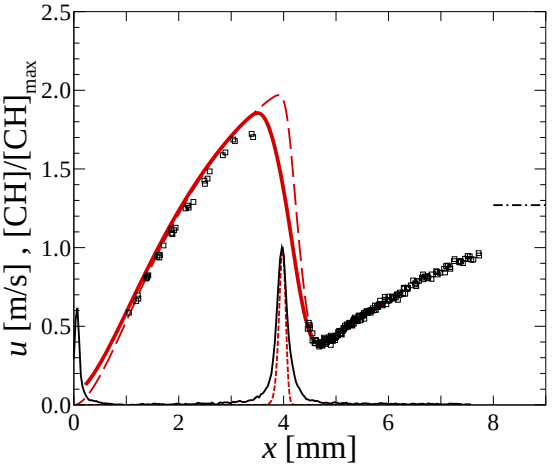

Figure G.28: CH_4-air flame profiles ($\Phi = 1.2$, run228). Legend as in Fig. G.1.

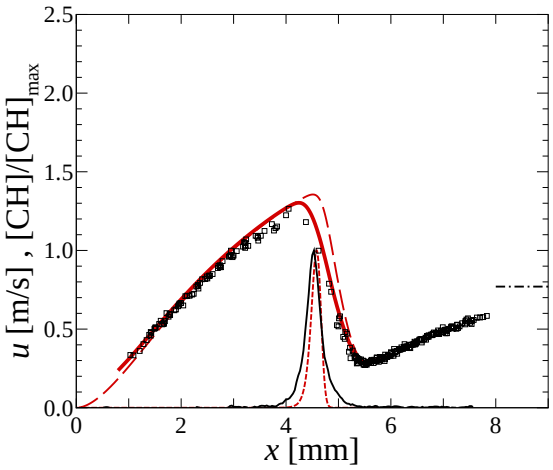

Figure G.29: CH_4-air flame profiles ($\Phi = 1.3$, run229). Legend as in Fig. G.1.

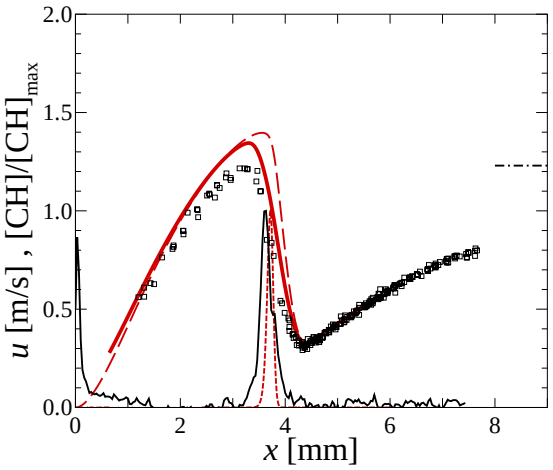

Figure G.30: CH_4-air flame profiles (Φ = 0.8, 21.0%O_2:(O_2+N_2), run240). Legend as in Fig. G.1.

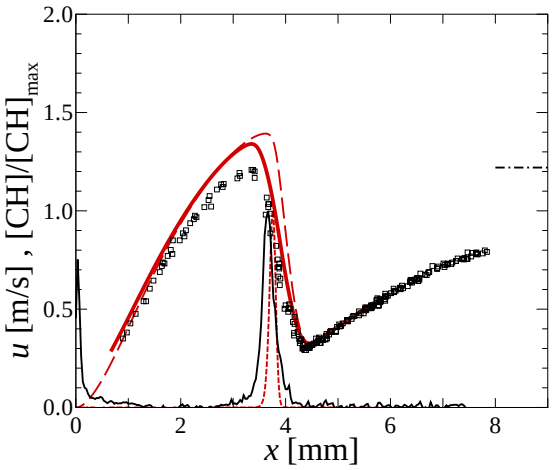

Figure G.31: CH_4-air flame profiles (Φ = 0.9, 19.5%O_2:(O_2+N_2), run239). Legend as in Fig. G.1.

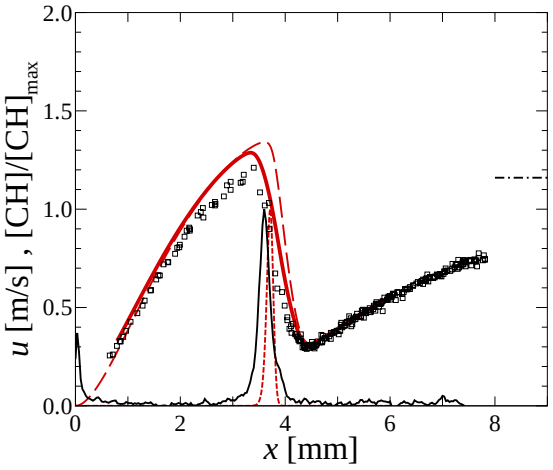

Figure G.32: CH_4-air flame profiles (Φ = 1.0, 18.5%O_2:(O_2+N_2), run238). Legend as in Fig. G.1.

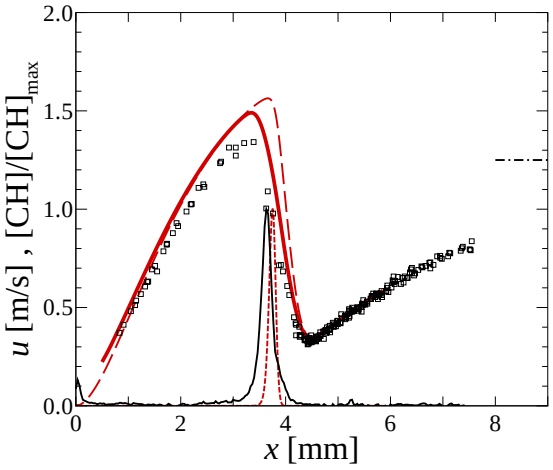

Figure G.33: CH_4-air flame profiles (Φ = 1.1, 19.0%O_2:(O_2+N_2), run237). Legend as in Fig. G.1.

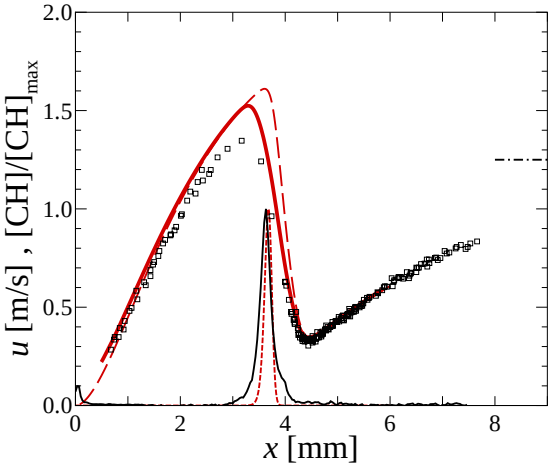

Figure G.34: CH_4-air flame profiles (Φ = 1.2, 20.0%O_2:(O_2+N_2), run236). Legend as in Fig. G.1.

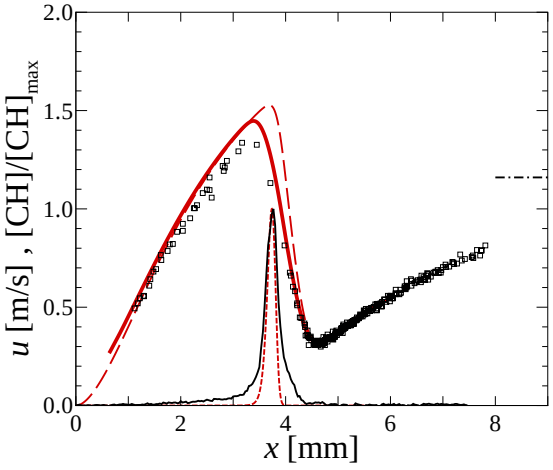

Figure G.35: CH_4-air flame profiles (Φ = 1.27, 21.0%O_2:(O_2+N_2), run235). Legend as in Fig. G.1.

Appendix H

Ethane flame profiles

Ethane-air flames are studied as a function of the imposed strain rate at stoichiometries of $\Phi = 0.7$, 1.0, and 1.4. The inlet mixture fraction is varied at a consistent flame location for ethane-air flames to study effects of varying stoichiometry. All flames in this Appendix were simulated using GRI-Mech 3.0, and were post-processed to determine the modeled-PSV profiles as discussed in Appendix A. The full profiles are presented here for reference.

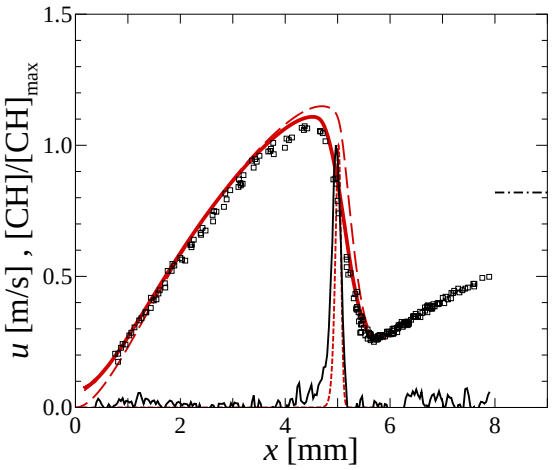

Figure H.1: C_2H_6-air flame profiles ($\Phi = 0.7$, $L/d = 0.8$, $\sigma = 121\,\mathrm{s}^{-1}$, run313). (dash-dot line) U_B, (□) PSV data, (solid black line) PLIF data, (long-dash red line) simulated velocity profile (GRI-Mech 3.0), (solid red line) modeled-PSV profile, (short-dash red line) simulated CH profile.

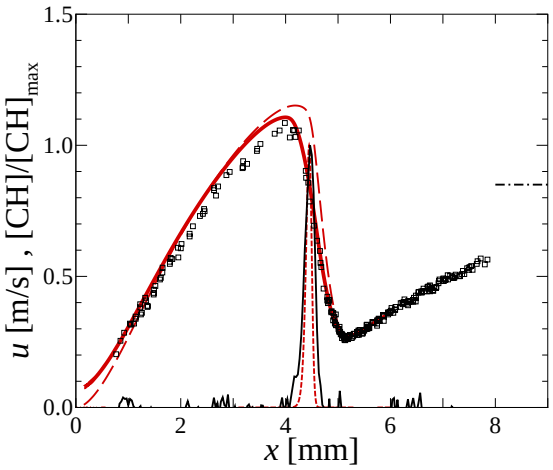

Figure H.2: C_2H_6-air flame profiles ($\Phi = 0.7$, $L/d = 0.8$, $\sigma = 127\,\mathrm{s}^{-1}$, run314). Legend as in Fig. H.1.

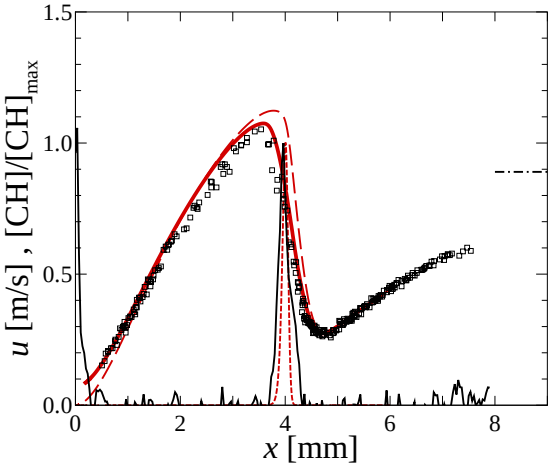

Figure H.3: C_2H_6-air flame profiles ($\Phi = 0.7$, $L/d = 0.8$, $\sigma = 136\,\mathrm{s}^{-1}$, run315). Legend as in Fig. H.1.

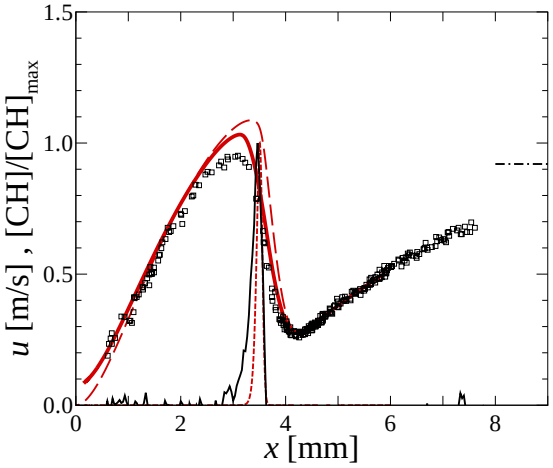

Figure H.4: C_2H_6-air flame profiles ($\Phi = 0.7$, $L/d = 0.8$, $\sigma = 156\,\mathrm{s}^{-1}$, run316). Legend as in Fig. H.1.

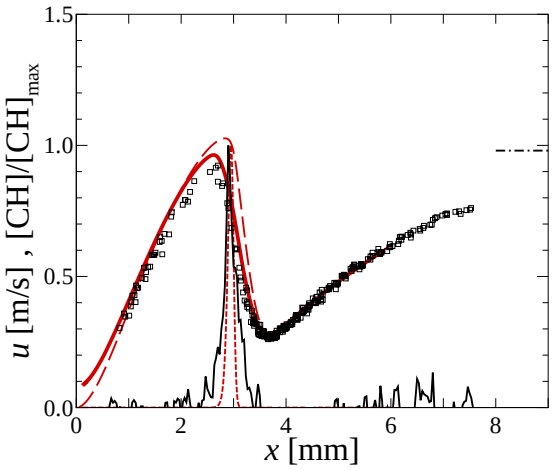

Figure H.5: C_2H_6-air flame profiles ($\Phi = 0.7$, $L/d = 0.8$, $\sigma = 171\,\mathrm{s}^{-1}$, run317). Legend as in Fig. H.1.

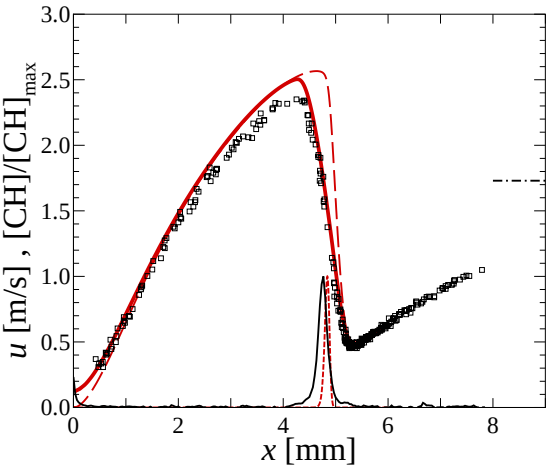

Figure H.6: C_2H_6-air flame profiles ($\Phi = 1.0$, $L/d = 0.8$, $\sigma = 278\,s^{-1}$, run319). Legend as in Fig. H.1.

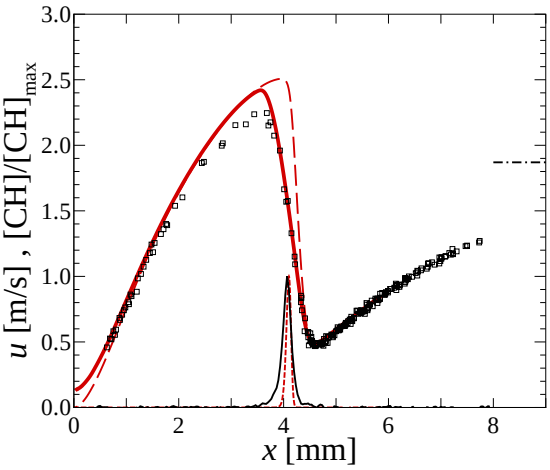

Figure H.7: C_2H_6-air flame profiles ($\Phi = 1.0$, $L/d = 0.8$, $\sigma = 317\,s^{-1}$, run320). Legend as in Fig. H.1.

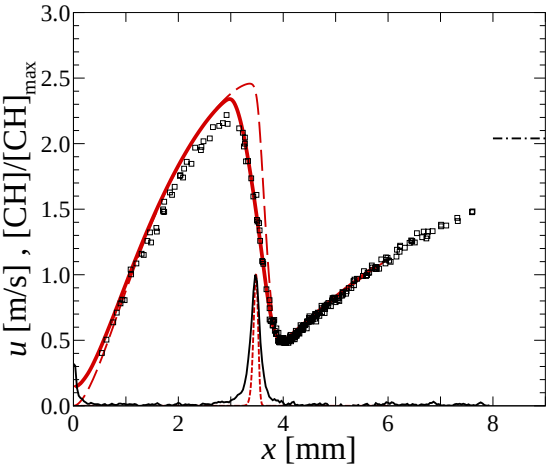

Figure H.8: C_2H_6-air flame profiles ($\Phi = 1.0$, $L/d = 0.8$, $\sigma = 355\,s^{-1}$, run321). Legend as in Fig. H.1.

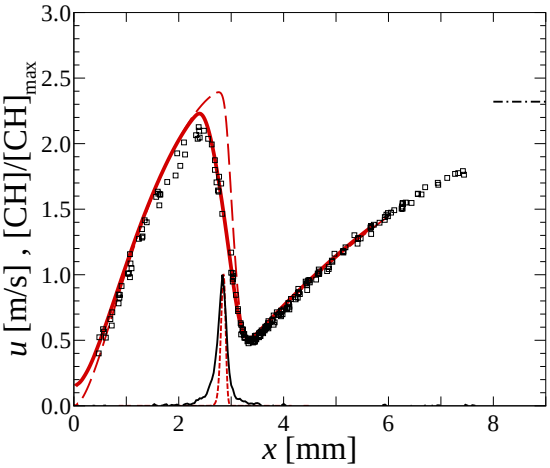

Figure H.9: C_2H_6-air flame profiles ($\Phi = 1.0$, $L/d = 0.8$, $\sigma = 413\,s^{-1}$, run322). Legend as in Fig. H.1.

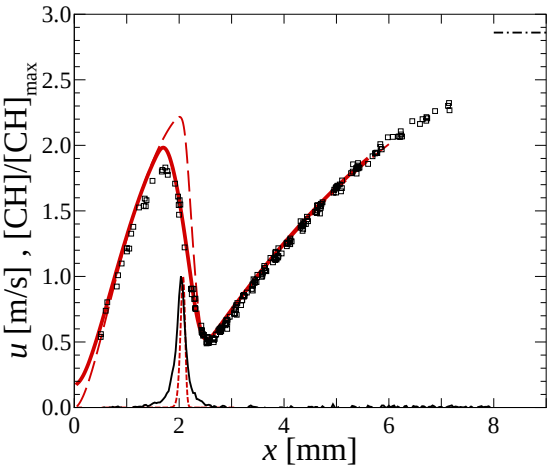

Figure H.10: C_2H_6-air flame profiles ($\Phi = 1.0$, $L/d = 0.8$, $\sigma = 553\,s^{-1}$, run323). Legend as in Fig. H.1.

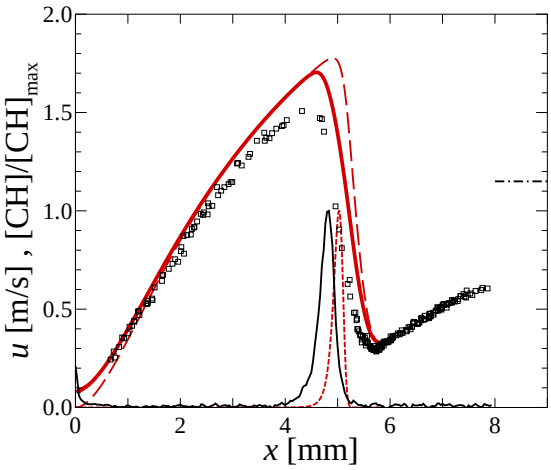

Figure H.11: C_2H_6-air flame profiles ($\Phi = 1.4$, $L/d = 0.8$, $\sigma = 167\,s^{-1}$, run324). Legend as in Fig. H.1.

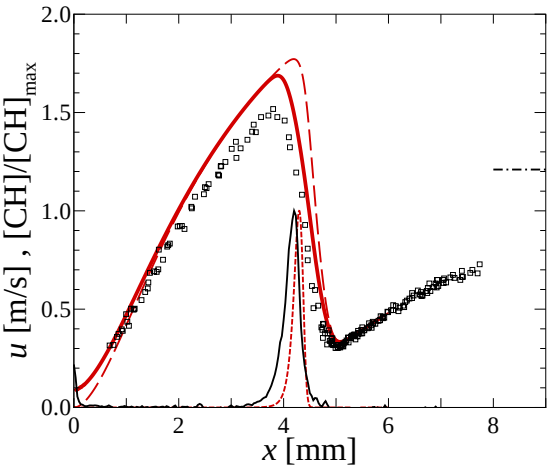

Figure H.12: C_2H_6-air flame profiles ($\Phi = 1.4$, $L/d = 0.8$, $\sigma = 185\,s^{-1}$, run325). Legend as in Fig. H.1.

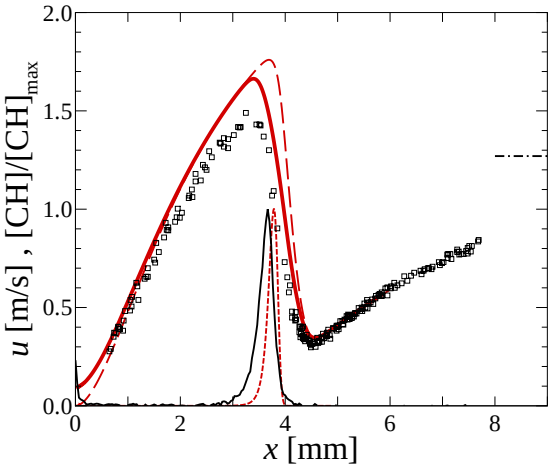

Figure H.13: C_2H_6-air flame profiles ($\Phi = 1.4$, $L/d = 0.8$, $\sigma = 201\,s^{-1}$, run326). Legend as in Fig. H.1.

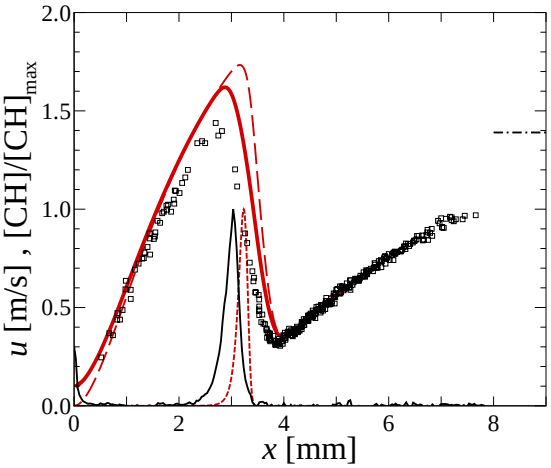

Figure H.14: C_2H_6-air flame profiles ($\Phi = 1.4$, $L/d = 0.8$, $\sigma = 220\,s^{-1}$, run327). Legend as in Fig. H.1.

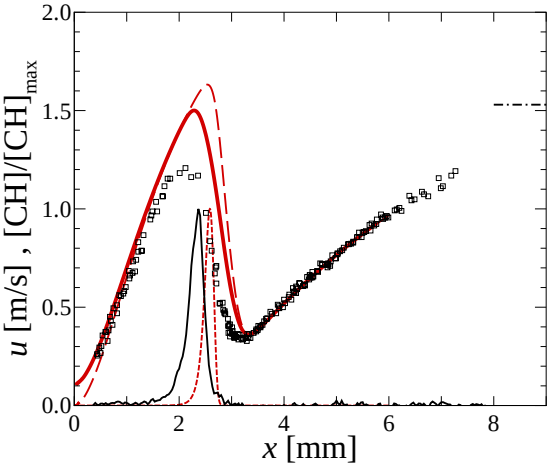

Figure H.15: C_2H_6-air flame profiles ($\Phi = 1.4$, $L/d = 0.8$, $\sigma = 256\,s^{-1}$, run328). Legend as in Fig. H.1.

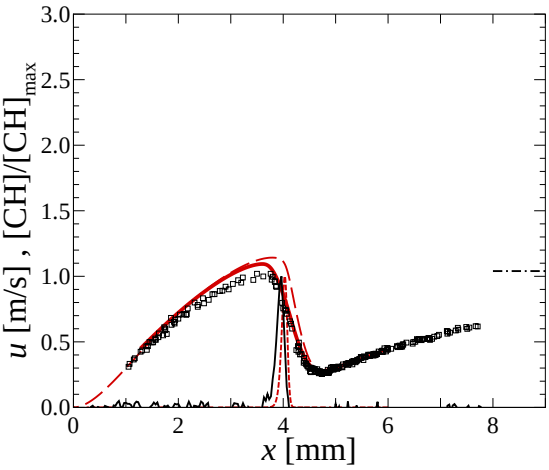

Figure H.16: C_2H_6-air flame profiles ($\Phi = 0.7$, run337). Legend as in Fig. H.1.

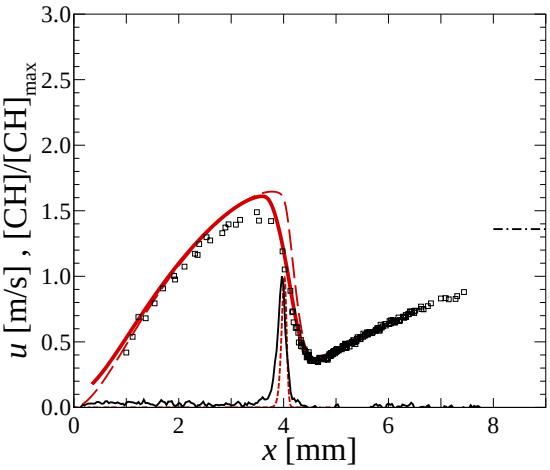

Figure H.17: C_2H_6-air flame profiles ($\Phi = 0.8$, run336). Legend as in Fig. H.1.

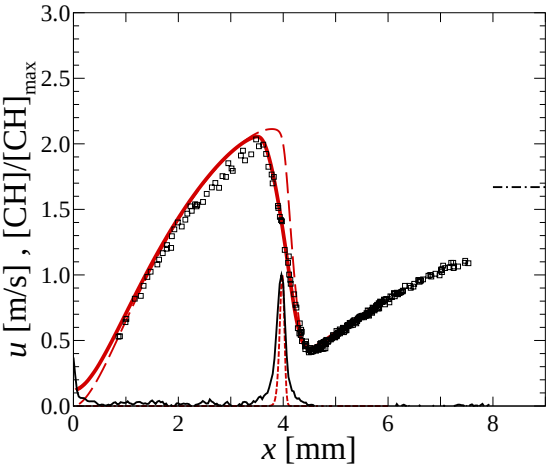

Figure H.18: C_2H_6-air flame profiles ($\Phi = 0.9$, run335). Legend as in Fig. H.1.

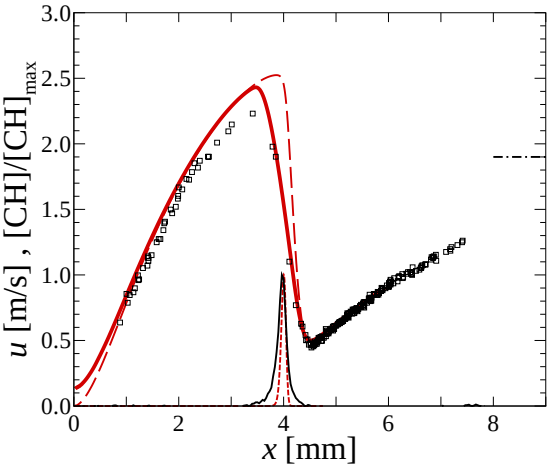

Figure H.19: C_2H_6-air flame profiles ($\Phi = 1.0$, run334). Legend as in Fig. H.1.

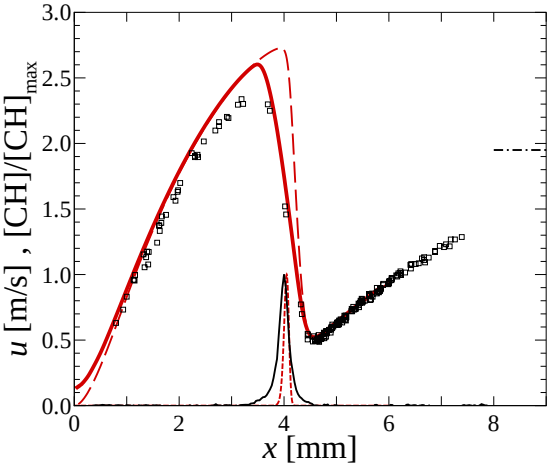

Figure H.20: C_2H_6-air flame profiles ($\Phi = 1.1$, run333). Legend as in Fig. H.1.

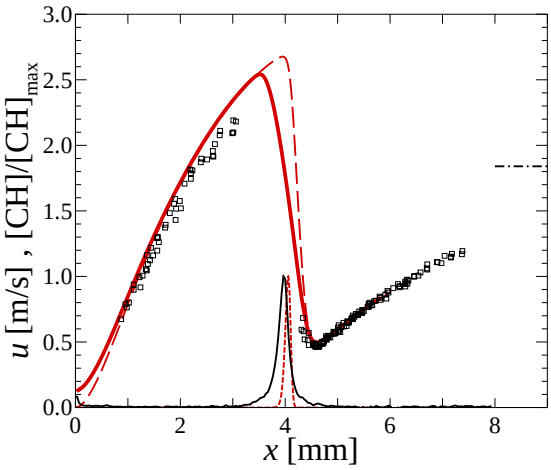

Figure H.21: C_2H_6-air flame profiles ($\Phi = 1.2$, run332). Legend as in Fig. H.1.

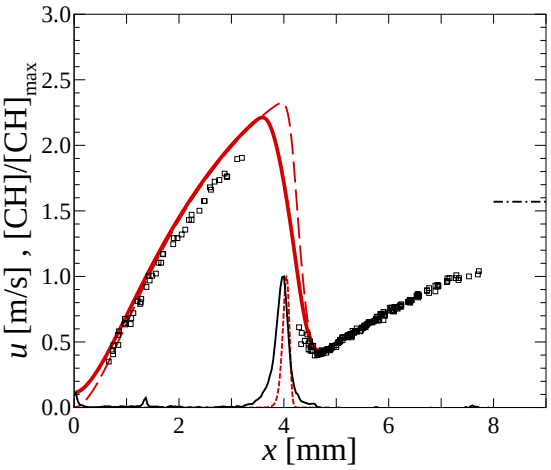

Figure H.22: C_2H_6-air flame profiles ($\Phi = 1.3$, run331). Legend as in Fig. H.1.

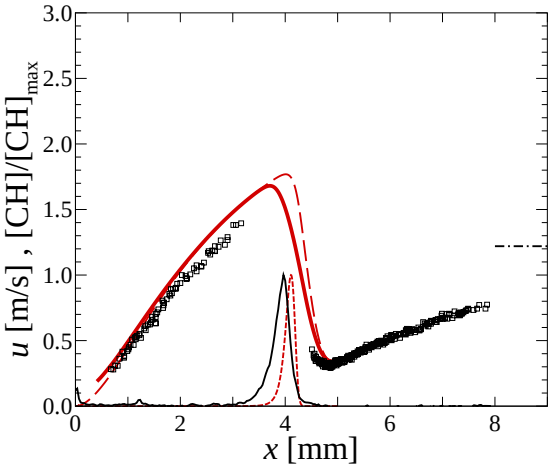

Figure H.23: C_2H_6-air flame profiles ($\Phi = 1.4$, run330). Legend as in Fig. H.1.

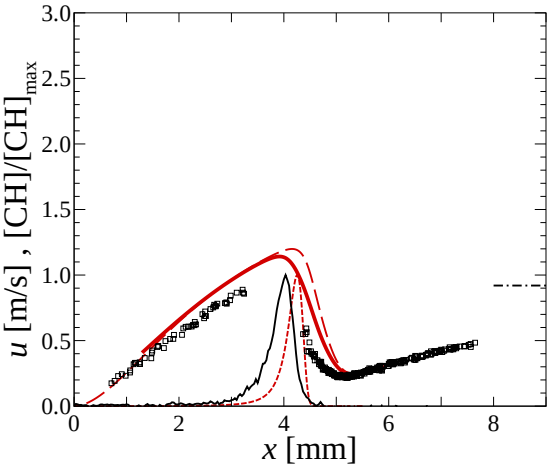

Figure H.24: C_2H_6-air flame profiles ($\Phi = 1.5$, run329). Legend as in Fig. H.1.

Appendix I

Ethylene flame profiles

Ethylene-air flames are studied as a function of the imposed strain rate at stoichiometries of $\Phi = 0.7$ and 1.6. Ethylene-oxygen-nitrogen flames are studied as a function of the inlet mixture fraction. Nitrogen dilution is utilized to maintain similar flame strength and flame location as the fuel to air ratio is varied. All flames in this Appendix were simulated using the C_3-Davis mechanism by Davis *et al.* (1999), and were post-processed to determine the modeled-PSV profiles as discussed in Appendix A. The full profiles are presented here for reference.

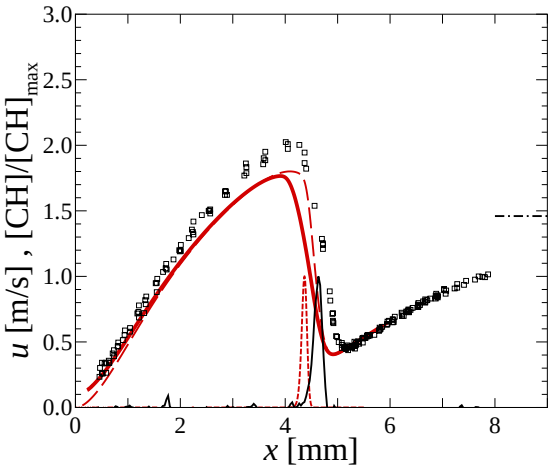

Figure I.1: C_2H_4-air flame profiles ($\Phi = 0.7$, $L/d = 0.8$, $\sigma = 254\,s^{-1}$, run302). ((dash-dot line) U_B, (□) PSV data, (black line) PLIF data, (long-dash red line) simulated velocity profile (C_3-Davis), (solid red line) modeled-PSV profile, (short-dash red line) simulated CH profile.

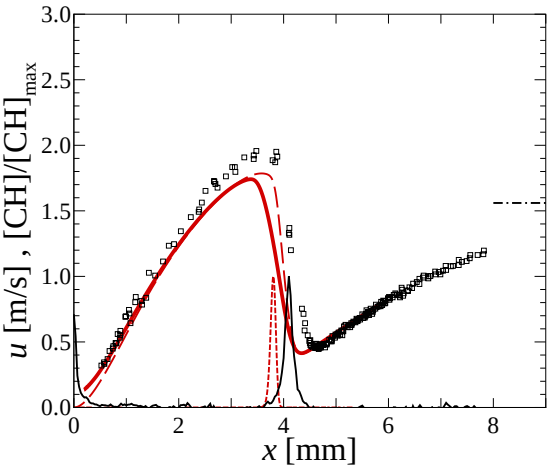

Figure I.2: C_2H_4-air flame profiles ($\Phi = 0.7$, $L/d = 0.8$, $\sigma = 291\,s^{-1}$, run303). Legend as in Fig. I.1.

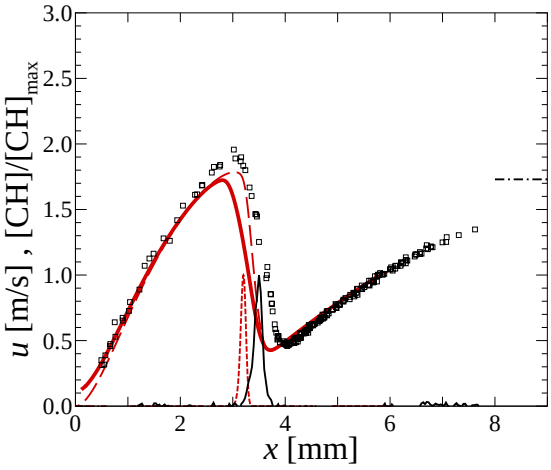

Figure I.3: C_2H_4-air flame profiles ($\Phi = 0.7$, $L/d = 0.8$, $\sigma = 324\,s^{-1}$, run304). Legend as in Fig. I.1.

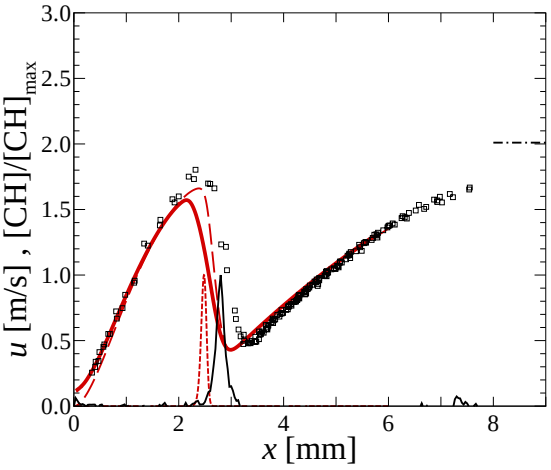

Figure I.4: C_2H_4-air flame profiles ($\Phi = 0.7$, $L/d = 0.8$, $\sigma = 381\,s^{-1}$, run305). Legend as in Fig. I.1.

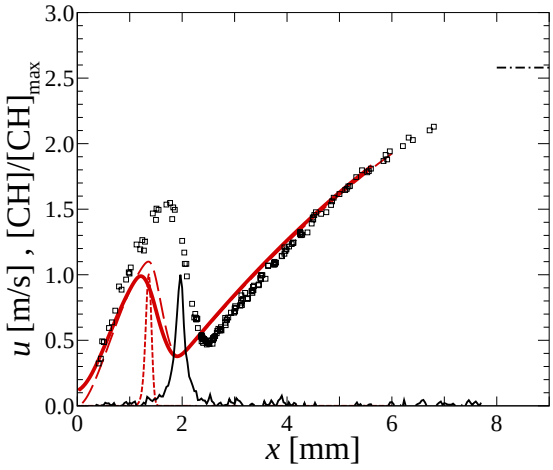

Figure I.5: C_2H_4-air flame profiles ($\Phi = 0.7$, $L/d = 0.8$, $\sigma = 492\,s^{-1}$, run306). Legend as in Fig. I.1.

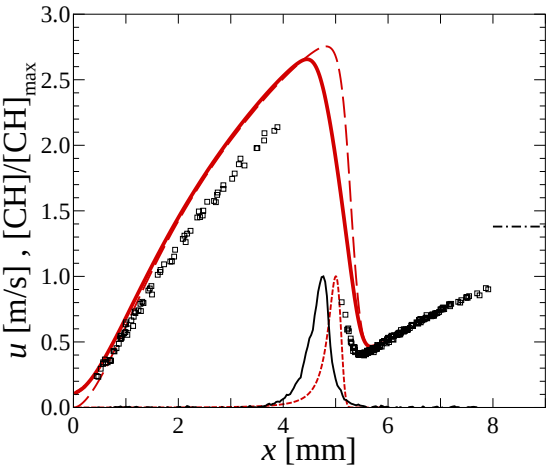

Figure I.6: C_2H_4-air flame profiles ($\Phi = 1.6$, $L/d = 0.8$, $\sigma = 236\,s^{-1}$, run307). Legend as in Fig. I.1.

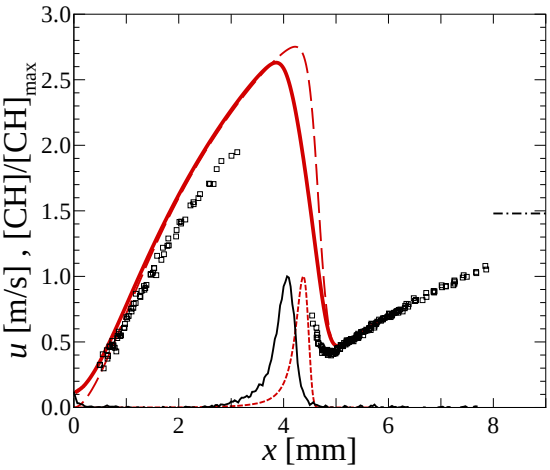

Figure I.7: C_2H_4-air flame profiles ($\Phi = 1.6$, $L/d = 0.8$, $\sigma = 265\,s^{-1}$, run308). Legend as in Fig. I.1.

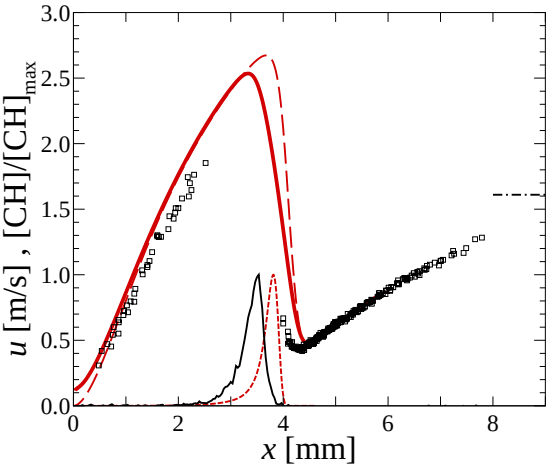

Figure I.8: C_2H_4-air flame profiles ($\Phi = 1.6$, $L/d = 0.8$, $\sigma = 286\,s^{-1}$, run309). Legend as in Fig. I.1.

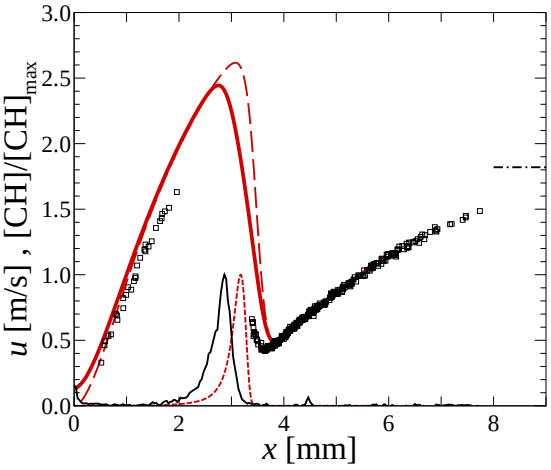

Figure I.9: C_2H_4-air flame profiles ($\Phi = 1.6$, $L/d = 0.8$, $\sigma = 340\,s^{-1}$, run310). Legend as in Fig. I.1.

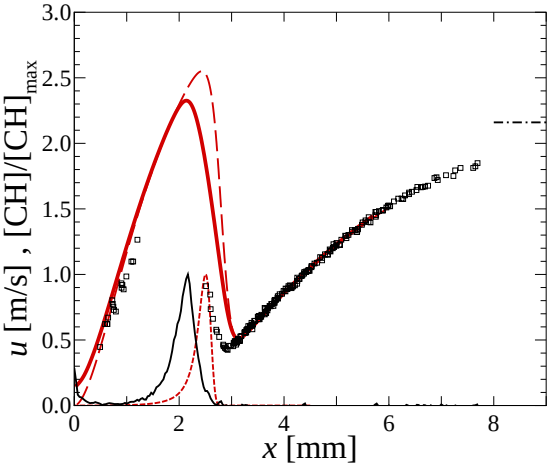

Figure I.10: C_2H_4-air flame profiles ($\Phi = 1.6$, $L/d = 0.8$, $\sigma = 418\,s^{-1}$, run311). Legend as in Fig. I.1.

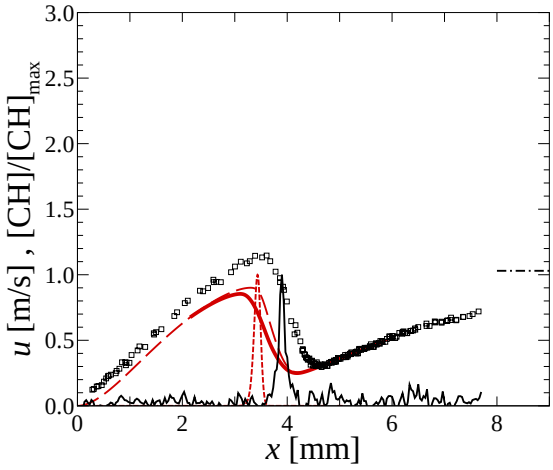

Figure I.11: C_2H_4-air flame profiles (Φ = 0.6, 21.0 %O_2:(O_2+N_2), run301). Legend as in Fig. I.1.

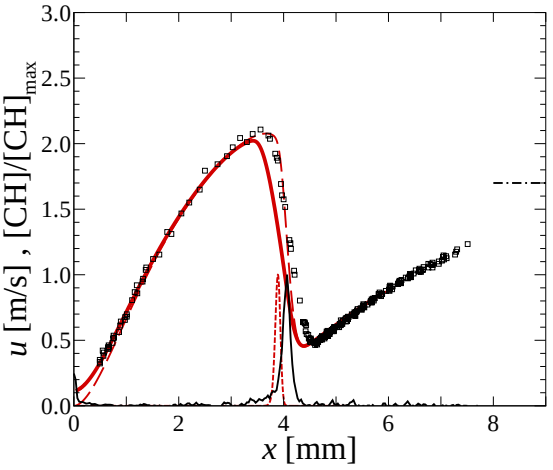

Figure I.12: C_2H_4-air flame profiles (Φ = 0.8, 19.5 %O_2:(O_2+N_2), run300). Legend as in Fig. I.1.

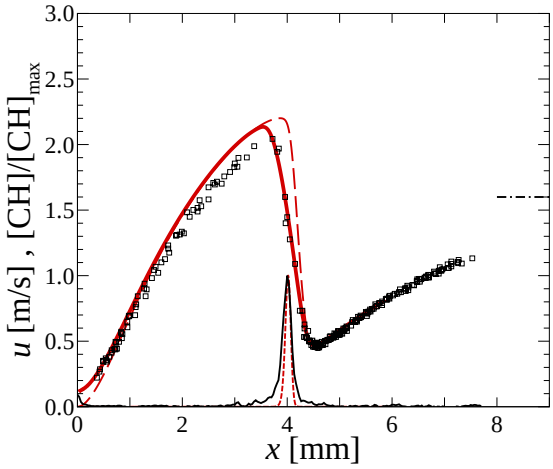

Figure I.13: C_2H_4-air flame profiles (Φ = 1.0, 17.0 %O_2:(O_2+N_2), run299). Legend as in Fig. I.1.

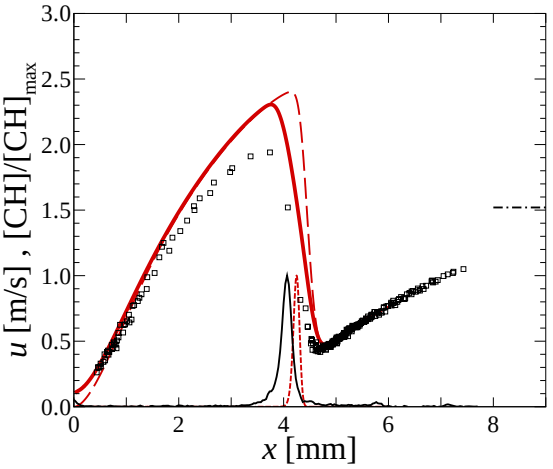

Figure I.14: C_2H_4-air flame profiles (Φ = 1.2, 16.5 %O_2:(O_2+N_2), run295). Legend as in Fig. I.1.

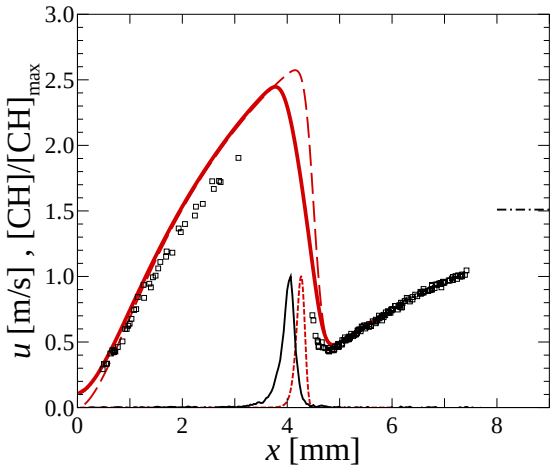

Figure I.15: C_2H_4-air flame profiles (Φ = 1.4, 18.0 %O_2:(O_2+N_2), run296). Legend as in Fig. I.1.

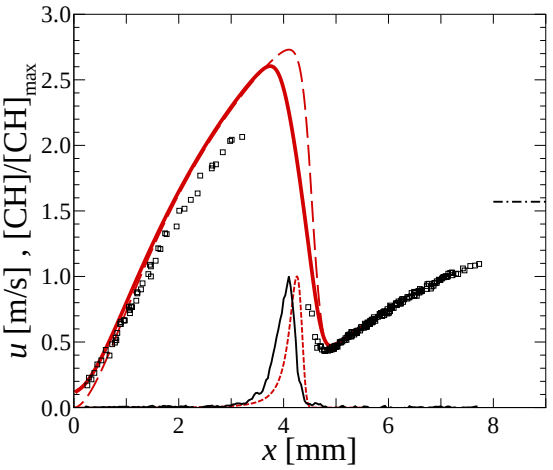

Figure I.16: C_2H_4-air flame profiles (Φ = 1.6, 21.0 %O_2:(O_2+N_2), run297). Legend as in Fig. I.1.

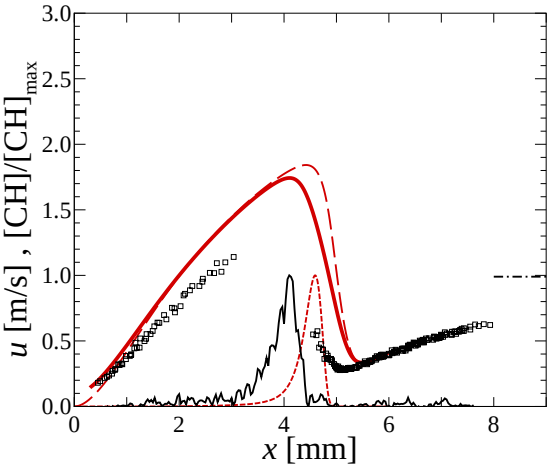

Figure I.17: C_2H_4-air flame profiles (Φ = 1.8, 21.0 %O_2:(O_2+N_2), run298). Legend as in Fig. I.1.

Appendix J

Premixed stagnation flame boundary conditions

The boundary conditions for each experimental run are reported here in Tables J.1-J.3.

run #	Φ	$\%O_2$:(O_2+N_2)	ℓ [mm]	u_ℓ [m/s]	V_ℓ [1/s]	T_ℓ [K]	T_{wall} [K]	U_{B} [m/s]
196	0.90	21.0	6	1.154	107	294.0	331.4	1.65
197	0.90	21.0	6	1.166	106	294.0	331.0	1.65
199	0.90	21.0	6	1.167	103	294.0	330.3	1.65
200	0.90	21.0	6	1.145	98	294.0	330.3	1.65
205	0.90	21.0	6	0.474	107	295.0	325.5	1.16
206	0.90	21.0	6	0.696	103	295.0	326.0	1.28
207	0.90	21.0	6	0.876	103	295.0	327.2	1.42
208	0.90	21.0	6	1.121	111	295.0	329.2	1.64
209	0.90	21.0	6	1.373	107	295.0	328.7	1.86
210	0.70	21.0	7	0.253	48	295.0	328.7	0.74
211	0.70	21.0	7	0.340	42	295.0	329.0	0.78
212	0.70	21.0	6	0.329	50	295.0	329.4	0.80
215	1.25	21.0	7	0.431	75	295.0	355.4	1.03
216	1.25	21.0	7	0.562	71	295.0	326.9	1.06
217	1.25	21.0	6	0.540	88	295.0	326.8	1.12
218	1.25	21.0	6	0.664	89	295.0	327.2	1.17
220	1.10	21.0	6	0.557	123	295.0	328.1	1.37
221	1.10	21.0	6	0.830	119	295.0	330.1	1.53
222	1.10	21.0	6	1.107	122	295.0	332.6	1.75
223	1.10	21.0	6	1.390	130	295.0	335.7	2.01
224	1.10	21.0	6	1.765	148	295.0	339.0	2.36
225	0.90	21.0	6	0.671	100	295.0	331.7	1.29
226	1.00	21.0	6	0.764	118	295.0	335.9	1.47
227	1.10	21.0	6	0.769	119	295.0	338.2	1.49
228	1.20	21.0	6	0.660	102	295.0	331.3	1.27
229	1.30	21.0	6	0.339	83	295.0	336.9	0.77
231	0.80	21.0	6	0.531	80	295.0	325.8	0.99
234	0.70	21.0	6	0.312	50	295.0	320.1	0.63
235	1.27	21.0	6	0.548	82	295.0	323.5	1.16
236	1.20	20.0	6	0.609	83	295.0	343.7	1.25
237	1.10	19.0	6	0.602	82	295.0	334.4	1.25
238	1.00	18.5	6	0.547	73	295.0	330.6	1.16
239	0.90	19.5	6	0.574	78	295.0	329.7	1.22
240	0.80	21.0	6	0.591	78	295.0	331.2	1.23
241	1.00	21.0	6	0.519	121	295.0	329.2	1.48
242	1.00	20.5	6	0.636	110	295.0	328.2	1.47
243	1.00	20.0	6	0.749	99	295.0	327.8	1.47
244	1.00	19.5	6	0.851	93	295.0	326.5	1.49
245	1.01	19.0	6	0.924	82	295.0	324.1	1.48

Table J.1: Boundary conditions for methane experiments.

run #	Φ	$\%O_2$:(O_2+N_2)	ℓ [mm]	u_ℓ [m/s]	V_ℓ [1/s]	T_ℓ [K]	T_{wall} [K]	U_{B} [m/s]
313	0.70	21.0	6	0.286	64	294.3	339.4	0.82
314	0.70	21.0	6	0.364	61	294.3	342.6	0.85
315	0.70	21.0	6	0.438	65	294.3	344.9	0.89
316	0.70	21.0	6	0.520	63	294.3	346.7	0.92
317	0.70	21.0	6	0.619	61	294.3	348.1	0.98
319	1.00	21.0	6	0.639	136	294.3	347.0	1.73
320	1.00	21.0	6	0.880	138	294.3	349.5	1.87
321	1.00	21.0	6	1.120	137	294.3	354.4	2.04
322	1.00	21.0	6	1.447	144	294.3	342.3	2.32
323	1.00	21.0	6	2.009	154	294.3	346.6	2.86
324	1.40	21.0	6	0.344	92	294.3	336.5	1.15
325	1.40	21.0	6	0.481	86	294.3	336.8	1.21
326	1.40	21.0	6	0.591	84	294.3	338.7	1.27
327	1.40	21.0	6	0.753	89	294.3	341.8	1.39
328	1.40	21.0	6	0.968	92	294.3	345.2	1.53
329	1.50	21.0	6	0.313	58	294.3	347.7	0.92
330	1.40	21.0	6	0.512	82	294.3	343.8	1.22
331	1.30	21.0	6	0.729	113	294.3	346.0	1.57
332	1.20	21.0	6	0.879	135	294.3	339.4	1.84
333	1.10	21.0	6	0.939	145	294.3	346.4	1.95
334	1.00	21.0	6	0.913	136	294.3	347.0	1.90
335	0.90	21.0	6	0.809	121	294.3	344.1	1.67
336	0.80	21.0	6	0.636	96	294.3	341.8	1.36
337	0.70	21.0	6	0.440	64	294.3	339.1	1.04

Table J.2: Boundary conditions for ethane experiments.

run #	Φ	$\%O_2$:(O_2+N_2)	ℓ [mm]	u_ℓ [m/s]	V_ℓ [1/s]	T_ℓ [K]	T_{wall} [K]	U_{B} [m/s]
302	0.70	21.0	6	0.652	123	294.3	339.3	1.46
303	0.70	21.0	6	0.819	123	294.3	340.9	1.56
304	0.70	21.0	6	1.037	122	294.3	343.4	1.73
305	0.70	21.0	6	1.354	127	294.3	344.3	2.01
306	0.70	21.0	6	1.924	146	294.3	348.8	2.58
307	1.60	21.0	6	0.515	119	294.3	335.9	1.38
308	1.60	21.0	6	0.693	119	294.3	340.5	1.48
309	1.60	21.0	6	0.879	123	294.3	344.7	1.61
310	1.60	21.0	6	1.132	125	294.3	350.4	1.82
311	1.60	21.0	6	1.511	129	294.3	335.6	2.16
295	1.20	16.5	6	0.765	118	294.3	339.4	1.52
296	1.40	18.0	6	0.742	118	294.3	338.4	1.51
297	1.60	21.0	6	0.742	126	294.3	341.5	1.57
298	1.80	21.0	6	0.402	76	294.3	334.9	0.99
299	1.00	17.0	6	0.837	122	294.3	340.0	1.60
300	0.80	19.5	6	0.882	135	294.3	340.8	1.70
301	0.60	21.0	6	0.518	77	294.3	325.5	1.03

Table J.3: Boundary conditions for ethylene experiments.

Appendix K

Reference flame speed tabulation

In stagnation flame experiments, the minimum of the velocity profile upstream of the flame is termed the reference flame speed, $S_{\mathrm{u,ref}}$. The velocity gradient upstream of the flame is taken to represent the imposed strain rate on the flame. For each experimental run, the velocity profile was fit using the function described in Appendix B. The minimum of the fit profile upstream of the flame was taken as an estimate of $S_{\mathrm{u,ref}}$, and a linear fit was performed on the velocity data in a 1 mm region upstream of the minimum to determine the imposed strain rate, $\sigma = \mathrm{d}u/\mathrm{d}x$. The values determined from these experiments are summarized in Tables K.1-K.3 for reference.

run #	Φ	$\%O_2$:(O_2+N_2)	σ [1/s]	$S_{u,ref}$ [m/s]
196	0.90	21.0	323	0.399
197	0.90	21.0	328	0.401
199	0.90	21.0	332	0.397
200	0.90	21.0	336	0.404
205	0.90	21.0	212	0.384
206	0.90	21.0	236	0.381
207	0.90	21.0	275	0.396
208	0.90	21.0	334	0.399
209	0.90	21.0	368	0.402
210	0.70	21.0	90	0.217
211	0.70	21.0	99	0.221
212	0.70	21.0	106	0.222
215	1.25	21.0	152	0.342
216	1.25	21.0	175	0.339
217	1.25	21.0	183	0.338
218	1.25	21.0	209	0.340
220	1.10	21.0	240	0.428
221	1.10	21.0	279	0.441
222	1.10	21.0	315	0.451
223	1.10	21.0	388	0.463
224	1.10	21.0	449	0.475
225	0.90	21.0	229	0.386
226	1.00	21.0	267	0.426
227	1.10	21.0	269	0.434
228	1.20	21.0	234	0.389
229	1.30	21.0	144	0.285
231	0.80	21.0	172	0.309
234	0.70	21.0	103	0.218
235	1.27	21.0	187	0.316
236	1.20	20.0	194	0.328
237	1.10	19.0	192	0.330
238	1.00	18.5	171	0.303
239	0.90	19.5	180	0.315
240	0.80	21.0	183	0.318
241	1.00	21.0	237	0.419
242	1.00	20.5	241	0.393
243	1.00	20.0	245	0.382
244	1.00	19.5	242	0.358
245	1.01	19.0	248	0.340

Table K.1: Reference flame speeds at various imposed strain rates for methane experiments.

run #	Φ	$\%O_2$:(O_2+N_2)	σ [1/s]	$S_{u,ref}$ [m/s]
313	0.70	21.0	121	0.263
314	0.70	21.0	127	0.268
315	0.70	21.0	136	0.266
316	0.70	21.0	156	0.270
317	0.70	21.0	171	0.268
319	1.00	21.0	278	0.466
320	1.00	21.0	317	0.476
321	1.00	21.0	355	0.489
322	1.00	21.0	413	0.487
323	1.00	21.0	553	0.514
324	1.40	21.0	167	0.303
325	1.40	21.0	185	0.319
326	1.40	21.0	201	0.321
327	1.40	21.0	220	0.328
328	1.40	21.0	256	0.340
329	1.50	21.0	116	0.225
330	1.40	21.0	187	0.313
331	1.30	21.0	252	0.423
332	1.20	21.0	315	0.476
333	1.10	21.0	348	0.500
334	1.00	21.0	323	0.476
335	0.90	21.0	286	0.429
336	0.80	21.0	221	0.356
337	0.70	21.0	150	0.266

Table K.2: Reference flame speeds at various imposed strain rates for ethane experiments.

run #	Φ	$\%O_2$:(O_2+N_2)	σ [1/s]	$S_{u,ref}$ [m/s]
302	0.70	21.0	254	0.445
303	0.70	21.0	291	0.459
304	0.70	21.0	324	0.456
305	0.70	21.0	381	0.477
306	0.70	21.0	492	0.487
307	1.60	21.0	236	0.402
308	1.60	21.0	265	0.412
309	1.60	21.0	286	0.432
310	1.60	21.0	340	0.434
311	1.60	21.0	418	0.438
295	1.20	16.5	276	0.437
296	1.40	18.0	262	0.439
297	1.60	21.0	273	0.429
298	1.80	21.0	150	0.281
299	1.00	17.0	270	0.459
300	0.80	19.5	306	0.486
301	0.60	21.0	165	0.308

Table K.3: Reference flame speeds at various imposed strain rates for ethylene experiments.

Appendix L

Electronic Appendix

This thesis includes a CD-ROM containing experimental data files for premixed stagnation flames of methane, ethane, and ethylene. The data files are accessible through tables embedded in an HTML file (Premixed_Flame_Data.htm) and information on the data files and formats are in a separate pdf file (Premixed_Flame_Data_Explanation.pdf). The table lists the boundary conditions for each experiment and links to the raw Particle Streak Velocimetry (PSV) data and CH Planar Laser Induced Fluorescence (PLIF) single-shot profiles. Also included are files for each fuel containing the fit parameters for the velocity profile and CH profile fitting functions. The data table is also available online (http://resolver.caltech.edu/CaltechETD:etd-05242005-165713).

Bibliography

Adamczyk, A. A. & Rimai, L., 1988. 2-Dimensional particle tracking velocimetry (PTV): technique and image processing algorithms. *Experiments in Fluids*, **6**:373–380.

Adrian, R. J., 1991. Particle-imaging techniques for experimental fluid mechanics. *Annual Review of Fluid Mechanics*, **23**:261–304.

Agüí, J. C. & Jiménez, J. J., 1987. On the performance of particle tracking. *Journal of Fluid Mechanics*, **185**:447–468.

Allen, M. D. & Raabe, O. G., 1985. Slip correction measurements of spherical solid aerosol particles in an improved Millikan apparatus. *Aerosol Science & Technology*, **4**:269–286.

Allen, M. G., Howe, R. D., & Hanson, R. K., 1986. Digital imaging of reaction zones in hydrocarbon-air flames using planar laser-induced fluorescence of CH and C_2. *Optics Letters*, **11** (3):126–128.

Altman, D. B., 1991. Statistics of optimal particle streak photography. *Physics of Fluids*, **3**: 2132–2137.

Ancimer, R., Wallace, J., & Jääskeläinen, H., 1999. Investigations into the effect of LDV seed particles on the operating characteristics of a spark ignition engine. *Experiments in Fluids*, **27**:175–180.

Andersen, J. W. & Fein, R. S., 1949. Measurements of normal burning velocities and flame temperatures of bunsen flames. *Journal of Chemical Physics*, **17**:1268–1273.

Andrews, G. E. & Bradley, D., 1972. Determination of burning velocities: a critical review. *Combustion & Flame*, **18**:133–153.

Bechtold, J. K. & Matalon, M., 1999. Effects of stoichiometry on stretched premixed flames. *Combustion & Flame*, **119**:217–232.

Bédat, B. & Cheng, R. K., 1996. Effects of buoyancy on premixed flame stabilization. *Combustion & Flame*, **107**:13–26.

Bergthorson, J. M., Goodwin, D. G., & Dimotakis, P. E., 2004. Experiments and modeling of impinging jets and premixed stagnation flames. In: *Proceedings of the Fifteenth Australasian Fluid Mechanics Conference*, M. Behnia, W. Lin, & G. D. McBain (Eds.). Paper number AFMC00087, `www.aeromech.usyd.edu.au/15afmc`.

Bergthorson, J. M., Goodwin, D. G., & Dimotakis, P. E., 2005a. Particle streak velocimetry and CH laser-induced fluorescence diagnostics in strained, premixed, methane-air flames. *Proceedings of the Combustion Institute*, **30**:1637–1644.

Bergthorson, J. M., Sone, K., Mattner, T. W., Dimotakis, P. E., Goodwin, D. G., & Meiron, D. I., 2005b. Experiments and modeling of impinging laminar jets at moderate separation distances. Technical Report GALCITFM:2005.003, Caltech. `http://resolver.caltech.edu/CaltechGALCITFM:2005.003`.

Birkhoff, G. & Zarantonello, E. H., 1957. *Jets, Wakes and Cavities*. Academic Press, New York.

Bonczyk, P. A. & Shirley, J. A., 1979. Measurement of CH and CN concentration in flames by laser-induced saturated fluorescence. *Combustion & Flame*, **34**:253–264.

Bosschaart, K. J. & de Goey, L. P. H., 2004. The laminar burning velocity of flames propagating in mixtures of hydrocarbons and air measured with the heat flux method. *Combustion & Flame*, **136**:261–269.

Box, G. E. P., Hunter, W. G., & Hunter, J. S., 1978. *Statistics for Experimenters: An Introduction to Design, Data Analysis and Model Building*. John Wiley & Sons, Inc., New York.

Bradbury, L. J. S., 1972. The impact of an axisymmetric jet onto a normal ground. *Aero Quart*, **23**:141–147.

Brock, J. R., 1962. On the theory of thermal forces acting on aerosol particles. *Journal of Colloid Science*, **17**:768–780.

Buckmaster, J., 1978. The quenching of a deflagration wave held in front of a bluff body. *Proceedings of the Combustion Institute*, **17**:835–842.

Burcat, A., 1984. Thermochemical data for combustion calculations, In: *Combustion Chemistry*, W. C. Gardiner, Jr. (Ed.), Chapter 8, pages 455–473, Springer-Verlag, New York.

Carter, C. D., Donbar, J. M., & Driscoll, J. F., 1998. Simultaneous CH planar laser-induced fluorescence and particle image velocimetry in turbulent nonpremixed flames. *Applied Physics B*, **66**:129–132.

Chao, B. H., Egolfopoulos, F. N., & Law, C. K., 1997. Structure and propagation of premixed flame in nozzle-generated counterflow. *Combustion & Flame*, **109**:620–638.

Chen, Y. & Mansour, M. S., 1997. Simultaneous Rayleigh scattering and laser-induced CH fluorescence for reaction zone imaging in high-speed premixed hydrocarbon flames. *Applied Physics B*, **64**:599–605.

Chung, S. H. & Law, C. K., 1988. An integral analysis of the structure and propaagation of stretched premixed flames. *Combustion & Flame*, **72**:325–336.

Chung, S. H. & Law, C. K., 1989. Analysis of some nonlinear premixed flame phenomena. *Combustion & Flame*, **75**:309–323.

Coltrin, M. E., Kee, R. J., & Evans, G. H., 1989. A mathematical-model of the fluid-mechanics and gas-phase chemistry in a rotating-disk chemical vapor-deposition reactor. *Journal of the Electrochemical Society*, **136**(3):819–829.

Crosley, D. R., 1989. Semiquantitative laser-induced fluorescence in flames. *Combustion & Flame*, **78**:153–167.

Daily, J. W., 1977. Saturation effects in laser induced fluorescence spectroscopy. *Applied Optics*, **16**:568–571.

Daily, J. W., 1978. Saturation of fluorescence in flames with a Gaussian laser beam. *Applied Optics*, **17**:225–229.

Daily, J. W., 1997. Laser induced fluorescence spectroscopy in flames. *Progress in Energy & Combustion Science*, **23**:133–199.

Daily, J. W. & Rothe, E. W., 1999. Effect of laser intensity and of lower-state rotational energy transfer upon temperature measurements made with laser-induced fluorescence. *Applied Physics B*, **68**:131–140.

Daneshyar, H. & Mendes-Lopes, J. M. C., 1982. Influence of strain on flame propagation in laminar flow. *International Journal of Mechanical Science*, **24**:529–535.

Daneshyar, H., Mendes-Lopes, J. M. C., & Ludford, G. S. S., 1982. Effect of strain fields on burning rate. *Proceedings of the Combustion Institute*, **19**:413–421.

Darahiba, N., Candel, S. M., & Marble, F. E., 1986. The effect of strain rate on a premixed laminar flame. *Combustion & Flame*, **64**:203–217.

Davis, S. G., Law, C. K., & Wang, H., 1999. Propene pyrolysis and oxidation kinetics in a flow reactor and laminar flames. *Combustion & Flame*, **119**:375–399.

Davis, S. G., Quinard, J., & Searby, G., 2001. A numerical investigation of stretch effects in counterflow, premixed laminar flames. *Combustion Theory & Modelling*, **5**:353–362.

Davis, S. G. & Searby, G., 2002. The use of counterflow flames for the evaluation of burning velocities and stretch effects in hydrogen/air mixtures. *Combustion Science & Technology*, **174**: 93–110.

Davis, S. G. & Wang, H., 2002. A new approach to response surface development for detailed combustion chemistry model development and optimization. (Unpublished).

Derjaguin, B. V., Rabinovich, YA. I., Storozhilova, A. I., & Shcherbina, G. I., 1976. Measurement of the coefficient of thermal slip of gases and the thermophoreses velocity of large-size aerosol particles. *Journal of Colloid and Interface Science*, **57**:451–461.

Derjaguin, B. V. & Yalamov, Y., 1965. Theory of thermophoresis of large aerosol particles. *Journal of Colloid Science*, **20**:555–570.

Derjaguin, B. V. & Yalamov, Y., 1966a. Authors' reply to Brock's discussion remarks on theory of thermophoresis of large aerosol particles. *Journal of Colloid Science*, **21**:256–257.

Derjaguin, B. V. & Yalamov, Y., 1966b. Correction. *Journal of Colloid Science*, **22**:195.

Deshpande, M. D. & Vaishnav, R. N., 1982. Submerged laminar jet impingement on a plane. *Journal of Fluid Mechanics*, **114**:213–236.

Dimotakis, P. E., Debussy, F. D., & Koochesfahani, M. M., 1981. Particle streak velocity field measurements in a two-dimensional mixing layer. *Physics of Fluids*, **24**:995–999.

Dixon-Lewis, G., 1990. Structure of laminar flames. *Proceedings of the Combustion Institute*, **23**: 305–324.

Dixon-Lewis, G. & Islam, S. M., 1982. Flame modelling and burning velocity measurement. *Proceedings of the Combustion Institute*, **19**:283–291.

Donbar, J. M., Driscoll, J. F., & Carter, C. D., 2000. Reaction zone structure in turbulent nonpremixed jet flames — from CH-OH PLIF images. *Combustion & Flame*, **122**:1–19.

Dong, Y., Andac, G. M., Egolfopoulos, F. N., Davis, S. G., & Wang, H., 2003. Experimental and numerical studies of flame extinction: validation of chemical kinetics. In *Proceedings of the Third Joint Meeting of the U.S. sections of the Combustion Institute.*

Dong, Y., Vagelopoulos, C. M., Spedding, G. R., & Egolfopoulos, F. N., 2002. Measurement of laminar flame speeds through digital particle image velocimetry: mixtures of methane

and ethane with hydrogen, oxygen, nitrogen, and helium. *Proceedings of the Combustion Institute*, **29**:1419–1426.

Dowling, D. R., 1988. *Mixing in gas phase turbulent jets.* Ph.D. thesis, California Institute of Technology.

Drazin, P. G. & Reid, W. H., 1981. *Hydrodynamic Stability.* Cambridge University Press, New York.

Durbin, P. A., 1982. The premixed flame in uniform straining flow. *Journal of Fluid Mechanics*, **121**:141–161.

Echekki, T. & Mungal, M. G., 1990. Flame speed measurements at the tip of a slot burner: Effects of flame curvature and hydrodynamic stretch. *Proceedings of the Combustion Institute*, **23**:455–461.

Eckbreth, A. C., 1996. *Laser Diagnostics for Combustion Temperature and Species, 2nd Edition.* Taylor & Francis, New York.

Egolfopoulos, F. N., 1994. Geometric and radiation effects on steady and unsteady strained laminar flames. *Proceedings of the Combustion Institute*, **25**:1375–1381.

Egolfopoulos, F. N. & Campbell, C. S., 1999. Dynamics and structure of dusty reacting flows: inert particles in strained, laminar, premixed flames. *Combustion & Flame*, **117**:206–226.

Egolfopoulos, F. N., Cho, P., & Law, C. K., 1989. Laminar flame speeds of methane-air mixtures under reduced and elevated pressures. *Combustion & Flame*, **76**:375–391.

Egolfopoulos, F. N. & Dimotakis, P. E., 2001. A comparative numerical study of premixed and non-premixed ethylene flames. *Combustion Science & Technology*, **162**:19–35.

Egolfopoulos, F. N., Zhang, H., & Zhang, Z., 1997. Wall effects on the propagation and extinction of steady, strained, laminar premixed flames. *Combustion & Flame*, **109**:237–252.

Egolfopoulos, F. N., Zhu, D. L., & Law, C. K., 1990. Experimental and numerical determination of laminar flame speeds: mixtures of C_2-hydrocarbons with oxygen and nitrogen. *Proceedings of the Combustion Institute*, **23**:471–478.

Eiteneer, B. & Frenklach, M., 2003. Experimental and modeling study of shock-tube oxidation of acetylene. *International Journal of Chemical Kinetics*, **35**:391–414.

Escudié, D., Haddar, E., & Brun, M., 1999. Influence of strain rate on a premixed turbulent flame stabilized in a stagnating flow. *Experiments in Fluids*, **27**:533–541.

Eteng, E., Ludford, G. S. S., & Matalon, M., 1986. Displacement effect of a flame in stagnation-point flow. *Physics of Fluids*, **29**:2172–2180.

Fang, M., Schmitz, R. A., & Ladd, R. G., 1971. Combustion of a premixed system in stagnation flow — II. experiments with carbon monoxide oxidation. *Combustion Science & Technology*, **4**: 143–148.

Frenklach, M., 1984. Modeling, In: *Combustion Chemistry*, W. C. Gardiner, Jr. (Ed.), Chapter 7, pages 423–453, Springer-Verlag, New York.

Frenklach, M. & Bornside, D. E., 1984. Shock-initiated ignition in methane-propane mixtures. *Combustion & Flame*, **56**:1–27.

Frenklach, M., Packard, A., & Seiler, P., 2002. Prediction uncertainty from models and data. In *Proceedings of the American Control Conference*, pages 4135–4140. IEEE Catalog Number 02CH37301C.

Frenklach, M., Packard, A., Seiler, P., & Feeley, R., 2003. Collaborative data processing in developing predictive models of complex reaction systems. *International Journal of Chemical Kinetics*, **36**:57–66.

Frenklach, M., Wang, H., & Rabinowitz, M. J., 1992. Optimization and analysis of large chemical kinetic mechanisms using the solution mapping method – combustion of methane. *Progress in Energy & Combustion Science*, **18**:47–73.

Fristrom, R. M., 1954. Erratum: Flame zone studies by the particle track technique. I. Apparatus and technique. *Journal of Chemical Physics*, **22**:1145.

Fristrom, R. M., Avery, W. H., Prescott, R., & Mattuck, A., 1954. Flame zone studies by the particle track technique. I. Apparatus and technique. *Journal of Chemical Physics*, **22**: 106–109.

Fristrom, R. M., Prescott, R., Neumann, R. K., & Avery, W. H., 1953. Temperature profiles in propane-air flame fronts. *Proceedings of the Combustion Institute*, **4**:267–274.

Fristrom, R. M. & Westenberg, A. A., 1965. *Flame Structure*. McGraw-Hill, Inc., New York.

Frouzakis, C. E., Lee, J., Tomboulides, A. G., & Boulouchos, K., 1998. Two-dimensional direct numerical simulation of opposed-jet hydrogen-air diffusion flame. *Combustion & Flame*, **116**:546–566.

Garland, N. L. & Crosley, D. R., 1985. Energy transfer processes in CH $A^2\Delta$ and $B^2\Sigma^-$ in an atmospheric pressure flame. *Applied Optics*, **24**:4229–4237.

Gilbert, M., Davis, L., & Altman, D., 1955. Velocity lag of particles in linearly accelerated combustion gases. *Jet Propulsion*, **25**:26–30.

Giovangigli, V. & Smooke, M. D., 1992. Application of continuation methods to plane premixed flames. *Combustion Science & Technology*, **87**:241–256.

Glarborg, P. & Miller, J. A., 1994. Mechanism and modeling of hydrogen-cyanide oxidation in a flow reactor. *Combustion & Flame*, **99**:475–483.

Glumac, N. G. & Goodwin, D. G., 1996. Diagnostics and modeling of strained fuel-rich acetylene/oxygen flames used for diamond deposition. *Combustion & Flame*, **105**(3):321–331.

Goldenberg, M. & Frenklach, M., 1995. A post-processing method for feature sensitivity coefficients. *International Journal of Chemical Kinetics*, **27**:1135–1142.

Gomez, A. & Rosner, D. E., 1993. Thermophoretic effects on particles in counterflow laminar diffusion flames. *Combustion Science & Technology*, **89**:335–362.

Goodwin, D. G., 2003. An open-source, extensible software suite for CVD process simulation. In *Proc. of CVD XVI and EuroCVD Fourteen,* Electrochem. Soc., pages 155–162.

Grcar, J. F., Kee, R. J., Smooke, M. D., & Miller, J. A., 1986. A hybrid Newton/time-integration procedure for the solution of steady, laminar, one-dimensional, premixed flames. *Proceedings of the Combustion Institute*, **21**:1773–1782.

Günther, R. & Janisch, G., 1972. Measurements of burning velocity in flat flame front. *Combustion & Flame*, **19**:49–53.

Gurevich, M. I., 1965. *Theory of Jets in Ideal Flows.* Academic Press, New York.

Haghgooie, M., Kent, J. C., & Tabaczynski, R. J., 1986. Verification of LDA and seed generator performance. *Experiments in Fluids*, **4**:27–32.

Han, D. & Mungal, M. G., 2003. Simulataneous measurements of velocity and CH distributions. Part 1: jet flames in co-flow. *Combustion & Flame*, **132**:565–590.

Hanson, R. K., 1988. Planar laser-induced fluorescence imaging. *Journal of Quantitative Spectroscopy & Radiative Transfer*, **40**:343–362.

Hanson, R. K., Seitzman, J. M., & Paul, P. H., 1990. Planar laser-fluorescence imaging of combustion gases. *Applied Physics B*, **50**:441–454.

Henderson, R. D. & Karniadakis, G. E., 1995. Unstructured spectral element methods for simulation of turbulent flows. *Journal of Chemical Physics*, **122**:191–217.

Herbon, J. T., Hanson, R. K., Golden, D. M., & Bowman, C. T., 2002. A shock tube study of the enthalpy of formation of OH. *Proceedings of the Combustion Institute*, **29**:1201–1208.

Hirasawa, T., Sung, C. J., Joshi, A., Yang, Z., Wang, H., & Law, C. K., 2002. Determination of laminar flame speeds using digital particle image velocimetry: binary fuel blends of ethylene, *n*-butane, and toluene. *Proceedings of the Combustion Institute*, **29**:1427–1434.

Hishida, K. & Sakakibara, J., 2000. Combined planar laser-induced fluorescence–particle image velocimetry technique for velocity and temperature fields. *Experiments in Fluids*, **29**:S129–S140.

Holley, A., Balteria, A., Dong, Y., Fan, Y., & Egolfopoulos, F. N., 2003. Premixed flame extinction of practical liquid fuels: experiments and simulations. In *Proceedings of the Third Joint Meeting of the U.S. sections of the Combustion Institute*, number PD11.

Houtman, C., Graves, D. B., & Jensen, K. F., 1986. CVD in stagnation point flow — an evaluation of the classical 1D-treatment. *Journal of the Electrochemical Society*, **133**(5):961–970.

Hughes, K. J., Turányi, T., Clague, A. R., & Pilling, M. J., 2001. Development and testing of a comprehensive chemical mechanism for the oxidation of methane. *International Journal of Chemical Kinetics*, **33**:513–538.

Incropera, F. P. & De Witt, D. P., 1990. *Fundamentals of Heat and Mass Transfer, 3rd Edition*. John Wiley & Sons, Inc., New York.

Ishizuka, S. & Law, C. K., 1982. An experimental study on extinction and stability of stretched premixed flames. *Proceedings of the Combustion Institute*, **19**:327–335.

Ishizuka, S., Miyasaka, K., & Law, C. K., 1982. Effects of heat loss, preferential diffusion, and flame stretch on flame-front instability and extinction of propane/air mixtures. *Combustion & Flame*, **45**:293–308.

Jackson, G. S., Sai, R., Plaia, J. M., Boggs, C. M., & Kiger, K. T., 2003. Influence of H_2 on the response of lean premixed CH_4 flames to high strained flows. *Combustion & Flame*, **132**: 503–511.

Ju, Y. & Minaev, S., 2002. Dynamics and flammability limits of stretched premixed flames stabilized by a hot wall. *Proceedings of the Combustion Institute*, **29**:949–956.

Karniadakis, G. E. & Sherwin, S. J., 1999. *Spectral/hp element methods for CFD*. Oxford University Press, New York.

Kee, R. J., Coltrin, M. E., & Glarborg, P., 2003. *Chemically Reacting Flow - Theory & Practice*. John Wiley & Sons, Inc., New Jersey.

Kee, R. J., Miller, J. A., Evans, G. H., & Dixon-Lewis, G., 1988. A computational model of the structure and extinction of strained, opposed flow, premixed methane-air flames. *Proceedings of the Combustion Institute*, **22**:1479–1494.

Keh, H. J. & Ou, C. L., 2004. Thermophoresis of aerosol spheroids. *Aerosol Science & Technology*, **38**:675–684.

Kern, B., Lang, D. B., Martin, C., Dimotakis, P. E., & Wadsworth, M., 2001. A high-speed quadrature-phase rotation-shearing interferometer for imaging through turbulence. *AIAA Paper*, **2001**:2797.

Kim, J. S., Libby, P. A., & Williams, F. A., 1992. On the displacement effects of laminar flames. *Combustion Science & Technology*, **87**:1–25.

Kim, Y. D. & Matalon, M., 1988. Propagation and extinction of a flame in a stagnation-point flow. *Combustion & Flame*, **73**:303–313.

Kim, Y. J. & Kim, S. S., 1991. Particle size effects on the particle deposition from non-isothermal stagnation point flows. *Journal of Aerosol Science*, **22**:201–214.

Kohse-Höinghaus, K., Heidenreich, R., & Just, TH., 1984. Determination of absolute OH and CH concentrations in a low pressure flame by laser-induced saturated fluorescence. *Proceedings of the Combustion Institute*, **20**:1177–1185.

Kohse-Höinghaus, K., Perc, W., & Just, TH., 1983. Laser-induced saturated fluorescence as a method for the determination of radical concentrations in flames. *Berichte Der Bunsen-Gesellschaft–Physical Chemistry Chemical Physics*, **87**:1052–1057.

Kostiuk, L. W., Bray, K. N. C., & Cheng, R. K., 1993. Experimental study of premixed turbulent combustion in opposed streams: Part I — non-reacting flow field. *Combustion & Flame*, **92**:377–395.

Kumar, A. & Pandya, T. P., 1970. Use of particle track technique in studies on flames. *Indian Journal of Pure & Applied Physics*, **8**:42–45.

Kurosoy, E. & Whitelaw, J. H., 2001. Opposed jets with small separations and their implications for the extinction of opposed flames. *Experiments in Fluids*, **31**:111–117.

Landau, L. D. & Lifshitz, E. M., 1987. *Fluid Mechanics, 2nd Edition*. Butterworth-Heinemann, Oxford.

Landreth, C. C. & Adrian, R. J., 1990. Impingement of a low Reynolds number turbulent circular jet onto a flat plate at normal incidence. *Experiments in Fluids*, **9**:74–84.

Law, C. K., Ishizuka, S., & Mizomoto, M., 1981. Lean-limit extinction of propane/air mixtures in the stagnation-point flow. *Proceedings of the Combustion Institute*, **18**:1791–1798.

Law, C. K. & Sung, C. J., 2000. Structure, aerodynamics, and geometry of premixed flamelets. *Progress in Energy & Combustion Science*, **26**:459–505.

Law, C. K., Sung, C. J., Wang, H., & Lu, T. F., 2003. Development of comprehensive detailed and reduced reaction mechanisms for combustion modeling. *AIAA Journal*, **41**:1629–1646.

Law, C. K., Sung, C. J., Yu, G., & Axelbaum, R. L., 1994. On the structural sensitivity of purely strained planar premixed flames to strain rate variations. *Combustion & Flame*, **98**: 139–154.

Lewis, B. & von Elbe, G., 1943. Stability and structure of burner flames. *Journal of Chemical Physics*, **11**:75–97.

Lewis, B. & von Elbe, G., 1961. *Combustion, Flames and Explosions of Gases, 2nd Edition*. Academic Press, Inc., New York.

Li, W. & Davis, E. J., 1995a. Measurement of the thermophoretic force by electrodynamic levitation: Microspheres in air. *Journal of Aerosol Science*, **26**:1063–1083.

Li, W. & Davis, E. J., 1995b. The effects of gas and particle properties on thermophoresis. *Journal of Aerosol Science*, **26**:1085–1099.

Libby, P. A., 1998. Premixed laminar flames in impinging flows. *Combustion Science & Technology*, **131**:345–379.

Libby, P. A., Liñan, A., & Williams, F. A., 1983. Strained premixed laminar flames with nonunity Lewis numbers. *Combustion Science & Technology*, **34**:1–42.

Libby, P. A. & Smooke, M. D., 1997. The computation of flames in stagnation flows. *Combustion Science & Technology*, **127**:197–211.

Libby, P. A. & Williams, F. A., 1983. Strained premixed laminar flames under nonadiabatic conditions. *Combustion Science & Technology*, **31**:1–42.

Libby, P. A. & Williams, F. A., 1987. Premixed laminar flames with general rates of strain. *Combustion Science & Technology*, **54**:237–273.

Liepmann, H. W., 1943. Investigations on laminar boundary-layer stability and transition on curved boundaries. Technical report, NACA Wartime Report W-107. ACR No. 3H30.

Loyalka, S. K., 1992. Thermophoretic force on a single particle—I. Numerical solution of the linearized Boltzmann equation. *Journal of Aerosol Science*, **23**:291–300.

Luque, J. & Crosley, D. R., 1996. Absolute CH concentrations in low-pressure flames measured with laser-induced fluorescence. *Applied Physics B*, **63**:91–98.

Luque, J. & Crosley, D. R., 1999. Lifbase : database and spectral simulation program (Version 1.5). Technical Report MP 99-009, SRI International.

Luque, J., Klein-Douwel, R. J. H., Jeffries, J. B., & Crosley, D. R., 2000. Collisional processes near the CH $B^2\Sigma^-$ $v' = 0, 1$ predissociation limit in laser-induced fluorescence flame diagnostics. *Applied Physics B*, **71**:85–94.

Luque, J., Klein-Douwel, R. J. H., Jeffries, J. B., Smith, G. P., & Crosley, D. R., 2002. Quantitative laser-induced fluorescence of CH in atmospheric pressure flames. *Applied Physics B*, **75**:779–790.

Luque, J., Smith, G. P., & Crosley, D. R., 1996. Quantitative CH determinations in low-pressure flames. *Proceedings of the Combustion Institute*, **26**:959–966.

Marko, K. A. & Rimai, L., 1985. Video recording and quantitative analysis of seed particle track images in unsteady flows. *Applied Optics*, **24**:3666–3672.

Maurel, S. & Solliec, C., 2001. A turbulent plane jet impinging nearby and far from a flat plate. *Experiments in Fluids*, **31**:687–696.

Melling, A., 1997. Tracer particles and seeding for particle image velocimetry. *Measurement Science & Technology*, **8**:1406–1416.

Mendes-Lopes, J. M. C., 1983. *Influence of strain fields on flame propagation.* Ph.D. thesis, Cambridge University.

Mendes-Lopes, J. M. C. & Daneshyar, H., 1985. Influence of strain fields on flame propagation. *Combustion & Flame*, **60**:29–48.

Miller, J. A., Kee, R. J., & Westbrook, C. K., 1990. Chemical kinetics and combustion modeling. *Annual Review of Physical Chemistry*, **41**:345–387.

Nishioka, M., Law, C. K., & Takeno, T., 1996. A flame-controlling continuation method for generating S-curve responses with detailed chemistry. *Combustion & Flame*, **104**:328–342.

Norton, T. S. & Smyth, K. C., 1991. Laser-induced fluorescence of CH· in a laminar CH_4/air diffusion flame: implications for diagnostic measurements and analysis of chemical rates. *Combustion Science & Technology*, **76**:1–20.

Ono, H., Dobashi, R., & Sakuraya, T., 2002. Thermophoretic velocity measurements of soot particles under a microgravity condition. *Proceedings of the Combustion Institute*, **29**:2375–2382.

Pandya, T. P. & Srivastava, N. K., 1975. Structure of counterflow diffusion flame of ethanol. *Combustion Science & Technology*, **11**:165–180.

Pandya, T. P. & Weinberg, F. J., 1964. The structure of flat, counter-flow diffusion flames. *Proceedings of the Royal Society of London Series A–Mathematical and Physical Sciences*, **279A**: 544–561.

Paul, P. & Warnatz, J., 1998. A re-evaluation of the means used to calculate transport properties of reacting flows. *Proceedings of the Combustion Institute*, **27**:495–504.

Paul, P. H. & Dec, J. E., 1994. Imaging of reaction zones in hydrocarbon-air flames by use of planar laser-induced fluorescence of CH. *Optics Letters*, **19**:998–1000.

Peters, N., 1986. Laminar flamelet concepts in turbulent combustion. *Proceedings of the Combustion Institute*, **21**:1231–1250.

Phares, D. J., Smedley, G. T., & Flagan, R. C., 2000a. The inviscid impingement of a jet with arbitrary velocity profile. *Physics of Fluids*, **12**:2046–2055.

Phares, D. J., Smedley, G. T., & Flagan, R. C., 2000b. The wall shear stress produced by the normal impingement of a jet on a flat surface. *Journal of Fluid Mechanics*, **418**:351–375.

Prandtl, L. & Tietjens, O. G., 1954. *Applied Hydro- and Aeromechanics*. Dover Publications, Inc., New York.

Qin, Z., Lissianski, V. V., Yang, H., Gardiner, W. C., & Davis, S. G., 2000. Combustion chemistry of propane: a case study of detailed reaction mechanism optimization. *Proceedings of the Combustion Institute*, **28**:1663–1669.

Ratner, A., Driscoll, J. F., Donbar, J. M., Carter, C. D., & Mullin, J. A., 2000. Reaction zone structure of non-premixed turbulent flames in the "intensely wrinkled" regime. *Proceedings of the Combustion Institute*, **28**:245–252.

Renfro, M. W., Chaturvedy, A., & Laurendeau, N. M., 2001. Semi-quantitative measurements of CH concentration in atmospheric-pressure counterflow diffusion flames using picosecond laser-induced fluorescence. *Combustion Science & Technology*, **169**:25–43.

Rensberger, K. J., Dyer, M. J., & Copeland, R. A., 1988. Time-resolved CH ($A^2\Delta$ and $B^2\Sigma^-$) laser-induced fluorescence in low pressure hydrocarbon flames. *Applied Optics*, **27**:3679–3689.

Rogg, B., 1988. Response and flamelet structure of stretched premixed methane-air flames. *Combustion & Flame*, **73**:45–65.

Rolon, J. C., Veynante, D., Martin, J. P., & Durst, F., 1991. Counter jet stagnation flows. *Experiments in Fluids*, **11**:313–324.

Rubel, A., 1980. Computations of jet impingement on a flat surface. *AIAA Journal*, **18**:168–175.

Rubel, A., 1983. Inviscid axisymmetric jet impingement with recirculating stagnation regions. *AIAA Journal*, **21**:351–357.

Samimy, M. & Lele, S. K., 1991. Motion of particles with inertia in a compressible free shear layer. *Physics of Fluids*, **3**:1915–1923.

San Diego mechanism. Chemical-kinetic mechanisms for combustion applications, Center for Energy Research (Combustion Division), University of California at San Diego. `http://maeweb.ucsd.edu/combustion/cermech/`.

Santachiara, G., Prodi, F., & Cornetti, C., 2002. Experimental measurements on thermophoresis in the transition region. *Journal of Aerosol Science*, **33**:769–780.

Sato, J., 1982. Effects of Lewis number on extinction behaviour of premixed flames in stagnation flow. *Proceedings of the Combustion Institute*, **19**:1541–1548.

Schach, W., 1935. Deflection of a circular fluid jet by a flat plate perpendicular to the flow direction. *Ingenieur-Archiv*, **6**:51–59.

Schlichting, H., 1960. *Boundary Layer Theory*. McGraw-Hill, Inc., New York.

Seshadri, K. & Williams, F. A., 1978. Laminar flow between parallel plates with injection of reactant at high Reynolds number. *International Journal of Heat and Mass Transfer*, **21**:251–253.

Shan, J. W. & Dimotakis, P. E., 2001. Turbulent mixing in liquid-phase transverse jets. Technical Report CaltechGALCITFM:2001.006, Caltech. `http://resolver.library.caltech.edu/CaltechGalcitFM:2001.006`.

Simmie, J. M., 2003. Detailed chemical kinetic models for the combustion of hydrocarbon fuels. *Progress in Energy & Combustion Science*, **29**:599–634.

Sivashinsky, G. I., 1976. On a distorted flame front as a hydrodynamic discontinuity. *Acta Astronautica*, **3**:889–918.

Smith, F. A., 1937. Problems of stationary flames. *Chemical Reviews*, **21**:389–412.

Smith, G. P., Golden, D. M., Frenklach, M., Moriarty, N. W., Eiteneer, B., Goldenberg, M., Bowman, C. T., Hanson, R. K., Song, S., Gardiner, W. C., Jr., Lissianski, V. V., & Qin, Z. GRI-Mech 3.0. `http://www.me.berkeley.edu/gri_mech/`.

Smith, H. W., Schmitz, R. A., & Ladd, R. G., 1971. Combustion of a premixed system in stagnation flow — I. theoretical. *Combustion Science & Technology*, **4**:131–142.

Smooke, M. D., Crump, J., Seshadri, K., & Giovangigli, V., 1990. Comparison between experimental measurements and numerical calculations of the structure of counterflow, diluted, methane-air, premixed flames. *Proceedings of the Combustion Institute*, **23**:463–470.

Stårner, S. H., Bilger, R. W., Dibble, R. W., Barlow, R. S., Fourguette, D. C., & Long, M. B., 1992. Joint planar CH and OH LIF imaging in piloted turbulent jet diffusion flames near extinction. *Proceedings of the Combustion Institute*, **24**:341–349.

Stella, A., Guj, G., Kompenhans, J., Raffel, M., & Richard, H., 2001. Application of particle image velocimetry to combusting flows: design considerations and uncertainty assessment. *Experiments in Fluids*, **30**:167–180.

Strand, T., 1964. On the theory of normal ground impingement of axisymmetric jets in inviscid incompressible flow. *AIAA Paper*, **64–424**.

Sugiyama, G., 1994. Nonluminous diffusion flame of diluted acetylene in oxygen-enriched air. *Proceedings of the Combustion Institute*, **25**:601–608.

Sun, C. J. & Law, C. K., 2000. On the nonlinear response of stretched premixed flames. *Combustion & Flame*, **121**:236–248.

Sun, C. J., Sung, C. J., He, L., & Law, C. K., 1999. Dynamics of weakly stretched flames: quantitative description and extraction of global flame parameters. *Combustion & Flame*, **118**: 108–128.

Sun, C. J., Sung, C. J., Zhu, D. L., & Law, C. K., 1996. Response of counterflow premixed and diffusion flames to strain rate variations at reduced and elevated pressures. *Proceedings of the Combustion Institute*, **26**:1111–1120.

Sung, C. J., Kistler, J. S., Nishioka, M., & Law, C. K., 1996a. Further studies on effects of thermophoresis on seeding particles in LDV measurements of strained flames. *Combustion & Flame*, **105**:189–201.

Sung, C. J., Law, C. K., & Axelbaum, R. L., 1994. Thermophoretic effects on seeding particles in LDV measurements of flames. *Combustion Science & Technology*, **99**:119–132.

Sung, C. J., Liu, J. B., & Law, C. K., 1996b. On the scalar structure of nonequidiffusive premixed flames in counterflow. *Combustion & Flame*, **106**:168–183.

Sutton, J. A. & Driscoll, J. F., 2003. Optimization of CH fluorescence diagnostics in flames: range of applicability and improvements with hydrogen addition. *Applied Optics*, **42**:2819–2828.

Takubo, Y., Yano, H., Matsuoka, H., & Shimazu, M., 1983. Saturation behavior of laser-induced CH fluorescence in a propane-air flame. *Journal of Quantitative Spectroscopy & Radiative Transfer*, **30**:163–168.

Talbot, L., 1980. Thermophoresis—a review, In: *Rarefied Gas Dynamics—Part I*, S. S. Fisher (Ed.), volume 74, pages 467–488, American Institute of Aeronautics and Astronautics, New York.

Talbot, L., Cheng, R. K., Schefer, R. W., & Willis, D. R., 1980. Thermophoresis of particles in a heated boundary layer. *Journal of Fluid Mechanics*, **101**:737–758.

Tewari, G. P. & Weinberg, F. J., 1967. Structure of flame quenched by cold surfaces. *Proceedings of the Royal Society of London Series A–Mathematical and Physical Sciences*, **296**:546–565.

Tien, J. H. & Matalon, M., 1991. On the burning velocity of stretched flames. *Combustion & Flame*, **84**:238–248.

Toda, A., Ohi, Y., Dobashi, R., Hirano, T., & Sakuraya, T., 1996. Accurate measurement of thermophoretic effect in microgravity. *Journal of Chemical Physics*, **105**:7083–7087.

Toda, A., Ohnishi, H., Dobashi, R., Hirano, T., & Sakuraya, T., 1998. Experimental study on the relation between thermophoresis and size of aerosol particles. *International Journal of Heat and Mass Transfer*, **41**:2710–2713.

Turányi, T., Zalotai, L., Dóbé, S., & Bérces, T., 2002. Effect of the uncertainty of kinetic and thermodynamic data on methane flame simulation results. *Physical Chemistry Chemical Physics*, **4**:2568–2578.

Vagelopoulos, C. M., 1999. *An experimental and numerical study on the stability and propagation of laminar premixed flames*. Ph.D. thesis, University of Southern California.

Vagelopoulos, C. M. & Egolfopoulos, F. N., 1998. Direct experimental determination of laminar flame speeds. *Proceedings of the Combustion Institute*, **27**:513–519.

Vagelopoulos, C. M., Egolfopoulos, F. N., & Law, C. K., 1994. Further considerations on the determination of laminar flame speeds with the counterflow twin-flame technique. *Proceedings of the Combustion Institute*, **25**:1341–1347.

Verdieck, J. F. & Bonczyk, P. A., 1981. Laser-induced saturated fluorescence investigations of CH, CN and NO in flames. *Proceedings of the Combustion Institute*, **18**:1559–1566.

Vincenti, W. G. & Kruger, C. H., Jr., 1965. *Introduction to Physical Gas Dynamics*. John Wiley & Sons, Inc., New York.

Wagner, A. F., 2002. The challenges of combustion for chemical theory. *Proceedings of the Combustion Institute*, **29**:1173–1200.

Warnatz, J., 1984a. Chemistry of high temperature combustion of alkanes up to octane. *Proceedings of the Combustion Institute*, **20**:845–856.

Warnatz, J., 1984b. Rate coefficients in the C/H/O system, In: *Combustion Chemistry*, W. C. Gardiner, Jr. (Ed.), Chapter 5, pages 197–360, Springer-Verlag, New York.

Warnatz, J., 1992. Resolution of gas phase and surface combustion chemistry into elementary reactions. *Proceedings of the Combustion Institute*, **24**:553–579.

Westbrook, C. K. & Dryer, F. L., 1984. Chemical kinetic modeling of hydrocarbon combustion. *Progress in Energy & Combustion Science*, **10**:1–57.

White, F. M., 1991. *Viscous Fluid Flow, 2nd Edition*. McGraw-Hill, Inc., New York.

Williams, F. A., 2000. Progress in knowledge of flamelet structure and extinction. *Progress in Energy & Combustion Science*, **26**:657–682.

Wu, C. K. & Law, C. K., 1984. On the determination of laminar flame speeds from stretched flames. *Proceedings of the Combustion Institute*, **20**:1941–1949.

Yang, M. H. & Puri, I. K., 1993. Experimental investigation of stretched premixed flames burning mixtures of methane and methyl chloride in air and comparison with numerical simulations. *Combustion & Flame*, **94**:25–34.

Yang, Z., Yang, B., & Wang, H., 2001. The influence of H-atom diffusion coefficient on laminar flame simulation. *Proceedings of the second joint meeting of the U.S. Sections of the Combustion Institute*. Oakland, CA.

Zhang, H. & Egolfopoulos, F. N., 2000. Extinction of near-limit premixed flames in microgravity. *Proceedings of the Combustion Institute*, **28**:1875–1882.

Zheng, F., 2002. Thermophoresis of spherical and non-spherical particles: a review of theories and experiments. *Advances in Colloid and Interface Science*, **97**:255–278.

Zhu, D. L., Egolfopoulos, F. N., & Law, C. K., 1988. Experimental and numerical determination of laminar flame speeds of methane/(Ar, N_2, CO_2)-air mixtures as function of stoichiometry, pressure, and flame temperature. *Proceedings of the Combustion Institute*, **22**:1537–1545.